DISSERTATION

# THE IMPACT OF SEVERAL HAIL PARAMETERS ON SIMULATED SUPERCELL STORMS

Submitted by

Susan Claire van den Heever

Department of Atmospheric Science

In partial fulfillment of the requirements

For the Degree of Doctor of Philosophy

Colorado State University

Fort Collins, Colorado

Fall, 2001

ProQuest Information and Learning Company
300 North Zeeb Road
P.O. Box 1346
Ann Arbor, MI 48106-1346

COLORADO STATE UNIVERSITY

November 2, 2001

WE HEREBY RECOMMEND THAT THE DISSERTATION PREPARED UNDER OUR SUPERVISION BY SUSAN CLAIRE VAN DEN HEEVER ENTITLED THE IMPACT OF SEVERAL HAIL PARAMETERS ON SIMULATED SUPERCELL STORMS BE ACCEPTED AS FULFILLING IN PART REQUIREMENTS FOR THE DEGREE OF DOCTOR OF PHILOSOPHY.

Committee on Graduate Work

Advisor

Department Head

# ABSTRACT

## THE IMPACT OF SEVERAL HAIL PARAMETERS ON SIMULATED SUPERCELL STORMS

Most modeling studies of supercell storms neglect the ice phase. However, supercells are often prolific producers of hail and extend deep enough in the troposphere that active participation by the ice phase in storm dynamics would be expected. Therefore, the sensitivity of simulated supercell characteristics to variations in the settings of several ice parameters is investigated.

In the first sensitivity test, decreasing the mean hail diameter affects the hail size distribution by increasing the number of smaller hailstones and decreasing the number of larger hailstones. Melting and evaporation rates are greater in the smaller hail diameter cases, which result in stronger low-level downdrafts and more intense cold pools. The stronger downdrafts enhance the low-level convergence within the updraft, thereby forcing stronger updrafts and greater low-level vertical vorticity through stretching. However, the stronger downdrafts also occlude the low-level updrafts more rapidly, and the storms are shorter-lived. The longevity of the left-moving storm decreases as the mean hail diameter decreases, and is controlled primarily by the low-level buoyant forcing which is negative.

The maximum surface precipitation is greater in the larger hail cases, but the precipitation covers a smaller area. The storms in the small hail cases resemble classic supercells, whereas those in the large hail cases possess high-precipitation supercell characteristics. This suggests that the precipitation characteristics of the storm may determine the type of supercell that develops.

Increasing the shape parameter of the hail size distribution in the second sensitivity test decreases the low-level downdrafts and associated divergence. However, the distance between the downdraft and updraft also decreases as the shape parameter increases, thereby increasing the low-level convergence within the updraft, and hence the updraft strength and low-level vertical vorticity.

Excluding all hail-related processes in the third sensitivity test results in greater rain mixing ratios, however, the rain remains suspended at higher levels. The presence of hail therefore affects the rain distribution within the storm by increasing rain in the lower levels through melting, and reducing rain in the upper levels through droplet freezing. Excluding hail delays the development of the low-level mesocyclone, through the slower evolution of the low-level downdrafts.

In the final sensitivity test, the use of two-moment bulk microphysics results in the presence of larger hail below cloud base and smaller hail above the melting level, a wider vertical and horizontal distribution of hail, and reduced rain mixing ratios at the surface. Several supercell characteristics were better developed when using the two-moment scheme.

All of the sensitivity tests indicate that if a steady, long-lived updraft and low-level mesocyclone are to develop, a balance is needed between the characteristics of the hail size distribution which influence the strength and position of the low-level downdrafts, and the strength of the low-level environmental winds which prevent the gust front from outrunning the storm. The balance is sensitive to the parameters determining the hail size distribution, and thus these parameters need to be determined accurately.

Susan Claire van den Heever
Department of Atmospheric Science
Colorado State University
Fort Collins, Colorado 80523
Fall 2001

# ACKNOWLEDGEMENTS

I would like to thank my advisor Bill Cotton for his guidance, insight and flexibility. I have greatly benefited from his vast practical and theoretical expertise in cloud microphysics and dynamics. I would also like to thank my committee members Dick Johnson, Wayne Schubert and Gerald Taylor. Wayne Schubert patiently answered many atmospheric dynamics questions, and Dick Johnson's class on mesoscale dynamics was most useful.

Lewis Grasso allowed me to perform simulations on his computer, and provided me with code. We also had numerous valuable discussions on the analysis of severe storms. His input is greatly appreciated. Bob Walko is also acknowledged for answering questions about RAMS.

Brian Gaudet is thanked for many informative discussions on severe storms and supercells, and for his moral support. The technical advice and sense of humor of Travis Ashby are appreciated. Chris Golaz, Hans Verlinde, Mark Sellers, Alex Costa and Ting Wu are acknowledged for their moral and/or scientific contributions.

Ed Brandes is thanked for providing me with initial radar data on hail storms. The advice of Lou Wicker is appreciated.

Joan Hellmund is thanked for her extensive proof reading of this dissertation. I am grateful to Brenda Thompson for her administrative assistance. The assistance of Jason Connor with computer issues is acknowledged.

A dissertation is never completed without the help of many people behind the scenes. Judy Arledge, the Hellmund family and the Juell family are gratefully acknowledged in all that they have done in this respect.

Liz Page has taught me much about operational meteorology and the problems facing forecasters. She is thanked for her encouragement and support throughout the course of this study, for helping me see the funnier side of things, and for the friendship we have.

Lastly, I would like to express my appreciation for my family. Thanks are extended to my parents, Pam and Andrew Dickson, who first stimulated my interest in science, and who have continued to support me in all my activities. The joy and love of my children, Nicola and Mathew, have been a daily inspiration. I thank them for their enthusiasm and help. Finally, I am grateful to my husband Steve, for his love and patience, for his flexibility, for his encouragement when the going got tough, for his faith in my ability, and for his unwavering support. Without him, I would not have started, nor finished, my PhD.

Financial support for this research was provided by the National Science Foundation under grant No. ATM-9900929.

# TABLE OF CONTENTS

# 1

# Introduction

Many numerical simulations of supercells have been conducted without ice microphysics. This is despite the fact that supercells often produce large quantities of hail, and that the presence of ice is thought to have a significant effect on both the thermodynamics and dynamics of severe storms. While some success has been achieved when modeling supercell storms without the ice phase, the impact of excluding ice is not well understood. Several numerical simulations conducted over the last decade demonstrate that the absence of ice can have a significant effect on supercell development and characteristics (Jewett et al., 1990; Johnson et al., 1993; Tartaglione et al., 1996).

In the past, the ice phase has been excluded from supercell simulations due to time and computer constraints, and the lack of implementation of ice physics schemes into mesoscale models. Given the computer resources and microphysical schemes that are currently available, as well as the apparent influence of ice on supercell storms, future numerical modeling of these storms should, at the very least, include initial sensitivity tests to the determine the impact of excluding ice processes.

After deciding on which microphysical scheme to use, of which there are many (e.g. Lin et al., 1983; Farley and Orville, 1986; Ferrier, 1993; Walko et al., 1995; Reisin, 1996; Meyers et al., 1997; Hong and Pen, 1999), further decisions frequently need to be

made involving specific microphysical parameters. Selecting which microphysical species to represent and determining an appropriate size distribution of the species, are examples of some of the options that may need to be considered when using a single-moment bulk microphysics scheme. Also, the parameters may need to be set for a broad range of storm systems if the model is used in operational mode, where "tweaking" of the parameters is not an option.

Determining suitable values for the microphysical parameters is made difficult by the lack of in-situ cloud data, and the fact that the values can vary significantly from one storm system to another. As a result of these difficulties, the parameter values are often chosen somewhat arbitrarily, or the default values are employed. Given the difficulties in determining appropriate parameter settings and the apparent significance of ice processes in supercell storm development, it is important that we understand the impact of the ice parameters on severe storm simulations. The goal of the work presented in this dissertation is to determine the sensitivity of simulated supercell storms to several ice parameters.

The outline of this manuscript is as follows. In Chapter 2, a literature survey of the dynamical and precipitation characteristics of supercell storms is conducted, and previous simulations investigating the impact of ice on supercell storm dynamics are presented. The model configuration and experiment design are presented in Chapter 3. Results showing the impact of changing the mean hail diameter on simulated supercells are presented and analyzed in Chapter 4. In Chapter 5, mechanisms responsible for enhancing the longevity of the left-moving supercell in the large hail cases are presented. The sensitivity of the simulated supercells to excluding ice processes, to changes in the shape of the hail distribution, and to using a more sophisticated two-moment scheme is presented in Chapter 6. Final conclusions are drawn and suggestions for future work are made in Chapter 7.

# 2

# Background

## 2.1 Introduction

More than 90% of supercells are associated with severe weather (tornadoes, large hail, flash flooding, strong straight-line winds), about half of all supercells produce tornadoes, and the majority of strong or violent tornadoes are generated by supercells (Davies-Jones, 1982; Moller et al., 1994; Burgess and Lemon, 1991). Supercell storms are relatively rare compared with other types of storms. However, their contribution to thunderstorm-related damage and loss of life is proportionately high (Moller et al., 1994), making the prediction of such storms an important forecasting problem.

The term "supercell" was first introduced by Browning (1964). Browning (1977) recognized the importance of the mesocyclone in supercell dynamics, and used it to distinguish supercells from other thunderstorm types. Weisman and Klemp (1984) demonstrated, through the use of mesoscale models, that it is the presence of the mesocyclone that make supercells dynamically different from other forms of convective storms, and that there is a strong degree of correlation between the mesocyclone and an updraft. Currently it appears that the most widely accepted definition of a supercell is a "*convective storm that contains a deep, persistent mesocyclone*" (Johns and Doswell, 1992; Doswell and Burgess, 1993; Moller et al., 1994; Doswell, 1996; Markowski and

Straka, 2000). 'Deep' is taken to mean that the mesocyclone extends and is continuous throughout a significant fraction (>~1/3) of the depth of the storm; 'persistent' means in comparison to a convective time scale which is defined as the time it takes for a parcel to rise through the updraft (~ 10 to 20 minutes); and mesocyclone is generally defined to be a region of vertical vorticity of magnitude greater than 0.01 $s^{-1}$ (Brandes, 1984; Doswell and Burgess, 1993; Doswell, 1996). Although this supercell definition is somewhat arbitrary, is does appear to assist in separating those storms that are capable of producing severe weather from those that are less likely to (Moller et al., 1994), and thus, will be used for the research presented here.

## 2.2 Supercell Environments

Supercells occur throughout the world, and have been documented in numerous regions including Argentina (e.g. Nunez, 1980), Australia (e.g. Moller et al., 1994), Belgium (e.g. Vertez, 1992), Canada (e.g. Chisolm and Renick, 1972), England (e.g. Browning and Ludlam, 1962), France (e.g. Dessens and Snow, 1989), Japan (e.g. Niino et al., 1993), Russia (e.g. Goral and Fedchenko, 1992), South Africa (e.g. Admirat, 1985), Switzerland (e.g. Schmid et al., 1997), and the USA (e.g. Browning, 1964; Ray et al., 1975; Doswell and Burgess, 1993). Within the United States, supercells are most common in the central regions. However, they also occur to the east of the Appalachians and have even been observed west of the Continental Divide (Moller et al., 1994).

Two predominant environmental factors that determine what type of convective storm will develop are buoyancy (Convective Available Potential Energy) and vertical wind shear (particularly in lower 3 to 4 km), with the latter appearing to have the greater effect. Both observations and numerical models show that environments of moderate to high buoyancy and high vertical wind shear appear to favor supercell storms (e.g. Fawbush and Miller, 1954; Chisolm and Renick, 1972; Maddox, 1976; Darkow and

McCann,1977; Fankhauser and Mohr, 1977; Weisman and Klemp, 1982, 1984; Rasmussen and Wilhelmson, 1983; Burgess and Curran, 1985). Convective Available Potential Energy (CAPE) values for supercell environments are usually greater than 2000 J $kg^{-1}$, although many develop in environments with CAPE less than 1500 J $kg^{-1}$, and have even been observed to occur when the CAPE is as little as 200 J $kg^{-1}$ (Johns and Doswell, 1992). Vertical wind shear magnitudes of greater than 20-25 $m.s^{-1}$ of wind variation over the lowest 4-6 km AGL seem necessary to support supercell development (Weisman and Rotunno, 2000). It has also been suggested recently that the strength of the mid-level (3-7km AGL) (Brooks et al., 1994b) and upper-level (9-10km AGL) (Rasmussen and Straka, 1998) shear may be important in supercell development.

In an attempt to quantify the relationship between buoyancy and shear in determining the type of storm that is likely to be develop, Weisman and Klemp (1982, 1984) introduced the bulk Richardson number (BRN), which is the ratio of CAPE to the density-weighted vertical wind shear over the lowest 6km. They suggested from their modeling study that supercells are favored when the BRN is between 15 and 35, while multicell storms are more predominant for a BRN greater than 35.

Two other measures of the atmosphere's potential to produce a mesocyclone are helicity and storm-relative helicity (SRH). Helicity is defined in general as $H = \vec{V}.\vec{\omega}$, where H is the helicity, $\vec{V}$ is the three-dimensional wind vector, and $\vec{\omega}$ is the vorticity vector. It has been shown from observations and model simulations of supercells (e.g. Weisman and Klemp, 1982, 1984) that there are strong, positive correlations between vertical velocity and vertical vorticity. The resultant magnitude of helicity for supercells is therefore large. Lilly (1986) suggested that as helicity suppresses the turbulent energy cascade to smaller scales, and as supercells are largely helical, that these storms are less subject to dissipation through turbulence than other thunderstorms.

The vertical component of SRH is given by

$$SRH = -\int_{0}^{d} \vec{k} \cdot (\bar{V} - \bar{c}) \times \frac{\partial \bar{V}}{\partial z} dz \qquad (2.1)$$

where d is the depth of the layer of interest (normally ~3km), $\vec{k}$ is the unit vector in the vertical direction, $\bar{c}$ is the storm velocity vector, and z is the vertical direction component; all other symbols have been previously defined. SRH is therefore dependant on the strength of the storm-relative winds and on the streamwise vorticity (see below) and has proved useful in the forecasting environment (Davies-Jones et al., 1990). The critical value above which supercells are possible lies between SRH ≥ 100-150 $m^2s^{-2}$ (Davies-Jones et al., 1990; Moller et al., 1994) and SRH ≥ 250 $m^2s^{-2}$ (Droegemeier et al., 1993).

The nature of the wind profile in the storm inflow layer (Weisman and Klemp, 1982, 1984), and the strength of the storm-relative inflow (Lazarus and Droegemeier, 1990) have also been found important to supercell genesis and maintenance. In general, strong low-level winds, veering of hodographs with height, and storm motion to the right of the mean wind, favor the development of mesocyclones, although these conditions are not necessary for mesocyclogenesis. One of the weaknesses of the BRN is that although it makes use of the low-level shear, it does not account for any directional changes in the shear vector with height. Droegemeier et al. (1993) found that several different types of convection were possible for the same magnitude of CAPE and shear, and hence for the same BRN. SRH may therefore be a better indicator of the possibility of mesocyclone development.

In a study using more than 6000 soundings taken during 1992, Rasmussen and Blanchard (1998) evaluated the use of several wind and CAPE parameters in discriminating between nonsupercell thunderstorms, supercells without tornadoes, and supercells with tornadoes. They found that parameters that combine the effects of buoyancy and shear on supercells, like the energy-helicity index ($EHI = \frac{(CAPE)(SRH)}{1.6 \times 10^5}$)

(Hart and Korotky, 1991; Davies, 1993) and the vorticity generation parameter ($VGI = S(CAPE)^{1/2}$, where S is the mean shear) (Rasmussen and Wilhelmson, 1983), appear to have more value in predicting supercell environments than those parameters that include only one of these effects. The EHI, which includes the directional influence of shear, appeared to be a better discriminator than the VGP.

## 2.3 Supercell Storm Structure and Dynamics

Browning (1964) developed a conceptual model of the three-dimensional flow and structure of a supercell, which has survived with only minor modifications. The development and improvement of Doppler radar (e.g. Ray et al., 1975, 1980, 1981; Brandes, 1978, 1981, 1984; Lemon and Doswell, 1979; Lemon, 1980; Bluestein and Woodall, 1990; Dowell et al., 1997; Bluestein and MacGorman, 1998) and three-dimensional numerical models (e.g. Klemp and Wilhelmson, 1978a,b; Klemp et al., 1981; Weisman and Klemp, 1982, 1984; Weisman and Bluestein, 1985; Brooks and Wilhelmson, 1992; Brooks et al., 1994b; Finley, 1997; Kulie and Lin, 1998; Adlerman et al., 1999) since then have enhanced our understanding of supercell storm dynamics and structure.

### 2.3.1 *Supercell Storm Structure*

The basic idea of Browning's (1964) model is that a supercell storm achieves longevity through an airflow pattern that allows the updraft to unload its precipitation without disrupting the storm's inflow of warm, moist air. His model was based on a right-moving (RM) storm, although he later suggested the possibility of a left-moving (LM) storm that is the mirror image of the RM supercell discussed in his model (Browning, 1968). Browning (1964) recognized the role of strong vertical wind shear in the development of supercells, and stressed that the motion of the low- and mid-level

tropospheric winds toward the right flank of the storm is responsible for the supercell structure and characteristics that are observed.

Browning's model of airflow structure within a RM supercell is shown in Figure 2.1. Low-level (L) air that is moist and buoyant approaches the storm from the forward right flank where it rises in the rotating updraft. This inflow air, which is considered to be the origin of the updraft air, is then carried upwards through the storm and diverges in the anvil cloud (H). The coldest air entering the storm is generally located at middle levels (M) on the right rear flank. This cold, dry air flows ahead of the updraft through the region of precipitation where it is evaporatively cooled. A strong, evaporatively-induced downdraft develops and descends on the left rear flank of the updraft. Precipitation produced in the storm is transported out of the updraft and into the downdraft by the mid-level inflow (and enhanced by the rotational nature of the updraft). The precipitation produced by the supercell does not, therefore, interfere with the inflow of air into the storm.

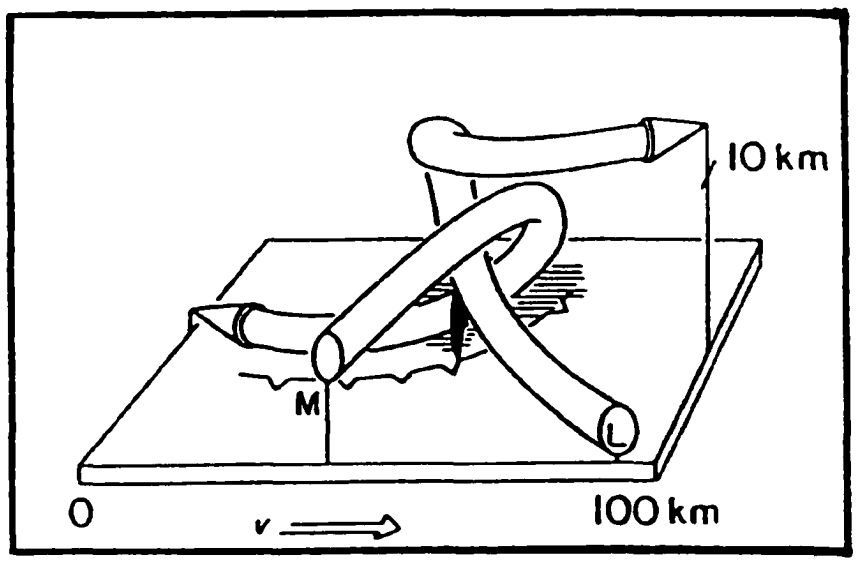


**Figure 2.1: A three-dimensional model of the airflow within a right-moving supercell storm. The updraft and downdraft circulations are shown relative to the storm. Convergence and divergence is neglected. L and M refer to the predominant origins of the updraft and downdraft, respectively. Also shown is the approximate area of precipitation at the surface, and the positions of the surface gust front and tornado (should one occur). The vertical scale has been exaggerated five times (after Browning, 1964).**

Evaporative cooling continues to strengthen the downdrafts, which diverge in all directions when reaching the surface. The resulting gust front along the forward right flank of the storm then enhances the influx of the low-level warm, moist air into the storm through convergence. The cycle continues and the storm strengthens. The separation of the updraft and downdrafts, the removal of precipitation from the updraft, and the enhanced convergence and moisture influx along the gust front all result in a self-perpetuating, long-lived storm. Klemp et al. (1981) stressed the dependence of the storm strength on the rotational nature of the storm, which separates the precipitation from the updraft, and orients the resulting downdrafts to enhance the low-level convergence zone along the gust front. The self-perpetuating structure, suggested by Browning, is supported by observations of supercell storms that have lasted for several hours (e.g. Browning and Foote, 1976).

Weisman and Klemp (1982) also investigated the conditions necessary for the development of a self-sustaining supercell storm. They found that if the low-level environment was too stable for the amount of CAPE available (buoyancy effect) or if the gust front moved away from the developing storm too quickly (shear effect), then successive storm development would not occur. Also, if there was sufficient CAPE but the vertical wind shear was too weak, the downdraft was not displaced away from the updraft and a self-sustaining structure could not develop. If the vertical wind shear was too strong, the developing storm would be sheared apart. The BRN provides an indication of the balance that is needed between the buoyancy and shear effects if supercells are to develop.

Radar signatures, like the hook echo, have long been recognized as indicators of severe storms and possible tornadic activity (Fujita, 1958; Battan, 1959; Browning and Donaldson, 1963). The radar characteristics of a typical supercell are shown in Figure 2.2. The prominent features include a large, overhanging echo ahead of the storm, a region of low reflectivity (vault or bounded weak echo region (BWER)) which extends

a)

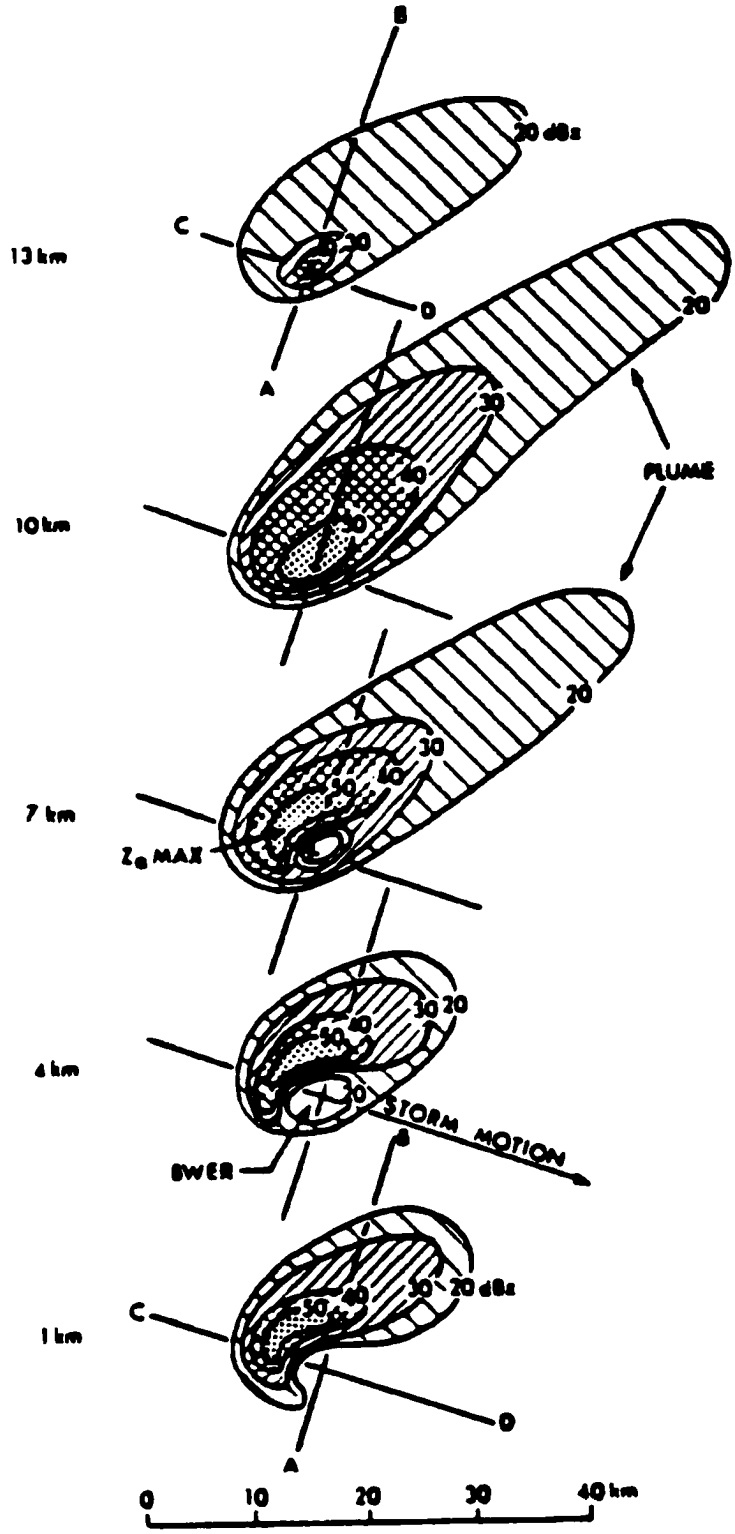


**(Figure continues on the next page)**

b)

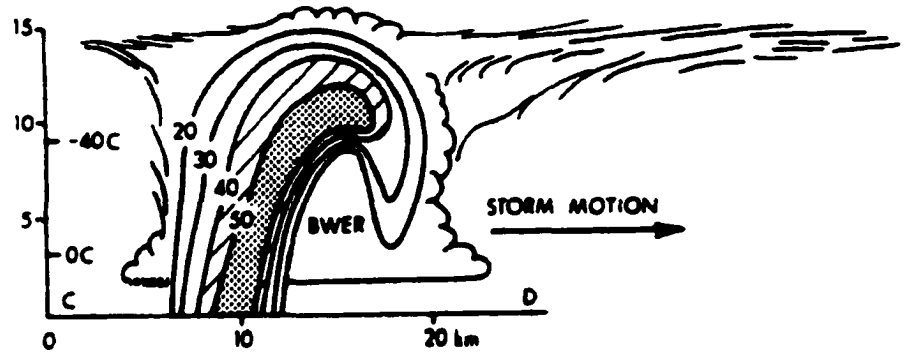


**Figure 2.2: (a) Schematic diagram showing horizontal sections of the radar structure of a supercell storm at 1,4,7,10 and 13km AGL. Reflectivity contours are labeled in dBz. Note the indentation on the right front quadrant of the storm at 1km which appears as a weak echo vault (or BWER) at 4 and 7km. On the left rear side of the vault is a reflectivity maximum that extends from the top of the vault to the ground. (b) Schematic vertical section along the line CD shown in (a). Note the reflectivity maximum (often referred to as the hail cascade), which is situated on the left, rear flank of the BWER. The overhanging region of the echo bounding the other side of the vault is referred to as the embryo curtain. Some of the embryos from this region are recycled across the updraft to grown into large hailstones (after Chisholm and Renick, 1972).**

into the storm below its highest top, and an intense hook echo which surrounds the vault at the lower levels. Browning's three-dimensional model of supercell airflow supports these radar features that are often, although not always, observed with supercell storms.

Browning's model is most applicable to the developing and mature stage of a supercell storm. The transition of a supercell into its collapsing phase was examined in detail by Lemon and Doswell (1979). An intense updraft and two downdrafts are the main structural features of their model (Figure 2.3), which in spite of some modifications, is still consistent with Browning's model. The forward flank downdraft (FFD) is located downwind of the mid-level (3-5 km) flow in the region of strong precipitation. The rear flank updraft (RFD) lies upwind of the updraft (relative to the 7-10 km flow). Their model may be described as follows: as the storm begins to collapse, precipitation starts to occur in the updraft, the reflectivity increases within the BWER, and the mid-level mesocyclone shifts upwind from the BWER region to the region of greatest vertical

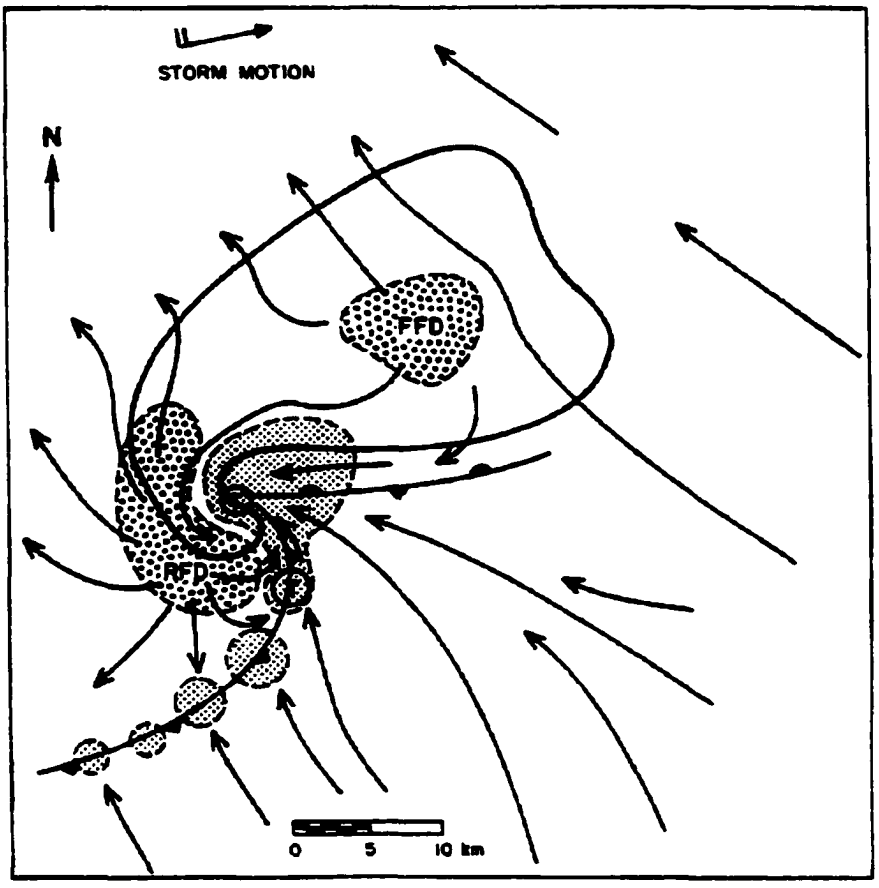


**Figure 2.3: The low-level airflow structure and precipitation distribution of a supercell thunderstorm based on surface observations and radar analysis (from Lemon and Doswell, 1979; adapted by Davies-Jones, 1986). FFD is the forward flank downdraft, RFD is the rear flank downdraft and T indicates the position most conducive for tornado formation.**

velocity gradients between the updraft and the RFD. It is only after the development of this divided (part of it is in the updraft, and part in the downdraft) mesocyclone structure that tornadoes have been observed to form (Brandes, 1978). As the updrafts weaken, the RFD strengthens and interacts with FFD outflow, thereby forming the occlusion. The mesocyclone then descends as the RFD increases, and the RFD wraps cyclonically around the low-level mesocyclone. Tornadoes are normally located at the tip of the occlusion (on the updraft side of the updraft-downdraft interface), but may also develop along the trailing gust front. As the occluding gust front progresses, the low-level inflow of warm, moist air is cut off and the storm collapses.

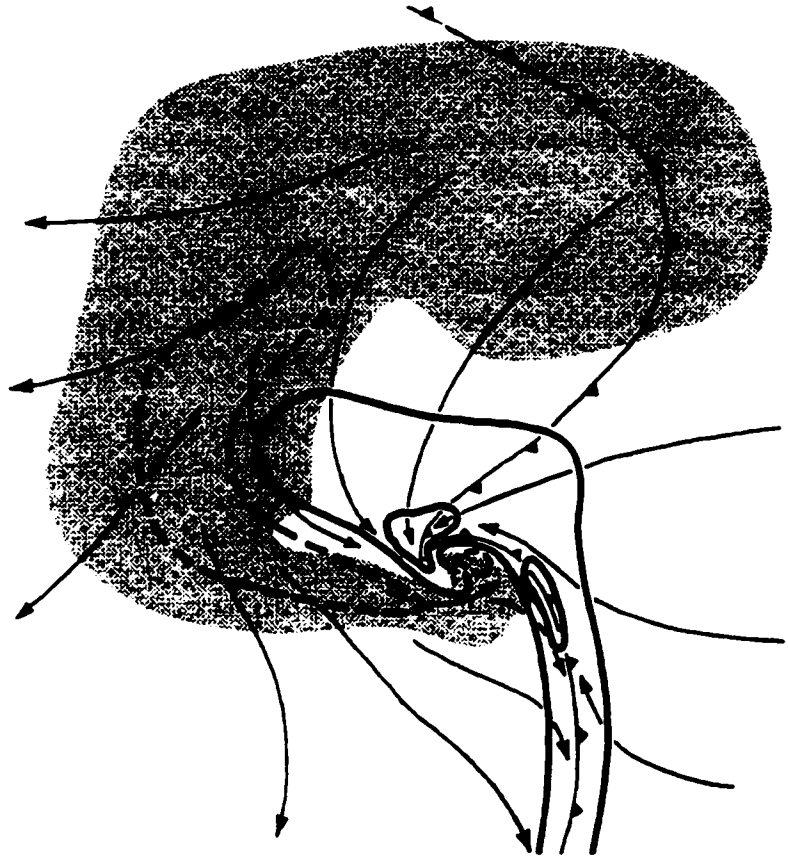

**Figure 2.4: Schematic low-level flow field composite from the low-level storm-scale and finer-scale resolution simulations of Klemp and Rotunno (1983). Vertical velocity is represented by the thick solid and dashed lines at a contour interval of 2m/s with the zero line omitted. The -1°C isotherm is denoted by conventional frontal symbols. Flow arrows represent storm relative surface streamlines and the region where rainwater exceeds 0.5 g.kg$^{-1}$ is shaded. The location of maximum vertical vorticity is marked with a T. Both the rear flank downdraft to the west of the updraft and the occlusion downdraft near the center of circulation are evident (after Klemp and Rotunno, 1983).**

Klemp and Rotunno (1983) simulated many of the supercell occlusion phase features described by Lemon and Doswell (1979) using a one-way nested grid with horizontal grid resolution of 250m. They observed that as the storm progressed to the tornadic phase strong rotation at low levels along the line of convergence caused a low pressure to develop in the low levels, coincident with the circulation center. The resultant downward- directed pressure gradient force (PGF) enhanced the development of a small-scale occlusion downdraft, which developed first at low levels and then extended upward as the flow adjusted to the vertical pressure gradient (Figure 2.4). This dynamically-driven occlusion downdraft, which is distinct from the RFD, enhanced the development

of the occlusion and divided the updraft at mid-levels. Wicker and Wilhelmson (1995) have also observed the role of the occlusion downdraft in their simulations of tornadogenesis.

### 2.3.2 *Storm Splitting and Subsequent Storm Motion*

#### *Storm Splitting*

Storm splitting was first observed using radar reflectivity fields during the 1960s (e.g. Fujita and Grandoso, 1968). Two storm cells develop following the splitting process. The right-moving (RM) storm moves to the right (e.g. Browning and Donaldson, 1963; Marwitz, 1972) and the left-moving (LM) storm moves to the left (Browning, 1968; Charba and Sasaki, 1971) of the mean wind. Browning (1964) was the first to associate rightward motion with a cyclonically rotating updraft. Others soon discovered that LM storms rotate anticyclonically (e.g. Fujita and Grandoso, 1968). Browning and Landry (1963) and Barnes (1970) first hypothesized that it is the tilting of horizontal vorticity that results in the cyclonically rotating updraft. However, their theories did not consider the anticyclonically rotating updrafts. The development of dual-Doppler radar has since shown that storm splitting begins with the splitting of the updraft core (Bluestein and Sohl, 1979; Knupp and Cotton, 1982), and storm propagation and rotation are closely linked (Browning, 1977). Simulations utilizing three-dimensional numerical cloud models have also enhanced our understanding of storm splitting, and the subsequent storm propagation and rotation (e.g. Klemp and Wilhelmson, 1978a,b; Wilhelmson and Klemp, 1978, 1981; Thorpe and Miller, 1978; Clark, 1979; Schlesinger, 1980; Klemp at al., 1981; Rotunno and Klemp, 1982, 1985; Weisman and Klemp, 1984; Tripoli and Cotton, 1986; Grasso, 2000).

Two questions need to be addressed: 1) how does storm splitting actually occur, and 2) what causes the RM storm to rotate cyclonically, while the LM rotates anticyclonically. Three-dimensional numerical models with unidirectional, westerly hodographs have been used to investigate these issues (e.g. Schlesinger, 1975; Klemp and Wilhelmson, 1978a; Rotunno, 1981). In the initial stage, a horizontal vortex tube is associated with the vertical wind shear. As there is no horizontal variation in the environmental wind shear, there is no vertical vorticity or divergence initially. Following the development of a convective updraft, the horizontal vortex tube is tilted into the vertical by the horizontal gradients in vertical velocity. A cyclonically (anticyclonically) rotating vortex develops on the right (left) of the updraft (with respect to the shear vector) at both the mid- and low-levels (Figure 2.5a). The vertical vorticity will be greatest just below the region of maximum vertical velocity in the updraft, where the horizontal vertical velocity gradients are greatest. Stretching amplifies, but does not significantly change, the distribution of the mid-level vertical vorticity. The next phase begins with the weakening of vertical velocity in the updraft center. As the downdraft develops, the vortex tubes are tilted downward and two vortex pairs develop, one on either side of the shear vector (Figure 2.5b). Finally, the central portion of the updraft is replaced by a downdraft and the initial cell splits, producing two storms, each containing a vortex couplet. The storm with the cyclonically (anticyclonically) rotating updraft moves to the right (left) of the mean wind.

The vorticity distribution may be further investigated, as described by Rotunno (1981), using the vertical vorticity equation linearized about the environmental wind. The vertical vorticity equation is given by

$$\frac{D\zeta}{Dt} = \frac{\partial \zeta}{\partial t} + U\frac{\partial \zeta}{\partial x} = \vec{\omega}_h \cdot \nabla_h w \tag{2.2}$$

where $D/Dt = \partial/\partial t + U\partial/\partial x$ and $\vec{\omega}_h \cdot \nabla_h w = \partial U/\partial z \cdot \partial w/\partial y$ in this case. Here, $\zeta$ is the vertical component of vorticity, t is time, x and y are the horizontal components of

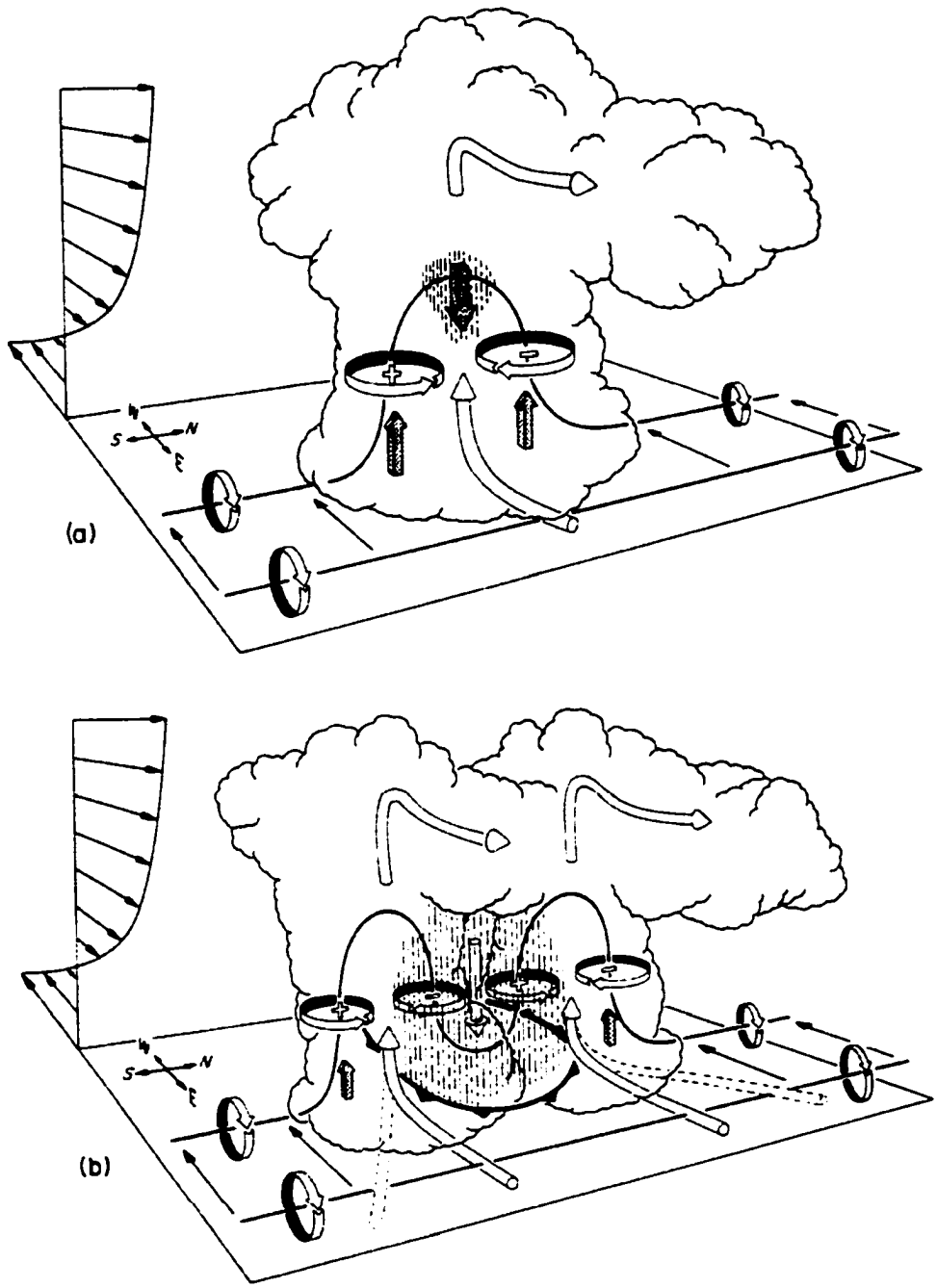


**Figure 2.5: Schematic showing how a horizontal vortex tube generated by westerly environmental shear is tilted as it interacts with a convective cell. Cylindrical arrows show the direction of the storm-relative airflow, and heavy solid lines represent vortex lines with the sense of rotation indicated by circular arrows. Shaded arrows represent the forcing influences that promote new updraft and downdraft growth. Vertical dashed lines denote regions of precipitation. The cold outflow beneath the storm is represented by conventional frontal symbols. (a) Initial stage: horizontal vortex tube is swept into the vertical by the developing updraft. (b) Splitting stage: a downdraft forms between the splitting updraft cells and this tilts the vortex tubes in this region downward, producing two vortex pairs (adapted by Klemp (1987), from Rotunno, 1981).**

direction, w is the vertical velocity, and the subscript h refers to the horizontal. As the environmental wind is westerly and increases with height, $\partial U / \partial z > 0$, and positive (negative) vorticity will be generated on the south (north) of the updraft where $\partial w / \partial y$ is positive (negative). As the downdraft develops, $\partial w / \partial y$ changes sign causing the development of negative (positive) vorticity on the north (south) side of the split pair (Bluestein and Sohl, 1979; Rotunno, 1981; Rotunno and Klemp, 1985).

How then does storm splitting actually occur? Klemp and Wilhelmson (1978a) and Wilhelmson and Klemp (1978) attributed splitting to strong water loading that developed in the center of the initial updraft following the development of rain. The precipitation-induced downdraft caused an initial split of the updraft at lower levels and also generated a gust front beneath the storm. The enhanced convergence between the gust front and the ambient air increased the influx of warm, moist air into storm, thereby increasing the low-level updrafts located on the flanks of the initial cell. The low-level updrafts continued to move apart as the gust front split and propagated outward. The upper level updrafts then split as they followed the low-level updrafts. The downdraft then also split. A simulation in which precipitation was not allowed to develop revealed that the cell did not split.

Schlesinger (1980) found from his numerical simulations that strong rainwater loading within the cloud did contribute to splitting, however, contributions made by the vertical perturbed pressure gradient force (PGF) were of a comparable magnitude. A downward directed PGF in the middle of the initial cell acted in the same direction as the drag to enhance the downdraft, and an upward directed PGF on both storm flanks enhanced updraft development in these locations. In this manner, the PGF aided storm splitting. Schlesinger cited observational evidence that dynamical processes initially control the splitting process (although water loading may later enhance the process); two updrafts are often evident before the radar echo splits. He also found that ingestion and

mixing of cool environmental air into the downdraft enhanced the splitting process. Clark (1979) drew a similar conclusion from his simulations regarding entrainment.

Klemp and Wilhelmson (1978a) found that when there was no vertical shear, the initial cell did not split, and that negative buoyancy associated with precipitation loading soon resulted in cell dissipation. Wilhelmson and Klemp (1978) showed that directionally varying shear was not necessary for storm splitting. They also found that the low-level shear needed to be sufficiently strong to inhibit the gust front from propagating away from the storm too quickly. If the low-level shear was too strong, splitting did not occur as the updraft and downdrafts were both weak due to mixing. Therefore, water loading, the PGF and vertical wind shear all appear to have an impact on storm splitting.

***Storm Motion***

Storms move to the left and right of the mean wind following the splitting of the initial cell. RM storms are observed more frequently (in the northern hemisphere). RM (LM) storms maintain their intensity by propagating slower and to the right (faster and to the left) of the mean wind. This ensures the maximum inflow of air from the front and right (left) into the storm at low and mid-levels respectively for the RM (LM) (Browning, 1968; Fankhauser, 1971).

Klemp and Wilhelmson (1978b) used their numerical model to investigate the environmental conditions that favor RM or LM storms following splitting. They found from varying the hodograph, that clockwise turning (veering) of the hodograph with height favors RM storms, whereas counterclockwise turning (backing) of the hodograph favors LM storms. This bias is most pronounced for hodograph curvature in the lower levels. Klemp and Wilhelmson suggested the following hypothesis: when the hodograph turns clockwise with height, the mid-level inflow into the downdraft of the RM is increased, thereby enhancing the downdraft, the low-level outflow and the development

of the gust front. This in turn strengthens convergence along the gust front and storm longevity. Clockwise turning of the hodograph with height reduces the mid-level inflow of air into the LM, which produces the opposite effects to those for the RM. The LM storm is therefore weak and short-lived. The situation is reversed when the hodograph backs with height, and the LM is then the long-lived storm. Their hypothesis also shows that when the hodograph is unidirectional (and with no Coriolis force), the RM and LM storms will be mirror images of one another. Wilhelmson and Klemp (1981) found from their case study simulation that veering of the hodograph tended to slow the development of the LM, due to an unfavorable pressure gradient; however, convergence along the gust front prevented its demise.

Rotunno and Klemp (1982) made use of linear theory to further investigate the bias in storm rotation and propagation that was observed in their simulations. They presented the following scenario: the perturbation pressure is proportional to $\frac{d\bar{V}_h}{dz} \cdot \nabla_h w'$. where $'$ represents perturbations from the mean or base state. From this relation it is apparent that a negative pressure gradient develops across the updraft in the direction of the shear vector. If the shear vector does not change direction with height, areas of relative high (low) pressure will be stacked above areas of relative high (low) pressure, and the storm will develop symmetrically (Figure 2.6a). However, if the shear vector changes direction with height, then vertical pressure gradients will develop that favor storm development on one side of the original cell and suppress storm development on the other side (Figure 2.6b). Typically, when the hodograph veers (backs) with height, the right (left) flank of the original cell is favored (looking along the shear vector). The result is a dominant RM (LM) supercell. From the perturbation vorticity equation

$$\frac{D}{Dt}\zeta' = \bar{k} \cdot \left( \frac{d\bar{V}_h}{dz} \times \nabla_h w' \right) \tag{2.3}$$

it is evident that cyclonic (+) and anticyclonic (-) vorticity centers will develop on the right and left side of the shear vector respectively. Using the same argument as for the

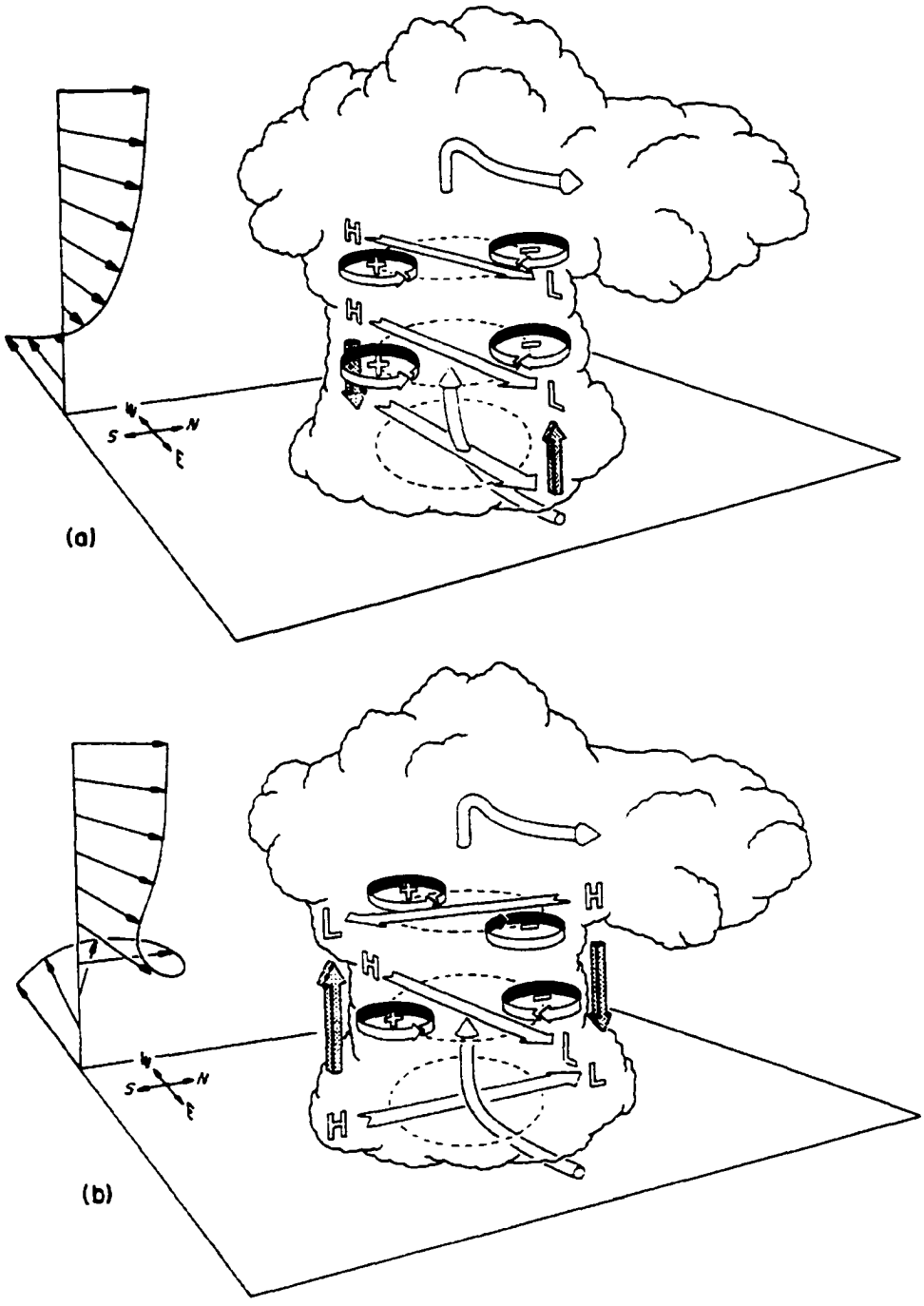


**Figure 2.6: Schematic showing the distribution of pressure and vertical vorticity perturbations that develop as an updraft interacts with an environmental shear vector that (a) is unidirectional with height and (b) veers with height. The high (H) to (L) horizontal pressure gradients parallel to the shear vectors (flat arrows) are labeled along with the preferred location of cyclonic (+) and anticyclonic (-) vorticity. The shaded arrows depict the orientation of the resulting vertical pressure gradients (adapted by Klemp (1987) from Rotunno and Klemp (1982)).**

pressure distribution, Rotunno and Klemp showed that when the hodograph veers (backs) with height, the positive (negative) vertical vorticity and the updraft are positively correlated.

Rotunno and Klemp also analyzed the linear, nonlinear and buoyant contributions to the perturbation Exner function predicted by the model. They found that the nonlinear term induced uplift on both the left and right flanks of the updraft. Using the linearized divergence equation and the assumption that $\nabla^2\pi' \approx -\pi'$, where $\pi'$ is the perturbation Exner function, they showed that $\pi' \approx -\zeta^2$ for a wind field in pure rotation. Therefore, wherever there was rotation, the pressure was lowered. Low pressure was thus induced on both flanks of the initial cell, and this enhanced storm splitting. Thus, nonlinear effects appear to enhance storm splitting, whereas the linear terms determine the RM/LM bias. Storm splitting and the development of RM and LM storms can therefore develop with both unidirectional and directionally varying hodographs. However, the dominance of the RM of LM storm is directly related to the veering or backing motion of the shear vector.

Weisman and Klemp (1984) hypothesized that dynamically distinct processes control the low-level convergence feeding the updrafts on the flanks of the initial storm. Using a clockwise turning hodograph, and breaking the pressure field into its buoyant and dynamic contributions, they found that the left flank updrafts were predominantly forced by low-level convergence along the surface gust front, while the right flank updrafts were controlled by the development of a dynamically-induced vertical PGF, as described above (see Figure 2.6). Weisman et al. (1983) found from their model simulations that the dynamic forcing in the lower levels of the RM storm was approximately twice that of the buoyant forcing, while buoyant forcing was the larger force at higher levels.

Grasso (2000) recently suggested another mechanism that may contribute to the decay of the LM when the hodograph turns clockwise with height. He performed

numerical simulations using a hodograph that veered in the lowest 2km AGL. The LM storm dissipated soon after storm splitting. However, when the precipitation process was suppressed, the LM storm was long-lived. If the linear forcing described above was the dominant process controlling the longevity of the LM storm, then the LM should have dissipated soon after splitting, which was not the case. Upon examining the low-level buoyancy field, Grasso found that when precipitation was allowed to fall, the LM updraft ingested cool downdraft air, which was negatively buoyant as a result of precipitation effects. As the simulation progressed and the precipitation downdraft matured, the LM updraft became progressively less buoyant, the total vertical forcing became negative in the lower levels of the LM updraft, and the LM storm soon dissipated. The RM storm also ingested some of the cool downdraft air; however, this was offset by the ingestion of environmental air at the same time. This did not occur with the LM. Grasso's results, like those of Weisman and Klemp (1984), suggest that there may be other processes, apart from the linear pressure effect, that can affect the longevity of the LM storm.

In summary, supercell storms have been observed to split into storms that move to the right and left of the mean tropospheric winds. When the shear vector veers (backs) with height, the cyclonically (anticyclonically) rotating RM (LM) storm is enhanced while development of the LM (RM) is suppressed. Precipitation loading and nonlinear pressure effects seem to control the splitting process. Linear pressure effects appear to determine whether the LM/RM storm is favored based on the turning of the hodograph, although convergence along the LM gust front may offset this effect, and other factors, like buoyancy, need to be considered.

### 2.3.3 *Rotation*

Rotation within supercells has been recognized since the 1950s and 1960s (e.g. Stout, 1957; Browning and Landry, 1963; Browning, 1964; Fujita and Grandoso, 1968). The development of Doppler radar in the 1970s confirmed the existence of rotation in thunderstorms, and revealed the cyclonic-anticyclonic couplet at mid-levels, and the predominantly cyclonic (anticyclonic) structure at low levels in RM (LM) storms (e.g. Ray, 1976). Lemon and Doswell's (1979) analysis of vorticity production in supercell storms showed that the tilting term appeared to predominate, but that solenoidal effects might be important at the interface between the RFD and the updraft.

Numerical modeling in the late 70s and early 80s showed rotating updrafts and downdrafts (e.g. Schlesinger, 1975; Klemp and Wilhelmson, 1978a,b), that horizontal vortex tubes could be tilted into the vertical when interacting with a convective updraft (e.g. Schlesinger, 1975; Klemp and Wilhelmson, 1978a,b), and that the mid-level cyclonic-anticyclonic vortex pair is aligned in the direction of the environmental vorticity vector (Blechman, 1981). The relationship between vertical velocity and vertical vorticity was also quantified by obtaining correlation coefficients (e.g. Clark, 1979; Weisman et al, 1983; Weisman and Klemp, 1984; Droegemeier et al., 1993), and a high correlation between the updraft and vertical vorticity was suggested as a classification criterion for supercells (Weisman and Klemp, 1984). Past studies suggest that mid-level (3-10km AGL) mesocyclones develop by different processes than low-level (below 1km AGL) mesocyclones. The development of mid- and low-level rotation will now be examined.

#### *Mid-Level Rotation*

The mechanism for the development of mid-level rotation is generally agreed upon (e.g. Rotunno, 1981; Klemp and Rotunno, 1983; Davies-Jones, 1984). This mechanism was described above and summarized in Figure 2.5. The development of mid-level rotation has been examined mathematically by Rotunno (1981). He used the vertical

vorticity equation linearized about a mean flow $\overline{U}(z)$ in the x direction, but also included the nonlinear stretching term that has been found to be important (Ray, 1976; Brandes, 1978; Bluestein and Sohl, 1979). The vorticity equation is represented by

$$\frac{\partial \zeta}{\partial t} + U_s \frac{\partial \zeta}{\partial x} = \frac{\partial \overline{U}}{\partial z}\frac{\partial w}{\partial y} + \zeta \frac{\partial w}{\partial z} \tag{2.4}$$

where $\overline{U}_s \approx \overline{U}$ and is a constant in the advection term. His analysis may be described as follows: assume that the x-axis falls along the line of symmetry in the east-west direction and the y-axis lies along the western vortex tube shown in Figure 2.5. The initial vertical velocity reaches a maximum near y=0. As $\partial w/\partial y > 0$ ($\partial w/\partial y < 0$) on the southern (northern) side of the updraft, it is apparent from Eq. (2.4) that there will be positive (negative) vorticity to the south (north) of the updraft. This may be interpreted as vortex tilting. The magnitude of the vertical vorticity will be greatest where the gradients in vertical velocity are greatest. During the second stage, as the updraft weakens, $\partial w/\partial y$ changes sign, and the mid-level vorticity of the right (left) flank storm develops a negative (positive) component near y=0, which again points to the impact of vortex tilting. It is apparent from the description above and the mathematical analysis shown here that mid-level rotation is initially generated by the tilting of horizontal vorticity, and is strengthened later by stretching and further tilting.

***Low-Level Rotation***

Observations show at mid-levels, a vorticity couplet is observed in both LM and RM storms, but that at low levels positive (negative) vorticity completely dominates the negative (positive) vorticity in the RM (LM) (e.g. Ray, 1976). Rotunno (1981) found from his analytical model that the mid-level and low-level solutions were initially comparable. As the storm developed, the vertical velocity increased, $\partial w/\partial z > 0$, and both the positive and negative vorticity magnitudes increased. However, as the downdraft developed, $\partial w/\partial z < 0$, the magnitude of which was great in the lower levels where

downdrafts were forced to rapidly decelerate upon reaching the surface. As a result, vortex *compression* occurred, and the negative (positive) vorticity at low-levels of the RM (LM) was greatly decreased. Numerous others have also recognized the importance of the stretching term at low-levels (e.g. Ray, 1976; Wilhelmson and Klemp, 1978; Brandes, 1978; Bluestein and Sohl, 1979).

Numerical simulations and observations have shown that strong cyclonic vorticity is first generated at mid-levels. After that, low-level rotation develops at mid-levels, and it is significantly greater in magnitude (e.g. Klemp and Rotunno, 1983; Rotunno and Klemp, 1985). The two regions of vertical vorticity appear to develop independently. The low-level vorticity does not appear to develop as a result of the mid-level vorticity descending, as has been previously hypothesized (e.g. Lemon and Doswell, 1979). While the mechanism for generating mid-level rotation is generally agreed upon, two different mechanisms have been suggested for the generation of low-level vertical vorticity. Baroclinic generation of vorticity is considered important in both theories. However, in the first theory, tilting and then stretching of horizontal vorticity by the updraft is considered important (Klemp and Rotunno, 1983; Rotunno and Klemp, 1985); whereas, in the second theory, tilting of vorticity by both the updraft and downdraft are found to be necessary (Davies-Jones 1992a,b; Davies-Jones and Brooks, 1993). These theories will now be examined in more detail.

In the first theory (Klemp and Rotunno, 1983; Rotunno and Klemp, 1985), low-level vertical vorticity is initially generated through tilting. It is enhanced by strong low-level convergence along the gust front, which develops as the downdraft develops (Figure 2.7a). The vorticity maximum then moves from the front to the back of the convergence line and increases rapidly (Figure 2.7b,c). This is related to baroclinic processes. As the cold outflow air progresses underneath the storm, the inflow air from the northeast flows almost parallel to the forward-flank outflow boundary, and horizontal vorticity develops through baroclinic forcing. This horizontal vorticity is then tilted into the vertical as it

encounters the updraft. As the horizontal vorticity vectors and the storm-relative inflow point in the same direction, positive vertical vorticity is produced in the updraft. This may be seen by examining the vertical component of the inviscid, Boussinesq vorticity equation given by

$$\frac{\partial \zeta}{\partial t} = -\bar{V} \cdot \nabla \zeta + \vec{\omega}_h \cdot \nabla_h w + \zeta \frac{\partial w}{\partial z} \tag{2.5}$$

(Rotunno and Klemp, 1985). The tilting term is the dot product of the horizontal component of vorticity with the horizontal gradient of vertical velocity. If these two vectors point in the same direction, the tilting term is positive, and the vertical vorticity is enhanced. Maximum positive contributions from tilting therefore occur on the left (north) side of the updraft, while negative values occur on the right (south). This is completely the opposite of what tilting the environmental vorticity would give. Finally, convergence effects then enhance the low-level vertical vorticity. Low-level rotation is therefore acquired from upward tilting of the baroclinically generated horizontal vorticity that develops along the gust front northeast (upstream) of the low-level updraft.

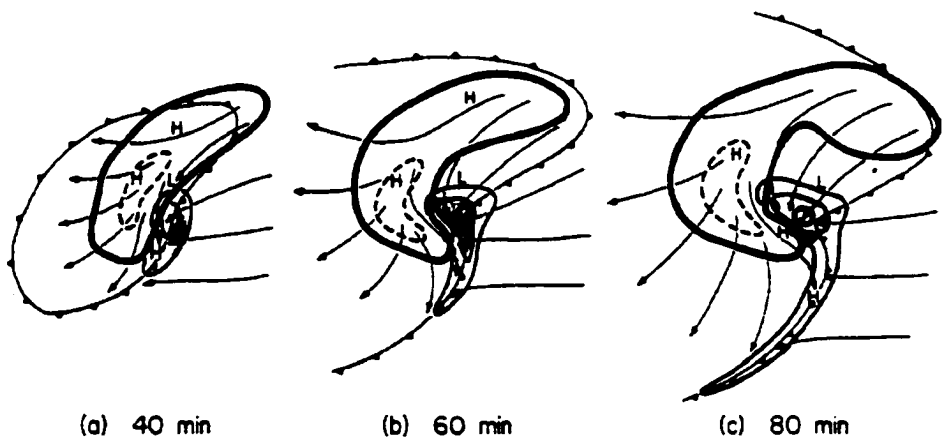


**Figure 2.7: Flow field from the storm scale (1km grid resolution) model simulation performed by Klemp and Rotunno (1983) at z=250m at (a) 40 min, (b) 60 min and (c) 80 min. Vertical velocity is contoured at 1m.s$^{-1}$ intervals with the zero line omitted. Arrows represent storm-relative streamlines at the surface. The thick solid line shows the 0.5 g.kg$^{-1}$ rainwater contour. A potential temperature perturbation of –1°C is indicated using frontal symbols. The location of maximum vertical vorticity is marked by a black circle with the region of $\zeta$>0.002 s$^{-1}$ being shaded. The locations of surface high and low pressure are shown using H and L respectively (after Klemp and Rotunno, 1983).**

In a simulation without rain, Rotunno and Klemp found that the low-level rotation was hardly noticeable, however, the storm still propagated to the right of the mean winds and rotated cyclonically at mid-levels. They hypothesized that the primary importance of the mid-level rotation is to transport potentially dry, cool air to regions where it can be evaporatively cooled, descend, produce cold air outflow, and generate the thermodynamic gradients in regions suitable for the baroclinic generation of low-level horizontal vorticity

In the second theory, evaporative and baroclinic processes are also considered to be crucial in the generation of low-level vertical vorticity (Davies-Jones, 1982a,b; Davies-Jones and Brooks, 1993). Davies-Jones and Brooks (1993) performed simulations with and without precipitation and found that the maximum vertical vorticity at 100m AGL was 6 or more times greater with full microphysics. However, Davies-Jones and Brooks claimed that although baroclinic effects along the gust front would greatly enhance horizontal vorticity, tilting of horizontal vorticity into the vertical by the updraft would still not produce the magnitude of vertical vorticity observed in the lowest 1km AGL.

Davies-Jones and Brooks (1993) hypothesized that downdrafts play an important role in low-level mesocyclogenesis and observed, from their simulations, that there was positive vorticity at the lowest levels in the downdraft. They showed that tilting of crosswise (Figure 2.8 top) and streamwise horizontal vorticity (Figure 2.8 middle) by the downdraft could not cause the vorticity reversal of the descending parcels, but that the baroclinic generation of streamwise vorticity could (Figure 2.8 bottom). This process operates as follows: consider a cool mass of air descending on the north side of the mesocyclone and spreading out toward the south so that it is nearly parallel to the isotherms of the gust front. Warm air exists to the east of this cool air due to the presence of the updraft. Horizontal vorticity is generated baroclinically as a result of the temperature gradient between the updraft and downdraft, the vector of which points to the south. As the downdraft descends, the vortex lines turn downward due to barotropic

effects. However, they are inclined less than the trajectories due to the contributions from the baroclinic forcing, which are in a southward, *horizontal* direction. As the air approaches the ground, the barotropic effects turn the vortex lines, which now have a baroclinic, horizontal contribution, upward. Positive vertical vorticity is therefore generated in the lowest levels of the downdraft. This air, which already has a positive component of vertical vorticity, is then entrained into the updraft on the southwest side of the storm below ~100m AGL, from where the vertical vorticity is significantly enhanced by stretching, and tilting to a lesser degree. Baroclinic generation of streamwise vorticity therefore explains the vorticity reversal in the downdraft, and the strength of the convergence term near the ground. If the horizontal vorticity were simply tilted into the updraft, there would be no vertical vorticity adjacent to the surface to stretch, since the updraft speeds at the surface are near zero and tilting is thus weak. This mechanism is also suggested in the simulations by Grasso and Cotton (1995).

Davies-Jones and Brooks' mechanism differs from that of Rotunno and Klemp's in that the air tilted into the updraft already has a component of positive vertical vorticity, and convergence in the lower levels can immediately amplify this vertical vorticity. In Rotunno and Klemp's mechanism, the vertical vorticity first needs to be generated through tilting before it may be stretched which, according to Davies-Jones and Brooks, cannot produce strong rotation very near the ground. Wicker and Wilhelmson (1995), recently found, from their simulations, that vertical vorticity within the low-level mesocyclone was initially due to the tilting of barotropic and baroclinically-generated horizontal vorticity along the forward flank gust front. They also claimed that tilting of the horizontal vorticity by the updrafts and the subsequent stretching of the vertical vorticity could generate large values of vertical vorticity near the surface (z~100m). However, their analysis could not identify the mechanisms whereby rotation was generated next to the surface, and they did not observe positive vertical vorticity in the lowest levels of the downdraft as suggested by Davies-Jones and Brooks (1993).

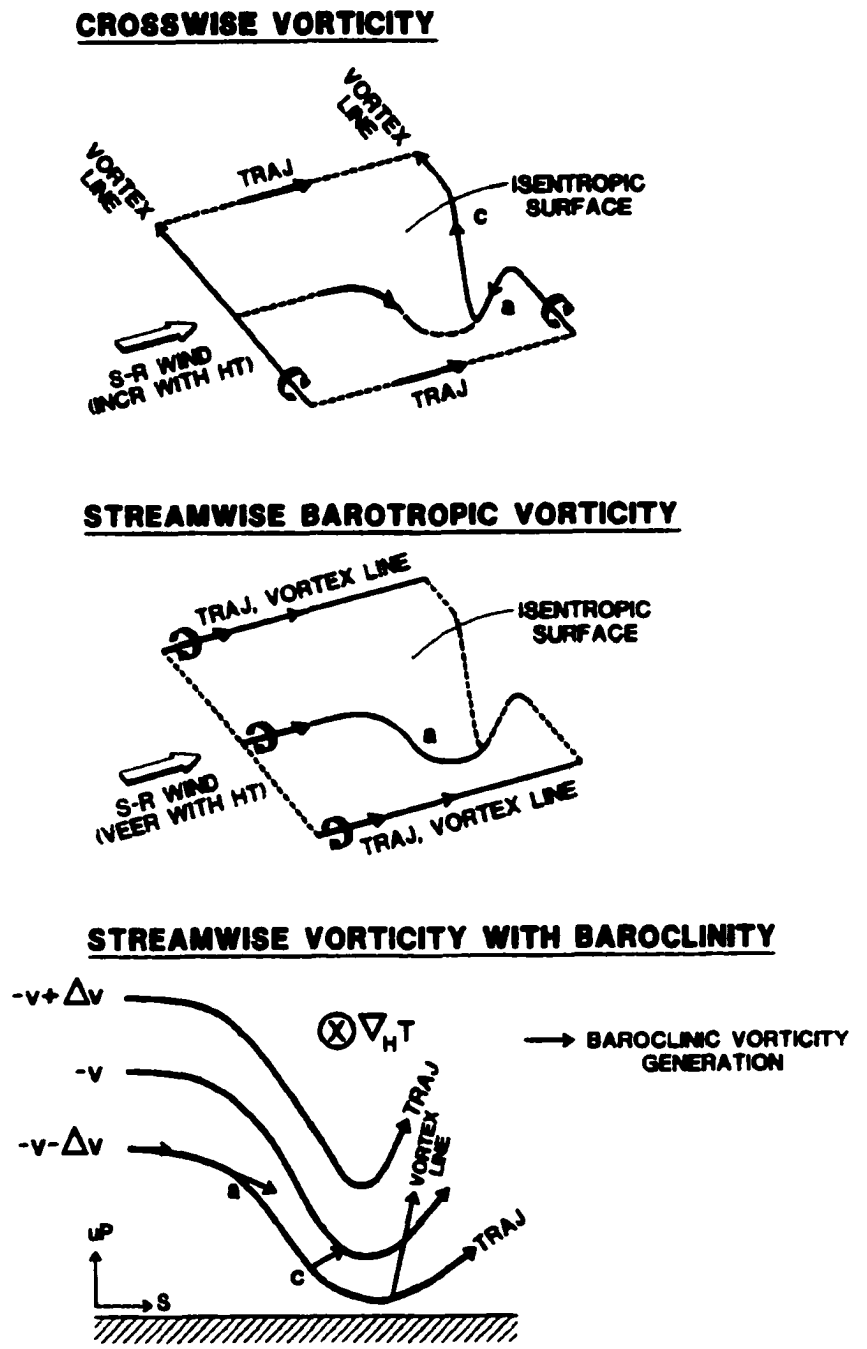


**Figure 2.8: Schematic diagram showing how cyclonic vorticity may be generated in a downdraft through the tilting of barotropic and baroclinic horizontal vorticity. For crosswise barotropic vorticity (top diagram), tilting by the downdraft produces cyclonic (anticyclonic) vorticity on the left (right) of the downdraft in the direction of the storm-relative wind vector. For streamwise barotropic vorticity (middle diagram), tilting by the downdraft produces a purely anticyclonic downdraft and a cyclonic updraft. In the streamwise case in which there is flow to the right of the horizontal buoyancy gradient and a southerly shear component (bottom diagram), both tilting and baroclinic generation of vorticity causes a change in sign of the vorticity of the parcels in the downdraft from anticyclonic to cyclonic while the parcel is still descending (after Davies-Jones and Brooks, 1993).**

***Rotation and Storm Propagation***

We have examined how mid- and low-level rotation develops. The question that now needs addressing is - how are rotation and storm propagation linked? Two theories have been developed in response to this question. In the first, Rotunno and Klemp (1985) found that dynamic forcing was responsible for the southward propagation of the storm, being positive (negative) on the southern (northern) flank of the updraft. Using the Exner function perturbation equation

$$\nabla \cdot (c_p \bar{\rho} \bar{\theta} \nabla \pi_{dn}) = -2\bar{\rho}\left[\frac{\partial v}{\partial x}\frac{\partial u}{\partial y} + \frac{\partial u}{\partial z}\frac{\partial w}{\partial x} + \frac{\partial v}{\partial z}\frac{\partial w}{\partial y}\right] - \bar{\rho}\left[\left(\frac{\partial u}{\partial x}\right)^2 + \left(\frac{\partial v}{\partial y}\right)^2 + \left(\frac{\partial w}{\partial z}\right)^2 - \frac{d^2 \ln \bar{\rho}}{dz^2} w^2\right] \tag{2.6}$$

where $C_p$ is the specific heat capacity, u and v are the horizontal wind components, $\bar{\rho}$ is the base state density, $\bar{\theta}$ is the base state potential temperature, the subscript dn refers to the dynamic forcing, and the assumption that $\nabla \cdot (c_p \bar{\rho} \bar{\theta} \nabla \pi_{dn}) \approx -\pi$, they showed that the negative pressure anomaly that developed on the right flank of the storm was produced predominantly by negative values of the non-linear shearing terms, which are associated with rotational flow. The negative pressure perturbation reached a maximum at the mid-levels of the storm. The vertical vorticity therefore generated an upward directed vertical pressure gradient on the storm flanks through non-linear processes. The enhanced vertical PGF strengthened the updraft and caused it to move in the direction of the storm flank, which resulted in a stronger correlation between the updraft and the vertical vorticity. Following this, the 'new' updraft then tilted more environmental horizontal vorticity into the vertical along the storm flank, and a continuous cycle of updraft regeneration and propagation developed. This non-linear process also accounts for the leftward and rightward movement of storms under unidirectional environmental wind shear, when high and low pressure centers cannot become favorably aligned through the veering or backing of the hodograph (Klemp and Rotunno, 1982). Therefore, it is apparent that the rightward/leftward propagation of the storm is primarily due to rotational effects, the cold

pool effects are secondary, and storm splitting and storm motion off a straight-line hodograph are due to non-linear effects.

In the second theory, which is based on linear assumptions, streamwise (parallel to the mean winds) and crosswise (normal and to the left of the mean flow) vorticity are used to predict the rotational characteristics of a quasi-steady updraft that is already propagating (Rotunno, 1981; Davies-Jones, 1984; Lilly, 1986). Streamwise vorticity is given by $\omega_s = \bar{\omega} \cdot \bar{p}$, where p is the unit vector in the direction of the storm-relative wind, and is simply the component of environmental vorticity in the direction of the storm-relative winds. The theory may be outlined as follows: when the storm-relative velocity vector and the horizontal vorticity vector are perpendicular (purely crosswise vorticity, Figure 2.9 top), the horizontal vortex lines are tilted by air flowing into the updraft, and cyclonic (anticyclonic) vorticity is generated on the right (left) side of the peak. There is no correlation between vertical velocity and vertical vorticity, and hence no net rotation in the updraft. When the storm-relative flow vector and the horizontal vorticity vector are parallel (purely streamwise vorticity, Figure 2.9 bottom), the horizontal vortex lines are again tilted by the updraft. However, vertical vorticity and vertical velocity are now positively correlated, and the updraft gains a net cyclonic rotation. Hence, the covariance of vertical velocity and vertical vorticity is proportional to the storm-relative environmental streamwise vorticity.

According to the second theory, changes in storm motion can affect storm rotation by changing the angle between the storm-relative winds and the environmental vorticity vector. Also, if an updraft propagates along the direction of the mean vertical shear vector (on the hodograph), there is no net updraft rotation; whereas, if the updraft propagates across the mean vertical wind shear vector (off the hodograph), the updraft will rotate cyclonically (anticyclonically) as it moves to the right (left) of the shear vector. Davies-Jones et al. (1990) suggested that the magnitude of the streamwise vorticity could be

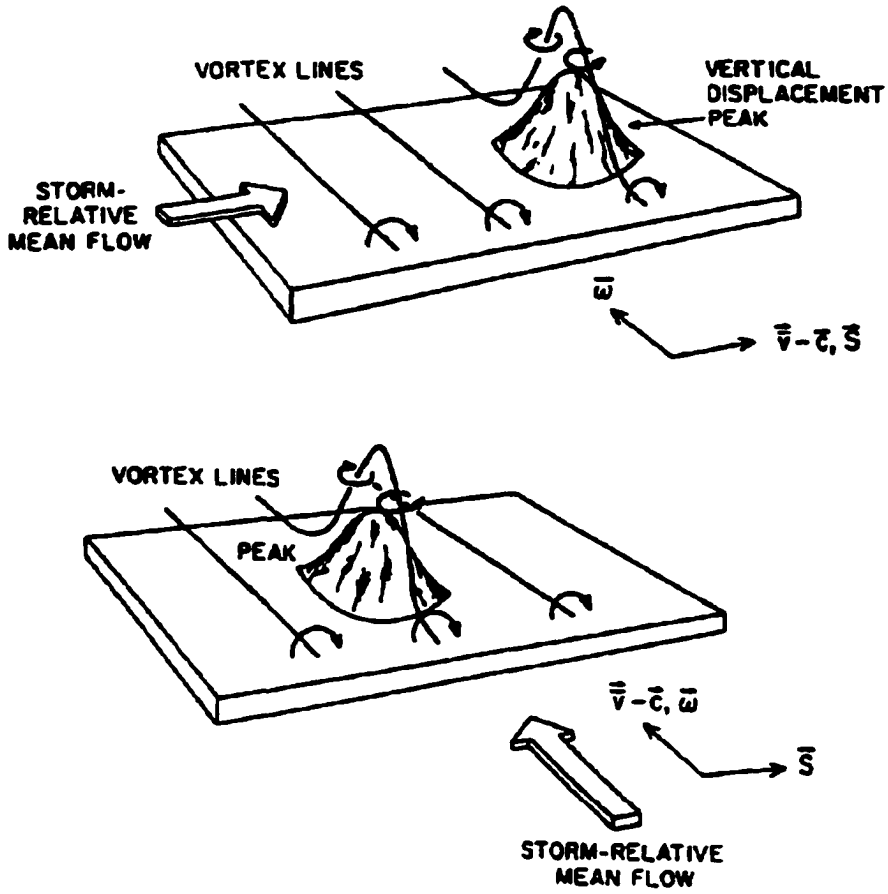


**Figure 2.9:The conceptual model of Davies-Jones (1984) showing the importance of streamwise vorticity in the development of thunderstorm rotation. Introducing a displacement variable and using linear theory, Davies-Jones (1984) makes use of isentropic surfaces in which the streamlines and vortex lines follow these surfaces. A thunderstorm may be thought of as a vertical displacement of the isentropic surface. With purely crosswise vorticity (top figure), the storm-relative vector is perpendicular to the vorticity vector. In this situation, cyclonic vorticity develops on the right side and anticyclonic vorticity on the left side of the updraft, and there is no correlation between vertical velocity and vertical vorticity. With purely streamwise vorticity (bottom figure) the storm-relative vector and the vorticity vector are in the same direction. Here the upslope (downslope) side of the peak is also the region of cyclonic (anticyclonic) vorticity and vertical velocity and vertical vorticity are positively correlated (after Davies-Jones, 1984).**

integrated over the depth of the main inflow layer to determine the tendency of the storm rotation. This quantity is the SREH.

It is apparent from the discussion above that two different approaches are used to understand supercell storm dynamics, either the role of vertical wind shear (e.g. Rotunno and Klemp, 1982, 1985) or of SREH (e.g. Davies-Jones, 1984). In the vertical wind shear

approach, the focus is the way an updraft interacts with the environmental vertical wind shear to produce a quasi-steady, rotating storm. In the SREH approach, the existence of a steady, propagating storm is assumed and the storm motions that cause a rotating updraft through the tilting of environmental streamwise vorticity are then considered. There are several limitations of the SREH theory: the storm is assumed to be quasi-steady, the propagation of the storm needs to be known, and the rotating updrafts cannot be explained when the hodograph is unidirectional. Davies-Jones suggested non-linear processes dominate storm dynamics when the hodograph is unidirectional, but linear effects are important when the hodograph is curved. This differs from Rotunno and Klemp who found that nonlinear processes are significant when the hodograph is both unidirectional and curved, while linear processes simply determine the RM/LM bias. Weisman and Rotunno (2000) also found that storm splitting, updraft development and enhancement, storm rotation and storm propagation, were all independent of the hodograph curvature. They believe their results support the vertical wind approach. however, they suggested the most applicable theory may depend on the characteristics of the supercell under investigation.

In summary, it is apparent from both observational and modeling studies that the mid-level mesocyclone is generated through the tilting of streamwise horizontal vorticity by the updraft. The low-level mesocyclone develops as a result of the reorientation of the baroclinically-generated horizontal vorticity, either by the updraft (Klemp and Rotunno, 1983; Rotunno and Klemp, 1985), or both the downdraft and the updraft (Davies-Jones and Brooks, 1993; Brooks et al., 1993; Brooks et al., 1994a). Non-linear processes appear to control storm splitting, storm rotation, updraft enhancement, and storm propagation, whereas linear processes determine the LM/RM dominance.

### 2.3.4 *Cyclic Mesocyclogenesis*

The process whereby a supercell can produce a periodic succession of mesocyclones, both at mid- and low-levels, is called cyclic mesocyclogenesis. This process has been observed since the 1950s (e.g. Hoecker, 1959). In a study by Darkow and Roos (1970) of Missouri tornadoes, 20% of the thunderstorms were observed to produce multiple tornadoes. Recent radar (Dowell et al., 1997) and modeling studies (e.g. Kulie and Lin, 1998; Adlerman et al., 1999) have also revealed cyclic mesocyclogenesis

Lemon and Doswell (1979) hypothesized that if the storm is to persist following the occlusion and dissipation of the tornado, then a new updraft must develop elsewhere. They suggested that such an updraft may develop to the southeast of the original updraft (see Figure 2.3). Once this updraft was established, the same storm evolution as that of the original updraft could take place, thereby producing periodic mesocyclones and tornadoes from the same storm. This theory has been supported by observations (e.g. Rasmussen et al., 1982; Burgess et al., 1982).

In an extensive investigation of mesocyclones from 1971 to 1977 using NSSL single-Doppler radar data, Burgess et al. (1982) found that the majority of mesocyclones (76%) were comprised of just one core (an area of solid body rotation within a larger region of cyclonic rotation about 20km across) during their lifetime. They also noted that the first core of the multi-core mesocyclones was identical in nature to the core of the single-core mesocyclones, and that 3 was the most likely number of cores for the multi-core mesocyclones in their study, although one storm did produce six. Burgess et al. developed a conceptual model of cyclic mesocyclogenesis (Figure 2.10): the gust front is accelerated around the right flank of the mesocyclone by the strong low-level rotation. Occlusion occurs, thereby separating the original mesocyclone from its warm inflow, and the first core dissipates. Strong convergence occurs at the point of the occlusion and a

new vortex core develops. The cycle then repeats itself. The second core develops far more rapidly than the first since it forms in an environment rich in vorticity.

In a recent study, Adlerman et al (1999) used a numerical model to investigate cyclic mesocyclogenesis in a classic supercell thunderstorm. During the four-hour simulation, two distinct occlusions and the beginning of a third were evident. They found from their simulation that cyclic mesocyclogenesis could be divided into five stages: the first stage begins as the RFD intensifies, wraps cyclonically around the updraft, and forces the gust front to bow outward. At the same time the low-level mesocyclone intensifies due to the tilting and stretching of low-level (<500m) streamwise vorticity which is generated through baroclinic processes, crosswise exchange, and streamwise stretching in the descending RFD. In the second stage, the RFD forces the gust front to propagate even further eastward. This produces an updraft on the east (downshear) side of the storm, and results in a dual updraft structure at mid-levels. During the third stage, the low-level mesocyclone/updraft center occludes and the vertical vorticity near the surface rapidly increases. Following the development of the occlusion downdraft, the old updraft and mesocyclone separate from the gust front and a new updraft and mesocyclone develop further downshear in the fourth stage. In the final stage, the old updraft has completely dissipated after being cut off from its source of buoyant air by the gust front. However, the downshear updraft continues to strengthen and move eastward. The new supercell is very similar to the original supercell. The cycle is then repeated. Adlerman et al. stressed the importance of the residual cold pool which provided buoyancy gradients that are perfectly positioned for the reoccurrence of horizontal vorticity generation through baroclinic effects. Although it took almost two hours for the first occlusion to take place, the second occlusion occurred just one hour later.

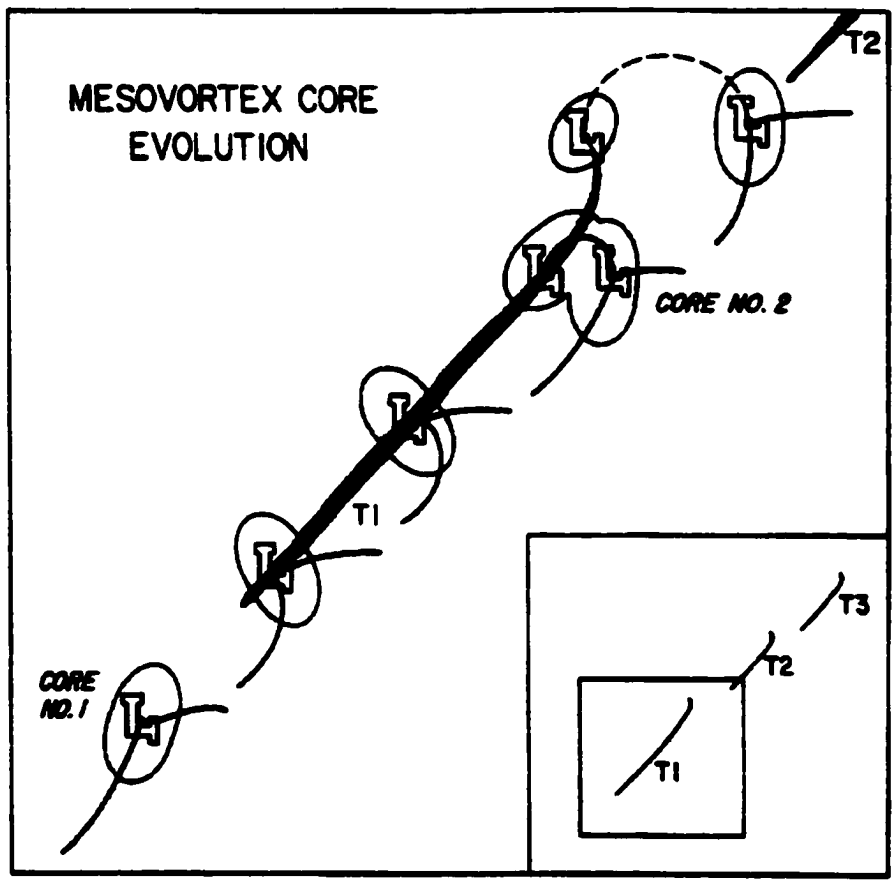


**Figure 2.10: Conceptual model of mesocyclone core evolution as hypothesized by Burgess et al. (1982). Tornado tracks are represented by the dark, shaded lines, and the low-level wind discontinuities (gust fronts) are given by the thin lines (after Burgess et al., 1982).**

## 2.4 Supercell Spectrum

Many of the radar signatures described as being characteristic of supercells refer to what are termed classic (CL) supercells. Some storms exhibit rotational characteristics, yet are not easily identifiable on radar because they produce very little precipitation. Other storms reveal mesocyclonic characteristics on radar, yet are not easily identified in the field because they produce copious amounts of precipitation that obscures the rotating updraft. A spectrum of supercell types, based on where the precipitation is situated with respect to the updraft and on the amount of precipitation they produce, was developed in

order to enhance the operational recognition of supercell storms (Doswell et al., 1993; Moller et al., 1994; Rasmussen and Straka, 1998). The spectrum consists of three supercell types. Low-precipitation (LP) supercells produce little, if any, precipitation (e.g. Burgess and Davies-Jones, 1979; Bluestein and Parks, 1983). Classic (CL) supercells produce moderate amounts of precipitation (e.g. Browning, 1964; Lemon and Doswell, 1979). High-precipitation (HP) supercells are copious producers of precipitation (e.g. Doswell et al., 1990; Moller et al., 1994). All of these supercells have a deep, persistent mesocyclone, despite their varying precipitation characteristics. Observations show that the three supercell types are archetypes, and that actual storms follow a range of types. Also, supercells may transition from being an LP supercell, through the CL type, to an HP storm (e.g. Burgess and Curran, 1985; Bluestein and Woodall, 1990; Brooks and Wilhelmson, 1992; Curran and Rust, 1992). Nevertheless, partitioning supercells into types does appear to aid, in some degree, the identification of the severe weather characteristics associated with each type.

### 2.4.1 *Classic Supercells*

The conceptual models of Browning (1964) and Lemon and Doswell (1979) were based on CL supercells. These models are still valid for CL type storms, and most of the earlier supercell references in the literature pertain to CL storms (Figure 2.11). CL supercells have been investigated observationally (e.g. Browning, 1964; Lemon and Doswell, 1979; Moller et al., 1994; Dowell et al., 1997; Rasmussen and Straka, 1998). They have the following characteristics:

- **Precipitation:** moderate amounts.

- **Environment:** moderate to high moisture, low to intermediate LFC values, and strong low- and mid-level shear; most common in the southern Great Plains. Develop away from competing storms.

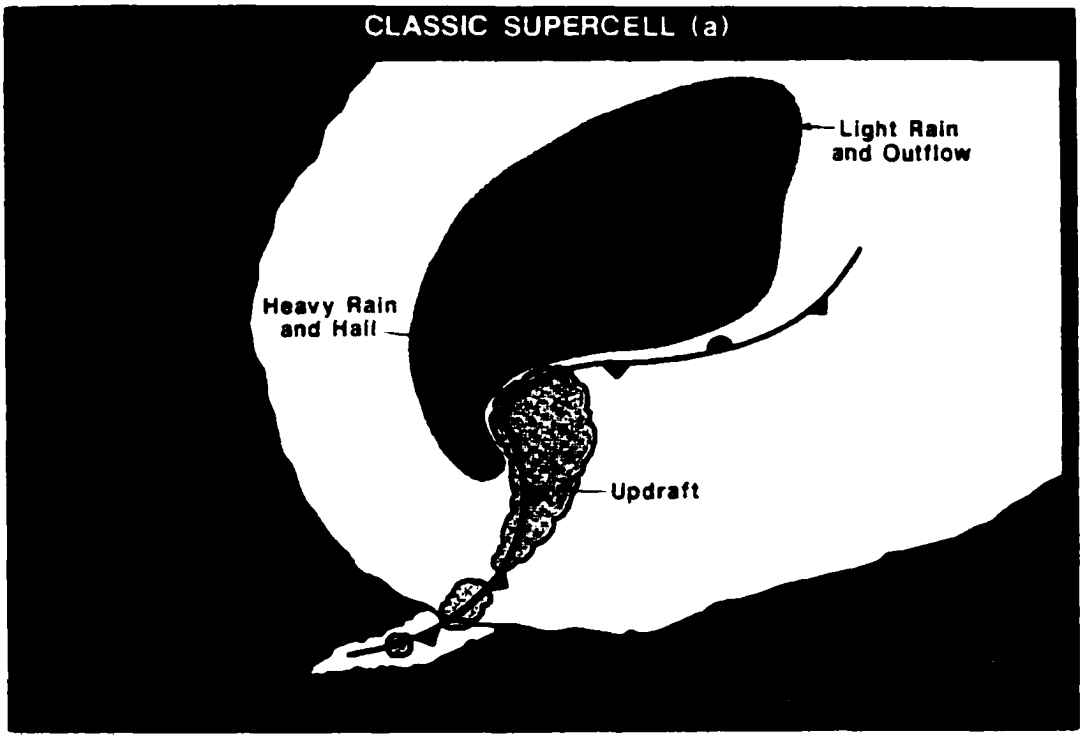


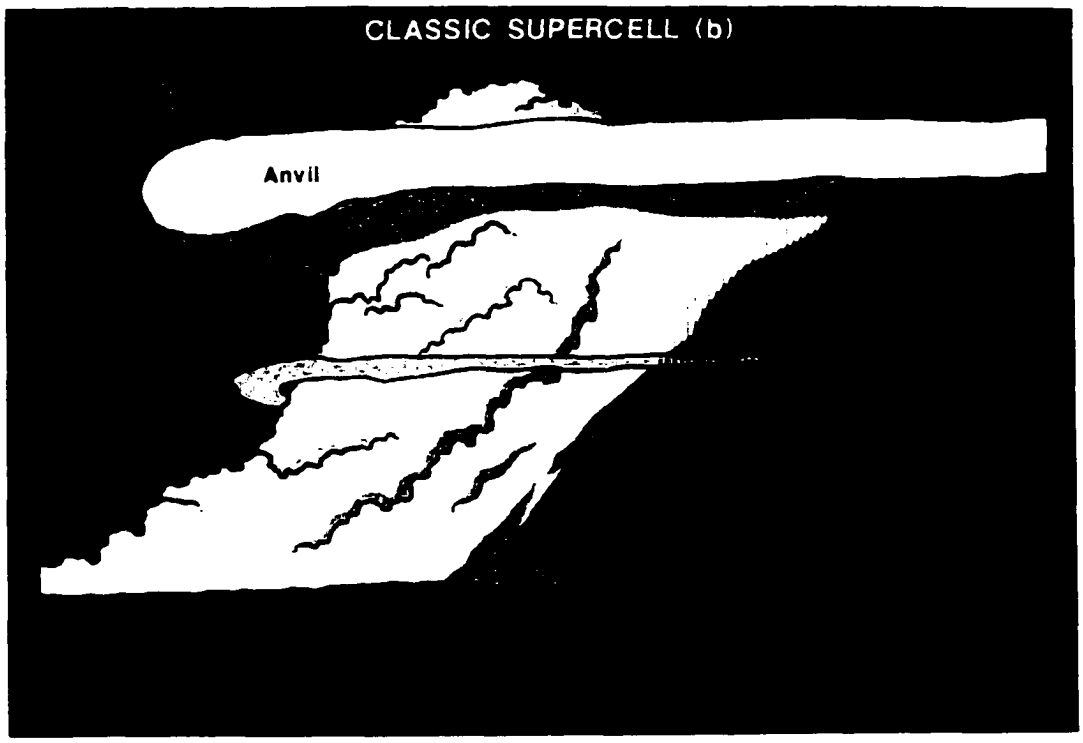


**(Figure continues on the next page)**

(c)

**Figure 2.11: Classic supercell features shown by (a) a plan view of the precipitation (stippling), surface outflow boundaries (frontal symbols), updraft maxima (scalloped line) and cloud boundaries (also scalloped) (after Doswell and Burgess, 1993), (b) a schematic indicating the visual characteristics seen by an observer on the ground (after Doswell and Burgess, 1993), and (c) a photograph of a classic supercell that occurred near Alma, Nebraska on 30 May 1991 (after Rasmussen and Straka, 1998).**

• **Severe Weather:** most prolific producers of severe weather like large hail and tornadoes; not often associated with flash flooding; account for the majority of F4 and F5 tornado occurrences.

• **Appearance:** CL supercells are easily detectable both visually and via radar. The updraft is highly visible and usually free of precipitation, although some precipitation may wrap around to the left and rear of the updraft (along storm motion). The cloud base is normally precipitation-free, although scattered hail and raindrops may occur. A region of heavier precipitation is clearly evident downshear of the updraft. Flanking convective lines are often visible. Some precipitation usually occurs within the mesocyclone, however, it is not heavy. If a hook echo should occur, as they frequently do, then radar reflectivities within the hook are generally less than those in the precipitation core.

• **Special Characteristics:** often exhibit well-known radar signatures e.g. WER/BWERs, storm-top above the low-level hook echo, v notch, etc.

Numerical simulations of CL supercells appear frequently in the literature (e.g. Wilhelmson and Klemp, 1978; Klemp et al., 1981; Weisman and Klemp, 1982, 1984; Klemp and Rotunno, 1983; Rotunno and Klemp, 1985; Brooks et al., 1994). Most of the simulations are idealized simulations; however, many of the characteristics of CL

supercells, including RFDs and FFDs, low- and mid-level mesocyclones, hook echoes, BWERs, and the v notch are evident.

### 2.4.2 *Low-Precipitation Supercells*

LP supercells were first described in the 1960s and 70s (e.g. Donaldson et al., 1965; Marwitz, 1972; Davies-Jones et al., 1976; Burgess and Davies-Jones, 1979), and were later classified by Bluestein and Parks (1983). It was noted that although these storms produced relatively little precipitation and did not exhibit all the classic supercell radar characteristics, they did show visible signs of rotation (Figure 2.12). Observational studies of LP storms have been conducted (e.g. Bluestein, 1984; Bluestein and Woodall, 1990; Curran and Rust, 1992; Bluestein and MacGorman, 1998). The following are characteristic of LP supercells:

- **Precipitation:** characterized by a relative absence of rain in and near a deep rotating updraft and by the occurrence of light to moderate rain and/or large hail falling from the anvil; most of the precipitation appears to consist of large hail and/or a few large raindrops; considered to be low precipitation efficiency storms.

- **Environment:** low to moderate moisture, relatively high LFC values, and slightly weaker low- and mid-level shears compared with CL supercells; occur predominantly near the surface dryline; found mainly in the High Plains east of the Rocky Mountains and in the western regions of the Great Plains; tend to develop as isolated cells.

- **Severe Weather:** large hail; weak tornadoes occasionally.

- **Appearance:** LP supercells are highly visible. The dry environment in which they develop prevents much of the intervening cloudiness. There is relatively little rain in, and near, the deep rotating updraft, and the cloud base is precipitation free. Light to moderate rain, and/or large hail fall from the anvil. Flanking lines are not often observed. The lack of precipitation in and around the updraft and mesocyclone makes the rotation associated with these storms difficult to detect on radar. Reflectivities associated with LP supercells are often low, even though they may produce large hail. Low-level hook echoes should not exist, and the precipitation core is displaced away from the updraft.

- **Special Characteristics:** strong evaporatively-cooled downdrafts are absent.

Several simulations of LP supercells have been conducted. Proctor (1983) suggested from his simulations that the strength of the updrafts in LP supercells prevented precipitation from falling through the updrafts and reaching the surface. Weisman and Bluestein (1985) were able to simulate an LP-type supercell by suppressing rain processes, which prevented the development of the evaporatively-generated downdrafts and cold pool. When rain was allowed to fall, low-level clouds developed, the anvil was not as well developed, and the system tilted to the west. They hypothesized that certain microphysical parameters, like cloud condensation nuclei (CCN) concentrations, which can affect the drop-size spectrum, may be important in controlling the precipitation efficiency of LP storms. These parameters depend on the type of air mass in which the storm develops and may help explain the development of LP storms near the dryline.

More recently, Brooks and Wilhelmson (1992) simulated what they called an LP supercell by using a smaller thermal perturbation to produce convection. They claimed that their simulations corroborate the hypothesis made by Bluestein and Parks (1983) that the size of the thermal generating the first convective updraft may be smaller for LP supercells than for other supercells. However, as Rasmussen and Straka (1998) pointed out, the updrafts that developed when Brooks and Wilhelmson used the smaller thermal bubbles were much weaker than those of the observed storm; and thus why the storm produced less precipitation. McPherson and Droegemeier (1991) also found that their supercell simulations were sensitive to the way in which they initiated convection in the model.

In a Doppler radar study of LP supercells, Bluestein and Woodall (1990) hypothesized that LP storms are a type of supercell in which hail formation is favored over rain formation due to the nature of precipitation trajectories. However, they could not determine why the rain process was so inefficient during the LP phase. They suggested reduced shedding and collision-coalescence processes due to the narrow

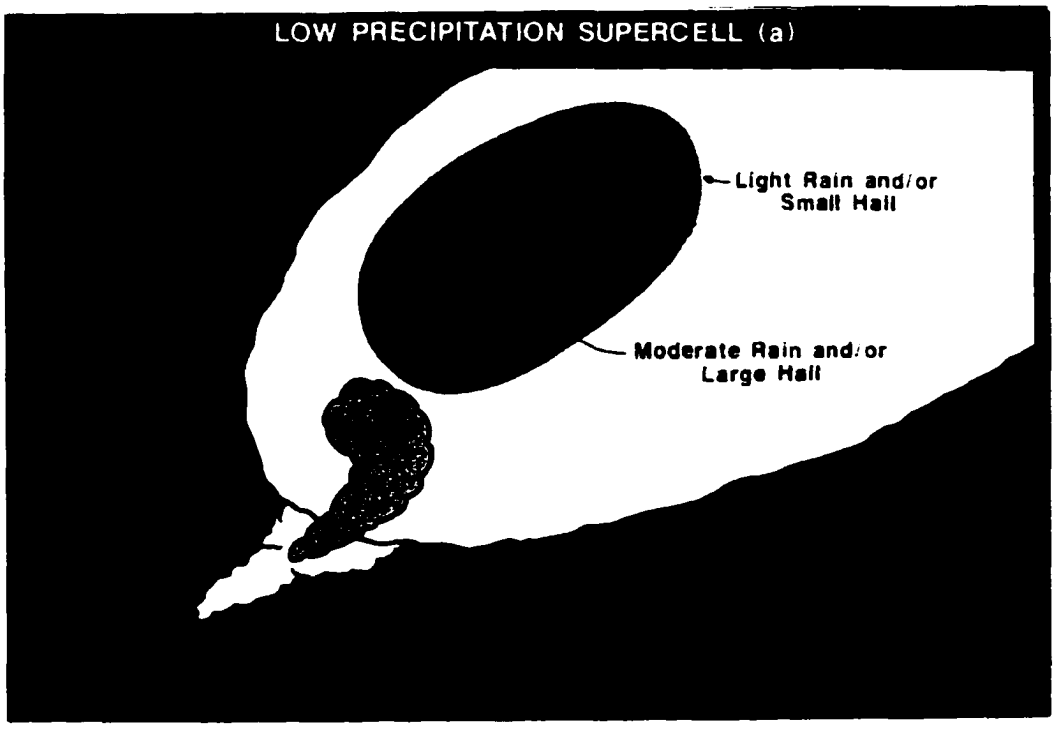


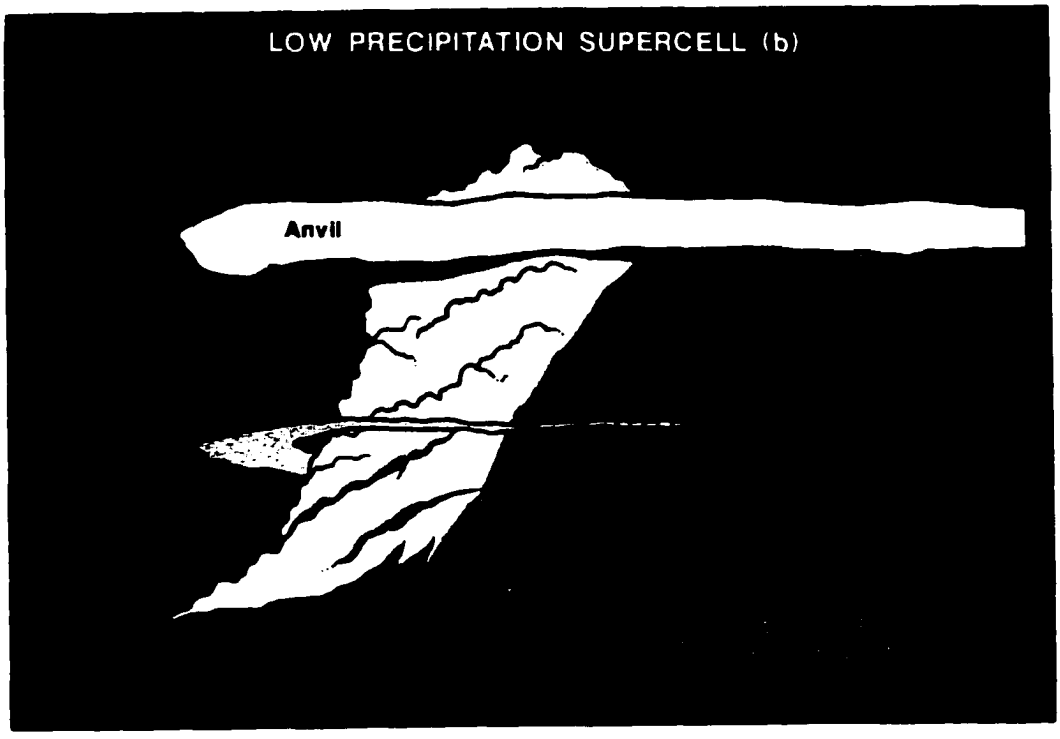


**(Figure continues on the next page)**

(c)

**Figure 2.12: Low-precipitation supercell features shown by (a) a plan view of the precipitation (stippling), updraft maxima (scalloped line) and cloud boundaries (also scalloped) (after Doswell and Burgess, 1993), (b) a schematic indicating the visual characteristics seen by an observer on the ground (after Doswell and Burgess, 1993), and (c) a photograph of a low-precipitation supercell that occurred in the Texas panhandle on 28 May 1994 (after Rasmussen and Straka, 1998).**

updraft, as two possible reasons. Thus, the rain process in LP supercells may be inefficient since these storms are small, narrow and unicellular in nature.

### 2.4.3 *High-Precipitation Supercells*

The defining characteristic of HP supercells is substantial precipitation in the mesocyclone (Figure 2.13). HP supercells are the most common supercell type. Of the three supercell types, HP supercells have been classified most recently (e.g. Moller and Doswell, 1988; Moller et al., 1990; Doswell and Burgess, 1993; Johns et al., 1993; Moller et al., 1994; Brooks et al., 1994a; Brooks et al., 1994b; Kulie and Lin, 1998; Rasmussen and Straka, 1998), although HP hybrid events had been described earlier (e.g. Weaver and Nelson, 1982; Foote and Frank, 1983; Foote, 1984; Nelson, 1987). The general characteristics of HP supercells are:

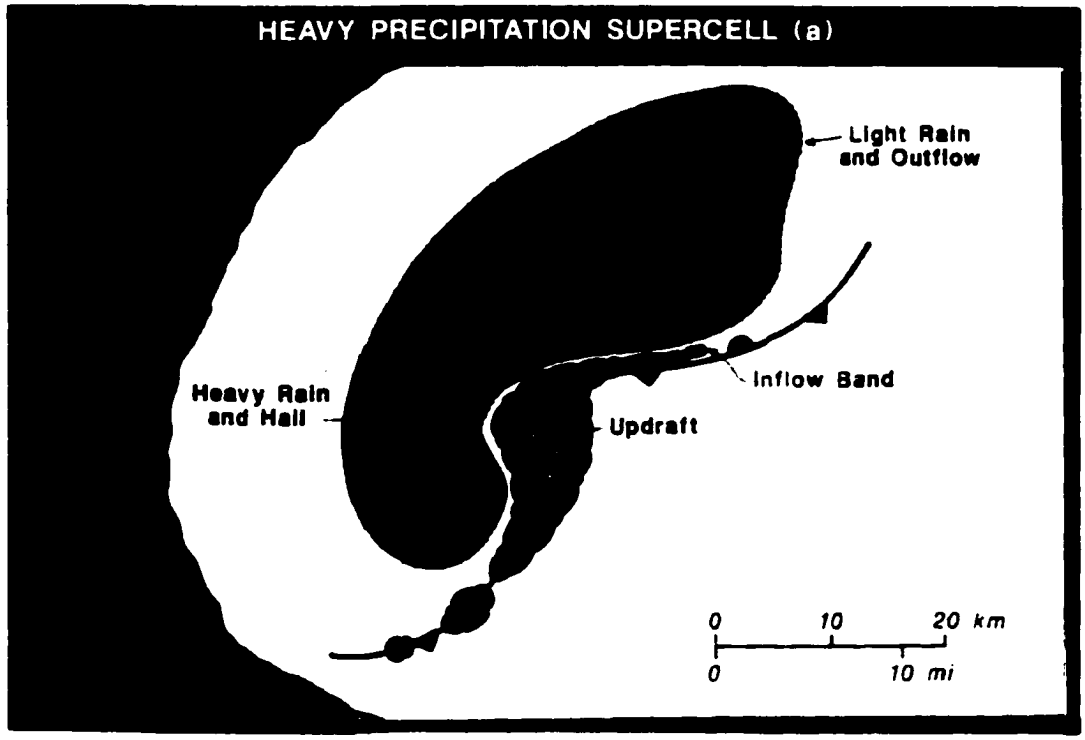


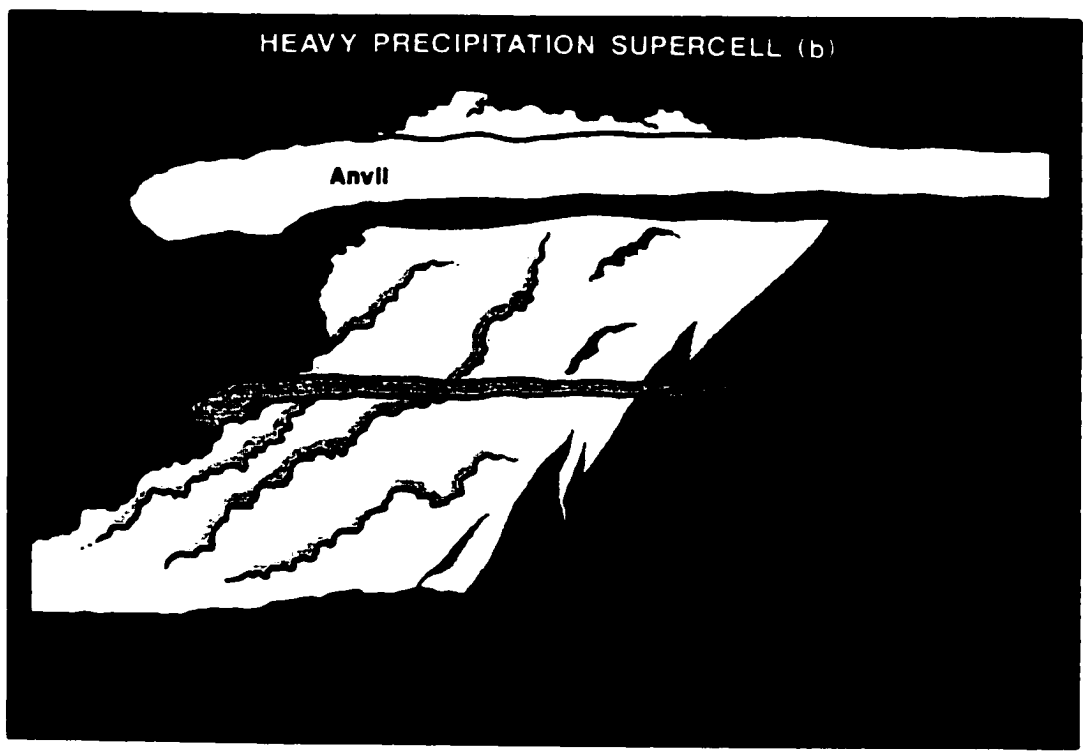


**(Figure continues on the next page)**

(c)

**Figure 2.13: High-precipitation supercell features shown by (a) a plan view of the precipitation (stippling), surface outflow boundaries (frontal symbols), updraft maxima (scalloped line) and cloud boundaries (also scalloped) (after Doswell and Burgess, 1993), (b) a schematic indicating the visual characteristics seen by an observer on the ground (after Doswell and Burgess, 1993), and (c) a photograph of a high-precipitation supercell that occurred in southwest Oklahoma on 19 April 1992 (after Rasmussen and Straka, 1998).**

• **Precipitation:** substantial precipitation within the mesocyclone.

• **Environment:** humid, cloud-filled environments; often travel along pre-existing thermal boundaries where baroclinically-generated vorticity may enhance the mesocyclone; develop in all regions of the United States; often develop near other storms.

• **Severe Weather:** downbursts and flash flooding; tornadoes, however, they are not normally as strong, violent or frequent as those with CL supercells; large hail and strong winds.

• **Appearance:** The humid, cloud-filled environment and the precipitation in the updraft make it difficult to visually identify the mesocyclone and tornadoes. Should they be visible, then heavy precipitation under the updraft and the forward anvil are evident. The heavy precipitation within the updraft makes HP supercells easy to detect using radar. A distinguishing radar characteristic of these storms is their prominent mesocyclones. If a hook echo is present, which it often is not, reflectivities within the hook echo are comparable to or larger than those in the precipitation core.

• **Special Characteristics:** Moller et al. (1994) warn that the HP supercell category is used as a "catchall" category for any storm that has a deep, persistent mesocyclone embedded in precipitation. This results in a large range of HP supercell storm structures and radar signatures, enhancing the difficulties in identifying these storms.

Moller et al. (1990) found that HP supercells may follow several different life cycles. Some transition from an LP supercell, through a CL phase to an HP supercell (LP-CL-HP), although the more common transition is simply CL to HP. HP supercells may then evolve into bow echo (BE) storms with rotating comma heads (HP-BE). These life cycles are shown in Figure 2.14. The CL-HP transition (2 through 4) may result in a BE (2 through 8a) or in the 2 through 7b life cycle. Moller et al. (1990) have found that cyclic mesocyclogenesis may occur with either of the life cycles. A new mesocyclone in its formative stages is evident in 7b on the storm's upshear flank.

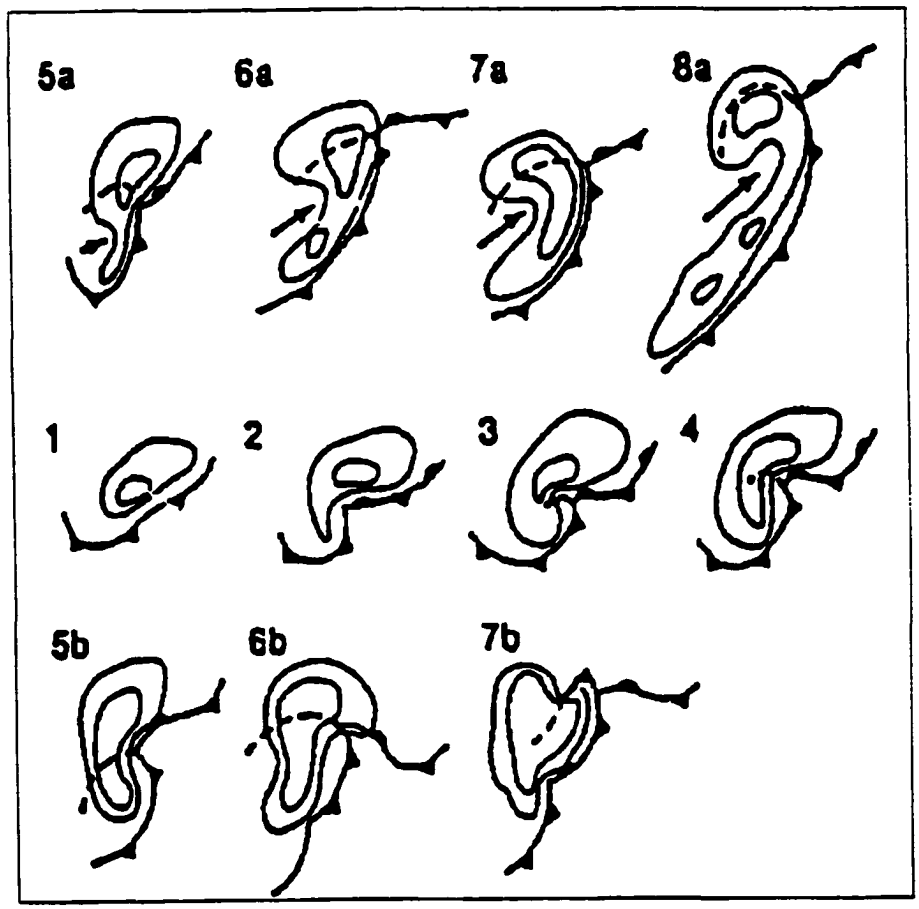


**Figure 2.14: Schematic showing two composite life cycles associated with high precipitation supercells (1-8a and 1-7b). Two radar reflectivity contours are shown, and the gust front positions are shown using conventional frontal symbols. The small dark arrows in the "a" life cycle indicate the location of the rear downdraft/outflow (after Moller et al., 1994, adapted from Moller et al., 1990).**

Relatively few numerical simulations of HP supercells have been reported in the literature. HP supercells frequently develop along pre-existing boundaries, making it difficult to simulate these storms if traditional homogeneous initialization procedures are used. Also, the CL-HP life cycle requires longer simulation times. Brooks et al. (1994b) simulated an HP-type supercell by reducing the mid-level (3-7 km) storm-relative wind speed (discussed below). Kulie and Lin (1998) simulated an observed hybrid multicell-supercell thunderstorm complex that produced an HP supercell. Many features of the actual case study were well represented, however, the actual storm was influenced by a pre-existing mesoscale boundary that could not be simulated using the horizontally homogeneous initialization. Variable initialization procedures may prove to be more successful when simulating HP supercells.

There are several problems associated with this precipitation-based classification spectrum (Rasmussen and Straka, 1998). The importance of the precipitation rate beneath the forward flank anvil is not clearly stated. For example, would a storm having little precipitation below the updraft but heavy precipitation below the anvil be classified as an LP supercell or something else? Another weakness of the precipitation-based classification is its subjectivity, relying on an observer's impressions of the precipitation intensity beneath the updraft. Nevertheless, when the typical features of these various storm types are observed, it does enhance our ability to predict the potential of tornadoes in the CL case, large hail in the LP case, and flash-flooding with HP supercells.

### 2.4.4 *The Impact of Vertical Wind Shear on the Supercell Spectrum*

Two hypotheses have recently emerged regarding the importance of mid-level (3-7km AGL) and upper-level (8-10km AGL) vertical shear on the supercell spectrum. Brooks et al. (1994b) used a numerical model to investigate the impact of mid-level winds on low-level mesocyclogenesis. They found that if a long-lived, low-level mesocyclone is to develop, a balance is needed between the strength of the mid-level

mesocyclone, which acts to wrap the rain around the updraft, and the mid-level storm-relative environmental winds, which blows rain away from the updraft. Such a balance results in the rain being deposited relatively close to the updraft, the baroclinic generation of low-level vorticity near the updraft, a gust front that propagates with the storm and the development of a persistent low-level mesocyclone.

If the mid-level winds were too strong with respect to the mid-level mesocyclone intensity, Brooks et al. found that more rain was blown away from the updraft, low-level baroclinic generation of vorticity was decreased, and a low-level mesocyclone did not develop. If the mid-level storm-relative winds were weak, large amounts of rain were carried by the mesocyclone to the west of the updraft, the rain fell in and near the updraft and a low-level mesocyclone developed rapidly as the baroclinic generation of vorticity was large. However, if the downdraft and resultant outflow were too strong, the cold air undercut the updraft, causing an early demise of the storm. They likened the weak shear storm to an HP-type supercell in that the precipitation falls close to the updraft. They also suggested that the early dissipation of the mesocyclone in this case may explain the relatively low frequency of tornadoes associated with these storms. Thompson (1998) examined observations and forecasts from the operational Eta Model of 131 supercells and found that storm-relative wind speeds at the surface and 250 mb were similar between tornadic and nontornadic supercells, but that there were significant differences at 500 mb, which supports the importance of the mid-level shear.

In an important observational study, Rasmussen and Straka (1998) analyzed 43 supercells to investigate the role that upper-level (8-10km AGL) storm-relative flow has on storm morphology. Their hypothesis is summarized as follows: the primary cause of the morphology and precipitation variations across the supercell spectrum is the degree to which storm updrafts re-ingest hydrometeors that descend from the anvil, or from other storms. Given supercell updraft strengths and resultant parcel residence times within the storm, precipitation near the updraft most likely occurs as a result of the ingestion of

hydrometeors from outside the updraft. Embryos that fall near the updraft have a greater chance of re-entering the updraft because the flow in the lower half of the storm generally converges toward the updraft. Hydrometeors are therefore more (less) likely to re-enter the updraft if the anvil-level storm-relative winds are weaker (stronger) as they fall closer to (further from) the updraft.

Rasmussen and Straka examined the wind field in LP. CL and HP supercell environments. They found:

1) The most significant differences between the hodographs occurred in the upper tropospheric levels (above ~7km AGL) (Figure 2.15). The winds backed relatively strongly in LP environments and veered in HP environments, while the mean CL winds fell between the HP and LP categories. This implies that LP supercells are not likely to occur if the hodograph veers between 5 and 9 km, and that HP supercells are unlikely if the hodograph backs.

2) The upper-tropospheric storm-relative flow was strongest in LP cases with the greatest increase occurring between 4 and 10 km AGL. For the HP cases, the storm-relative wind speed was almost constant throughout the depth of the troposphere. Therefore, in LP environments, the strong storm-relative upper-level flow will transport hydrometeors further away from the updraft than those associated with HP supercells, thereby reducing the number of potential hydrometeors that may be re-ingested and the amount of precipitation produced in the updraft. If there are fewer hydrometeors, competition for supercooled water is reduced. This may explain why large hail is often the only/dominant precipitation type observed with LP supercells. The weak storm-relative upper-level flow in the case of HP supercells allows for many more hydrometeors to be re-ingested into the updraft and the production of greater amounts of precipitation. This result also

implies that the type of supercell that develops may be strongly influenced by the storm motion itself, as the storm motion has an impact on the storm-relative flow.

3) Between 4 and 6km AGL, all three classes had weak SR flow. This is in conflict with Brooks et al. (1994b) who found that the anvil-level SR flow, rather than the mid-level flow, was important in determining the precipitation distribution within the storm. Rasmussen and Straka argued that Brooks et al. did not perform any simulations to test the sensitivity of precipitation distribution to the upper-level storm-relative flow, which is the region of slow-falling hydrometeors and more susceptible to gravitational sorting, and that the use of Kessler microphysics biased the precipitation distribution toward the updraft.

4) The lower-tropospheric shear was the weakest in the HP cases. LP storms had stronger low-level shear but the hodograph was relatively straight. CL supercells had the strongest low-level shear and the hodograph with the greatest curvature.

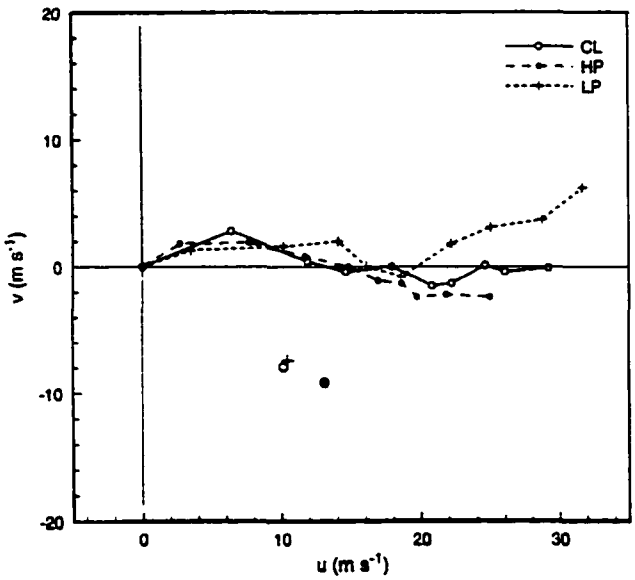


**Figure 2.15: Composite hodographs for the LP, CL and HP supercell classes. All hodographs are rotated so that the boundary layer to 4 km shear vector is orientated toward the east and boundary layer mean wind is at the origin, prior to compositing. The average motion of LP storms is represented by plus signs, of CL storms by open circles, and of HP storms by filled circles (after Rasmussen and Straka, 1998).**

The findings of Rasmussen and Straka do help elucidate some of the commonly observed characteristics of supercells. LP storms are often found near the dryline. The dryline environment suppresses the development of convection upstream from it, thus reducing the number of hydrometeors that would be available for re-ingestion from other storms. Whenever supercell storms interact with other storms, more hydrometeors become available for re-ingestion and the supercell will tend toward the HP side of the spectrum. This explains why HP supercells become more dominant further east as the occurrence of other storms within the supercell domain becomes more likely. HP supercells are the most commonly observed supercell type since convective storms do not often develop in isolation.

In summary, the common factor of all supercells is the presence of a deep, persistent mesocyclone. However, the distribution of precipitation within supercells, the amount of precipitation they produce, and the associated radar characteristics may vary substantially. Forecasting these supercell storms, and the severe weather associated with each type, is therefore very challenging. To assist with the recognition of these various supercell forms, a supercell spectrum, based on precipitation distribution and magnitude, has been developed.

## 2.5 Hail in Supercells

The initiation and growth of hail in supercells is a complex process. It is the result of a large number of dynamical and microphysical processes interacting on a wide range of spatial and time scales. The development of hail may also influence these processes in a feedback mechanism. The formation and distribution of precipitation within supercells may not only be indicative of the unique dynamics of supercell storms, it also may perform a crucial role in controlling storm dynamics.

### 2.5.1 *Environmental Conditions*

The size of the hailstones produced within severe convective storms is dependent on numerous factors (Danielson, 1977; List, 1982; Cotton and Anthes, 1989; Johns and Doswell, 1992). These include:

- **Atmospheric Instability:** The more unstable the atmosphere is, the more likely it is that thunderstorms will develop that have updrafts strong enough to support larger hail stones, thereby increasing their residence time in the storm.

- **Atmospheric Wind Field**: The wind field affects the transit time of a hailstone throughout a convective storm. Hailstorms often form in environments of strong vertical wind shear (e.g. Ludlam, 1963). This allows for the development of the self-sustained supercell storm structure and a resultant increase in transit times and hailstone recycling. However, damaging hail can also form under weak shear conditions (e.g. Renick, 1971).

- **Melting Level:** The height of the melting level (ML) determines the amount (if any) and size of the hail reaching the ground. The amount of melting is affected by the distance between the ML and the ground, the mean temperature of the downdraft air between the ML and the ground, and the hailstone size (Foote, 1984; Johns and Doswell, 1992).

- **Environmental Conditions:** Drier, warmer environmental air between the ML and the ground, and the entrainment of dry ambient air into the downdraft, all increase melting rates (Foote, 1984; Johns and Doswell, 1992). In the upper regions of the cloud, lower temperatures and greater amounts of supercooled liquid water in hail formation regions enhance the development of larger hailstones. Finally, collision-coalescence processes are likely to dominate when the cloud base is warm, thereby reducing the amount of supercooled water reaching hail producing regions (Cotton and Anthes, 1989).

- **CNN and IN Concentrations:** Greater CCN and IN concentrations increase the competition for supercooled water resulting in smaller hailstones. Concentrations that are too low reduce the chances of embryonic development (Danielson, 1977).

### 2.5.2 *Hail Formation*

Numerous accounts of supercell hailstorms have been described in the literature (e.g. Browning, 1964; Marwitz, 1972; Chisholm and Renick, 1972; Chisholm, 1973; Browning and Foote, 1976; Browning, 1977; Nelson, 1983; Foote, 1984; Krauss and Marwitz, 1984; Knight and Knupp, 1986; Musil et al., 1986; Miller et al., 1988; Miller et al., 1990; Hubbert et al., 1998). Even though supercells are infrequent, they generally

produce the largest hailstones across the longest and widest swathes, and are a major contributor to hail damage. For example, a supercell that developed on 5 July 1996 near the Montana-Wyoming-South Dakota border caused complete vegetation destruction along a path that was 120 km long and 7-11 km wide. Hail as large as 14-17 cm in diameter was observed (Klimowski et al., 1998). Nelson and Young (1979) performed a statistical analysis of the hailstorms that occurred over central Oklahoma for the months of April through June during 1974-1977. They found that 25% of the storms were supercell storms with a larger mean hail diameter (4.4cm) and a larger mean maximum swath width (18.3 km) than ordinary storms (1.4cm, 8.1 km).

A conceptual model of hail formation within supercells was developed by Browning and Foote (1976). They based their model on the Fleming, Colorado hailstorm that occurred on 21 June 1972, which produced a hail swath about 300 km long and 15-20 km wide. Baseball-sized hail was observed near Fleming. A weakly developed hook echo (Figure 2.16a) and a BWER, surrounded by a hail cascade to the north and east, and an embryo curtain to the south (Figure 2.16b) were evident in the radar imagery.

Browning and Foote suggested that the growth of hail within supercells occurs in three stages (Figure 2.17). In the first stage, hail embryos develop in a relatively narrow region along the edge of the main updraft where wind speeds are about 10 $m.s^{-1}$. This allows them to grow to millimeter size. Those particles that develop on the western (right) flank have a good chance of moving into the embryo curtain (trajectory 1). The particles that develop near the core of the updraft experience speeds of around $30m.s^{-1}$ and cannot grow large due to insufficient time and glaciation effects. These particles form the WER, and most of them are exhausted through the anvil (trajectory 0).

During stage 2, the embryos that develop on the western edge of the updraft are transported southward by the diverging flow around the updraft. Some of the larger particles will fall into the weaker updrafts of the embryo curtain (trajectory 2). Some

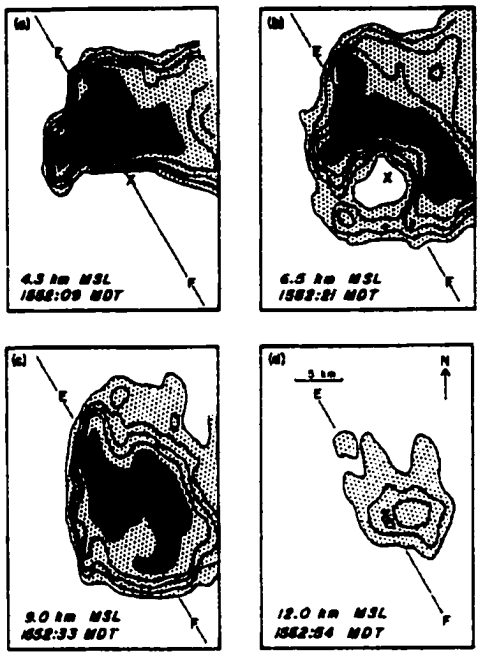

**Figure 2.16: Quasi-horizontal sections at four altitudes showing the radar reflectivity for the Fleming storm at 1552-1553 MDT. Reflectivity contours are at 5 dBz intervals. Areas in excess of 30 and 50 dBz, respectively, are stippled thinly and thickly. X is a fiducial mark (after Browning and Foote, 1976).**

particles will also move from the main updraft into the embryo curtain through the process of updraft erosion as the environmental air meets the updraft air on the western flank and then circulates southward. Further growth of the embryos is likely while they descend in the embryo curtain. The larger particles then fall to the tip of the curtain where they may be re-ingested into the main updraft.

In stage 3, the hailstones grow rapidly in size as they experience near adiabatic liquid-water contents while ascending in the main updraft. The growth occurs in a simple up-and-down cycle (trajectory 3), similar to that of Browning (1963) and English (1973). Those embryos that enter the updraft at lower levels are more likely to experience a near-balance between their fallspeeds and the updraft speed. This gives the embryo sufficient time to accrete large amounts of liquid water as they rise slowly through the updraft, eventually reaching a level of balance. Finally, their fall velocities will become large

enough to overcome the updraft velocities, and they descend into the downdraft region as they travel toward the north in the tilted updraft.

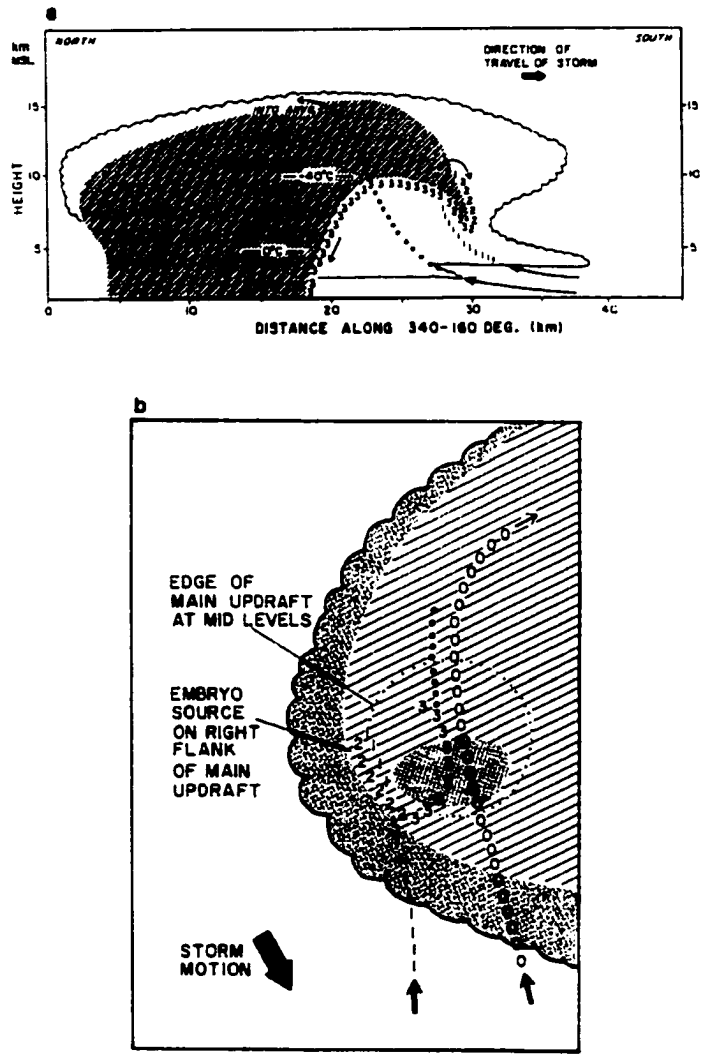


**Figure 2.17: (a) and (b) Schematic model of hailstone trajectories within a supercell storm based on the airflow model of Browning and Foote (1976). (a) shows hail trajectories in a vertical section along the direction of travel of the storm. (b) shows these same trajectories in plan view. Trajectories 1,2 and 3 represent the three stages of growth of large hailstones discussed in the text. The transition from stage 2 to 3 corresponds to the re-entry of a hailstone embryo into the main updraft prior to the final up-and-down trajectory during which the hailstone may grow large, especially if it grows close to the boundary of the vault. Other, slightly less favored hailstones will grow a little further away from the edge of the vault and will follow trajectories resembling the dotted trajectory. Cloud particles growing 'from scratch' within the updraft core are carried rapidly up and out into the anvil along trajectory 0 before they can attain precipitation size (after Browning and Foote, 1976).**

Both Browning (1963) and Browning and Foote (1976) emphasized that it is the need for the embryo fallspeeds to match the updraft speeds, rather than the scarcity of embryos, that cause the infrequent occurrence of large hail. Nelson (1983), like Browning and Foote (1976), also found that most of the hail growth occurs in a single pass across the updraft. He emphasized that a factor more crucial to the growth of large hail than abundant embryos and the updraft speed, is a broad region of moderate updrafts. This allows hailstones to remain at a level of balance in favorable growth regions for a longer time period. Narrow strong updrafts increase the potential for hailstones to exit through the anvil.

Miller et al. (1988) noticed in their study of a classic supercell that the recycling trajectory suggested by Browning and Foote was not present. They found that although some of the hail embryos did grow while ascending in the right flank of the updraft and descending around the front side of the updraft, the fallspeeds of these potential embryos were such that they did not recycle back into the strong updraft. Embryos for the last part of the recycling trajectory were more likely to come from shedding processes in the lower part of the forward overhang or the upwind stagnation zone.

Currently, the source of hail embryos in supercell storms is a point of controversy. Suggested regions include the edges of the main updraft and upshear of the updraft (Browning and Foote, 1976), small cells along the supercell flanks (Miller and Fankhauser, 1983) or fine-scale convective cells adjacent to the main updraft (Krauss and Marwitz, 1984), although these processes may be more representative of mulicell-supercell hybrid storms. Re-circulation from the forward overhang (Farley and Orville, 1986), various regions according to the fallout regions (Knight and Knupp, 1986), shedding in the overhang region and the gust front convergence zone (Miller et al., 1988), graupel grown along updraft fringes, and shedding of drops from melting graupel and hail (Miller et al., 1990) are other suggested sources. The source of hailstone embryos in supercells is therefore still not completely understood.

In summary, hail in supercell storms develops either after an embryo re-enters the updraft or a shed water droplet enters the updraft for the first time. The particle then grows through a single up-and-down pass through the updraft. Some aspects of hail development, like the origin of hail embryos, are still not generally agreed upon. It is apparent that the development of hail within supercells is a complicated process relying strongly on the dynamics of the storm. The question to be addressed now is whether hail processes have an impact on the storm dynamics of supercells.

## 2.6 Hail and Supercell Storm Dynamics

The presence of ice in severe thunderstorms is thought to have a significant effect on the storm dynamics (Jewett et al., 1990; Johnson et al., 1993). Using a one-dimensional model, List et al. (1968) showed that release of the latent heat of fusion associated with the riming process in hail development produced a much warmer cloud than when ice processes were not present. The freezing of water droplets to form hail and the deposition of water vapor onto ice particles can also release significant amounts of latent heat. This "thermal feedback" may then enhance cloud growth and storm strength. Melting of hail also affects the thermodynamic structure of the cloud by cooling the air, and several investigators have shown that ice processes can play an important role in the generation of low-level downdrafts (e.g. Krueger et al., 1986; Srivastava, 1987; Hjelmfelt et al., 1989; Proctor, 1988, 1989; Orville et al., 1989; Knupp, 1989).

The difference in fall speeds of hail and rain can also have an impact on the storm dynamics (Jewett et al., 1990). Large hail generally falls closer to the updraft than rain since it has a greater fall speed, although smaller ice hydrometeors may be distributed further away from the updraft than rain. Smaller ice hydrometeors may also be transported higher in the cloud and this may influence the storm thermodynamics. The amount and distribution of precipitation, with respect to the updraft, affect the strength

and position of the cold pool. As noted above, the storm propagation, the formation and decay of the low-level mesocyclone, and even the mid-level mesocyclone all depend in varying degrees on the low-level buoyancy gradients associated with the cold pool (Rasmussen and Straka, 1998). The impact that precipitation physics may have on supercell storm dynamics is only just beginning to be investigated and understood (e.g. Jewett et al., 1990; Johnson et al., 1993; Brooks et al., 1994b; Tartaglione et al., 1996; Rasmussen and Straka, 1998). Numerical models are very useful in determining this impact since ice processes may be "turned off". Simulations with and without ice processes may then be compared.

### 2.6.1 *Modeling Ice Processes in Supercell Storms*

Numerical models have been used since the early 1970s to simulate the development of cumulus convection and thunderstorms (e.g. Steiner, 1973; Schlesinger, 1973, 1975). Since then, considerable progress has been made in the representation of microphysical processes within cloud and mesoscale models. Numerous microphysical parameterization schemes that include ice processes are currently being utilized (e.g. Takahashi, 1976; Orville and Kopp, 1977; Cotton et al., 1982, 1986; Lin et al., 1983; Farley and Orville,1986; Farley, 1987a,b; Ferrier, 1993; Walko et al., 1995; Reisin et al., 1996; Meyers et al.,1997; Hong and Pen, 1999). These parameterizations vary in complexity from two to three dimensions, from single- to two-moment bulk microphysics, from bulk to bin microphysics, and from several to numerous microphysical species.

Many three-dimensional simulations of supercells have been performed using simple Kessler parameterizations (e.g. Klemp and Wilhelmson, 1978a,b; Weisman and Bluestein, 1985; Brooks et al., 1994b), even though ice processes are thought to have a significant effect on supercell storm dynamics and thermodynamics, and that graupel and hail are the predominant precipitation type in Great Plains thunderstorms (Knight et al.,

1974). The exclusion of ice processes has been forced, to some degree, by computer and time constraints, and also by a resistance to code and implement ice physics in mesoscale models. Omitting ice species may certainly be a valid assumption. The supercell simulations referred to above capture numerous aspects of the dynamical processes occurring within supercells. However, the significance of excluding ice processes on supercell storm dynamics is still not well understood. Producing accurate simulations of the precipitation characteristics of supercell storms has also proved challenging to the modeling community. Simulations of CL supercells appear regularly in the literature, whereas simulations of HP and LP supercells, where microphysical processes may play a more important role, appear less frequently. It would therefore appear that the impact of ice parameterization schemes on simulated supercell storm dynamics and precipitation needs further investigation.

Numerous researchers have drawn attention to the need to include ice processes in numerical models. Brooks and Wilhelmson (1992) state that the use of Kessler microphysics in their simulations of an LP supercell may be a serious limitation because LP storms are known to produce large hail thereby changing the distribution of latent heat release. Gilmore and Wicker (1998) stress that future downdraft modeling studies need to include ice microphysics in order to represent the complexities of entrainment and evaporation more accurately. Weisman and Klemp (1984) and Adlerman et al. (1999) all feel that their simulations could benefit from the inclusion of full ice microphysics. Brooks et al (1994b) claim that the absence of ice from their simulations does not appear to significantly affect the qualitative results of their simulation. However, as they have not rerun their simulations with ice microphysics, their statement seems to be unsubstantiated. They do speculate that the presence of ice may have a quantitative effect in that it could affect both the location and strength of the downdrafts, and that as the system is nonlinear, it could be important in certain marginal cases. Klemp and Wilhelmson (1978a) found that supercell dynamics is strongly influenced by negative

buoyancy, which in turn is controlled by water loading and latent heat release. They state that improving the microphysics would improve the water distribution throughout the storm. In spite of the attention placed on the need to determine the importance of ice microphysics in simulations of supercells, the impact of excluding ice processes on storm dynamics has only been examined relatively recently (Jewett et al., 1990; Johnson et al., 1993; Tartaglione et al.,1996; Schlesinger, 1999).

Jewett et al. (1990) performed a three-dimensional simulation of a severe storm with and without ice processes. In their no-ice run, all ice processes were turned off. Their simulations showed that the maximum updraft velocities were stronger and the maximum perturbation potential temperatures were greater in the ice simulation. In the no-ice case, the main downdraft was stronger and a secondary downdraft was evident due to the slower fall speeds of rain. However, the downdraft was positioned closer to the updraft in the ice simulation. For most of the simulation, the no-ice run had greater low-level vertical vorticity magnitudes than the ice run, due to the baroclinic effects associated with the stronger horizontal perturbation potential gradients along the gust front. Finally, more precipitation reached the ground in the ice simulation. These results show that the exclusion of ice can lead to significant differences in the storm structure, particularly at lower levels.

In a landmark paper, Johnson et al. (1993) used a numerical model to conduct a detailed investigation into the role that ice played in a case study of a highly glaciated supercell storm that passed through the Cooperative Convective Precipitation Experiment (CCOPE) in southeastern Montana on 2 August 1981 (Knight, 1982; Miller et al., 1988). The majority of hail stones ranged from 5mm to 3cm, with a few as large as 6 to 10 cm. They compared a simulation in which ice processes were included with a simulation in which all ice processes were "turned off". The simulations were otherwise identical. Johnson et al. found that both the ice and no-ice simulations produced many of the features characteristic of supercell storms like the BWER, hook echoes, rotating updrafts,

overshooting tops, upwind anvils and overhanging anvils; however, they were more pronounced and more representative of the actual observations in the ice simulation. The maximum vertical velocity and potential temperatures were greater in the ice simulation, but the cold pool was stronger in the no-ice simulation. The storms had similar vertical structures, but the downdraft was located further away from the updraft in the ice simulation as a result of hail and graupel falling from the anvil.

The most significant difference between the simulations of Johnson et al. was that the ice simulation storm had a much longer lifetime than the storm in the no-ice simulation. In the no-ice simulation, the low-level downdrafts were stronger which forced the gust front to propagate away from the storm, thereby causing its demise. In the ice simulation, the gust front propagated with the storm, which allowed the storm to exist throughout the entire simulation time. Johnson et al. also found that the LM and RM were initially of similar strength in the no-ice case, and the LM then split. However, the LM was always much weaker than the RM in the ice simulation, and the LM did not split. The LM was also slightly longer-lived in the ice simulation.

Surface rainwater mixing ratios were greater for the no-ice simulation, but the total surface precipitation was 10-20% greater in the ice case due to the slower storm movement and greater areal precipitation coverage. The greater region of rainfall in the ice simulation was due to the melting of small ice and hail that fell from the downwind anvil. Finally, the mid-level vertical vorticity maxima were similar between the no-ice and ice runs, however, the low-level vertical vorticity maxima differed (Figure 2.18). The low-level vertical vorticity was generally greater in the no-ice case than in the ice case, until the storm occluded in the former simulation. In the ice case, the low-level vertical vorticity increased linearly as the downdraft strengthened. Johnson et al. have therefore shown that the inclusion of ice in their simulation of a supercell strongly impacts the dynamics, kinematics, thermodynamics and distribution of precipitation in the cloud and at the surface.

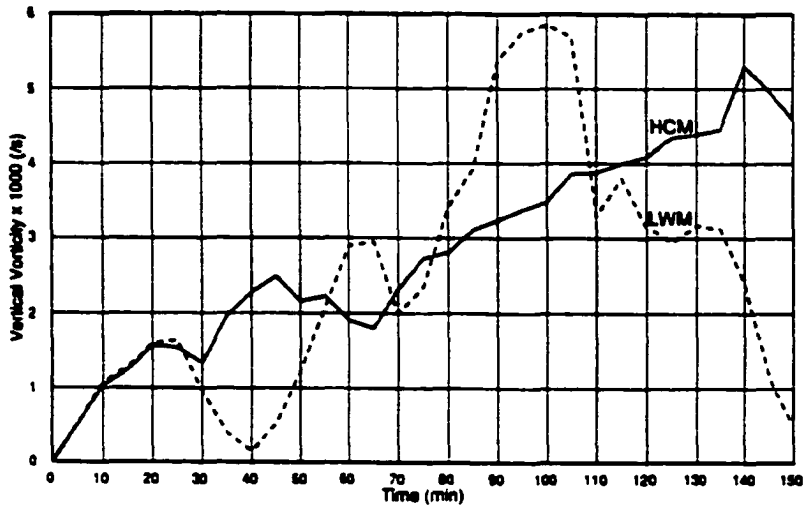


**Figure 2.18: Maximum vertical vorticity versus time below 1km in the HCM (solid) and LWM (dashed) simulations of Johnson et al. (1993) (after Johnson et al., 1993).**

Instead of incorporating ice variables into their model, Tartaglione et al. (1996) reduced the terminal fall velocity of precipitation in the coldest cloud layers to simulate one of the effects of the presence of ice. Phase transitions were not included. They compared a "no-ice" (standard Klemp-Wilhelmson fall velocity formulation) run with an "ice" (fall speeds adjusted to indicate presence of ice) simulation. They found from their simulations that the LM storm was of similar strength to the RM storm in the no-ice case, but was weaker than the RM in the ice case. The updraft, anvil, BWER and hook echo were all better developed, and the areal coverage of precipiation was greater in the ice case. They also observed that the low-level vertical vorticity was larger (in the mature phase) and the transition to the tornadic phase occurred earlier in the no-ice simulation, although the vorticity increased at all levels in the ice run which was more in keeping with observations (e.g. Klemp et al., 1981). As many of the features simulated by Johnson et al. (1993) were also captured by Tartaglione et al., the latter claimed that the fall speed of the ice phase was the most important of the microphysical effects on supercell dynamics, and thus the use of their simplified ice scheme was justified.

Schlesinger (1999) made use of a simple ice phase parameterization scheme to simulate a severe supercell storm over Oklahoma. He found that by omitting ice processes, the peak updraft of the supercell was reduced by ~ 10%, but that there was no systematic effect on the strength of the downdraft. He also found that without ice, there was a weakening of the supercell in the later stages of the simulation compared with the simulation in which ice was included. The heating and drying amplitudes were ~25% lower in the case without ice due to the absence of the latent heat of fusion and the decrease in condensation.

Meyers et al. (1997) developed a two-moment bulk microphysics scheme. The scheme predicts both the mixing ratio and number concentration of the microphysical species, and allows the mean hail diameter to evolve more realistically than in the single-moment scheme. Using a two-dimensional domain, they investigated the sensitivity of the microphysical characteristics of a convective storm to changes in the gamma distribution shape parameter, to the number concentration of cloud droplets, and to the use of a single-moment scheme. Meyers et al. found that their results were very sensitive to all three tests. The two-moment scheme produced smaller hail diameters than those in the single-moment scheme and, as a result, generated lower hail mixing ratios, reduced fallout rates, and lessened total precipitation at the ground. Reducing the number concentration of cloud droplets enhanced warm rain processes, whereas increasing the number concentration significantly reduced these processes. Increasing the shape parameter from 1 to 3 for all the species resulted in a threefold increase in precipitation due to the greater hydrometeor diameters. While the single-moment scheme also produced more precipitation, most of this was hail, whereas in the shape parameter sensitivity test, most of the precipitation was rain. These results demonstrate the sensitivity of hail production to numerous microphysical parameters, as well as the importance of correctly representing microphysical processes within our simulations of convective storms.

## 2.7 Goals

We have seen from the discussion above that microphysical processes appear to have a significant impact on the dynamical and thermodynamical structure of supercells. However, this relationship is still not well understood. While mesoscale models have been used fairly successfully to enhance our understanding of the dynamics of supercell storms, the forecasting of the precipitation characteristics of such storms has proved challenging to the modeling community.

Numerous choices need to be made regarding the representation of microphysical processes within a numerical model. These include the degree of the complexity of the scheme to be used, which often depends on whether the model is being run in operational or research mode. For example, a simple bulk microphysical scheme with limited species may be used if the model is to be run in operational mode, whereas a more sophisticated bin-type representation may be chosen for research purposes. Many of the simulations of supercell dynamics in the past have often, in light of computer constraints or lack of an ice scheme, been conducted without ice microphysics even though ice processes appear to have a significant effect on storm dynamics. Such simplifications, like using a bulk scheme over a bin scheme or excluding ice processes, may be justified, however the implications of such simplifications need to be understood. Relatively little research has been conducted into the effects of these simplifications on storm dynamics.

Further decisions need to be made involving specific microphysical parameters. Choosing which microphysical species to represent, determining an appropriate distribution for each species, and assigning a mean diameter for each species are examples of several of the options that need consideration when using a single-moment bulk microphysics scheme. Also, parameters may need to be set for a broad range of weather systems when models are used in operational mode, where the "tweaking" of parameters is not an option. This makes it more important that we understand the impact

of our parameter choices on severe storm simulations. As the microphysics of severe storms appears to have a significant effect on the storm dynamics, improving microphysical parameterization schemes in cloud and mesoscale models may be necessary, not only to improve our forecasts of supercell precipitation characteristics, but also to improve our simulations of supercell storm dynamics.

The broad goal of the research conducted here is to determine the impact that hail has on the characteristics of simulated supercell storms. This will be achieved by examining the influence the following have on the dynamics, thermodynamics, and morphology of simulated supercell storms:

1. changing the mean hail diameter,

2. changing the gamma distribution shape parameter of hail,

3. excluding all precipitation processes,

4. excluding only ice processes,

5. excluding only hail processes, and

6. varying the complexity of the parameterization scheme.

The results of these sensitivity tests will be presented following a discussion of the model that used to perform these simulations.

# 3

# Model Description and Experiment Setup

In this chapter, the primitive equation model that was used to determine the impact that hail has on the dynamics of modeled supercells is discussed. The model aspects specific to the simulations performed for this research are outlined in section 3.1. For a more general discussion on the numerous options available in the model the reader is referred to Pielke et al. (1992) and Cotton et al. (2001). The grid configuration and simulation initialization are described in section 3.2. Finally, the design of the experiments and sensitivity tests conducted will be presented in section 3.3.

## 3.1 Primitive Equation Model

The Regional Atmospheric Modeling System (RAMS) developed at Colorado State University was used for all the simulations that were conducted. RAMS utilizes the full set of nonhydrostatic, Reynold's averaged primitive equations (Tripoli and Cotton, 1986). The model solution is advanced in time using a hybrid timestep scheme in which the momentum and scalar fields are integrated using a second-order accurate leapfrog and forward scheme respectively. RAMS uses the staggered C grid (Mesinger and Arakawa, 1976), and a terrain-following $\sigma_z$ coordinate scheme in the vertical (Gal-Chen and Somerville, 1975; Clark, 1977; Tripoli and Cotton, 1982). The deformation K closure

scheme of Smagorinsky (1963), with some stability modifications (Lilly, 1962; Hill, 1974), constitutes the subgrid-scale turbulence parameterization scheme.

The basic radiative condition was applied at the lateral boundaries and the determination of the phase speed follows that of Klemp and Wilhelmson (1978). A rigid lid was used at model top and a Rayleigh friction layer was extended over the top 4 model levels to absorb gravity waves. The lower boundary was a free-slip boundary, with no surface fluxes of heat or moisture. Use of this condition also prevented the use of radiation schemes. This should not significantly affect the model solution given the duration of the simulations. The soil and vegetation schemes were also not activated. Coriolis force was turned on.

The microphysical species represented in RAMS include vapor, cloud droplets, rain, pristine ice, snow, aggregates, graupel and hail. Features of the microphysical scheme include generalized gamma distributions for each hydrometeor class (Flateau et al., 1989; Verlinde et al., 1990), the use of stochastic collection rather than continuous accretion (Verlinde et al., 1990), and a heat budget equation for each hydrometeor class that allows for heat storage on the hydrometeor surface as well as for mixed-phase species (Walko et al., 1995). The reader is referred to Walko et al. (1995) and Meyers et al. (1997) for a more detailed discussion of these features. Numerous microphysical schemes are available in RAMS. These include the single-moment bulk scheme in which the hydrometeor mixing ratios are predicted; the two-moment bulk scheme in which both the mixing ratio and number concentration of the species are predicted; and the bin model in which the size distribution of a species is represented by a series of discrete bins. For the simulations performed here, both bulk microphysical categories were used. One of our future research goals is to rerun these simulations using the bin model. Numerous microphysical parameters and options need to be set by the user. These include deciding on which species to incorporate, and then determining the distribution characteristics of

the species. The selections that were made for each of the sensitivity simulations are discussed in detail below.

## 3.2 Model Configuration

A single model grid (140x170x35) with grid spacing of 1 kilometer in the horizontal and variable grid spacing in the vertical was used. The lowest vertical grid spacing was 100 meters, and this was stretched using a stretch ratio of 1.1 until the vertical grid spacing reached 2000 meters, above which it was kept constant. This means that the model top was at approximately 23 kilometers AGL and that there were 9 model levels in the first 1 kilometer AGL. These resolutions are sufficient to resolve storm-scale features and processes, like the updraft and downdraft features and mesocyclogenesis, but are insufficient to simulate tornadogenesis. The long timestep was 5 seconds.

The model domain was initialized horizontally homogeneously using a sounding that is typical of severe storm days over Oklahoma (Figure 3.1). Grasso (2000) used a similar sounding. Convection was initiated using a warm (3K temperature perturbation), moist (20% moisture perturbation) bubble that was 10 by 10 kilometers in the horizontal, extending from the surface to approximately 2.5 kilometers AGL. All the simulations were allowed to develop for at least 2 hours. The details of the model configuration are summarized in Table 3.1.

## 3.3 Experiment Design

As discussed in the previous chapter, the goal of this research is to determine the impact that hail has on modeled supercell storm characteristics. The aspects specifically under investigation are the sensitivities to the mean hail diameter, to the size distribution shape parameter, to the exclusion of various ice species, and to the complexity of the microphysical parameterization. The experiments that were designed to achieve these

goals are described following a brief discussion of some of the microphysical parameterization aspects pertinent to these experiments. The details specific to each experiment, as well as the experiment names, are summarized in Table 3.2, toward the end of the chapter.

(a)

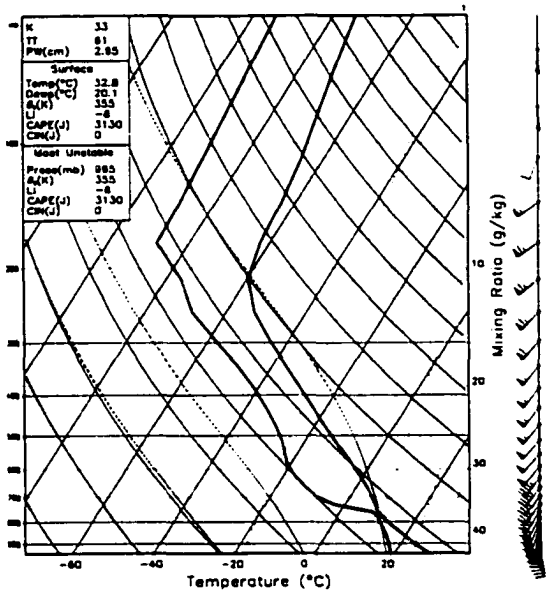


(b)

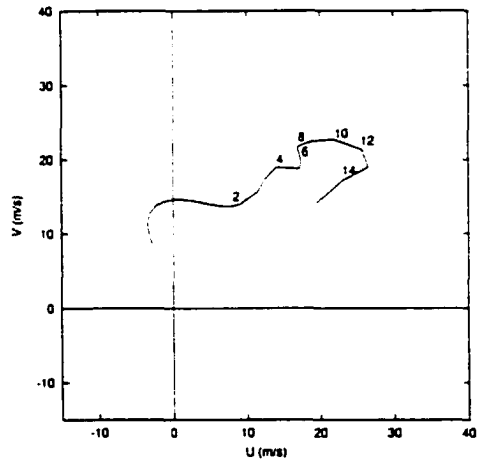


**Figure 3.1: The (a) sounding and (b) hodograph utilized in all of the simulations. Numbers on the hodograph indicate heights (km) AGL.**

**Table 3.1: Summary of the model configuration and options**

| PARAMETER / SCHEME | SETTING |
|---|---|
| • Grid | • Arakawa C grid<br>• Single grid<br>• Horizontal grid: $\Delta x = \Delta y = 1$km<br>140 x 170 points<br>• Vertical grid: $\Delta z$ variable<br>35 vertical levels<br>• Model top: ~23 km |
| • Initialization | • Horizontally homogeneous |
| • Timestep | • 5 seconds |
| • Simulation Duration | • 2 hours |
| • Microphysics | • Single-moment and two-moment bulk microphysics<br>• Vapor, cloud water, rain, pristine ice, snow, aggregates, graupel and hail all activated |
| • Convective Initiation | • Warm, moist bubble |
| • Boundary Conditions | • Radiative lateral boundary (Klemp and Wilhelmson, 1978)<br>• Rigid lid at model top with Rayleigh friction layer<br>• Free-slip lower boundary |
| • Turbulence Scheme | • Smagorinsky (1963) deformation K |
| • Radiation Scheme | • Off |
| • Surface Scheme | • Off |
| • Coriolis Force | • On |

It should be noted that the 3mm simulation, described below, served as a control run for all of the sensitivity tests that were conducted. The parameter settings in this simulation included the RAMS default setting for the mean hail diameter (3mm) and a shape distribution parameter of 1 (Marshall-Palmer distribution). The single-moment bulk microphysics scheme was employed. Similar settings are frequently used in various mesoscale models, and this therefore provides a basis for comparison.

### 3.3.1 *Some Microphysical Parameterization Considerations*

A generalized gamma distribution is assumed for each of the hydrometeor species, as described by Flateau et al (1989) and Verlinde et al (1990). The generalized gamma distribution is given by:

$$f_{gam}(D) = \frac{1}{\Gamma(\nu)}\left(\frac{D}{D_n}\right)^{\nu-1}\frac{1}{D_n}\exp\left(-\frac{D}{D_n}\right) \qquad (3.1)$$

where D is the diameter of an individual hydrometeor, $D_n$ is the characteristic diameter of the modified gamma distribution (used to non-dimensionalize D), $\nu$ is the gamma distribution shape parameter, $\Gamma(\nu)$ is the complete gamma function of $\nu$, and $f_{gam}(D)$ is the probability density function for the modified gamma distribution, which represents the fraction of total hydrometeors of a given category per unit increment of diameter D. The probability density function then needs to be multiplied by the total number concentration to obtain the number density distribution n(D):

$$n(D) = N_t f_{gam}(D) \tag{3.2}$$

where $N_t$ is the total number concentration.

The magnitude of $\nu$ controls the relative amounts of smaller versus larger hydrometeors in the hydrometeor size distribution. For a value of $\nu$=1, Eq. (3.1) reduces to the exponential or Mashall-Palmer distribution (Marshall and Palmer, 1948). The modal diameter ($D_{mode}$) is the diameter when $f_{gam}$ is at its maximum, and is related to the characteristic diameter by:

$$D_{mode} = (\nu - 1)D_n \ . \tag{3.3}$$

For $\nu$=1, the modal diameter is zero. Increasing $\nu$ increases the modal diameter. A series of gamma distribution curves demonstrating the impact of variations in $\nu$ on the distribution is shown in Figure 3.2.

As discussed in Walko et al. (1995), any moment P of the distribution, is given by:

$$\int_0^\infty D^P f_{gam}(D)dD = D_n^P \frac{\Gamma(\nu + P)}{\nu} \ . \tag{3.4}$$

Applying Eq. (3.4) to the diameter, we can obtain an expression that relates the mean diameter of the distribution ($D_{mean}$) to the $D_n$ and $\nu$:

(a) 3mm

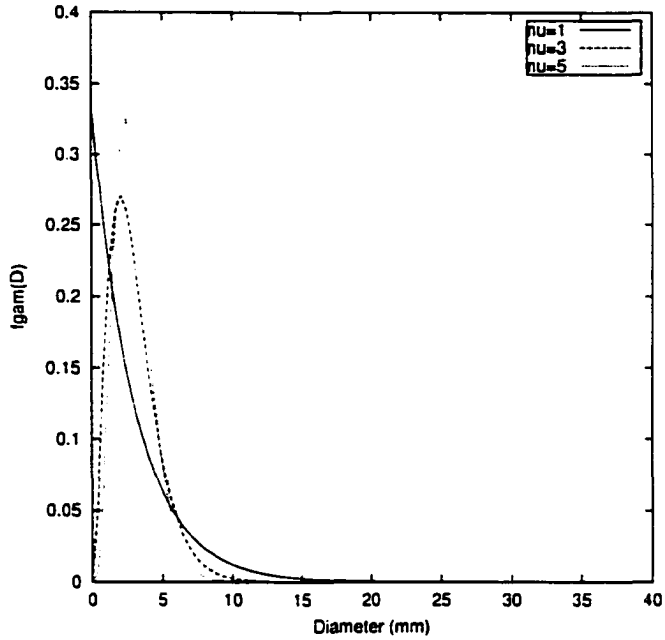


(b) 2cm

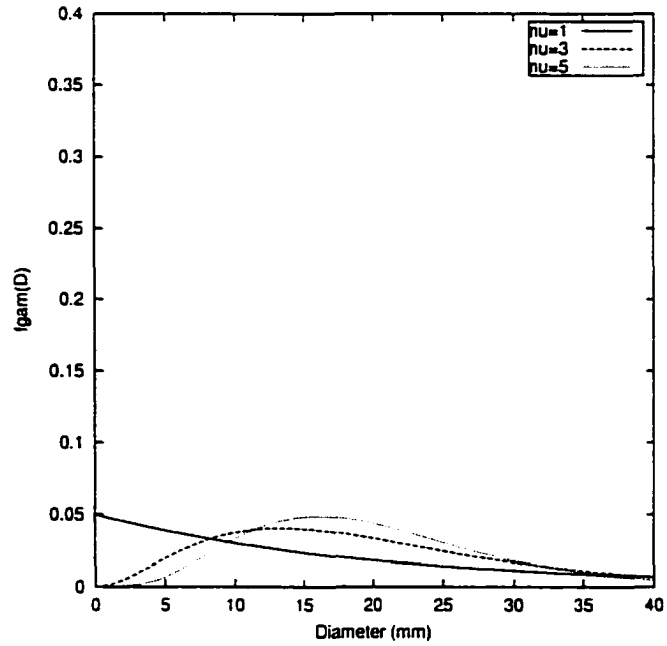


**Figure 3.2: A set of gamma distribution curves for hail obtained using v=1, v=3 and v=5, for a mean hail diameter of (a) 3mm and (b) 2cm.**

$$D_{mean} = \int_0^{\infty} D f_{gam}(D) dD = \frac{\Gamma(\nu+1)}{\Gamma(\nu)} D_n = \frac{\nu\Gamma(\nu)}{\Gamma(\nu)} D_n = \nu D_n \ . \quad (3.5)$$

It is apparent from this equation that increasing $D_{mean}$ of a hydrometeor species, while holding $\nu$ fixed, increases $D_n$, which in turn influences the size distribution of the species. The impact of the mean hydrometeor diameter on the size distribution is shown in Figure 3.3. Variations in $\nu$ and the mean diameter of a hydrometeor species have a significant impact on the size distribution of the species, particularly in the latter case. This in turn has an impact on the deposition and evaporation rates through the changes in the hydrometeor surface area, which then affects the release of latent heat within the storm. The impacts of these variations on simulated supercell characteristics will be investigated in the sensitivity tests. A description of the experiments that were conducted will be the focus of the remainder of the chapter.

### 3.3.2 *Sensitivity to Changes in the Mean Hail Diameter*

To determine the sensitivity of simulated supercell storm characteristics to changes in the mean hail diameter, four simulations were conducted in which mean hail diameters of 3 mm, 5 mm, 1 cm and 2 cm were used. The four simulations were otherwise identical. The single-moment bulk microphysics scheme was used, and all the available hydrometeor species (cloud water, rain, pristine ice, snow, aggregates, graupel and hail) were activated. The default mean diameters were used for rain (1 mm), snow (1 mm), aggregates (1 mm), and graupel (1 mm) in all of the simulations. Also, the defaults for cloud water and pristine ice, which involve the diagnoses and prediction for these species respectively (see Walko et al., 1995 for details), were utilized. It should be noted that the default value for the mean hail diameter is 3mm.

(a) v=1

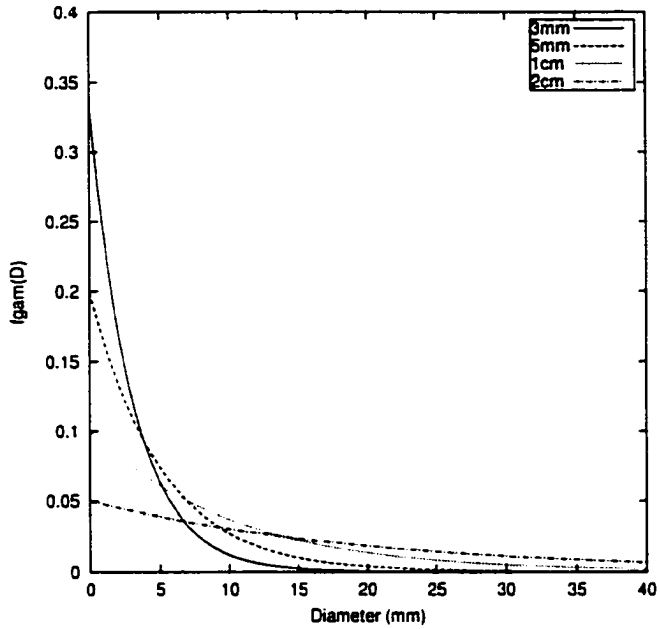


(b) v=3

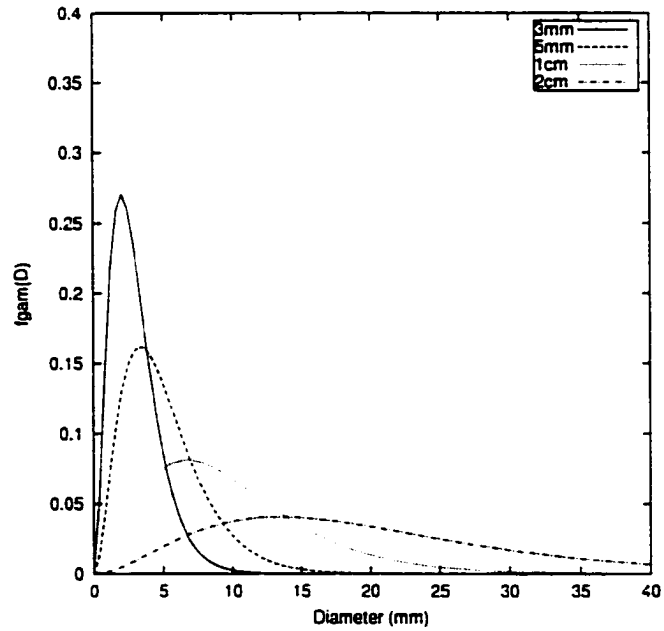


**(Figure continues on the next page)**

(c)v=5

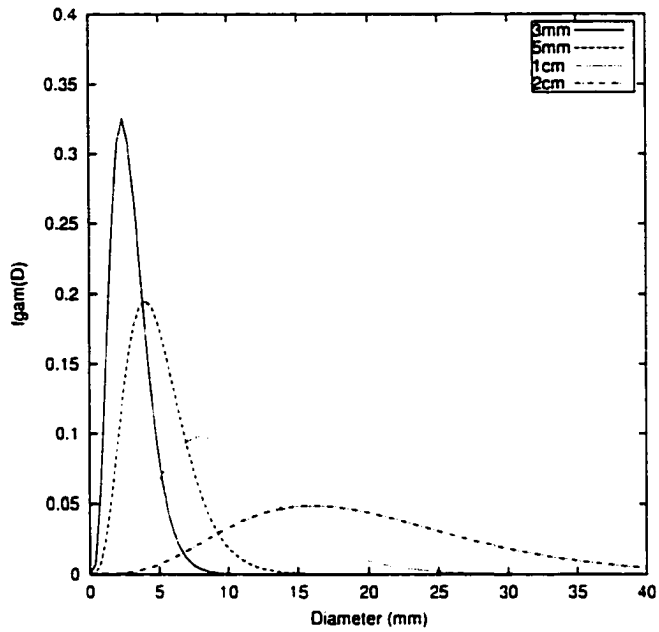


**Figure 3.3: A set of gamma distribution curves obtained by varying the mean hail diameter when (a) $\nu$ =1, (b) $\nu$=3, and (c) $\nu$=5.**

The Marshall-Palmer (exponential) size distribution ($\nu$=1) was used for each hydrometeor category in each of the four tests. This distribution is used in several other microphysical parameterization schemes including Kessler's (1969) scheme, which is frequently incorporated in many of the mesoscale models currently in use, e.g. the Klemp-Wilhelmson model (1978). This use of this distribution, as stated above, provides a basis for comparison with other model results. The parameter settings of this sensitivity test, as well as of those still to be discussed, are summarized in Table 3.2.

### 3.3.3 *Sensitivity to the Hydrometeor Species Included*

In this experiment, three simulations were run in which various hydrometeor species were excluded. These simulations were conducted in order to determine the impact that microphysical processes may have on the dynamic and thermodynamic structure of developing supercells, and extends the work of Weisman and Bluestein

(1985), Johnson et al. (1993), and Tartaglione et al. (1996). The results of these model runs were compared with those from the 3mm simulation, which served as a control simulation.

In the first simulation, condensate was allowed to develop, but precipitation was not allowed to occur. This was done in order to gain a better understanding of the importance of precipitation processes in supercell storm development. The condensate simply remained suspended at the model level where it originally developed. None of the hydrometeor species were allowed to develop. This model setup eliminates processes like drag due to precipitation loading and the development of features like the cold pool, although drag due to condensate is simulated. In the second simulation, all ice processes were excluded in order to determine the validity of excluding ice species from supercell storm simulations. Rain and cloud water were still simulated. Excluding all ice species affects processes such as latent heat release, fall speeds, and the precipitation characteristics and totals near the surface. Finally, in the third simulation, only hail and the processes related to hail were excluded. All of the other hydrometeor species were included. This test was conducted to determine the sensitivity of the supercell characteristics to hail specifically, rather than to ice in general.

### 3.3.4 *Sensitivity to Changes in the Shape Distribution Parameter ($\nu$)*

It is evident from the discussion above that variations in $\nu$ have a significant impact on the size distribution of a species. To determine the response of simulated supercells to such changes in the hail distribution, values of 3 and 5 for the $\nu$ parameter for hail were used in both the 3mm and 2cm simulations described above.

**Table 3.2: The parameter settings for the sensitivity tests discussed in the text**

| EXPERIMENT NAME | HAIL DIAMETER | HAIL ν | MOMENTS |
|---|---|---|---|
| | | | |
| MEAN HAIL DIAMETER | | | |
| 3mm | 3mm | 1 | Single |
| 5mm | 5mm | 1 | Single |
| 1cm | 1cm | 1 | Single |
| 2cm | 2cm | 1 | Single |
| | | | |
| SHAPE PARAMETER | | | |
| NU3 | 3mm | 3 | Single |
| NU5 | 3mm | 5 | Single |
| | | | |
| EXCLUSION OF SPECIES | | | |
| NOPREC | - | - | Single |
| NOICE | - | - | Single |
| NOHAIL | - | - | Single |
| | | | |
| TWO-MOMENT | | | |
| 2MOM | - | 1 | Two |

### 3.3.5 *Sensitivity to the Complexity of the Scheme*

Finally, as discussed in the previous chapter, it is sometimes felt that the more complicated a scheme is, the better the scheme should perform. In order to test this hypothesis, the two-moment bulk microphysics scheme was used instead of the single-moment scheme. The simulations were otherwise identical. In the two-moment parameterization, both the mixing ratio and number concentration are predicted. This allows for a variation in the mean hydrometeor diameters throughout the simulation, compared with having to fix the mean hydrometeor diameters in the single-moment scheme. The shape of the distribution does, however, still need to be specified in the two-moment scheme.

The results of all the sensitivity tests just discussed will be presented in the following chapters.

# 4

# Sensitivity to the Mean Hail Diameter

## 4.1 Introduction

It was noted in Chapter 2 that the presence of ice in severe thunderstorms has a significant effect on the storm dynamics. Numerical simulations have been conducted to investigate the impact including ice processes has on simulated severe storms. The results revealed that in the "ice" simulations, the storms were stronger and longer-lived, the supercell characteristics were better developed, and the vertical vorticity increased at all levels, compared with storms in the "no ice" simulations (Jewett et al., 1990; Johnson et al., 1993; Tartaglione et al., 1996).

When using a microphysical parameterization scheme in cloud and mesoscale models, numerous parameters often need to be set. The values for these parameters are frequently chosen somewhat arbitrarily, or the default values are used, since determining appropriate settings is made difficult by the lack of in situ cloud data. Also, the parameter magnitudes may vary substantially from storm system to storm system, making it difficult to select constant values for the parameters, when the model is to be used for forecasting purposes. These two aspects highlight the need to understand the impact that variations in microphysical parameter settings may have on simulated severe storms. Very little research has been conducted in this area. The aim of the research presented in

this chapter is to investigate the impact that changing the mean hail diameter has on the dynamics, thermodynamics, and precipitation characteristics of simulated severe storms.

To achieve the stated goal, four simulations were conducted in which the mean hail diameter was set to 3 mm, 5 mm, 1 cm and 2 cm. The simulations were otherwise identical. The details of the model setup for these experiments were shown and discussed in Chapter 3. These four sensitivity tests will be referred to as the 3mm, 5mm, 1cm and 2cm simulations. The word 'diameter' in this chapter will be used interchangeably with 'mean hail diameter' for the sake of clarity and brevity. At times, only the 3mm and 2cm simulations will be compared, as they are representative of the ends of the hail diameter spectrum tested here.

## 4.2 Some Size Distribution and Thermodynamic Considerations

The larger mean hail diameter cases have fewer small hailstones, more large hailstones, and fall faster as a category (see Figure 3.3). The size and fall velocity characteristics have several impacts on the thermodynamics of the simulated thunderstorms. The surface area-to-volume ratio of a hailstone, assuming that it is spherical, is given by 3/r where r is the radius of the hailstone. The ratio of the surface area to volume in the 2cm case for the mean hailstone size is 300 $m^{-1}$, whereas in the 3mm case this ratio is 2000 $m^{-1}$, when the hail mixing ratio is kept fixed. In general, for a given hail mixing ratio, the surface area-to-volume ratios are larger when the distribution contains proportionately more smaller hail particles. This implies that the melting and evaporation rates of hail will be larger for the same ice water content, and that the air will cool more rapidly in the smaller hail simulations. Also, the greater fall velocities of the larger hail mean that there is less time for melting and evaporation to occur between the melting level and the ground.

The vertical velocity tendency equation is given by:

$$\frac{dw}{dt} = -\theta_0 \frac{\partial \pi'}{\partial z} + g\left(\frac{\theta_v'}{\theta_0} - r_{cond}\right) + TURB \tag{4.1}$$

where w is the vertical velocity, t is the time, z is the vertical distance component, $\theta_0$ is the base state potential temperature, $\theta_v'$ is the perturbation virtual potential temperature, $\pi'$ is the perturbation Exner function, g is the acceleration due to gravity, $r_{cond}$ is the condensate mixing ratio and TURB is the turbulent forcing. Greater melting and evaporation rates in the small hail simulations cause a larger decrease in the virtual potential temperature, and hence a greater increase in downdraft strength, all other influences being constant. The predictive thermodynamic variable in RAMS is the ice-liquid potential temperature, from which the potential temperature is then diagnosed. The ice-liquid potential temperature is changed only by radiative heat fluxes and the sedimentation of water species. As hydrometeors fall into or out of a model level, so the ice-liquid potential temperature, and hence theta, varies. Therefore, the formation of hail at a particular model level increases the potential temperature through latent heat release, whereas the fallout of hail results in a decrease in potential temperature, both of which then affect the vertical velocity.

The formation of hail releases latent heat, thereby increasing the potential temperature. This in turn increases the updraft strength, which allows for the formation of more hail, thereby releasing even more latent heat. In this way a positive thermodynamic feedback develops. The latent heat release rates due to liquid water and vapor deposition on the hail surface will be greater in the smaller hail cases, where the exposed surface area is larger. However, in an updraft, most deposition occurs on cloud particles and smaller ice particles, the concentrations of which outnumber hail concentrations by several orders of magnitude. Thus, even though the formation of hail and the deposition of liquid water and vapor on the hail surface do contribute to the latent heat release within

the cloud, the release of latent heat associated with smaller ice particles and cloud droplets will be significantly larger.

Other factors related to the presence of hail may also affect the development of an updraft. It can be seen from Eq. (4.1) that the greater the condensate loading term, the weaker the updraft. Therefore, as more hail is formed, so more drag is placed on the updraft because it concentrates the ice water content. Eventually, the hail will become too heavy to be suspended by the updraft and fall out. This has two effects: 1) it reduces the ice-liquid potential temperature at the model level from which the hail fell, which has a negative thermodynamic effect, and (2) it reduces the condensate loading of the updraft, which has a positive mechanical effect.

Finally, further insight into the differences between the microphysical characteristics of the four mean hail diameter simulations may be gained by looking at the equation used to diagnose the number concentration in RAMS:

$$r = \frac{N_t}{\rho_a} \alpha_m D_n^{\beta_m} \frac{\Gamma(\nu + \beta_m)}{\Gamma(\nu)} \tag{4.2}$$

where r is the prognosed hail mixing ratio, $N_t$ is the total number concentration, $\rho_a$ is the dry air density, $\alpha_m$ coefficient in the mass power formula, $D_n$ is the characteristic diameter of the modified gamma distribution, $\beta_m$ is the exponent in the mass power law formula, $\nu$ is the gamma distribution shape parameter, and $\Gamma(\nu)$ is the complete gamma function of $\nu$. If the hail mixing ratio predicted in the 3mm and 2cm cases were the same (and assuming that the air densities are the same), the ratio of the total number concentration of the 3mm to the 2cm case is ~300. This means that for a given hail mixing ratio, the total number concentration in the 3mm case is 300 times greater than that in the 2cm case, which affects aspects like latent heat release rates, and melting and evaporation rates. Bearing all these aspects in mind, the results of the mean hail diameter simulations will now be presented.

## 4.3 Storm Movement

The storm tracks for the four mean hail diameter sensitivity tests are shown in Figure 4.1. Storm splitting is evident by about 30 minutes in all the simulations. After this time, differences in the structure of both the RM and LM storms become apparent. In the 3mm and 5mm cases (Figure 4.1a,b), the LM storm dissipates after about 45 minutes of simulation time. As the mean hail diameter is increased, so the strength and longevity of the LM storm is increased. In the 2cm simulation, the LM storm exists for the entire duration of the simulation, in spite of the clockwise curvature of the hodograph (see Fig. 3.4) below 2 km (Klemp and Wilhelmson, 1978b). Johnson et al. (1993) also noticed differences in the longevity of the LM storms in their "ice" versus "no ice" simulations – the LM was longer-lived in the ice simulation. The longevity and development of the LM storm will be discussed in detail in Chapter 5.

The RM storm is favored over the LM in all four sensitivity tests, which is in keeping with the low-level veering of the hodograph (Klemp and Wilhelmson, 1978b). However, significant differences in the structure and development of the RM storms become apparent after about 30 minutes. In the smaller mean hail diameter simulations, the RM storm develops relatively rapidly after storm splitting, reaching its maximum strength around 60 minutes (Figure 4.1a,b). After this time, the RM in both the 3mm and 5mm cases begins to weaken as the low-level updraft occludes, and a new updraft develops to the south of the original updraft. Evidence of this may be seen at 90 minutes in the 3mm case (Figure 4.1a) and 75 minutes in the 2cm case (Figure 4.1b). The updraft in both of these cases then re-develops. In the larger diameter cases, the low-level occlusion does not occur. The 1cm and 2cm RM storms develop into strong, steady storms after about an hour, and show relatively little change in structure throughout the rest of the simulation (Figure 4.1c,d). The occlusion in the small hail cases is examined in detail below.

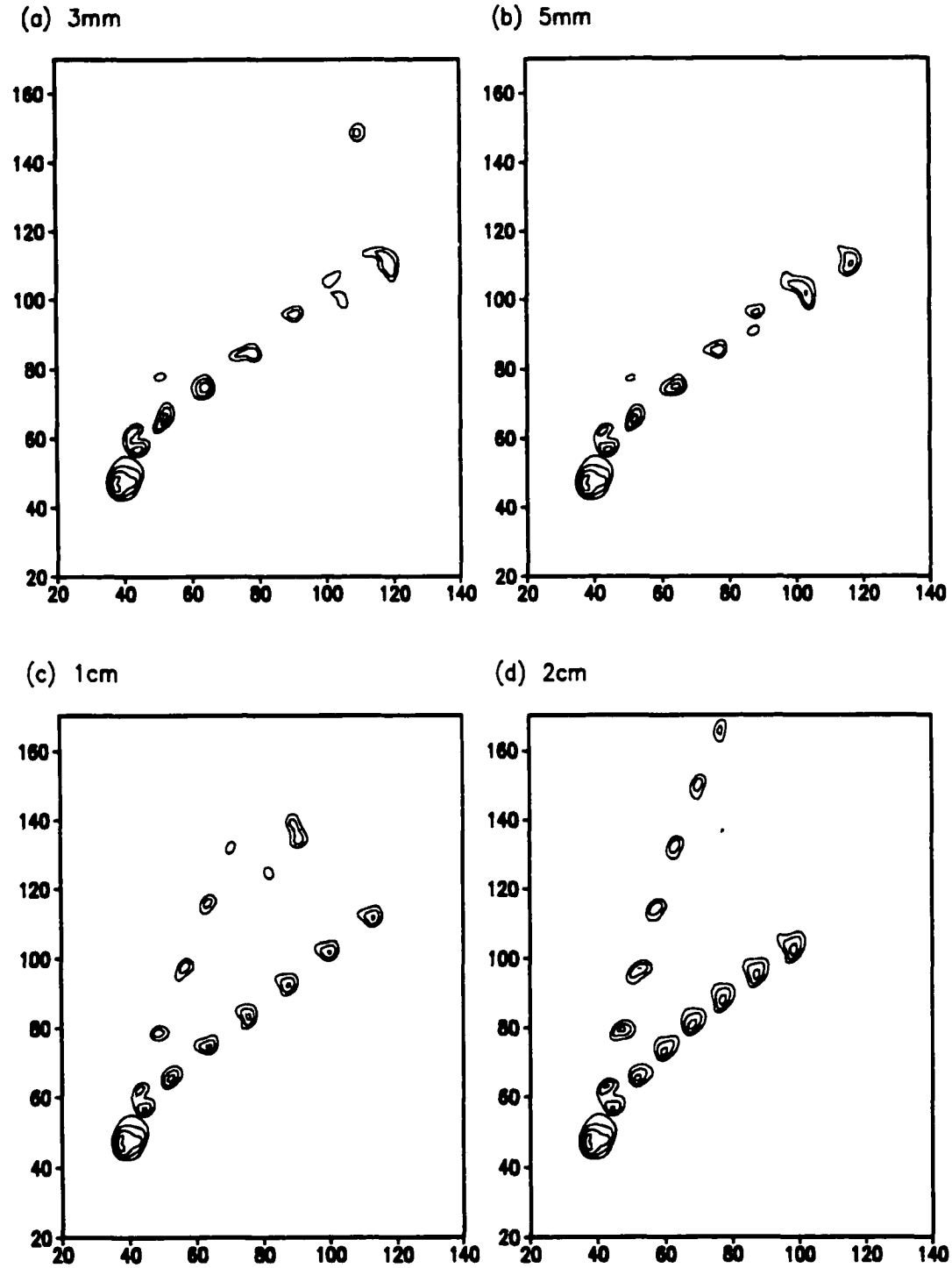


**Figure 4.1: Storm tracks of the (a) 3mm, (b) 5mm, (c) 1cm and (d) 2cm simulations. Field shown is vertical velocity ($m.s^{-1}$) at 4830m AGL. Contour interval is 10 $m.s^{-1}$ starting at 10 $m.s^{-1}$. Storm positions are shown at 15 minute intervals beginning from the southwest grid corner. Axes are distance (km) from the southwest grid point for all figures unless otherwise indicated.**

The mean speed of the RM storms from 30 to 120 minutes is 17.0 $m.s^{-1}$, 16.7 $m.s^{-1}$, 16.3 $m.s^{-1}$ and 13.1 $m.s^{-1}$ for the 3mm, 5mm, 1cm and 2cm cases respectively, and the storms are moving from 235°, 234°, 231° and 229°. An increase in the diameter thus causes the RM storm to move more slowly and slightly less to the right of the mean wind shear vector. While these differences may appear small, they result in the 3mm storm having traveled ~92 km from the storm's position at 30 minutes, while the 2cm storm only covers ~71 km by the end of the simulation. Also, the 3mm storm is situated 21 km further east and 7 km further north than the 2cm storm (Figure 4.1). The propagation further to the right of the mean shear vector may also have an impact on the RM storm dynamics (Browning, 1968; Fankhauser, 1971). Simply changing the mean hail diameter therefore has a significant effect on the strength, steadiness, longevity and movement of both the RM and LM storms.

## 4.4 Upper-Level Dynamic and Thermodynamic Characteristics

Differences in the storm intensities between the four simulations may be seen by examining the maximum vertical velocity (Figure 4.2) and maximum virtual potential temperature perturbations (Figure 4.3). The velocity and temperature curves closely mirror one another for the respective cases, revealing the impact of the buoyancy term on vertical velocity. It will be seen later that the velocity and temperature curves are also very similar to the maximum hail mixing ratios, which highlights the importance of the updraft strength in hail formation.

The maximum vertical velocities range between 55 and 65 $m.s^{-1}$ for the intense phases of the storms. These magnitudes are similar to those simulated by Johnson et al. (1993) in their simulation of a supercell, and also compare favorably with those described by Bluestein and Woodall (1990). All four simulations develop strong updrafts after about 15 minutes, in response to the buoyancy generated by the initial thermal

perturbation (Figure 4.3). Around 20 minutes, the updrafts collapse due to condensate loading, of which hail is by far the predominant species (Figure 4.2). The updrafts then start to recover following the fallout of hail. As the fall velocities in the larger hail cases are greater, the updraft in the 2cm case recovers first (25 minutes), followed by the 1cm (35 minutes) and 5mm (40 minutes) cases, and finally by the 3mm updraft (45 minutes). Associated with the hail fallout is a decrease in the virtual potential temperature, the rates of which also demonstrate the influence of the fall speeds (Figure 4.3). Although the small hail updrafts recover after those of the 1 and 2cm hail cases, they recover more rapidly, achieving their maximum strengths at between 55 and 60 minutes. The maximum updraft strengths, which are caused by low-level convergence, are examined in the next section.

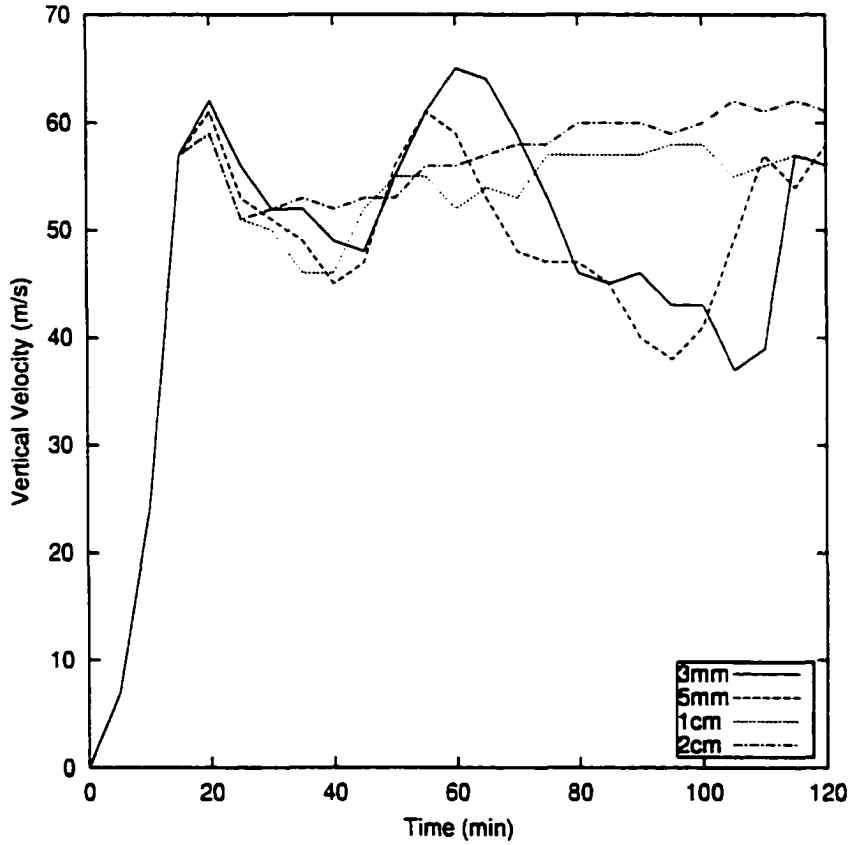


**Figure 4.2: Maximum updraft velocity as a function of time for the 3mm (solid line), 5mm (dashed line), 1cm (dotted line) and 2cm (dot-dash line) simulations.**

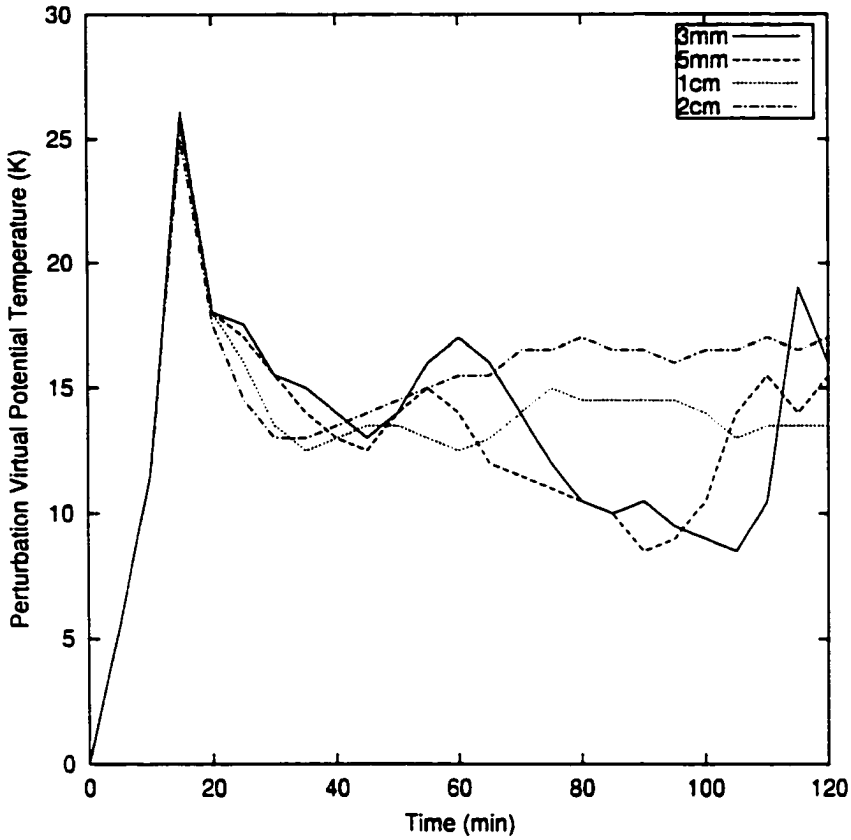


**Figure 4.3: Maximum perturbation virtual potential temperature (K) as a function of time for the 3mm (solid line), 5mm (dashed line), 1cm (dotted line) and 2cm (dot-dash line) simulations.**

The maximum updraft strength in all of the hail cases occurs around 11 km AGL. At this level, the temperature is ~ -40°C (Figure 4.4), which is the temperature below which the homogeneous nucleation of cloud droplets occurs. Homogeneous nucleation of cloud droplets within the updraft produces pristine ice mixing ratios of ~2.5 $g.kg^{-1}$ in the 3mm case. A similar situation is observed in all the other simulations (not shown). The latent heat release associated with the homogeneous nucleation of the cloud droplets enhances the updraft, the maximum strength of which coincides with the -40°C isotherm.

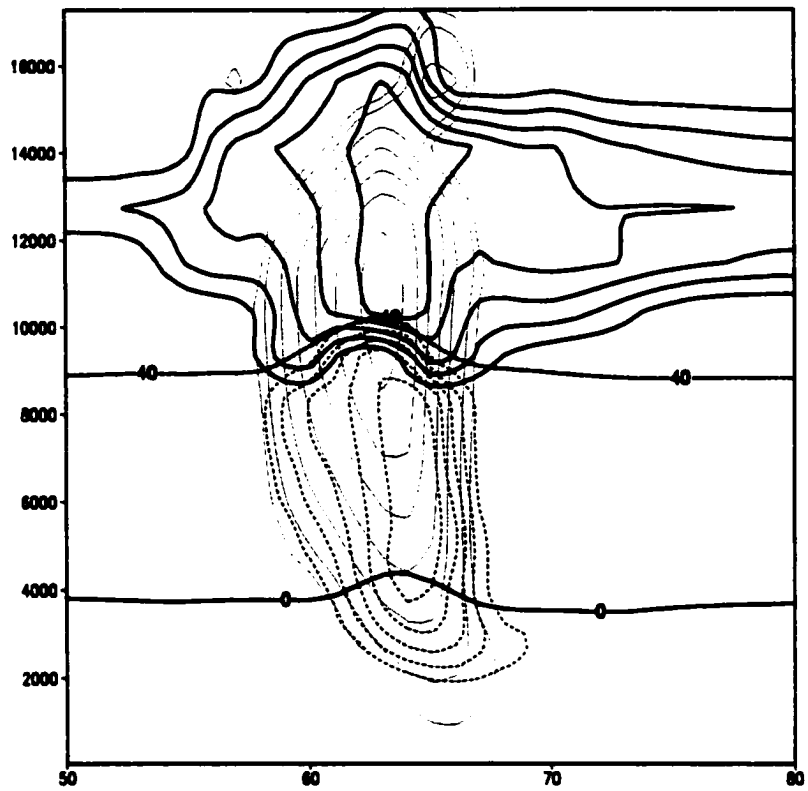


**Figure 4.4: Vertical cross section of vertical velocity (thin lines, interval 10 $m.s^{-1}$, 5 $m.s^{-1}$ isoline also shown), cloud mixing ratios (dashed lines, interval 0.5 $g.kg^{-1}$) and pristine ice mixing ratios (thick lines, interval 0.5 $g.kg^{-1}$) for the 3mm case at 60 minutes. Horizontal thick lines are isotherms at -40°C and 0°C. The ordinate is height (m) AGL and the abscissa is distance (km) from the southwest grid point. All zero lines, except for temperature, are excluded.**

## 4.5 Low-Level Dynamic and Thermodynamic Characteristics

Cooling within the low-level downdrafts occurs as a result of the melting of ice, the evaporation of water off the surface of hail, and the evaporation of rain. High cloud bases and a dry subcloud layer enhance evaporative cooling and stronger downdrafts. Knupp (1985) found, in his study of low-level downdrafts in convective High Plains storms, that melting can account for 10-60% of the total cooling within certain downdrafts, with evaporative cooling making up the difference. He also noted that the contribution of melting to the total downdraft cooling becomes greater when the cloud bases are lower and the subcloud layer is more moist, both of which inhibit evaporative cooling.

In the simulations presented here, the cloud bases are low, varying from 1300 to 1700 m AGL (the smaller hail cloud bases are closer to the ground), the subcloud layer is moist (see Fig 3.4), and the melting level occurs at ~4 km AGL. These all suggest, based on Knupp's (1985) findings, that melting may play an important role in cooling the downdraft air. Complete melting of hail is more mass dependent than evaporation, which is purely a surface process. However, the transfer of heat needed for melting is a surface process, and surface area therefore has an impact on the melting rates. More rapid melting rates and smaller terminal fall velocities (mean terminal velocity is 22.8 $m.s^{-1}$ for the 2cm case but only 8.8 $m.s^{-1}$ in the 3mm case) in the smaller hail cases, produce colder, stronger low-level downdrafts than those in the 1 and 2cm cases (Figure 4.5). Also, as smaller hailstones melt more quickly, they produce rain (through shedding or complete melting) more rapidly, and hence greater rates of evaporative cooling are achieved than in the larger hail runs. This further enhances the downdraft strengths in the small hail cases, not only through the greater evaporation rates, but also as the latent heat of vaporization is greater than that of fusion. The 3 and 5mm downdrafts peak later in the simulation as a result of the time required for the smaller hail to reach the melting and sub-cloud levels.

The cold pool originates through the transport of cold air by the downdrafts to the surface, after which it is forced to diverge through continuity arguments. The cold pools that develop in the four hail cases are shown at 30, 60, 90 and 120 minutes in Figure 4.6 through Figure 4.9. As the mean hail diameter decreases, the strength of the cold pool increases, due to the greater melting and evaporative cooling rates within the downdrafts. The cold pool temperature perturbations at 60 minutes differ by as much as 8K between the 3mm (-14K) and the 2cm (-6K) cases (Figure 4.7). The cold pools that develop initially present an exception to this trend in that the 3mm cold pool is warmer than those in the 5mm and 1cm cases at 30 minutes (Figure 4.6). This may be explained by looking at a vertical cross section through the hail mixing ratios at this time (Figure 4.10). Hail is

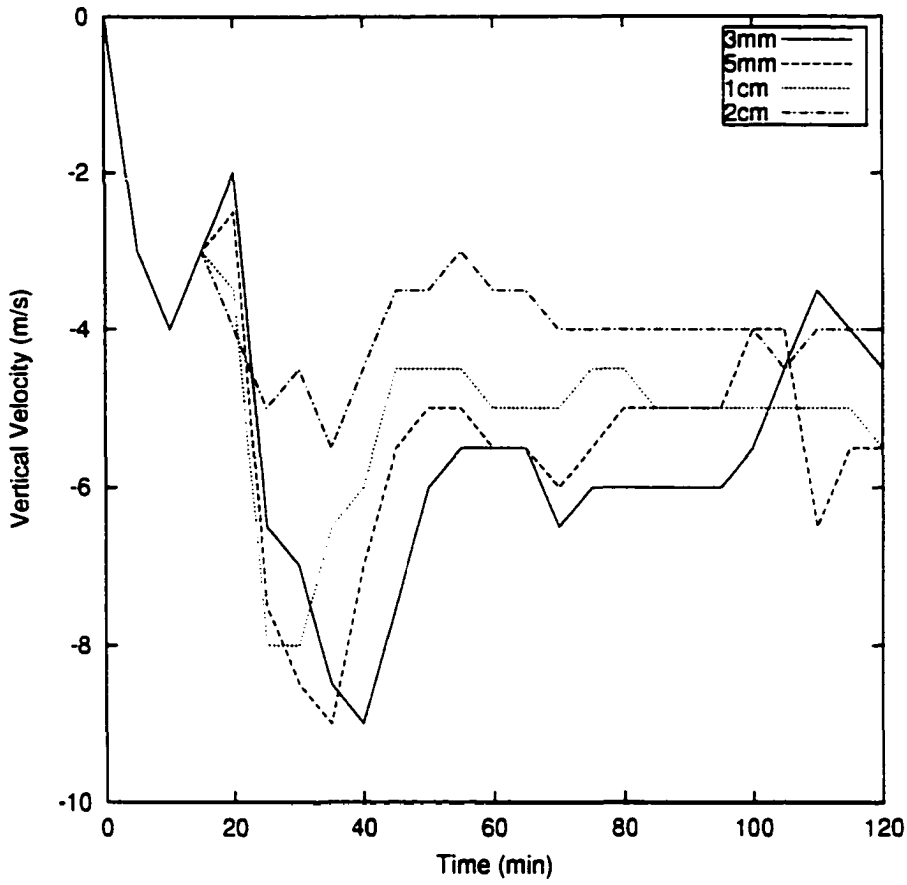


**Figure 4.5: Maximum downdraft strengths below 1km AGL as a function of time for the 3mm (solid line), 5mm (dashed line), 1cm (dotted line) and 2cm (dot-dash line) simulations.**

only just starting to extend below the melting level in the 3mm case, whereas in the 5mm and 1cm cases, the hail extends well below the melting level. This is a function of the difference in their fall speeds. As a result, very little melting has been able to occur in the 3mm case compared with the 5mm and 1cm cases. It is apparent from Figure 4.10d that most of the hail in the 2cm case has already reached the ground by this stage, thereby allowing little time for melting and the generation of a strong cold pool. By 60 minutes (Figure 4.7), the cold pool strengths for the four simulations (-14K, -12K, -8K and –6K for 3mm to 2cm respectively) are in keeping with the fall speed and surface area arguments made above. In the 1cm and 2cm simulations, the impact of the LM storm on the cold pool may be seen.

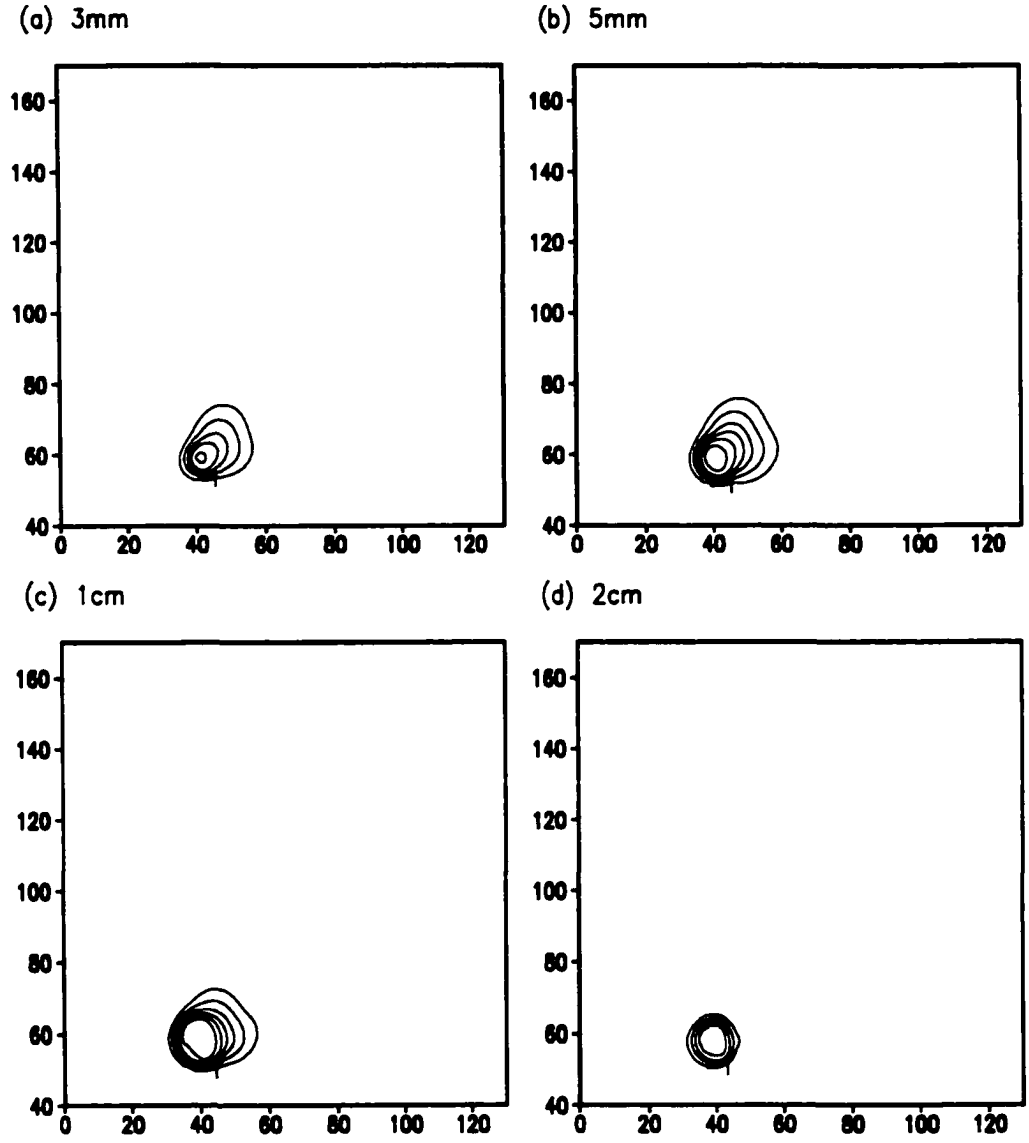


**Figure 4.6: Perturbation potential temperature (K) at the lowest model level (48m AGL) at 30 minutes for the (a) 3mm, (b) 5mm, (c) 1cm and (2) 2cm simulations. Contour interval is -2K. The -1K isotherm is also shown.**

Cross sections through the low-level downdrafts at 60 minutes are shown in Figure 4.11. The low-level downdrafts originate below the melting level. In the smaller hail cases, part of the downdraft originates within the cloud (albeit near the edge of the cloud), where evaporative processes are inhibited. This is suggestive of the importance of melting in the downdraft development and supports Knupp's (1985) observations. The downdrafts are deeper in the 3 and 5mm cases, which is a function of the cooling rates

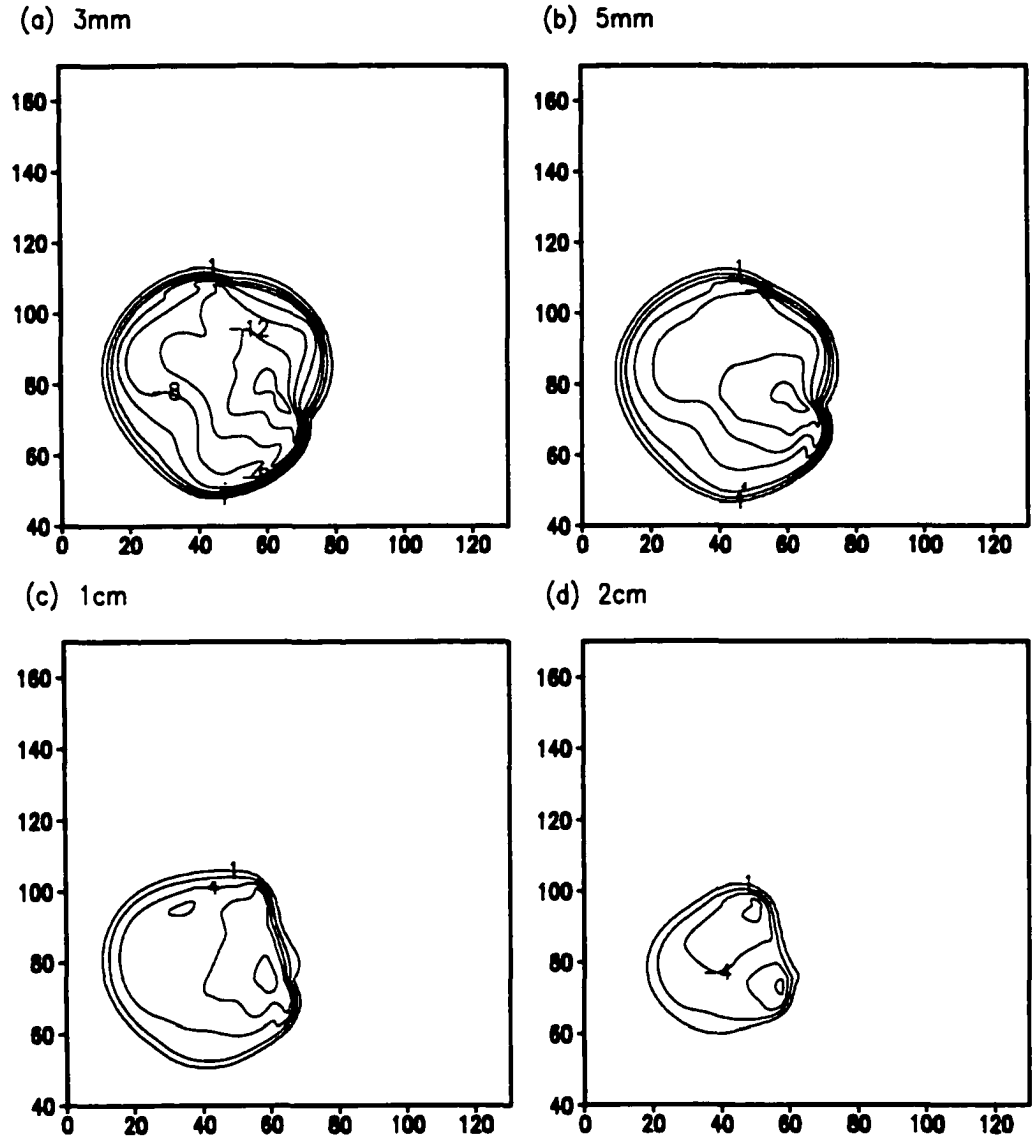


**Figure 4.7: Perturbation potential temperature (K) at the lowest model level (48m AGL) at 60 minutes for the (a) 3mm, (b) 5mm, (c) 1cm and (2) 2cm simulations. Contour interval is -2K. The -1K isotherm is also shown.**

and fall speeds. The maxima occur near the tip of the hail shaft, which further links melting to the downdraft development. The hail does not reach the ground in small diameter simulations as it is not large enough to withstand the melting. The origin of the low-level downdrafts in the 1 and 2cm cases is just below cloud base, occurring at a lower level than in the smaller hail cases due to the slower melting rates and the faster fall rates. The shallower downdrafts in the large hail cases also suggest that evaporative

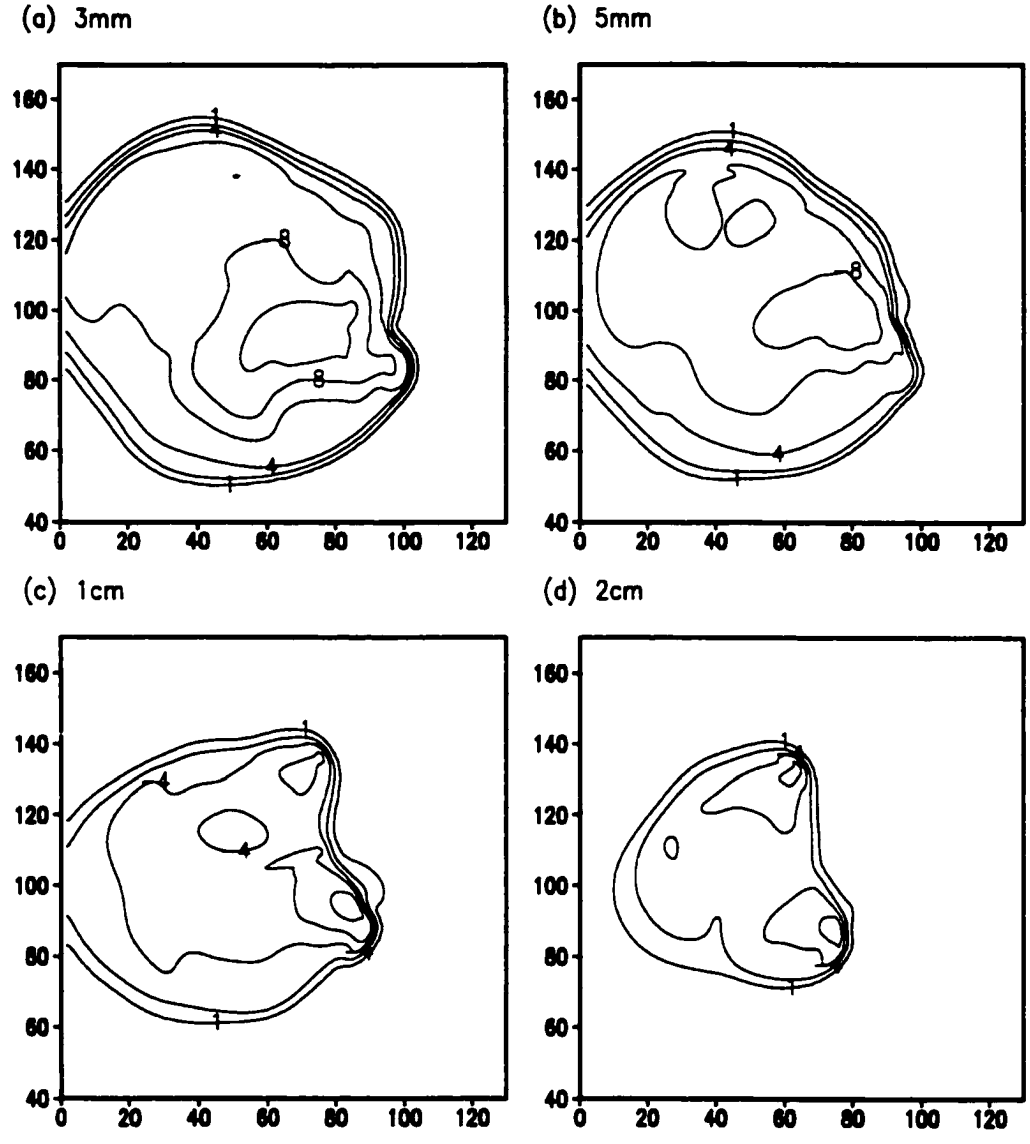


**Figure 4.8: Perturbation potential temperature (K) at the lowest model level (48m AGL) at 90 minutes for the (a) 3mm, (b) 5mm, (c) 1cm and (2) 2cm simulations. Contour interval is –2K. The –1K isotherm is also shown.**

processes may contribute more to the total cooling within the downdrafts than in the 3 and 5 mm runs. The hail shaft is also contained within the cloud to a greater extent in the large hail cases. This slows the subsequent evaporation of the liquid water generated by melting. In the smaller hail cases, the updraft is tilted to a greater degree, which allows for a larger displacement of the hail shaft away from the cloud in the lower levels, thereby enhancing evaporation.

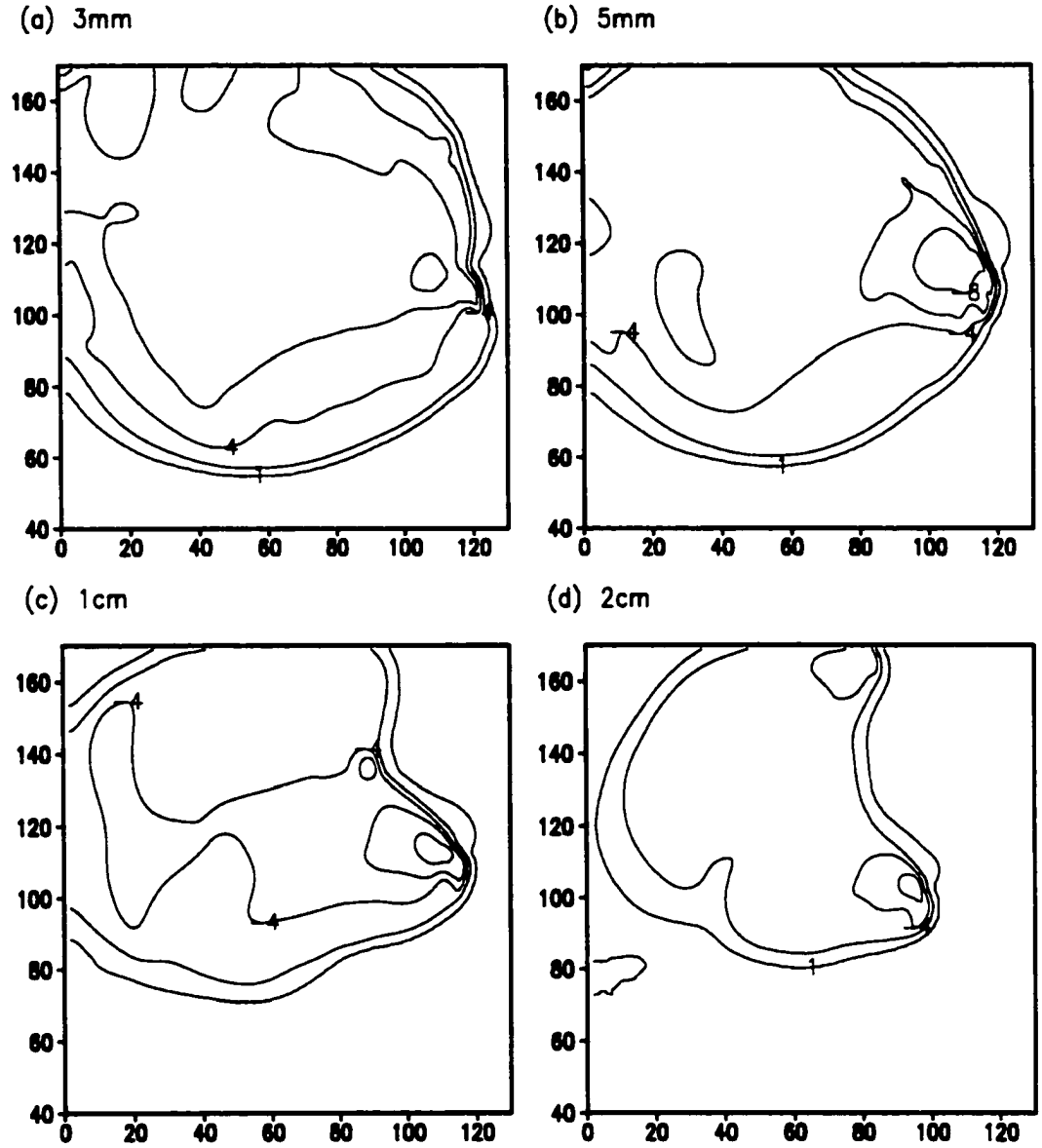


**Figure 4.9: Perturbation potential temperature (K) at the lowest model level (48m AGL) at 120 minutes for the (a) 3mm, (b) 5mm, (c) 1cm and (2) 2cm simulations. Contour interval is –2K. The –1K isotherm is also shown.**

Rotunno et al. (1988) used the expression

$$c^2 = -2g\int_0^H \frac{\theta'}{\theta_0(z)}dz \qquad (4.3)$$

to investigate the propagation of a two-dimensional density current under conditions of no shear. Here, $\theta'$ is the perturbation potential temperature within the cold pool, $\theta_0$ is the

base state potential temperature, c is the propagation speed relative to the undisturbed environmental flow, g is acceleration due to gravity, and H is the top of the cold pool above which $\theta'$ is assumed negligible. From this expression it is apparent that the greater the perturbation potential temperature within the cold pool, the greater the propagation speed of the cold pool. The impact that changing the mean hail diameter has on the cold pool strengths and resultant propagation speeds is apparent in Figure 4.6 through Figure 4.9. By 90 minutes, the faster moving cold pool in the 3mm case covers ~7850 $km^2$, whereas the slower propagating 2cm cold pool only covers ~3850 $km^2$.

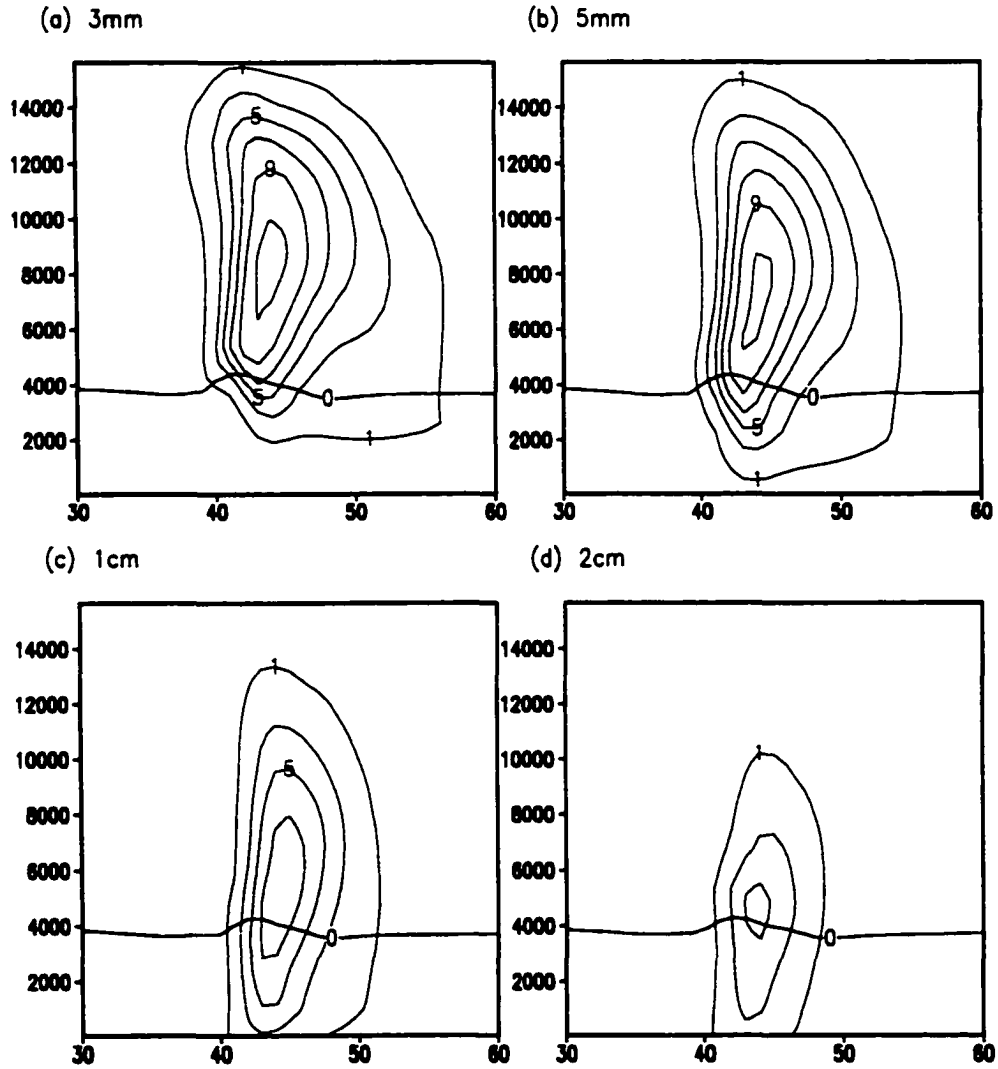


**Figure 4.10: Hail mixing ratio (interval 2 $g.kg^{-1}$ starting at $1g.kg^{-1}$) at 30 minutes as a function of height for (a) 3mm, (b) 5mm, (c) 1cm and (d) 2cm cases. The abscissa is distance (km) from the southwest grid point. The ordinate is height (m) AGL. The thick horizontal line is the melting level.**

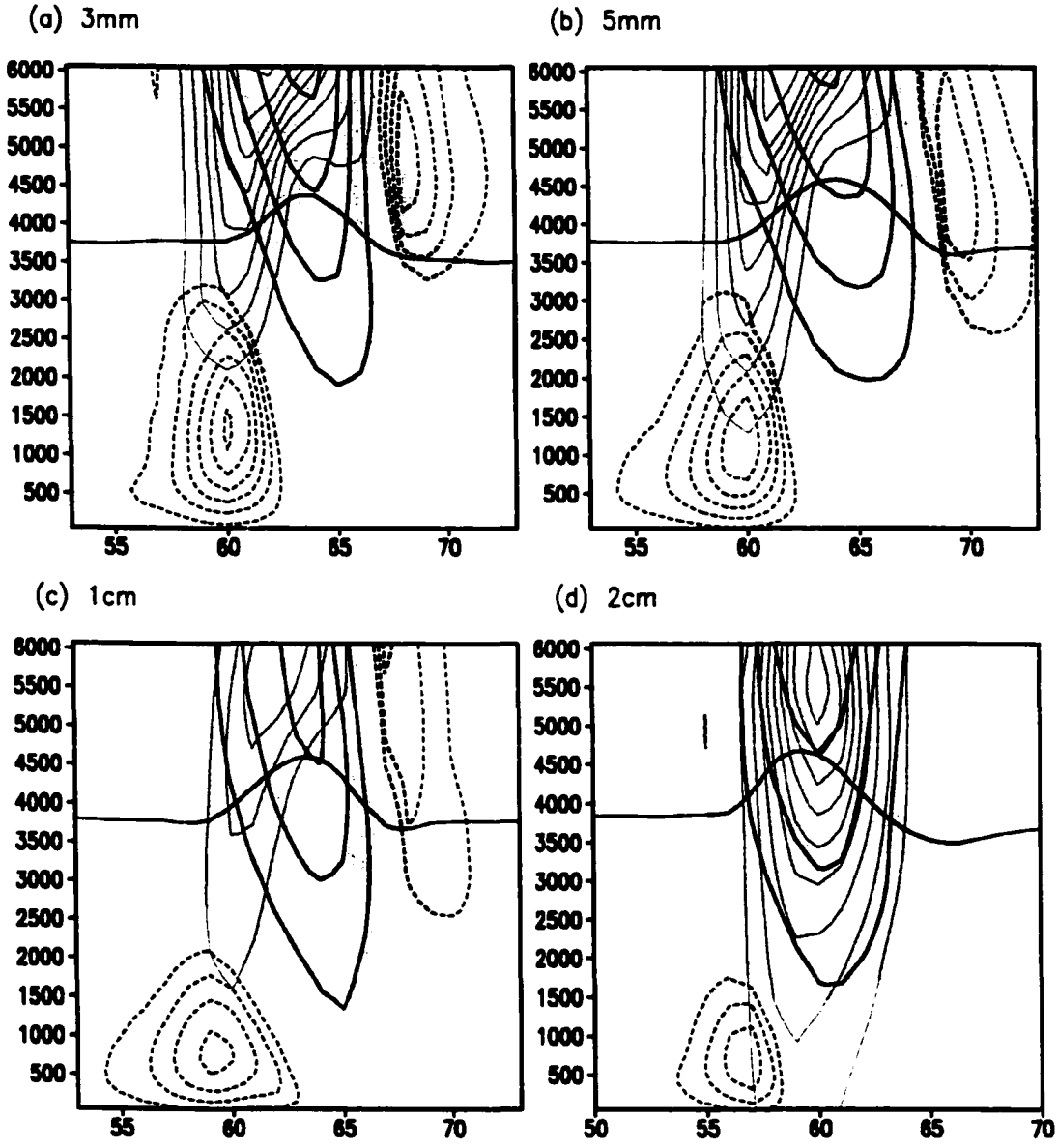


**Figure 4.11: Cross-section through the low-level downdraft (thick lines, interval 10 $m.s^{-1}$ for the updrafts, 1 $m.s^{-1}$ for the downdrafts) and hail shaft (thin lines, interval 1 $g.kg^{-1}$) at 60 minutes for (a) 3mm, (b) 5mm, (c) 1cm and (d) 2cm cases. Shading represents cloud water mixing ratios above zero. Solid lines indicate positive values and dashed lines indicate negative values in all the figures unless otherwise indicated. The zero line has been excluded for both the vertical velocity and hail mixing ratios. The thick horizontal line is the melting level. The ordinate is height (m) AGL.**

Changes in the cold pool strength and gust front speeds as a result of changing the mean hail diameter, influences the position of the mid- and upper-levels sections of the storm with respect to the gust front. The gust front enhances the convergence and uplift

of warm, moist air into the updraft, providing that it is situated just ahead of the main updraft. In the larger hail cases, the updraft moves at similar speeds to the gust front, thereby remaining in close proximity to it (Figure 4.12c,d). This allows for the continuous influx of energy and moisture into the storm and the development of the steady updrafts that are observed (Figure 4.2). In the 3mm and 5mm cases, the rapid movement of the colder, denser cold pool forces the gust front, situated to the southeast of the updraft, to surge out ahead of the updraft (Figure 4.12a,b). This reduces the influx of warm, moist air, thereby weakening the storm (Figure 4.2). As the 5mm cold pool is initially stronger than the cold pool in the 3mm simulation, eastward movement of the gust front relative to the updraft occurs about 5 minutes earlier in the 5mm run, resulting in the slightly earlier collapse of the updraft (Figure 4.2).

The depth of the cold pool (taken vertically through the point of maximum potential temperature perturbation) at 60 and 90 minutes is shown in Figure 4.13. Assuming that the top of the cold pool is given where $\frac{\theta'}{\theta_0} = 0$, the depths of the cold pools at 60 minutes vary from ~1600 m AGL in the 2cm case to 2000 m AGL in the 3mm run (Figure 4.13a). The cold pool depths increase as the mean hail diameters decrease, due to the stronger low-level downdrafts associated with the greater melting rates. In all 4 simulations, the cold pool extends above the cloud base. The height of the cold pool above cloud base is greatest in the 3mm case (~500m) and least in the 2cm case (~100m). That the cold pool extends above the cloud base again highlights the importance of melting in the development of the low-level downdrafts and associated cold pools. By 90 minutes the cold pool depths in the smaller hail cases have decreased due to the updraft collapse and

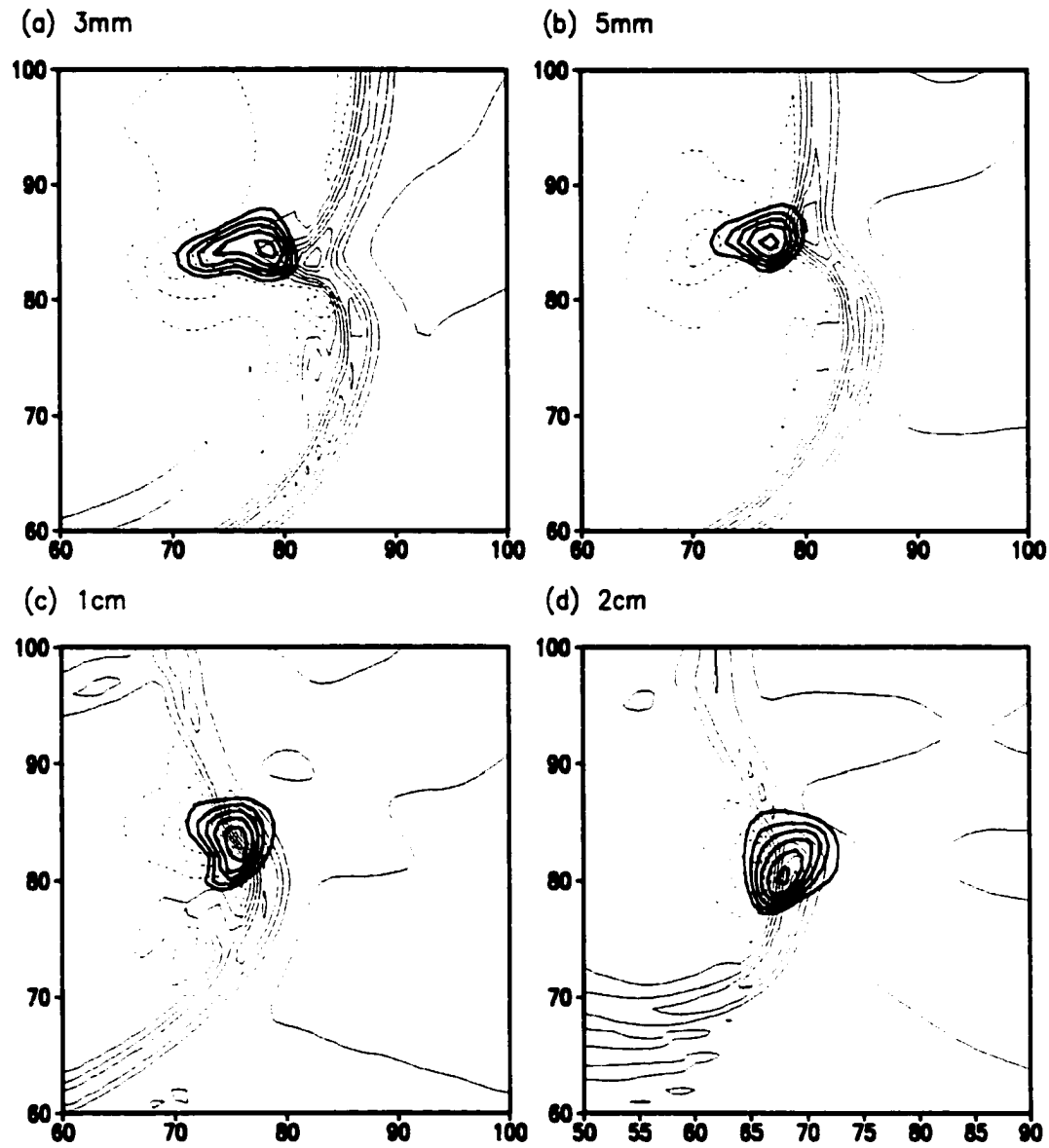


**Figure 4.12: Vertical velocity at 75 minutes at 48m AGL (thin lines; interval 0.3m.s$^{-1}$) and 4300m AGL (thick lines; interval 5m.s$^{-1}$ starting at 5m.s$^{-1}$) for the (a) 3mm, (b) 5mm, (c) 1cm and (d) 2cm cases.**

reduced hail production (Figure 4.13b). Their depths are now similar to those of the 1 and 2cm simulations. The large hail cold pool depths remain relatively steady in response to the stability of the storms at this stage, and the fairly constant production of hail (shown later).

a)

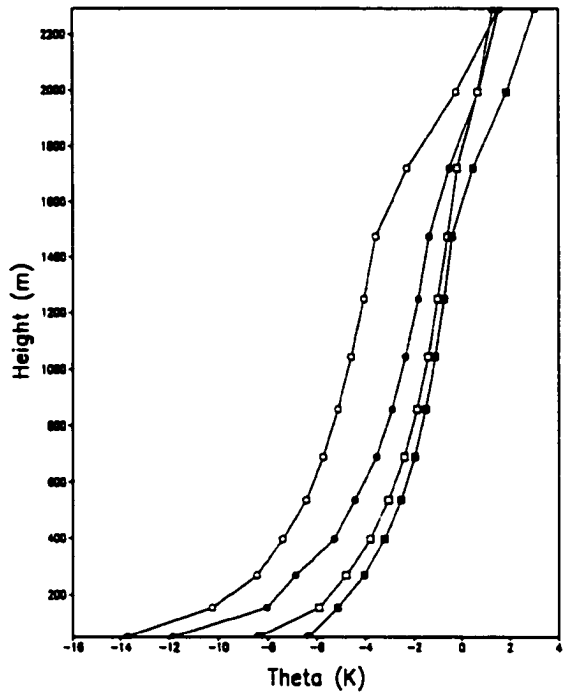


(b)

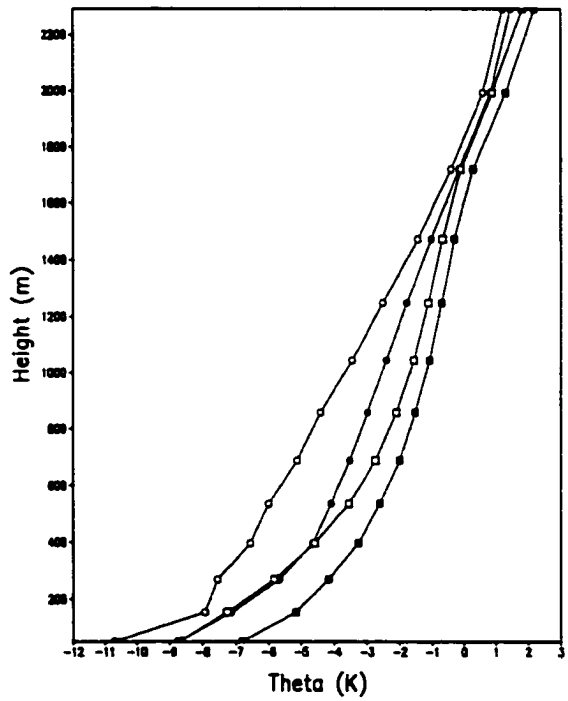


**Figure 4.13: Depth of the cold pool at (a) 60 minutes and (b) 90 minutes for the 3mm (open circles), 5mm (closed circles), 1cm (open squares) and 2cm (closed squares).**

We saw in the previous section that the smaller hail updrafts recovered more rapidly than those in the larger hail simulations. They reached a maximum around 60 minutes and then rapidly collapsed before increasing in strength again (Figure 4.2). Examining the convergence fields below 1 kilometer for the 3mm (Figure 4.14) and 2cm (Figure 4.15) simulations demonstrates why this occurs. In the 3mm case, the convergence within the region of the updraft at 150 m AGL increases by at least 50% from 50 to 60 minutes, remains constant from 60 to 70 minutes, and then decreases between 70 and 80 minutes (Figure 4.14a). A similar trend is seen at 400 and 1000 m AGL (Figure 4.14b,c), although the convergence has already started to weaken by 70 minutes at these levels. At 400 m, the development of convergence along the gust front to the east of the updraft is also visible. The peak in the 3mm updraft at 60 minutes (Figure 4.2) is therefore associated with an increase in the low-level convergence. The subsequent weakening of the updraft is representative of the decreased convergence. The slight, steady increase in the 2cm updraft between 50 and 80 minutes is forced by a similar trend in the low-level convergence during this time. The low-level convergence of air into the updraft appears to have an important effect on the updraft strength throughout the storm.

What then causes the observed differences in the simulated convergence fields between the 3mm and 2cm cases? These differences may be attributed to the strength and depth of the developing downdrafts. The greater melting and evaporation rates in the smaller hail cases create deeper, stronger downdrafts (Figure 4.14d) than those in the large hail cases (Figure 4.15d). The stronger downdrafts are associated with greater low-level divergence through continuity arguments, and this enhances the convergence of air into the lower regions of the updraft. In the larger hail cases, the downdrafts are weaker, the divergence occurs over a shallower depth, and the convergence of air into the lower regions of the updraft is weaker (Figure 4.15d). The convergence of air into the updrafts

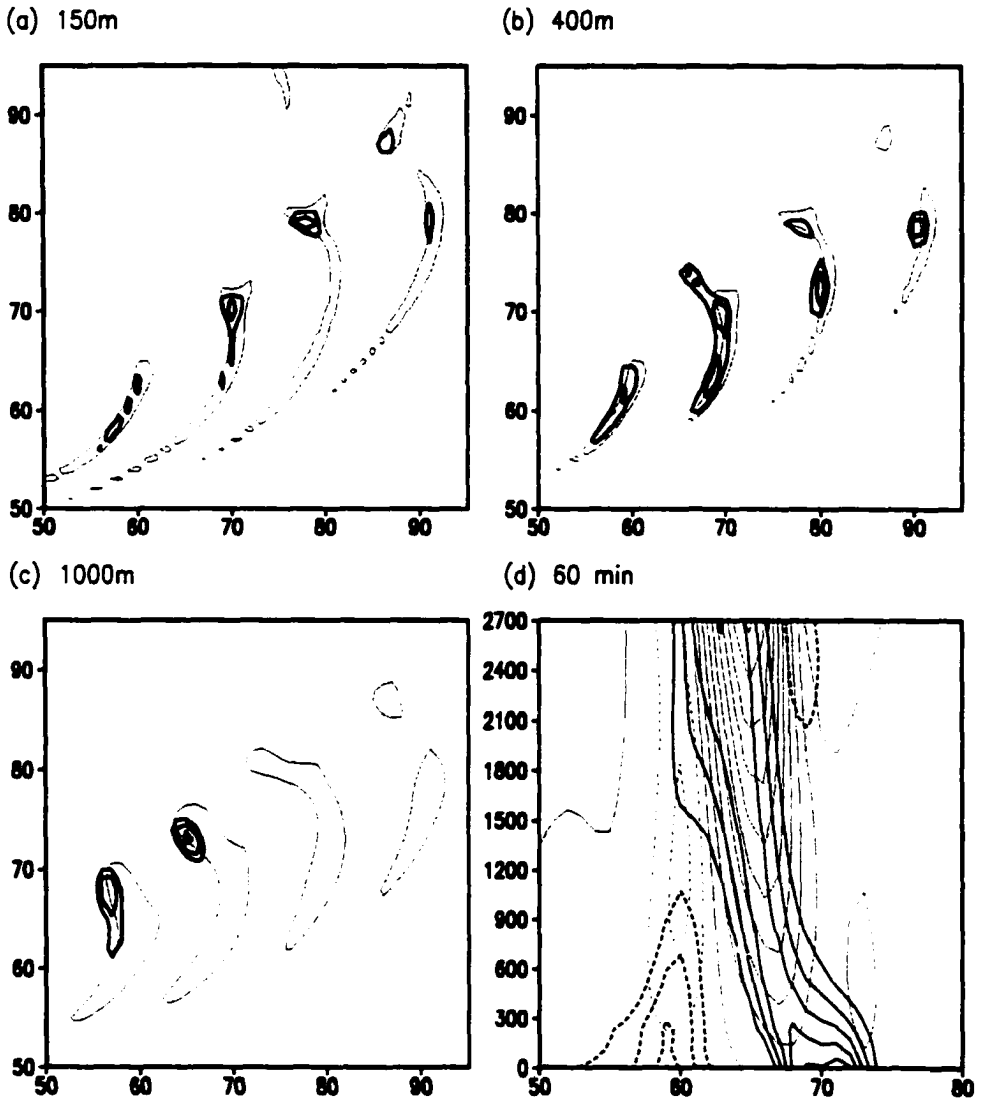


**Figure 4.14: Convergence (thick lines) and vertical velocity (thin lines) for the 3mm case at (a) 150m, (b) 400m and (c) 1000m AGL. In (d) a cross-section of the convergence (thick lines) and vertical velocity (thin lines) fields within the updraft is shown. The fields at 50, 60, 70, and 80 minutes (left to right) are shown in (a), (b), and (c), and the cross-section in (d) is taken at 60 minutes. Solid lines represent positive values and dashed lines represent negative values. The vertical velocity and convergence contour intervals are (a) 2 $m.s^{-1}$ and 0.01, 0.012 $s^{-1}$, (b) 4 $m.s^{-1}$ and 0.007, 0.008 $s^{-1}$, (c) 4 $m.s^{-1}$ and 0.005, 0.006, 0.007 $s^{-1}$, and (d) 2 $m.s^{-1}$ and 0.002 $s^{-1}$, respectively. The ordinate in (d) is height (m) AGL.**

in the smaller hail cases at around 60 minutes is associated with the occlusion of the updraft in the lower levels. This process is discussed in further detail below.

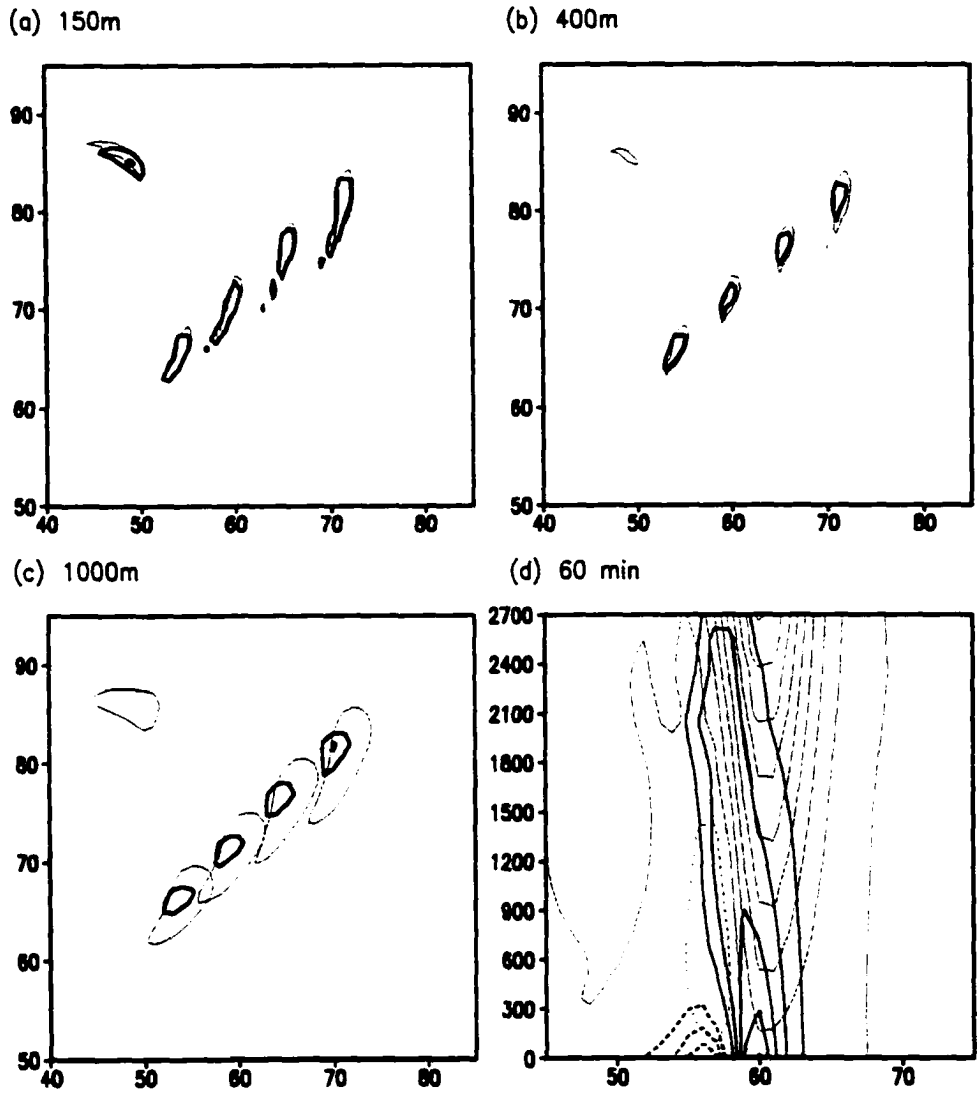


**Figure 4.15: Same as Figure 4.14 except for the 2cm case. The convergence contour interval in (a) is 0.008, 0.01 $s^{-1}$.**

## 4.6 Storm Structure and Precipitation Characteristics

The maximum hail mixing ratios in each simulation reach a peak at between 15 and 20 minutes in response to the development of the initial updraft (Figure 4.16). The 1cm simulation achieves a greater maximum than in the 2cm case because hail in the latter case is already reaching the ground (Figure 4.17). Following the initial maxima, the

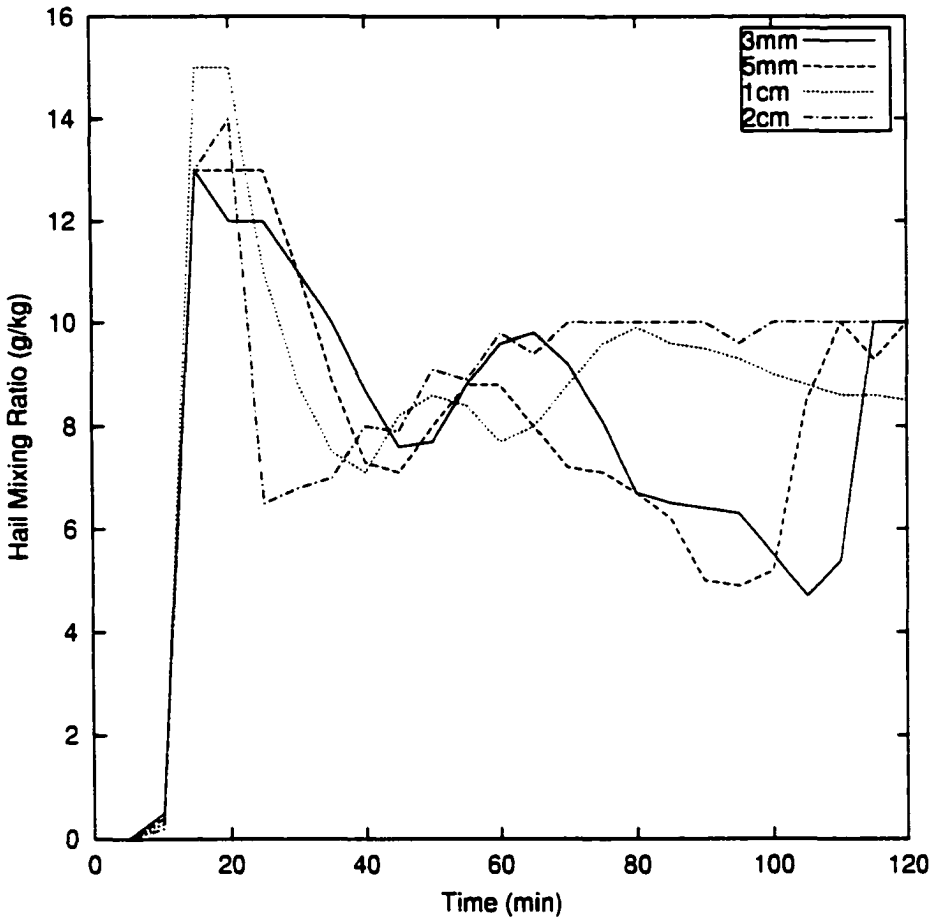


**Figure 4.16: Maximum hail mixing ratio ($g.kg^{-1}$) throughout the model domain as a function of time for the 3mm (solid line), 5mm (dashed line), 1cm (dotted line) and 2cm (dot-dash line) simulations.**

hail begins to fall out of the updraft as the vertical velocity becomes insufficient to support the amount of hail that develops. The larger hail diameter cases have greater fallout rates as a result of their greater terminal velocities (Figure 4.16). The earlier occurrence of the hail maxima at the ground in the larger hail cases (Figure 4.17) is also evidence of the greater fall speeds. Very little hail actually reaches the ground in the small hail cases due to the inability of the smaller stones to withstand melting.

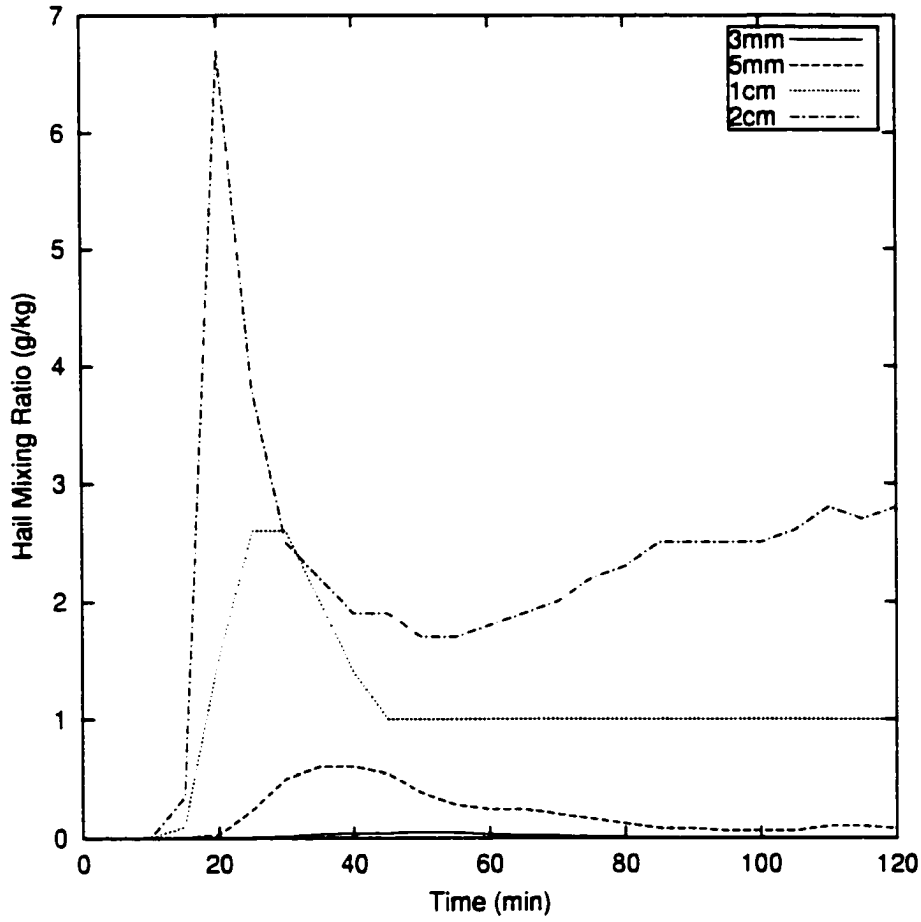


**Figure 4.17: Maximum hail mixing ratio ($g.kg^{-1}$) at the lowest model level (48m AGL) as a function of time for the 3mm (solid line), 5mm (dashed line), 1cm (dotted line) and 2cm (dot-dash line) simulations.**

The terminal velocity also has an impact on the height at which the hail maxima occur (Figure 4.18). At 15 minutes (Figure 4.18a), the hail maxima occur at similar heights in all four simulations as the updrafts and hail are just starting to develop. By 20 minutes (Figure 4.18b), the height at which the maximum hail mixing ratios occur are already sorted according to terminal velocity, with the smallest hail size occurring at highest levels and the largest at lower levels. Hail in the 1cm and 2cm cases is already reaching the ground. After 30 minutes (Figure 4.18c), the 3mm and 5mm hail maxima occur at lower levels as the slower falling hail has had time to move downward. Finally, at 90 minutes (Figure 4.18d), when the 1cm and 2cm storms are relatively steady, and the

(a)

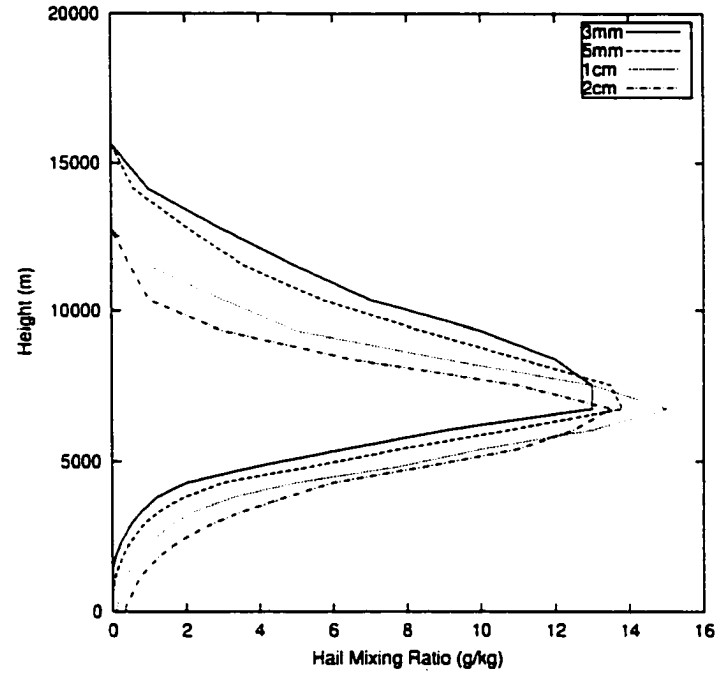


(b)

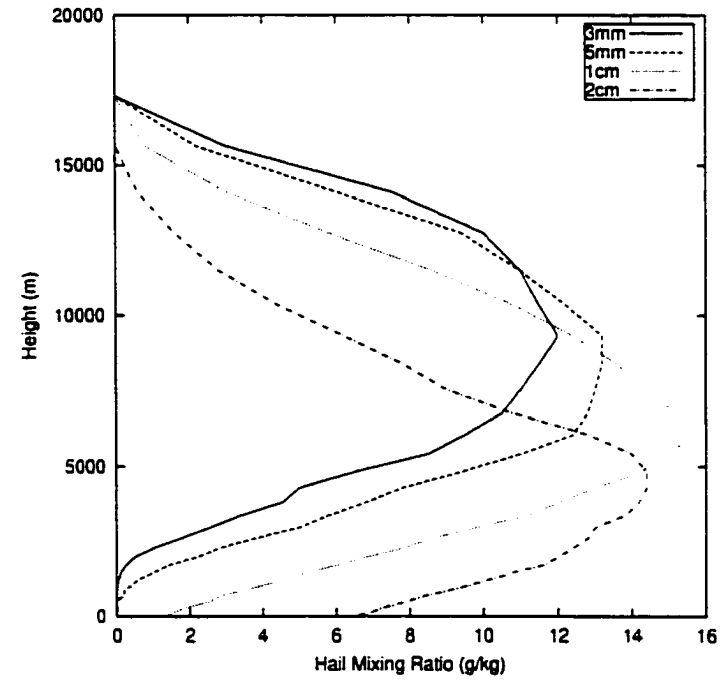


**Figure 4.18: Maximum hail mixing ratio as a function of height at (a) 15 minutes, (b) 20 minutes, (c) 30 minutes and (d) 90 minutes for the 3mm (solid line), 5mm (dashed line), 1cm (dotted line) and 2cm (dot-dash line) simulations. Figure continues on next page.**

(c)

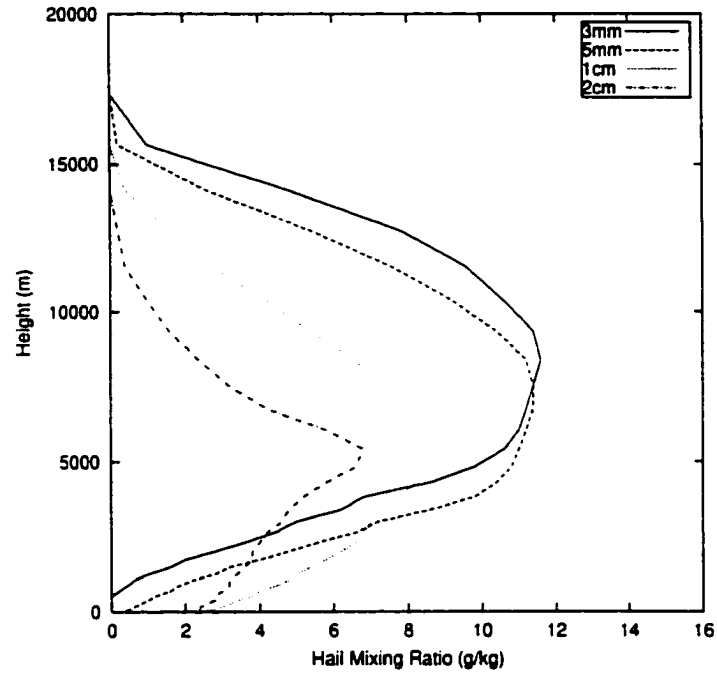


(d)

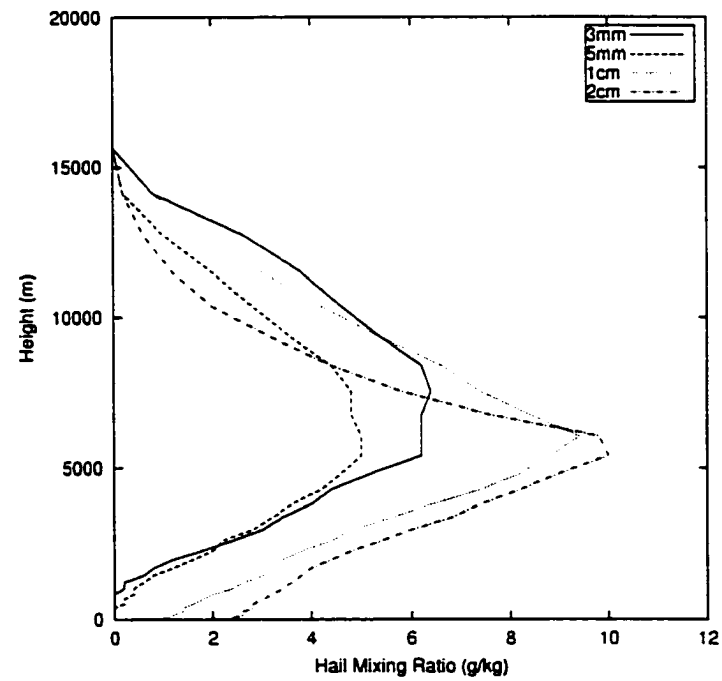


**(figure continues from previous page)**

3mm and 5mm updrafts are starting to develop again, the hail mixing ratio maxima occur at similar levels. This may be attributed to the developing updrafts in the smaller hail cases and the bigger fall velocities in the larger hail cases.

Horizontal cross-sections through the mid-level of the storm, near to or at its strongest stage, reveal a single updraft structure in each case (Figure 4.19). Each updraft is embedded within a mesocyclone, a characteristic of supercell storms (Doswell, 1985). The mesocyclone magnitudes range from 0.015 $s^{-1}$ for the 1 and 2cm cases, to 0.02 $s^{-1}$ for the 3 and 5mm cases. The low-level vorticity development associated with each storm is discussed in detail below. Relatively weak downdrafts to the east of the updraft are evident in the 3 and 5mm cases, but do not occur in the larger hail simulations. These downdrafts occur as a result of the melting of small hail falling from the anvil, which does not occur in the 2cm run.

A well-defined hook and a weak echo region (bounded at higher levels) are evident in the horizontal cross section of the condensate field of the 3mm case (Figure 4.20a). Such features are characteristics of supercell storms, although they do not always occur (Lemon, 1977; Doswell, 1985). The bounded weak echo region (BWER) and overhang are clearly evident in the vertical cross-section through the hail mixing ratio field (Figure 4.20b). They are facilitated by the small hail size which allows for more rapid vertical transport and easier movement around the mesocyclone. The BWER is about 1500m deep. Only a small indentation is visible in the 2cm horizontal condensate field (Figure 4.20c), and a very weak overhang is evident in the vertical cross-section. (Bear in mind that the outer 2 contours are only 0.1 and 0.5 $g.kg^{-1}$.)

Cross-sections through the 3mm (Figure 4.21) and 2cm (Figure 4.22) RM storms at their strongest stage reveal numerous supercell characteristics. An overshooting top, a classic supercell characteristic (Doswell, 1985), is evident in both of the simulations, and results from the strong updraft carrying air parcels above the equilibrium level. A large

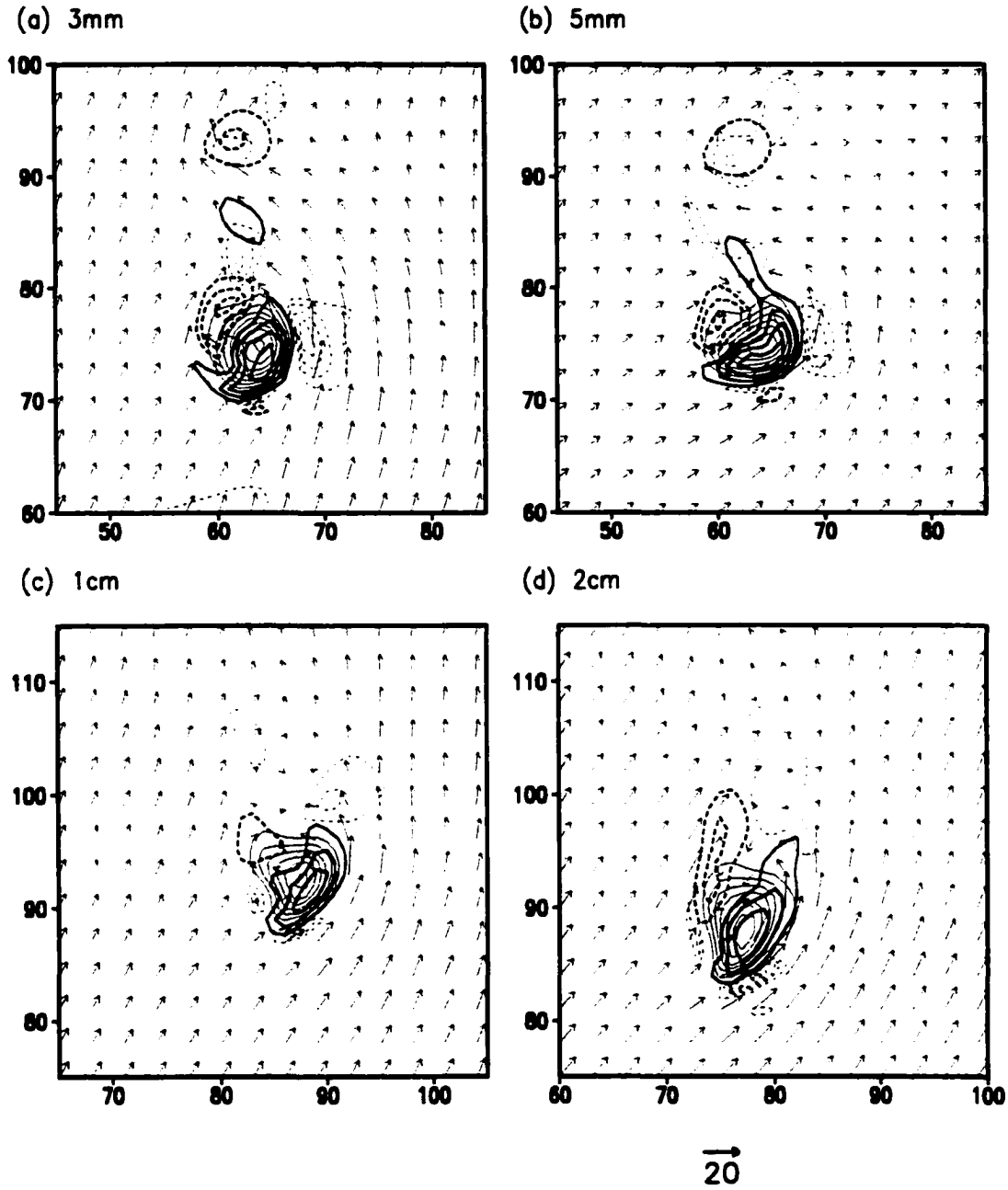


**Figure 4.19: Vertical velocity (thin lines, interval 5m.s$^{-1}$ for the updrafts, 1 m.s$^{-1}$ for the downdrafts), vertical vorticity (thick lines, interval 0.005 s$^{-1}$) and storm-relative wind vectors at 4830m AGL at 60 minutes for the (a) 3mm and (b) 5mm cases, and at 90 minutes for the (c) 1cm and (d) 2cm cases. The magnitude of the wind vectors is indicated at the bottom of the figure, and wind vectors are plotted at every third grid point. The zero lines have been excluded.**

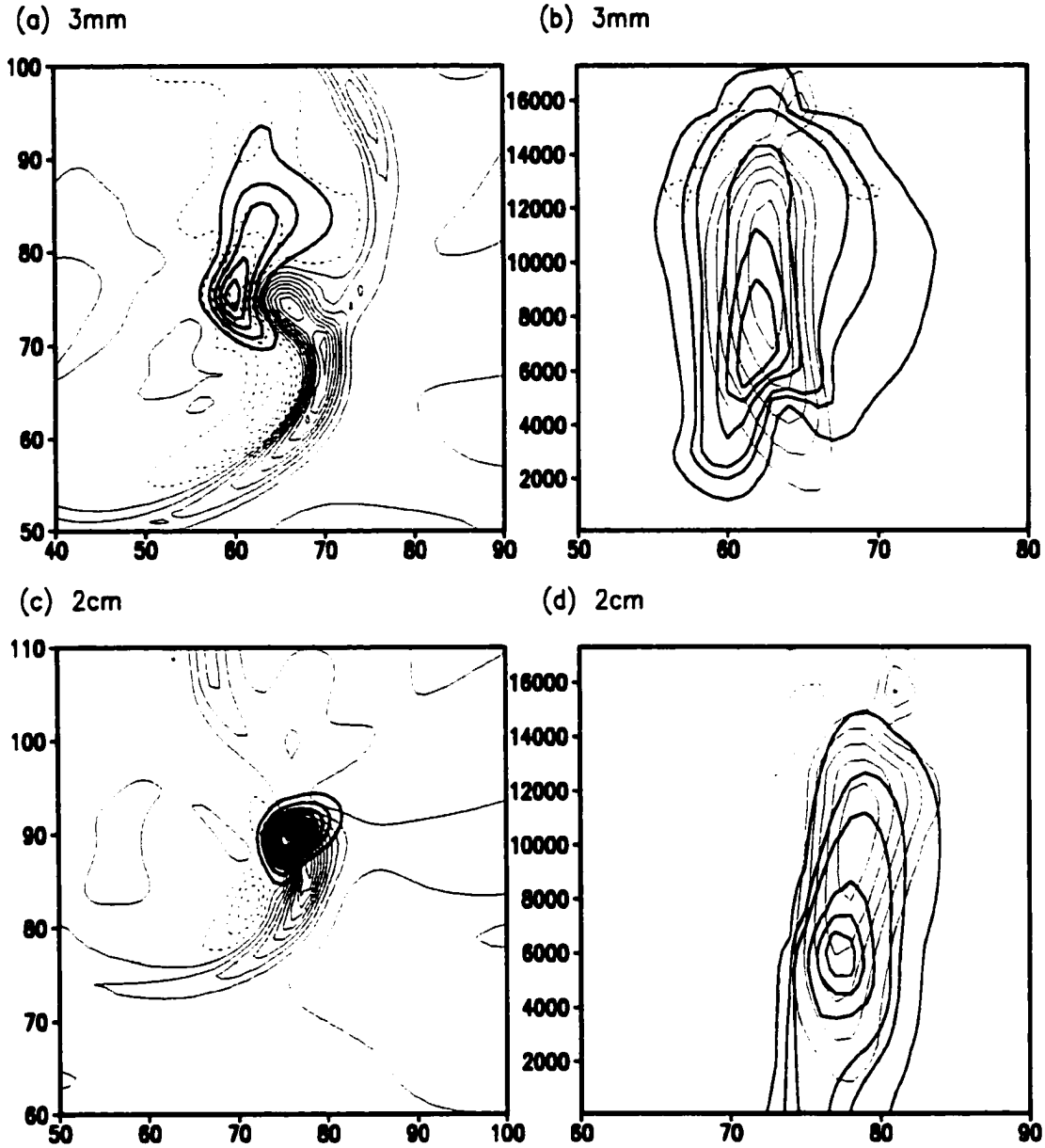


**Figure 4.20: Horizontal cross sections at 1040m AGL of the vertical velocity (thin lines, interval 1m.s$^{-1}$) and condensate mixing ratio (thick lines, interval 0.5 g.kg$^{-1}$) for (a) 3mm case and (c) 2cm case. Vertical cross sections of vertical velocity (thin lines, interval 5m.s$^{-1}$) and hail mixing ratio (thick lines, contours shown at 0.1,0.5,1,3,5,7,7,9 g.kg$^{-1}$) for the (b) 3mm case and (d) 2cm case.**

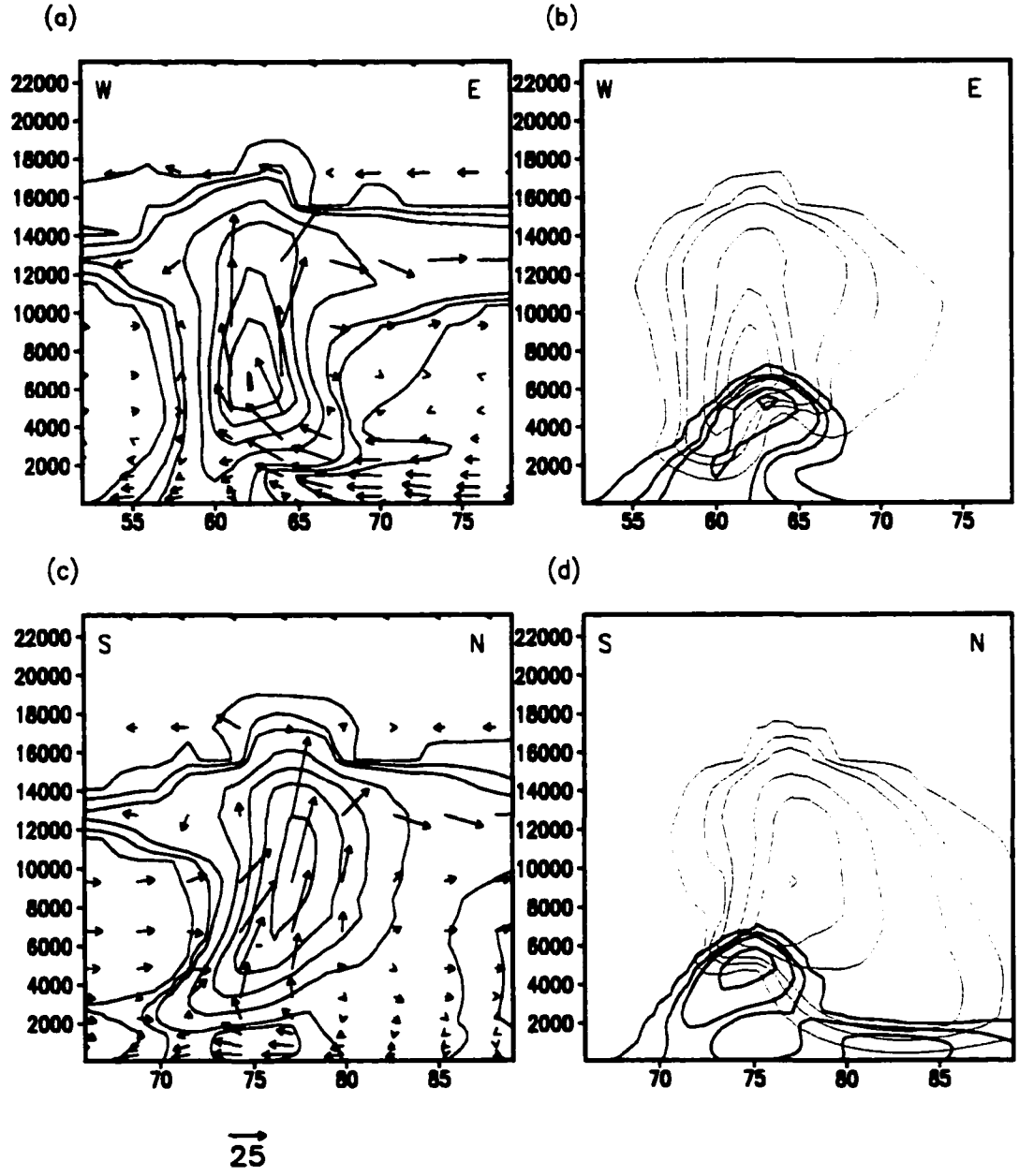


**Figure 4.21: Structure of the 3mm RM storm at 60 minutes shown in (a) east-west cross-section through the condensate mixing ratio (thick lines, contours at 0.1, 0.5, 1,3,5,7,9 g.kg$^{-1}$) with storm-relative wind vectors, (b) east-west cross-section through hail (thin lines, contours at 0.1, 0.5, 1,3,5,7,9 g.kg$^{-1}$) and rain (thick lines, contours at 0.1, 0.5, 1,3,5,7,9 g.kg$^{-1}$) mixing ratios, (c) north-south cross-sections through the condensate mixing ratio (thick lines, contours at 0.1, 0.5, 1,3,5,7,9 g.kg$^{-1}$) with storm-relative wind vectors, and (d) north-south cross-section through hail (thin lines, contours at 0.1, 0.5, 1,3,5,7,9 g.kg$^{-1}$) and rain (thick lines, contours at 0.1, 0.5, 1,3,5,7,9 g.kg$^{-1}$) mixing ratios. Magnitude of vectors is given at the bottom of the figure and vectors are plotted at every third grid point. It should be noted that the vertical and horizontal scale are the same. Ordinate is height (m) AGL.**

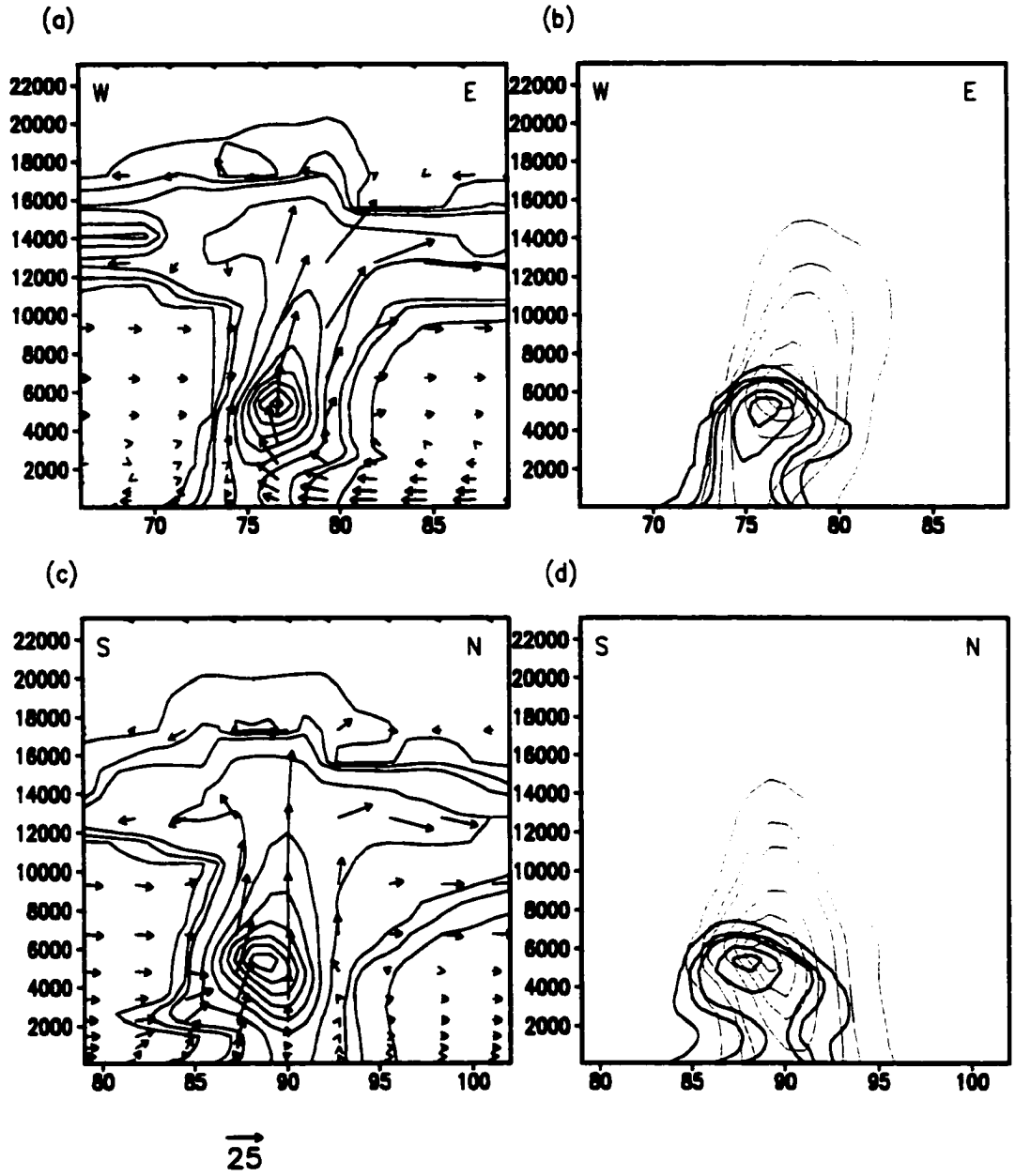


**Figure 4.22: Same as Figure 4.21 except for the 2cm case.**

anvil extending both upshear and downshear is also evident in both cases, and a feature resembling a shelf cloud may be seen at the lower levels. The storm heights are comparable between the two cases, but the 3mm storm is significantly wider than the 2cm storm. The updraft in the 3mm case tilts to the north and west, another typical

characteristic feature of supercells (Doswell, 1985). In the 2cm case, the updraft is almost vertical, tilting slightly to the east.

Both simulations demonstrate the flow structure shown in Browning's (1964) supercell model (Fig. 2.2). Low-level flow enters the storm from the south and east and rises in the updraft. Mid-level air enters the updraft from the south, and the updraft diverges at the tropopause level from where the majority of the outflow moves eastward with the upper-level westerlies. Low-level southerly and westerly flow, associated with the strong outward movement of the cold pool, is evident in the 3mm case, but only very weak westerly flow is apparent in the 2cm simulation.

The small hail size in the 3mm case allows for it to be transported further to the north and east of the updraft (Figure 4.21b,d; Figure 4.23b) than in the 2cm case, where the hail sizes limit the distance that it may be transported (Figure 4.22b,d; Figure 4.23d; Figure 4.24d). Hail extends ~12 km east of the updraft in the 3mm run, but only ~6 km in 2cm simulation. The vertical distribution of hail within the updraft is also greater in the 3mm case (Figure 4.21b,d; Figure 4.22b,d). As a result of both the greater transportability and more rapid melting rates of small hail, the low-level region of rainfall in the 3mm case extends much further from the updraft (Figure 4.21b,d; Figure 4.24a) than in the 2cm run (Figure 4.22b,d; Figure 4.24c), where the rainfall, hail and the updraft are closely co-located. The wider distribution of precipitation in the 3mm case generates a more expansive RFD (Figure 4.24a,b) than in the large hail case (Figure 4.24c,d). Also, in the 3mm case, as hail falls from the anvil region and melts, weak downdrafts form (near x=70 km in Figure 4.21a). These downdrafts were evident to the east of the updraft in Figure 4.19. Finally, while the rain and hail maxima values are greater in the large hail cases, the rain and hail are distributed over much greater spatial areas in the smaller hail cases.

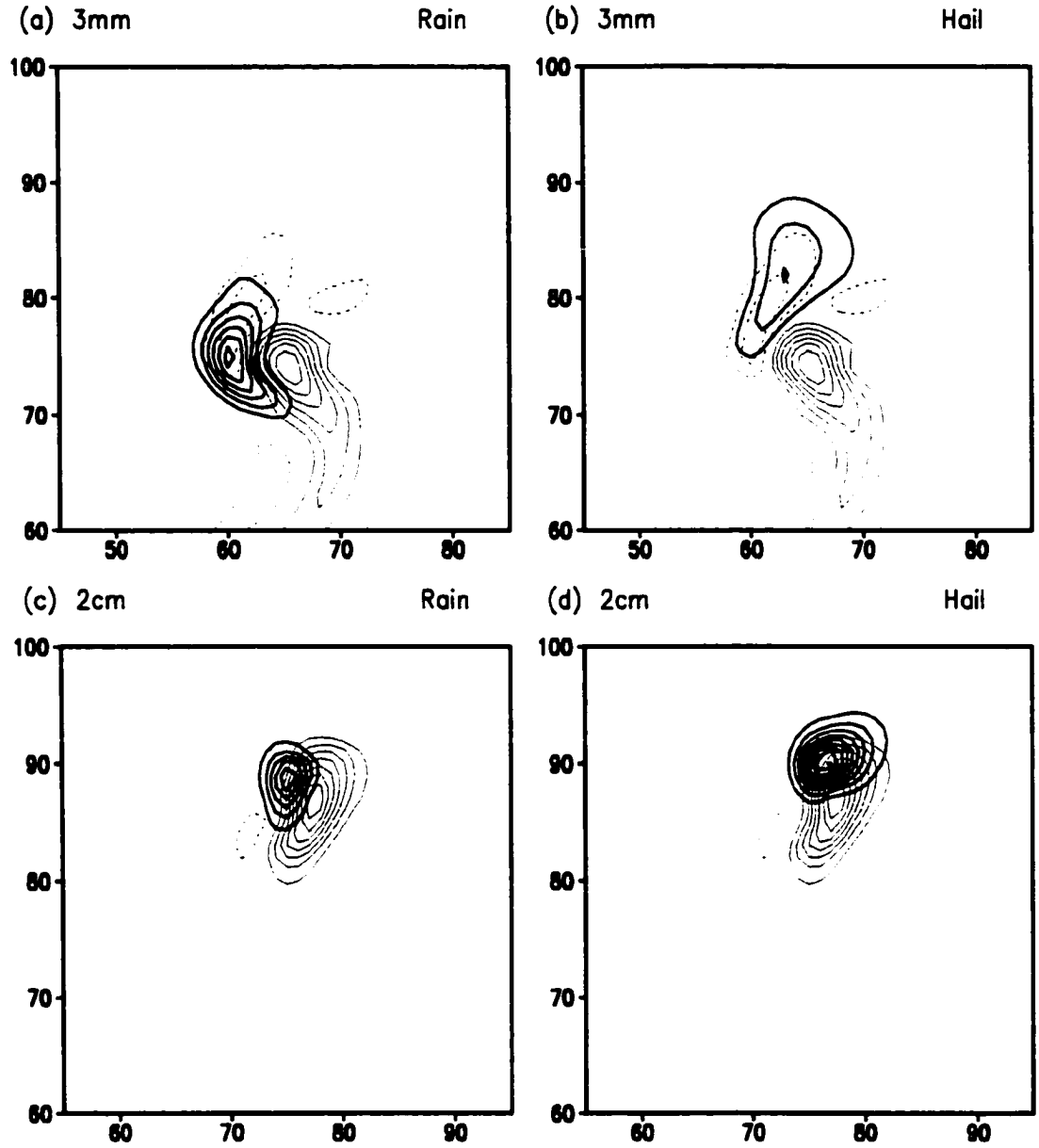


**Figure 4.23: Vertical velocity (thin lines, interval 2 $m.s^{-1}$), rain (thick lines in a,c, interval 0.5 $g.kg^{-1}$) and hail (thick lines in b,d, interval 0.5 $g.kg^{-1}$) mixing ratios at 2 km AGL at 60 minutes for the 3mm case (a,b) and at 90 minutes for the 2cm case (c,d). The zero line for the mixing ratios and vertical velocity is excluded.**

The variation in the mean hail diameter therefore has a significant effect on the strength and location of the low-level downdraft structure, on the cold pool properties,

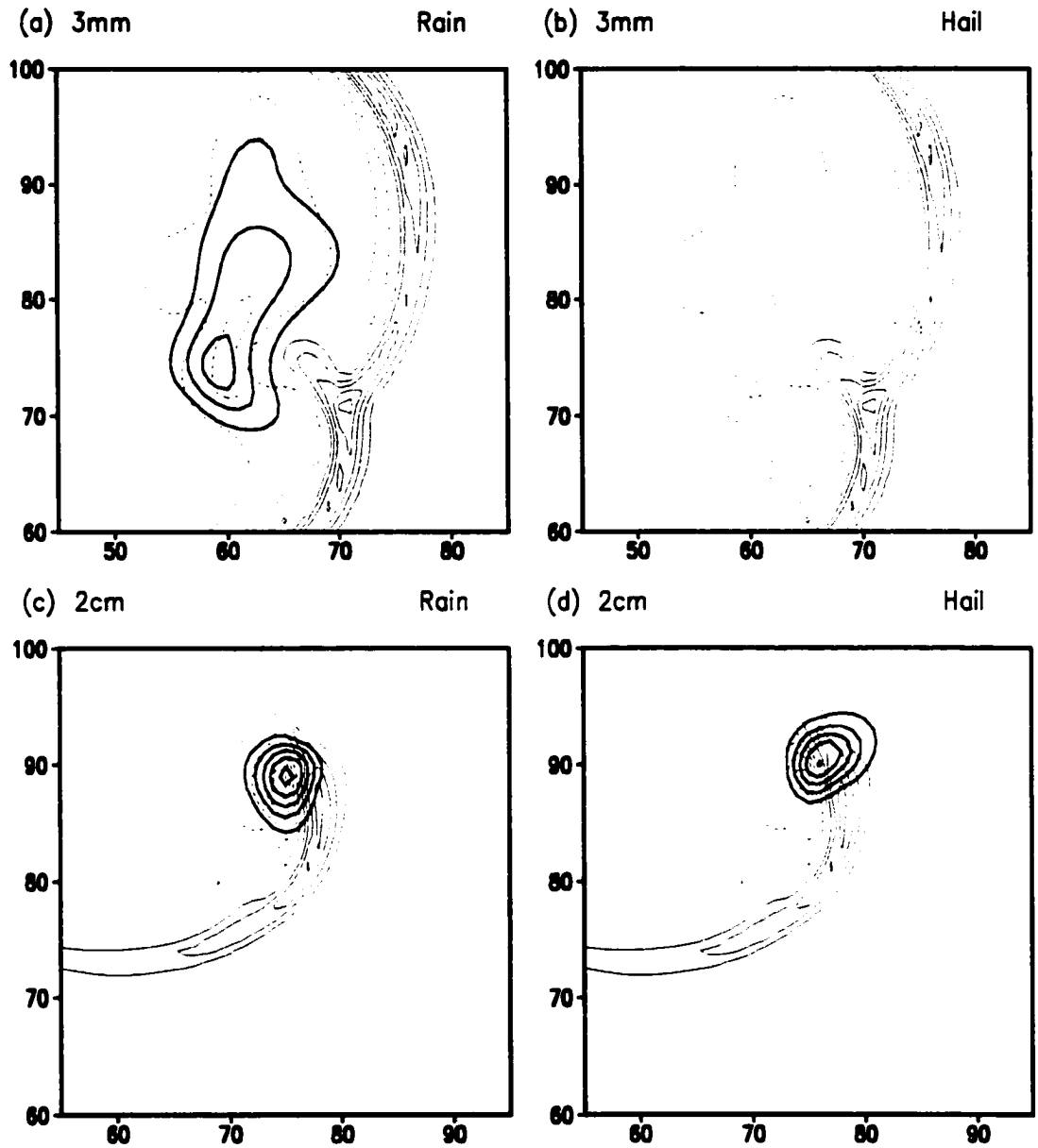


**Figure 4.24: Vertical velocity (thin lines, interval 0.3 $m.s^{-1}$), rain (thick lines in a,c, interval 0.5 $g.kg^{-1}$) and hail (thick lines in b,d, interval 0.5 $g.kg^{-1}$) mixing ratios at 48m AGL at 60 minutes for the 3mm case (a,b) and at 90 minutes for the 2cm case (c,d). The zero line for the mixing ratios and vertical velocity is excluded.**

and on the precipitation distribution, all of which have an influence on the storm structure and longevity.

## 4.7 Occlusion

We saw earlier that in both the 3mm and 5mm simulations, the updraft at ~4 km AGL becomes orientated in a more east-west direction at 75 minutes, followed by the appearance of two updrafts at 105 and 90 minutes, respectively (Figure 4.1a,b). We also observed that the vertical velocity in the smaller hail cases reaches a maximum around 60 minutes before decreasing rapidly, due to the effects of low-level convergence. This change in storm structure is caused by an occlusion of the low-level updraft.

At 60 minutes, the mesocyclone extends from 400m through 11 km, but the vertical vorticity does not exceed 0.01 $s^{-1}$ near the surface (Figure 4.25). At 55 minutes (not shown), mesocyclonic values were only evident above 1 km AGL, and the low-level vertical vorticity has therefore been increasing in strength. The hook echo apparent in the condensate mixing ratio field is evidence of the mesocyclonic rotation at this time. The evaporatively-driven RFD extends from the surface through 1 km AGL, but then decreases in strength, and is no longer obvious at 4 km. As a result of the eastward propagation of the RFD, convergence at the base of the updraft and along the low-level gust front is enhanced which causes the updraft maximum at this time (Figure 4.2).

By 70 minutes, the mesocyclone now extends from the surface through 11 km (Figure 4.26). The RFD increases in strength and continues to surge eastward, pushing the gust front outward. The movement of the RFD, together with the rotation around the mesocyclone, moves the updraft into a more east-west orientation as has been previously observed (Klemp and Rotunno, 1983; Wicker and Wilhelmson, 1995; Adlerman et al., 1999). The movement of the gust front due to the eastward forcing of the RFD, enhances convergence along the gust front in these regions, and a secondary updraft maximum becomes evident to the southeast of the original updraft between 400 and 1000m. This secondary updraft is not, however, evident at 4 km.

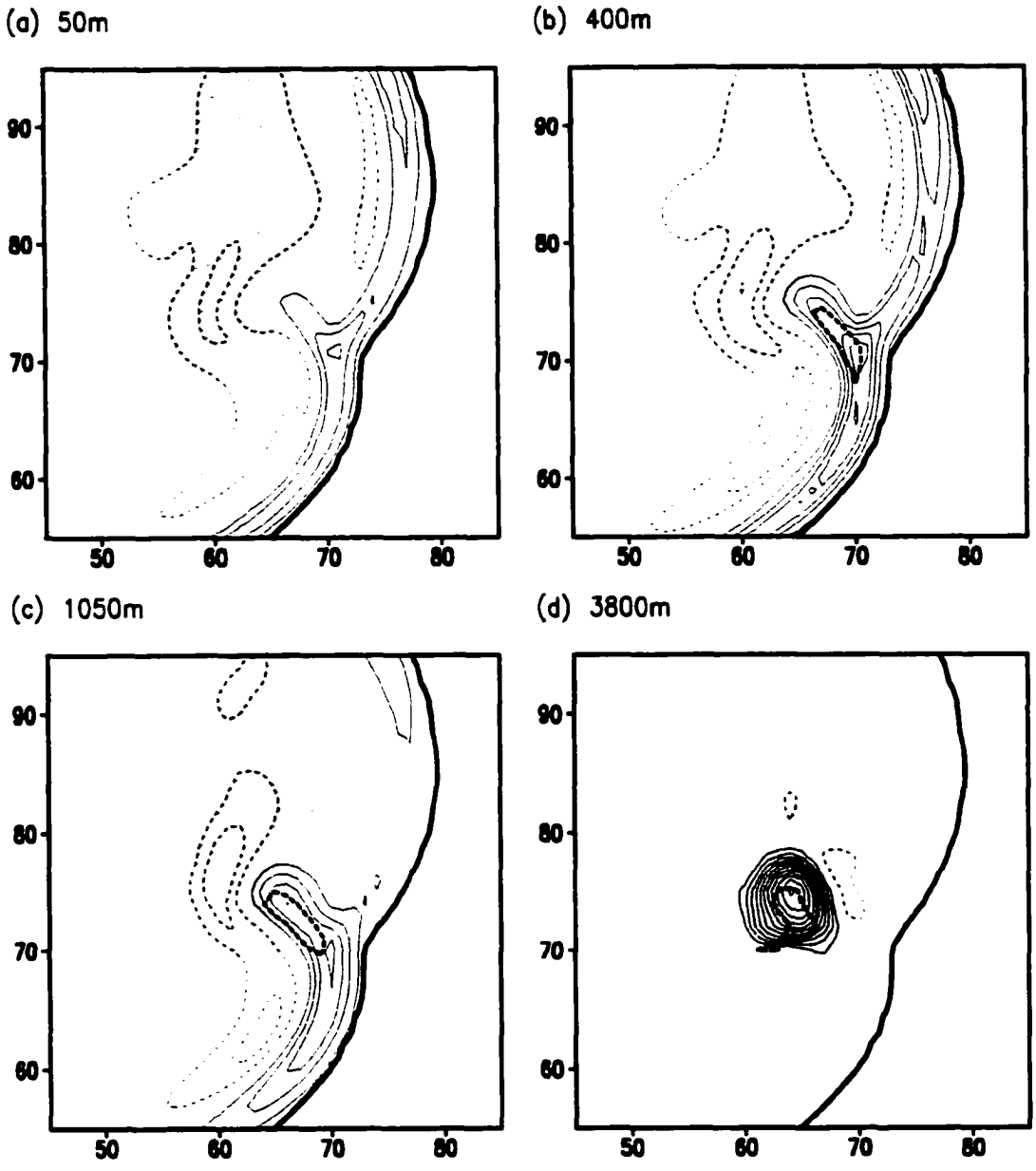


**Figure 4.25: Vertical velocity (thin lines), condensate mixing ratio (shaded), vertical vorticity greater than 0.01 $s^{-1}$ (within thick dashed circular line) and the position of the surface gust front (thick solid line) at 60 minutes for (a) 50 m, (b) 400 m, (c) 1050m, and (d) 3800m AGL. The 1°C temperature perturbation isotherm indicates the position of the gust front. The shading represents the region where condensate mixing ratios are greater than 0.5 $g.kg^{-1}$. Vertical velocity contour intervals are (a) 0.5 $m.s^{-1}$, (b) 1 $m.s^{-1}$, (c) 2 $m.s^{-1}$ and (d) 2.5 $m.s^{-1}$. The downdrafts in (a) are at 0.3 $m.s^{-1}$.**

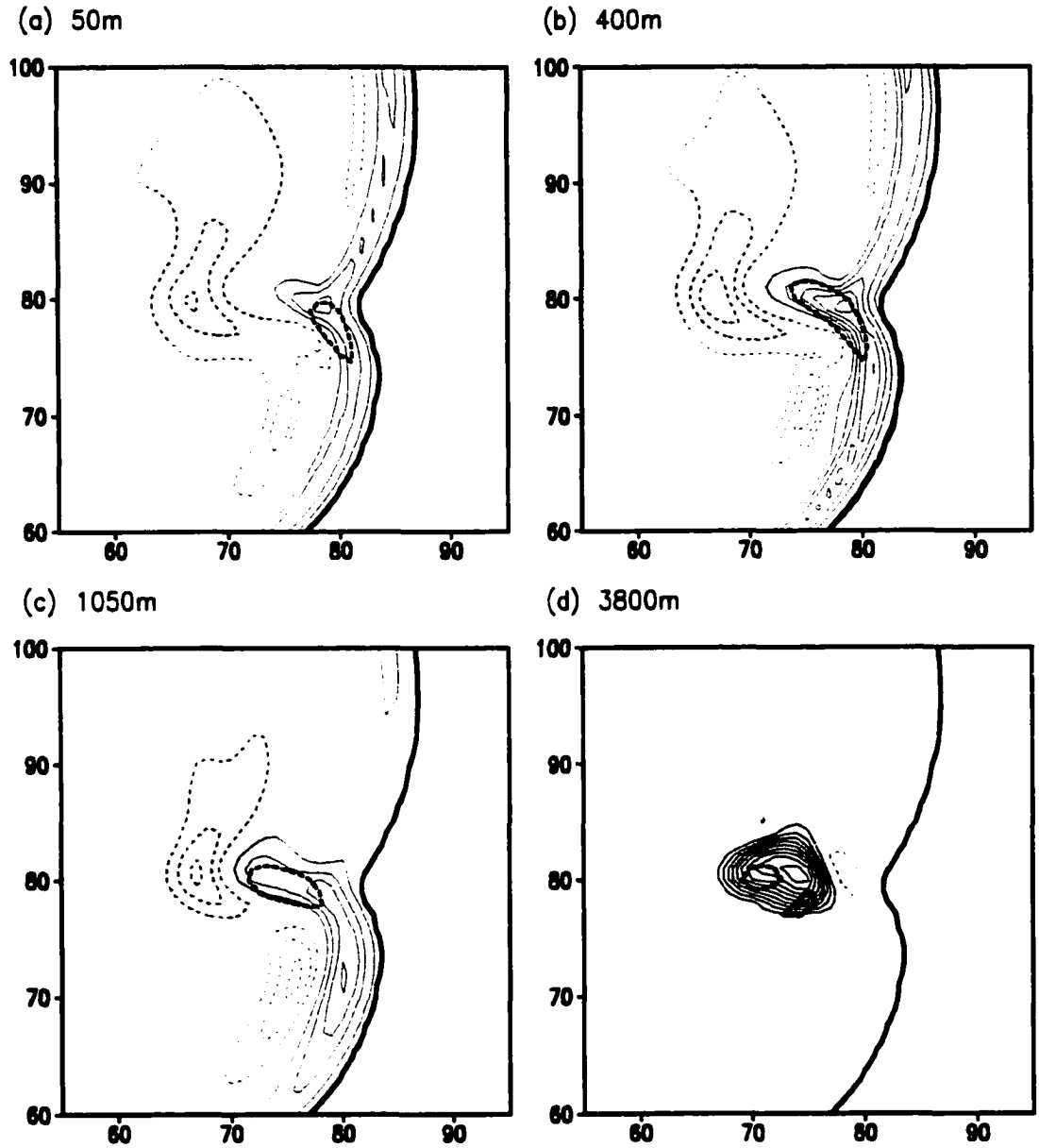


**Figure 4.26: Same as Figure 4.25 except for 70 minutes.**

The vertical vorticity near the surface attains its maximum value in the 3mm case at 75 minutes (Figure 4.27). The reasons for this will be addressed in the section on vorticity below. As discussed in Chapter 2, Rotunno and Klemp (1982) used the linearized divergence equation and the assumption that $\nabla^2\pi' \approx -\pi'$, to demonstrate that for a wind field in pure rotation, $\pi' \approx -\zeta^2$. Thus, wherever there is rotation, cyclonic or

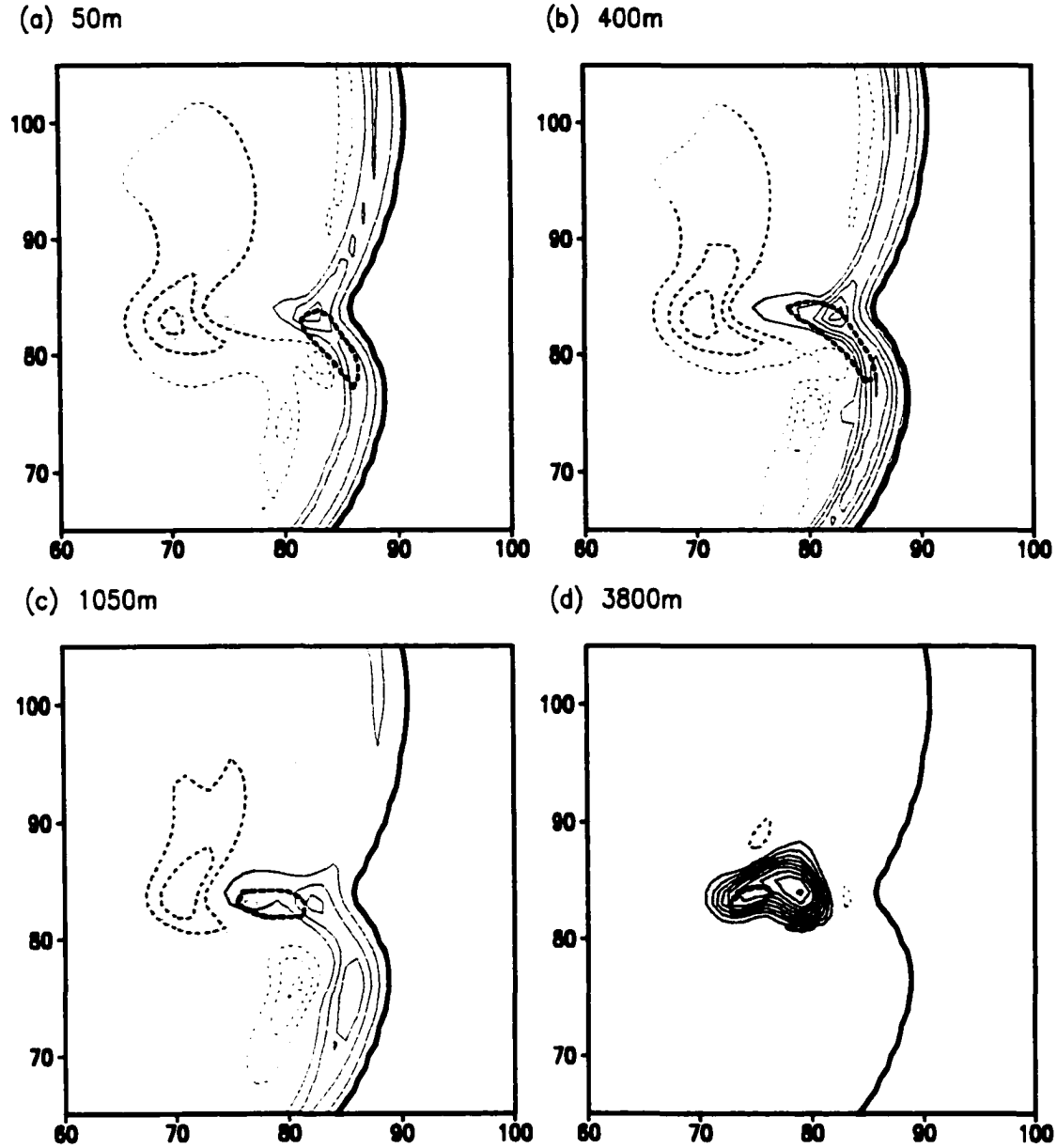


**Figure 4.27: Same as Figure 4.25 except for 75 minutes**

anticyclonic, the perturbation pressure is lowered. The rapid increase in the vertical vorticity near the surface at between 60 and 75 minutes, decreases the perturbation pressure near the surface, and thus generates a downward-directed vertical pressure gradient force in the lower levels. This results in the development of the small-scale downdraft, first evident at 70 minutes (x=78, y=77) (Figure 4.26), and which has

increased in strength by 75 minutes (x=83,y=80) (Figure 4.27). This small-scale downdraft, known as the occlusion downdraft (Rotunno and Klemp, 1983), extends to just below the 1 km level, and merges with the RFD. The mesocyclone is starting to take on a divided structure near the surface, with the updraft in the northwestern region and the occlusion downdraft moving into its southern region. A similar structure was described by Lemon and Doswell (1979), and simulated by Wicker and Wilhelmson (1995) and Adlerman et al. (1999). The divided mesocyclone does not, however, ever fully develop. The updraft at 4 km extends toward the west, and the velocity in the downshear region is greater. However, a true two-celled structure is not observed in the vertical velocity field at this level, as has been previously seen.

By 85 minutes (Figure 4.28), the downshear region of the updraft at 4 km is now significantly stronger than the upshear region. A "band" of vertical vorticity is evident in the lower levels. This band remains behind the convergence line, which is similar to what Klemp et al. (1981) observed in their coarse resolution simulation. The banded structure of the low-level mesocyclone, together with the retreat of the RFD, prevents the RFD from completely wrapping around the low-level updraft. It is suspected, like in the simulations of Klemp et al. (1981), that insufficient grid resolution, which is linked to weaker vertical vorticity values, is the primary factor inhibiting the downdraft from wrapping around the updraft. Around 4 km AGL, a weak updraft is seen to the south of the original updraft (Figure 4.28d). This is not the secondary updraft that is frequently seen to develop as a result of the enhanced convergence along the extended gust front (Moller et al., 1994; Adlerman et al., 1999). While upward lifting is associated with this region of convergence in the 3mm simulation, it is not the source of the updraft occurring to the south of the main updraft (Figure 4.29). The southern updraft originates within the cold pool region about 8 km behind the gust front (Figure 4.29a), and becomes better developed and more closely situated to the main updraft as the simulation progresses. It is apparent from the divergence fields at 400 m AGL (Figure 4.30), that a small region of

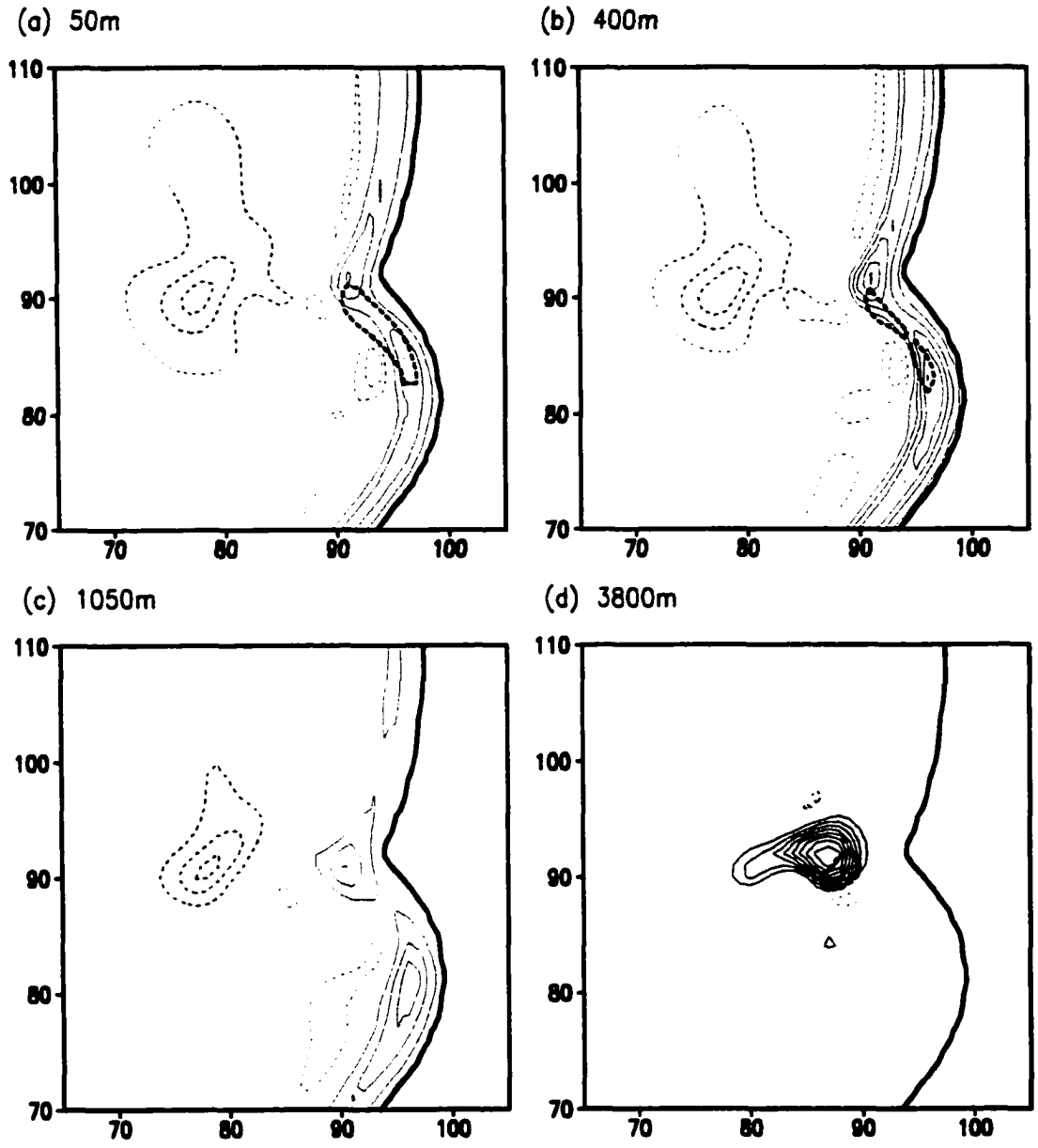


**Figure 4.28: Same as Figure 4.25 except for 85 minutes**

low-level convergence is associated with the development of this southern updraft. The convergence occurs as a result of the rotational flow around the band of vorticity and the inflow of easterly ambient flow into the region of the cold pool.

By 105 minutes, the gust front has straightened out again due to the reduction in the eastward forcing by the RFD, and the low-level vertical vorticity has decreased in

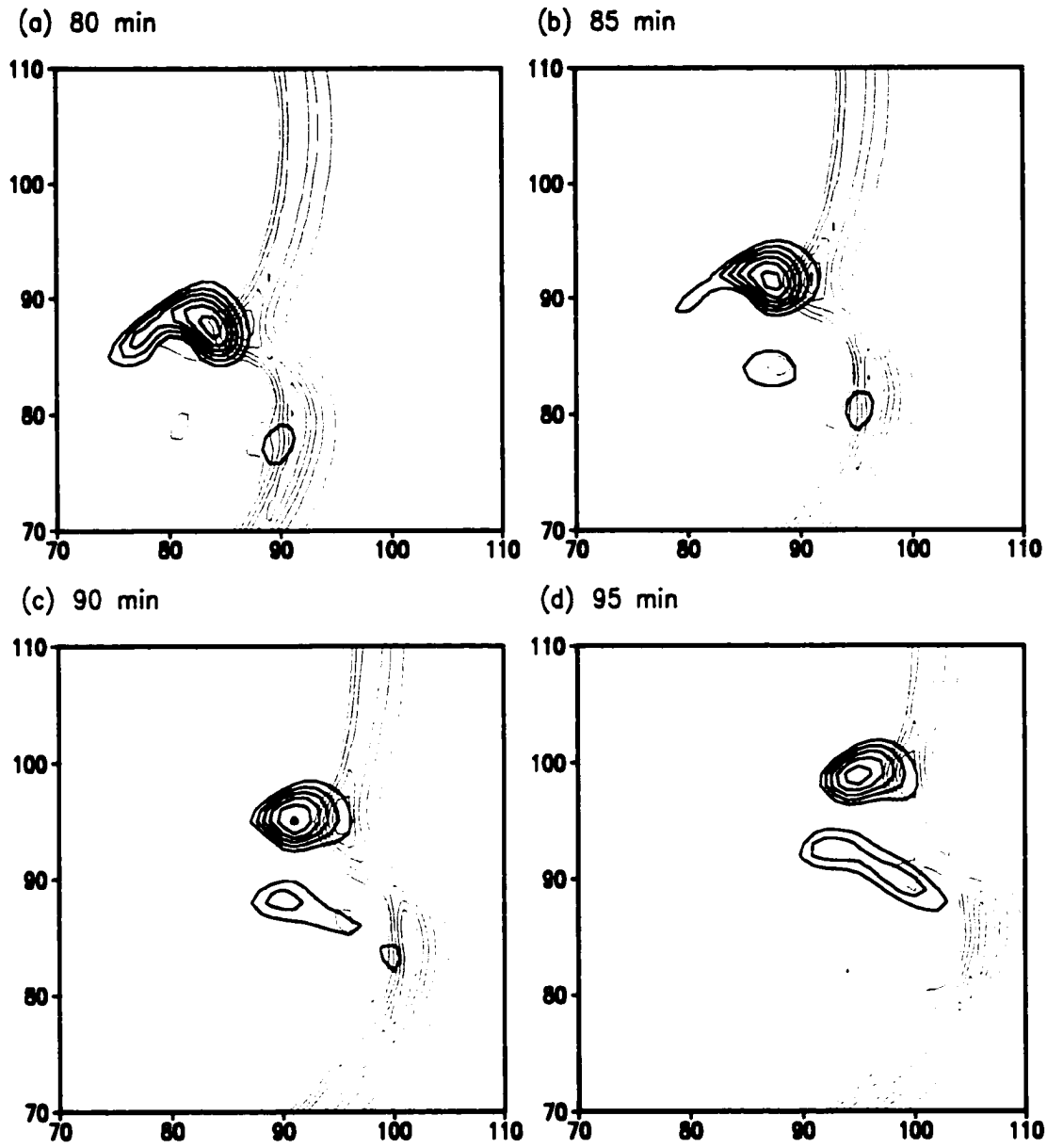


**Figure 4.29: Updrafts at 400 m (thin lines, interval 1m.s$^{-1}$) and 2500 m AGL (thick lines, interval 2m.s$^{-1}$) at (a) 80 minutes, (b) 85 minutes, (c) 90 minutes, and (d) 95 minutes.**

strength (Figure 4.31). In the upper levels, the southern updraft has now merged with the original updraft, which causes an overall strengthening of upward motion in this region. This concurs with the increase in vertical velocity seen at this time (Figure 4.2). The increase in the updraft strength between 105 and 115 minutes leads to the production of more hail, which then results in the re-development of the evaporatively-generated RFD

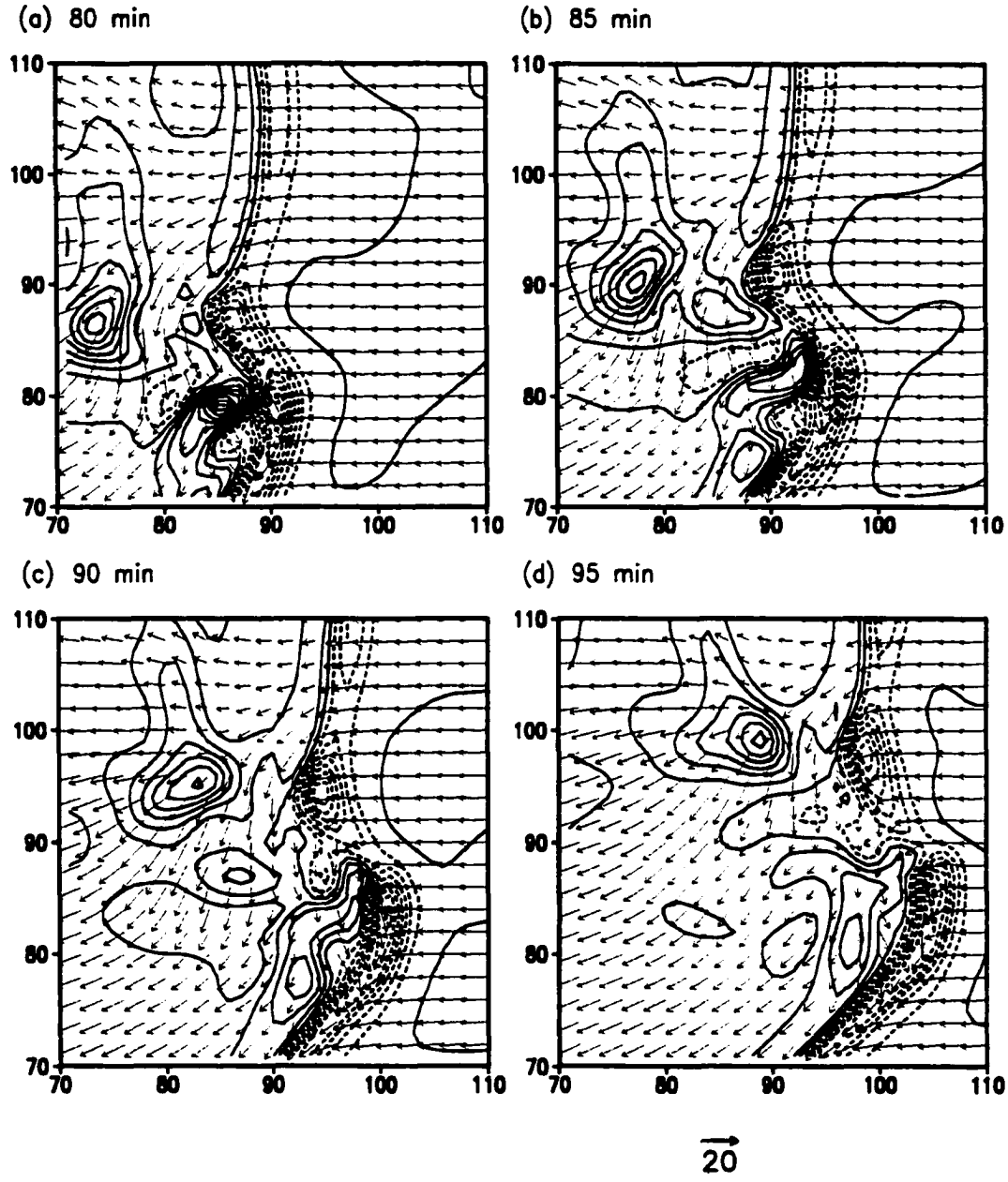


**Figure 4.30: Divergence (thick lines, interval 0.001 $s^{-1}$) and storm-relative wind vectors at 400 m AGL at (a) 80 minutes, (b) 85 minutes, (c) 90 minutes and (d) 95 minutes. Solid lines represent positive values; dashed lines represent negative values. Wind vector scale shown in the bottom right of the figure.**

(Figure 4.32). The RFD starts to surge eastward again, thereby increasing convergence into the updraft. This enhances both the updraft strength and the vertical vorticity, and a hook echo is once again obvious in the condensate mixing ratio field.

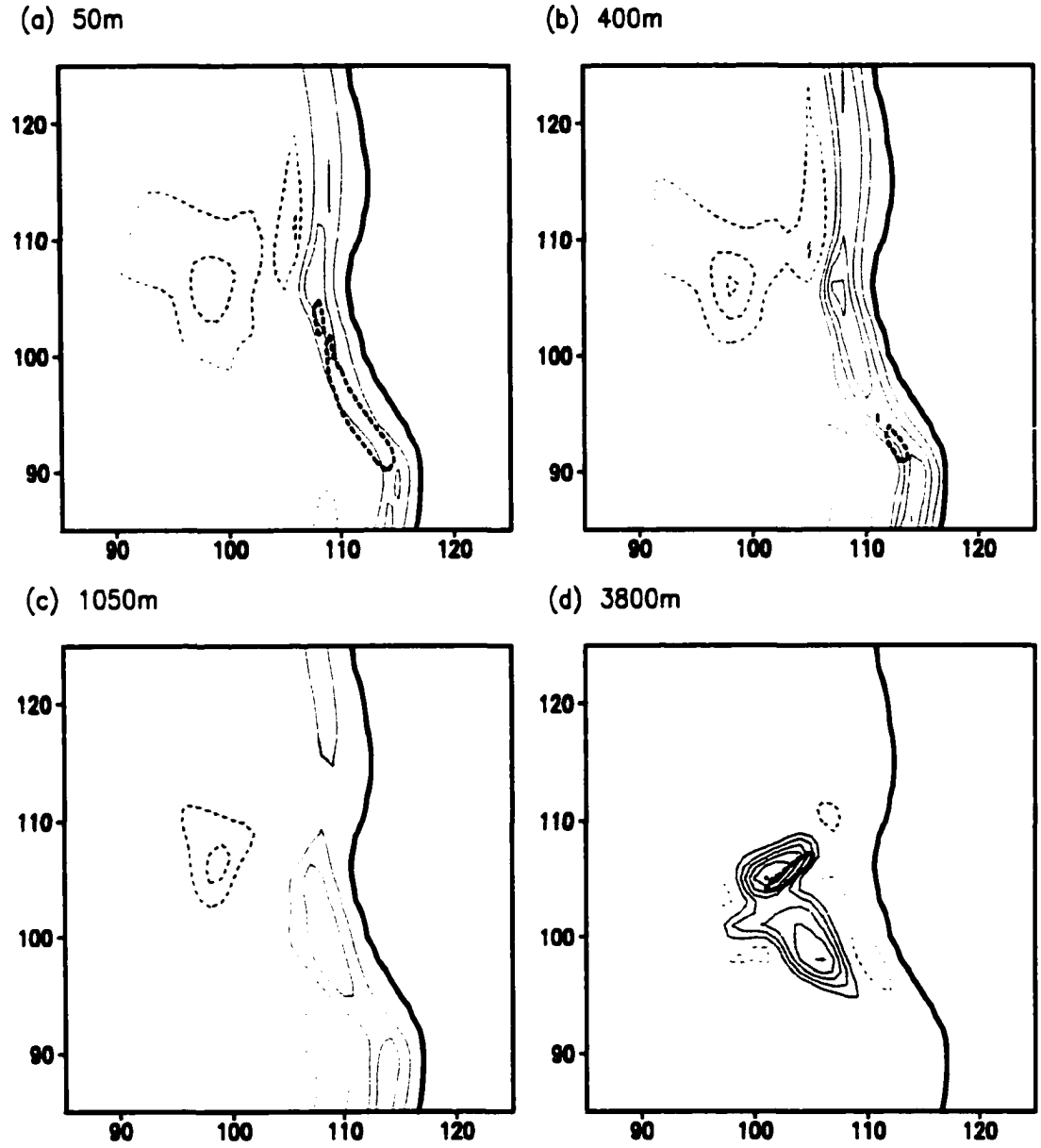


**Figure 4.31: Same as Figure 4.25 except for 105 minutes.**

Until ~75 minutes, the occlusion process in the 3mm simulation shows many similarities to the first three stages seen by Adlerman et al (1999) in their simulation, in which the horizontal grid spacing was 250 m. However, as the simulation progresses, the impact of insufficient grid resolution becomes apparent as the small-scale features start to play a more important role. This was also observed by Klemp et al. (1981), and Rotunno

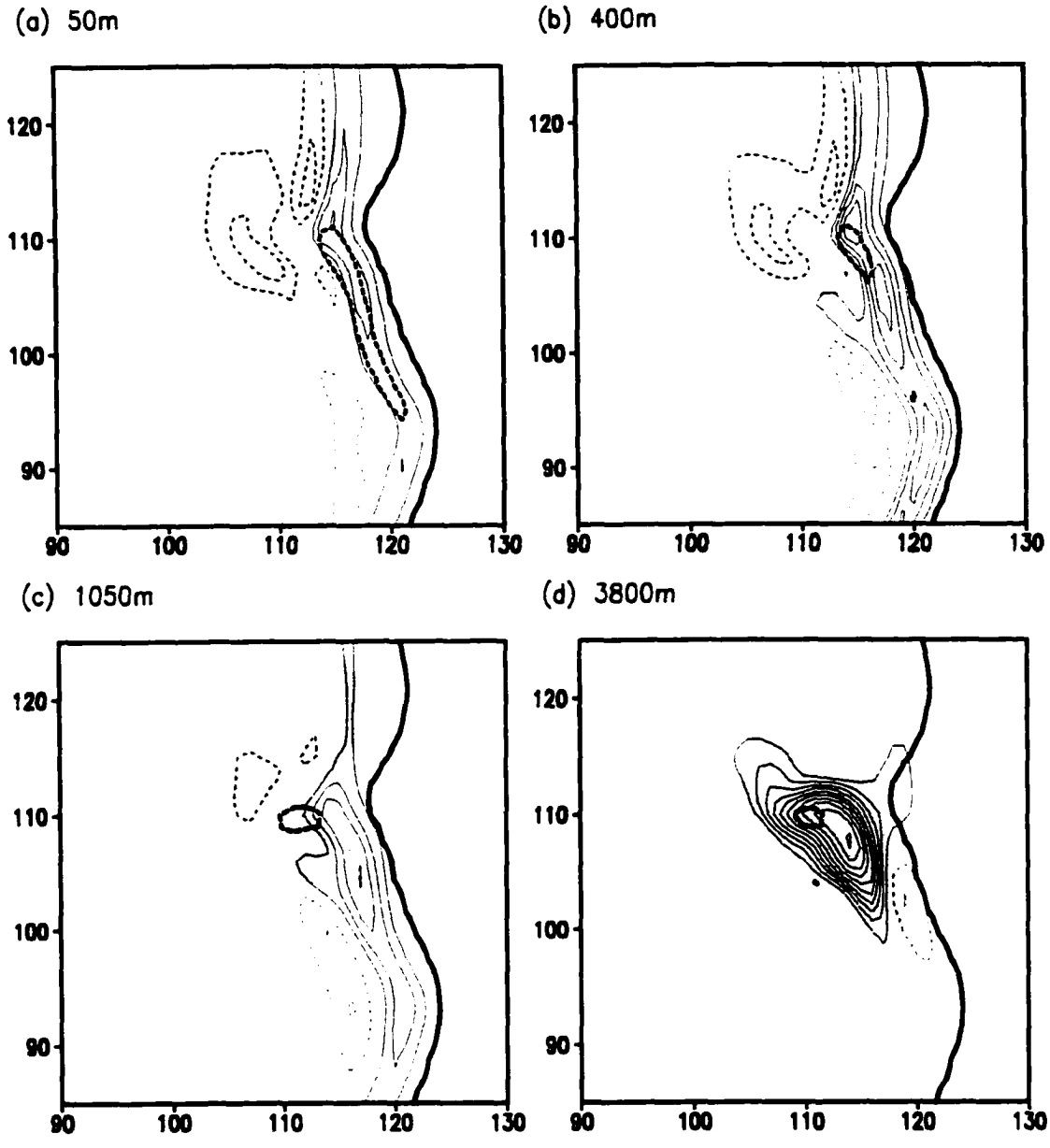


**Figure 4.32: Same as Figure 4.25 except for 115 minutes.**

and Klemp (1983), in their simulations in which the horizontal grid resolution was 1 km. Rotunno and Klemp found that by increasing the horizontal grid resolution to 250 m, the RFD wrapped around the updraft. Wicker and Wilhelmson (1995) also simulated the divided mesocyclone structure and the wrapping of the RFD around the updraft using a horizontal grid spacing of 120 m. It is highly likely that grid resolution is the main factor

limiting the complete occlusion of the updraft in the small hail simulations. However, these simulations would need to be rerun using a finer-resolution single grid setup, or by spawning a finer-resolution nested grid, in order to confirm this hypothesis.

The results from the 5mm case are very similar to those of the 3mm run, however, the 1cm and 2cm results differ significantly. In the 2cm case, the RFD does not surge eastward as in the 3mm case, and the mesocyclone is limited to above 3500 m AGL at 60 minutes (Figure 4.33). By 105 minutes, the mesocyclone extends from the surface through 11 km (Figure 4.34). There is some movement of the RFD to the south and east, however, it is not on the scale of the 3mm case. An occlusion does not take place in the 1cm and 2cm cases due to the shallow, limited RFD, which is a direct result of the reduced melting and evaporative cooling rates associated with the larger hail sizes. The weak low-level vertical vorticity in these cases is also a factor delaying the onset of the occlusion, as it cannot aid in the rotation of the RFD around the updraft. The factors controlling the low-level vertical vorticity will now be examined.

## 4.8 Low-Level Vorticity

As the mean hail diameter is decreased, the low-level maximum vertical vorticity within the RM storm increases (Figure 4.35). The peak vertical vorticity values in the smaller hail cases occur around 75 minutes being associated, as we have just seen, with the occlusion of the updraft in these cases. The vertical vorticity in the 2cm case increases slowly, only reaching mesocyclonic values after 85 minutes. What causes these differences in the low-level vertical vorticity structure?

At 70 minutes, both the low-level vertical and horizontal vorticity are significantly greater in the 3mm simulation (Figure 4.36a,b) than in the 2cm run (Figure 4.37a,b). The storm-relative streamlines indicate that in the 3mm case, the majority of air entering the updraft at this time comes from the regions to the north, northwest and northeast of the

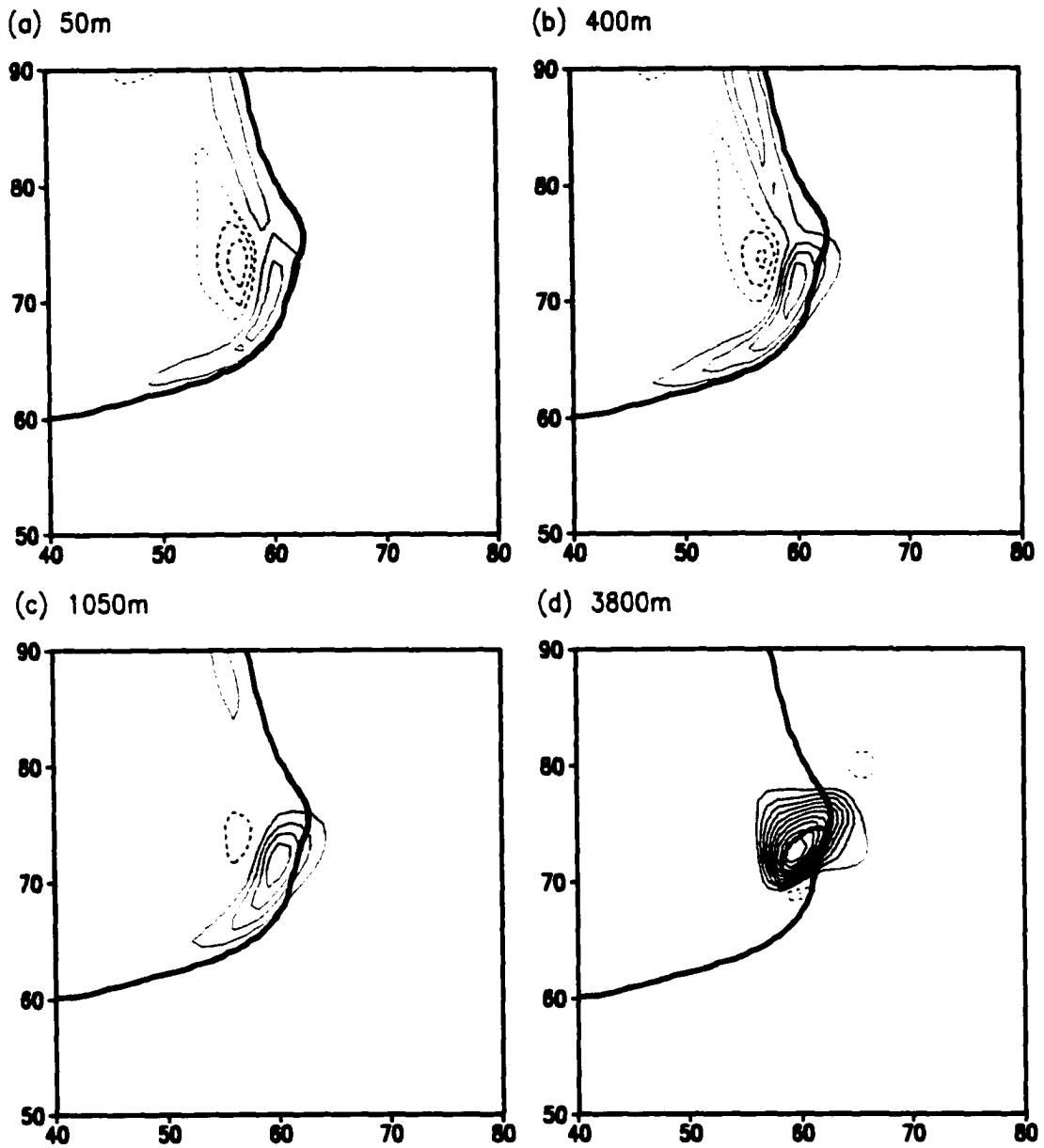


**Figure 4.33: Same as Figure 4.25 except for the 2cm case.**

updraft (Figure 4.36c). The magnitude and orientation of the horizontal vorticity vectors in these regions indicate, that the regions will be a source of strong streamwise vorticity. Tilting of this strong horizontal vorticity by the updraft, will enhance the vertical vorticity in the lower regions of the updraft. In the 2cm case, the storm-relative streamlines imply

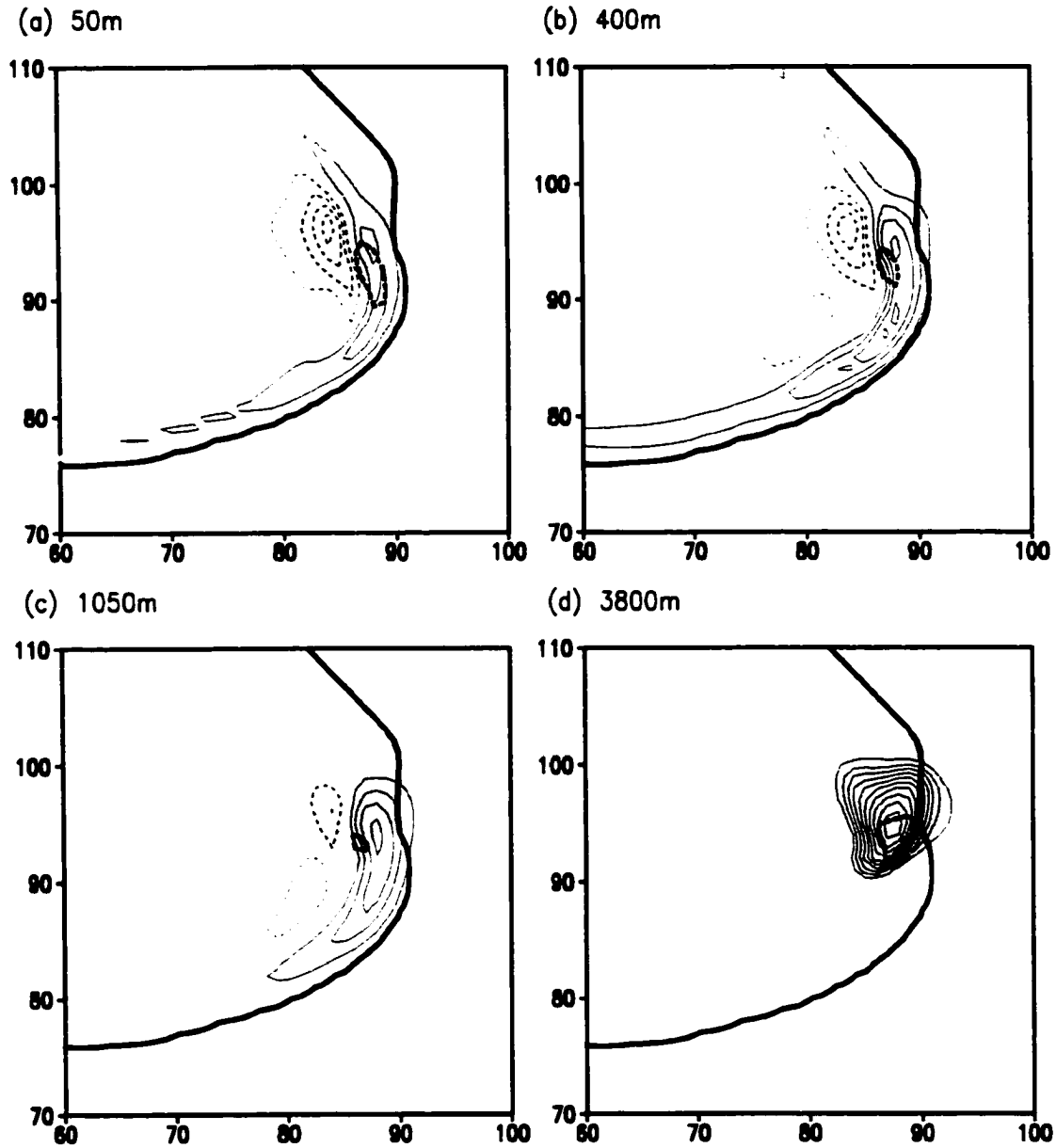


**Figure 4.34: Same as Figure 4.33 except at 105 minutes.**

that the majority of air entering the updraft at this stage, is from the region to the east of the updraft (Figure 4.37c). The horizontal vorticity in this region is weak.

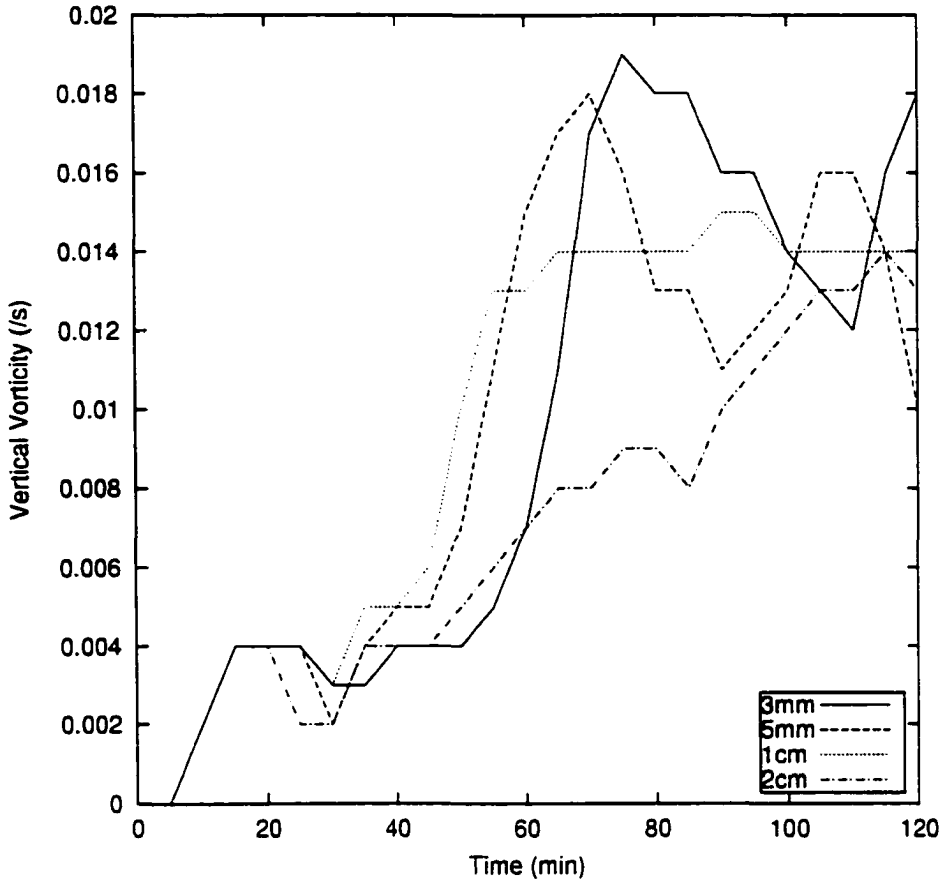


**Figure 4.35: Vertical component of vorticity ($s^{-1}$) at 150m AGL as a function of time for the 3mm (solid line), 5mm (dashed line), 1cm (dotted line) and 2cm (dot-dash line) simulations.**

The x and y components of the vorticity tendency equation are given by:

$$\frac{D\xi}{Dt} = \eta\frac{\partial u}{\partial y} + \zeta\frac{\partial u}{\partial z} - \xi\left(\frac{\partial v}{\partial y} + \frac{\partial w}{\partial z}\right) + \frac{\partial B}{\partial y} + \text{TURB} \tag{4.4}$$

and

$$\frac{D\eta}{Dt} = \xi\frac{\partial v}{\partial x} + \zeta\frac{\partial v}{\partial z} - \eta\left(\frac{\partial u}{\partial x} + \frac{\partial w}{\partial z}\right) - \frac{\partial B}{\partial x} + \text{TURB} \tag{4.5}$$

respectively, where $\xi$ and $\eta$ are the x and y components of vorticity vector respectively, and B is the numerical buoyancy (discussed further in chapter 5). The first two terms on the right hand side of equations (4.5) and (4.6) comprise the tilting term, the third term is the stretching term, the fourth term is the baroclinic generation term, and the fifth term is

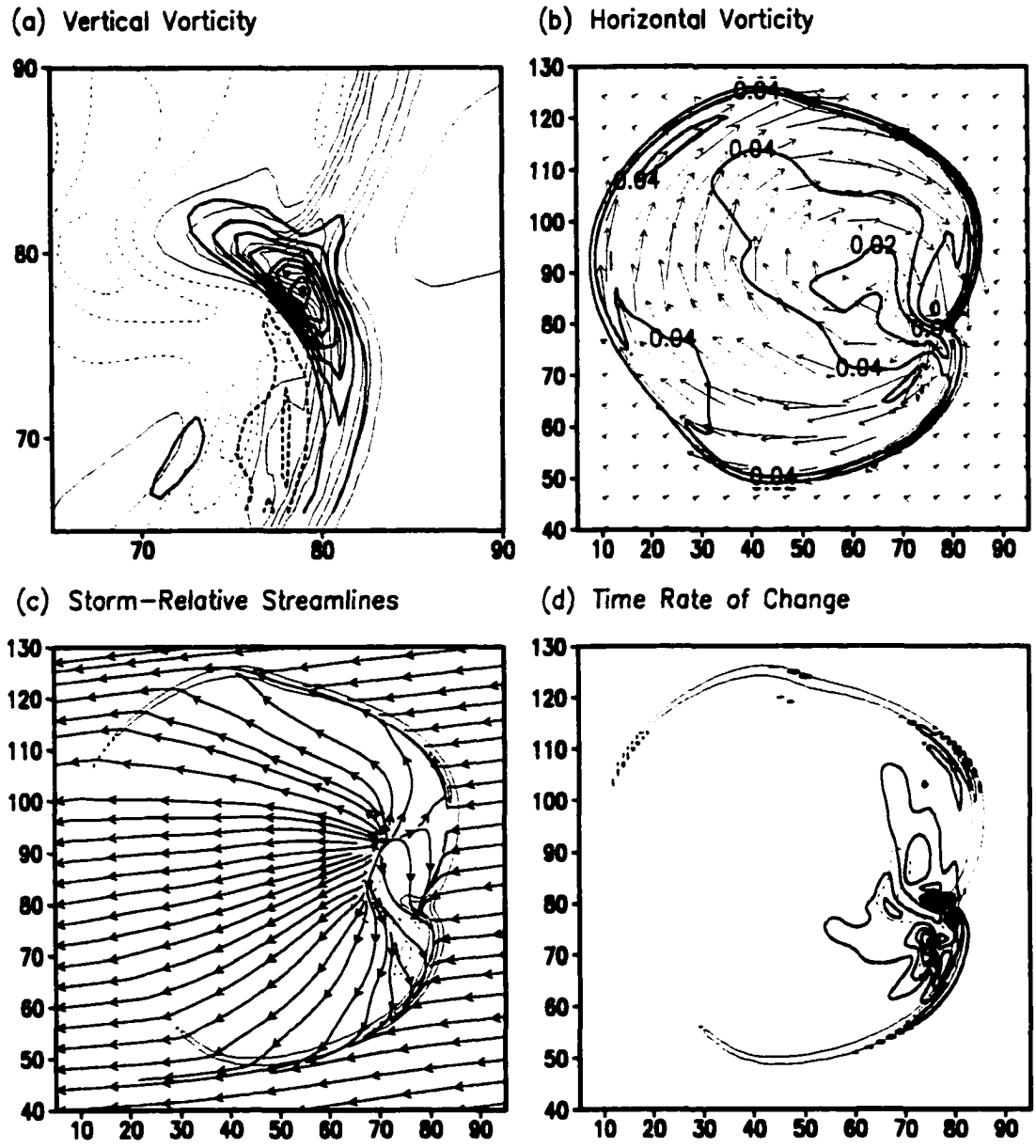


**Figure 4.36: (a) Vertical velocity (thin lines, interval 0.5 m.s$^{-1}$) and vertical vorticity (thick lines, interval 0.002 s$^{-1}$), (b) vertical velocity (thin lines, contours at –2, -1, 1, 2 m.s$^{-1}$), horizontal vorticity vectors, and magnitude of horizontal vorticity (thick lines, interval 0.02 s$^{-1}$), (c) vertical velocity (thin lines, contours at –2, -1, 1, 2 m.s$^{-1}$) and storm-relative streamlines, and (d) vertical velocity (thin lines, contours at –2, -1, 1, 2 m.s$^{-1}$) and the magnitude of ($D\omega_H/Dt$)*1e5 (thick lines, interval 5 s$^{-2}$) for the 3mm case at 70 minutes at 150m AGL**

the turbulence term. The magnitude of the time rate of change of the horizontal vorticity ($|\frac{D\vec{\omega}_h}{Dt}|$) in the 3mm case is greatest to the north of the updraft, in the region of the greatest influx of air into the updraft (Figure 4.36d). It is also large to the south of the

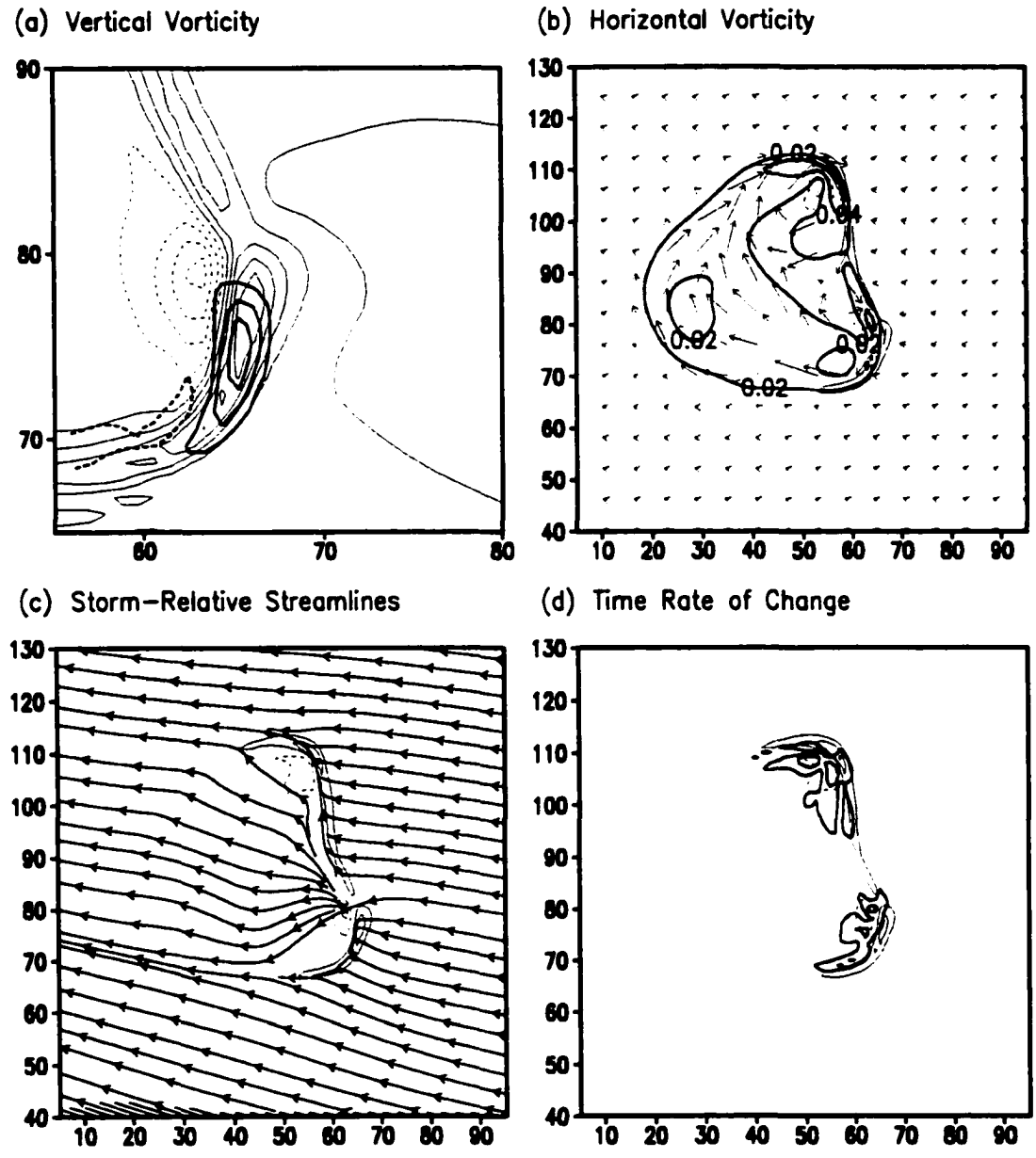


**Figure 4.37: Same as Figure 4.36 but for the 2cm case.**

updraft; however, as the storm-relative flow in this region is away from the updraft, its impact on the updraft is limited.

The magnitude of the contribution of the stretching, tilting, baroclinic and turbulent terms to the horizontal vorticity tendency equation is shown for the 3mm and

2cm runs in Figure 4.38 and Figure 4.39, respectively. As the fields shown are vector magnitudes, they give no indication as to whether they are increasing or decreasing the horizontal vorticity. However, the relative magnitudes of each contributing term can still be compared. In the 3mm case, the stretching term is the greatest of all four terms, and reaches its maximum within the region of the low-level updraft (Figure 4.38). It is likely to decrease the horizontal vorticity in this region, as the air is converging within the updraft. The magnitude of the stretching contribution is also the dominant contributor in the source region to the north of the updraft. In this region, there is acceleration of air away from the downdraft, and the resultant divergence will, in all likelihood, enhance the horizontal vorticity in this region. The tilting term also contributes to the horizontal vorticity and is greatest in the region of the gust front, where the ambient airflow is forced upward over the cold pool boundary, and in the region of the updraft, where horizontal gradients in the vertical velocity are large. The baroclinic contribution is greatest to the south of the updraft; however, it also contributes to the changes in horizontal vorticity along the forward flank gust front, and along the boundary of the RFD to the north of the updraft (Figure 4.38c). It is not surprising that the solenoid term is greatest along the gust front and edge of the RFD, as these are regions of strong temperature gradients. It appears, that the horizontal vorticity generated baroclinically in the regions of the downdraft, is then stretched by the acceleration of the air away from the downdraft. The turbulence term acts to dissipate horizontal vorticity in the inflow regions.

In the 2cm case, the tilting contribution is greater in magnitude than the stretching term (Figure 4.39). Baroclinic generation of horizontal vorticity is also found to the north and south of the updraft in the 2cm run, but is not as strong as that in the 3mm case. This is due to the greater horizontal temperature gradients associated with the stronger cold pool in the 3mm case. All of the contribution terms in the 2cm case are smaller than their respective counterparts in the 3mm case at this stage.

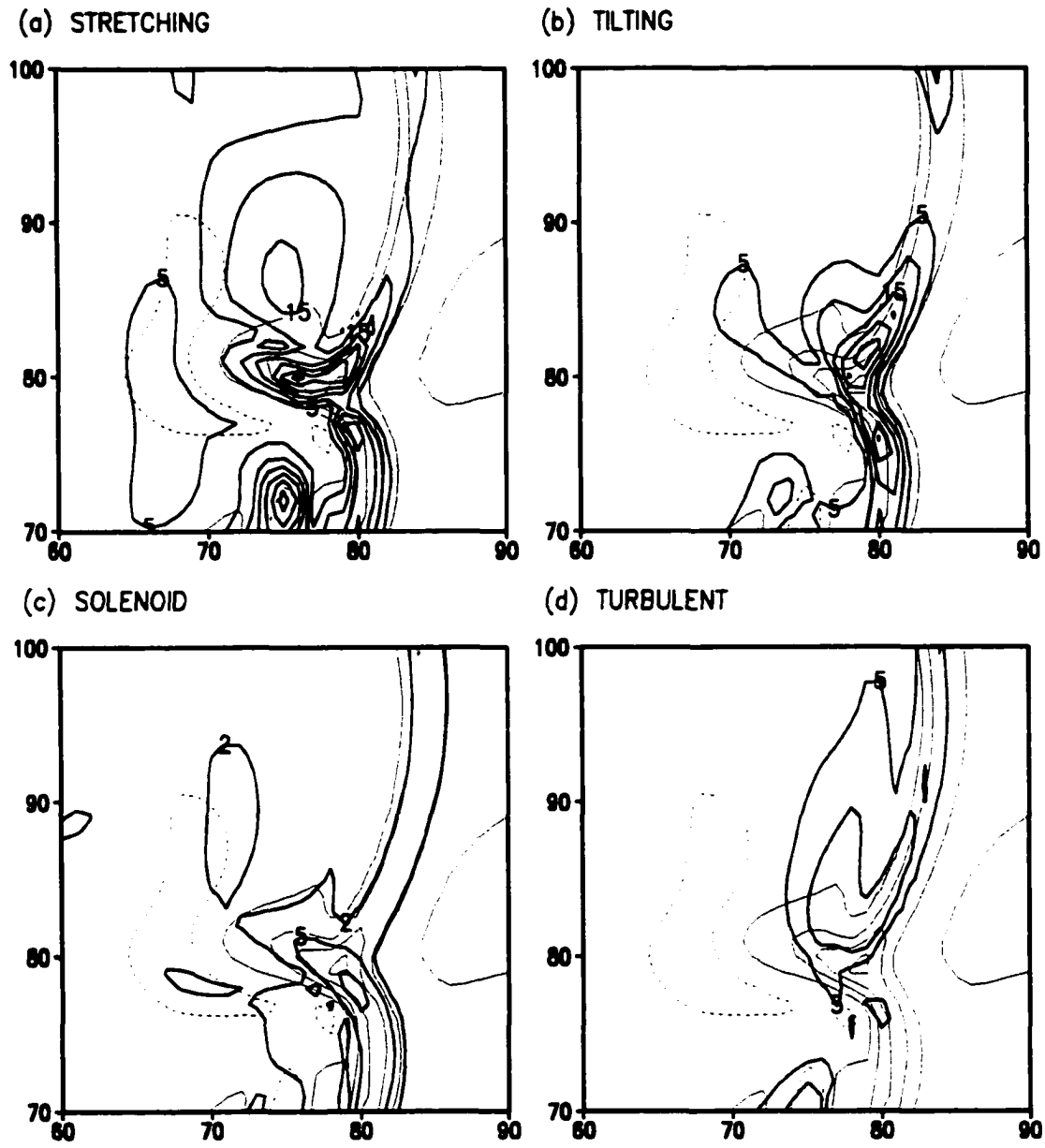


**Figure 4.38: Magnitude of the terms in the horizontal vorticity tendency equation ($D\omega_H/Dt$) for the 3mm case at 150m AGL at 70 minutes. (a) Vertical velocity (thin lines, interval 1 $m.s^{-1}$) and the magnitude of the stretching term (thick lines, interval 5 $s^{-2}$), (b) vertical velocity (thin lines, interval 1 $m.s^{-1}$) and the magnitude of the tilting term (thick lines, interval 5 $s^{-2}$), (c) vertical velocity (thin lines, interval 1$m.s^{-1}$) and the magnitude of the solenoid term (thick lines, interval 5 $s^{-2}$, 2 $s^{-2}$ contour is shown), and (d) vertical velocity (thin lines, interval 1$m.s^{-1}$) and the magnitude of the turbulent forcing (thick lines, interval 5 $s^{-2}$). All the vorticity contribution terms are multiplied by 1e5.**

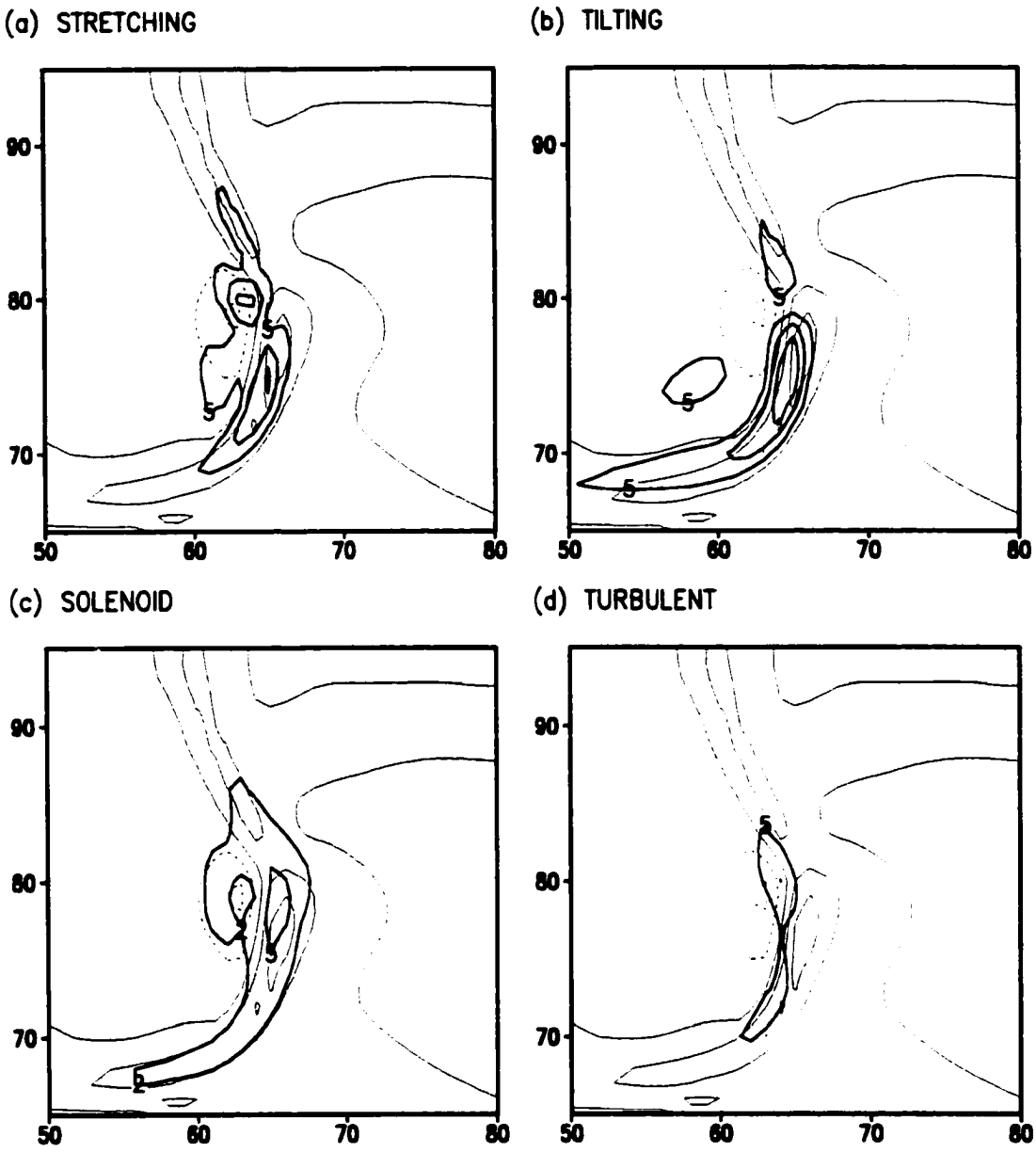


**Figure 4.39: Same as Figure 4.38 except for the 2cm case.**

The vertical vorticity tendency equation is given by:

$$\frac{D\zeta}{Dt} = \bar{\omega}_h \cdot \nabla w + \zeta \frac{\partial w}{\partial z} + TURB \qquad (4.6)$$

where $\bar{\omega}_h$ is the horizontal component of the vorticity vector, and TURB represents turbulent mixing and diffusion. All other symbols have been defined previously. Only the

stretching and tilting terms will be shown for the vertical vorticity tendency equation. There is no baroclinic generation term in the vertical vorticity tendency equation (Eq. 4.6), and the turbulent forcing while obvious, is much weaker than the stretching and tilting terms. In the 3mm case, the stretching term reaches its maximum value around 70 minutes (not shown), after which it decreases until around 100 minutes and then increases again. This closely follows the trend of the total vertical vorticity (see Figure 4.35), which indicates the dominance of the stretching term. This trend also, not surprisingly, closely follows the development of the low-level convergence of the horizontal winds in the region of the updraft. The stretching term is greatest near the surface and deceases with height in the lower levels (Figure 4.40a,c). Even though the stretching term decreases with height, it remains significantly greater than the tilting term, which increases with height in the lower levels (Figure 4.40b,d). The tilting term reaches it maximum value about 10 minutes earlier than the stretching term (not shown), thereby providing low-level vertical vorticity which then can be stretched. The stretching term within the region of the updraft is entirely positive, whereas the tilting term, which occurs on either side of the updraft in the regions of the greatest vertical velocity gradients, has both a positive and negative contribution (Figure 4.40). The negative tilting arises as a result of the horizontal vorticity vectors pointing away from the updraft in this region (Figure 4.36b). The contributions, both by stretching and tilting, are significantly greater in the 3mm case than in the 2cm run (Figure 4.41). In the 2cm run, the stretching term reaches its maximum much later, corresponding to the vertical vorticity maximum, and the tilting term is small and relatively steady. The contribution of the stretching term in the vertical vorticity tendency equation is therefore clearly dominant in both simulations, demonstrating the importance of the low-level horizontal convergence, and the magnitude of the vertical acceleration, in low-level mesocyclogenesis. However, even though the tilting term is smaller than the stretching term, it is necessary for the development of the mesocyclone, as without this term there would be no vertical vorticity to be stretched.

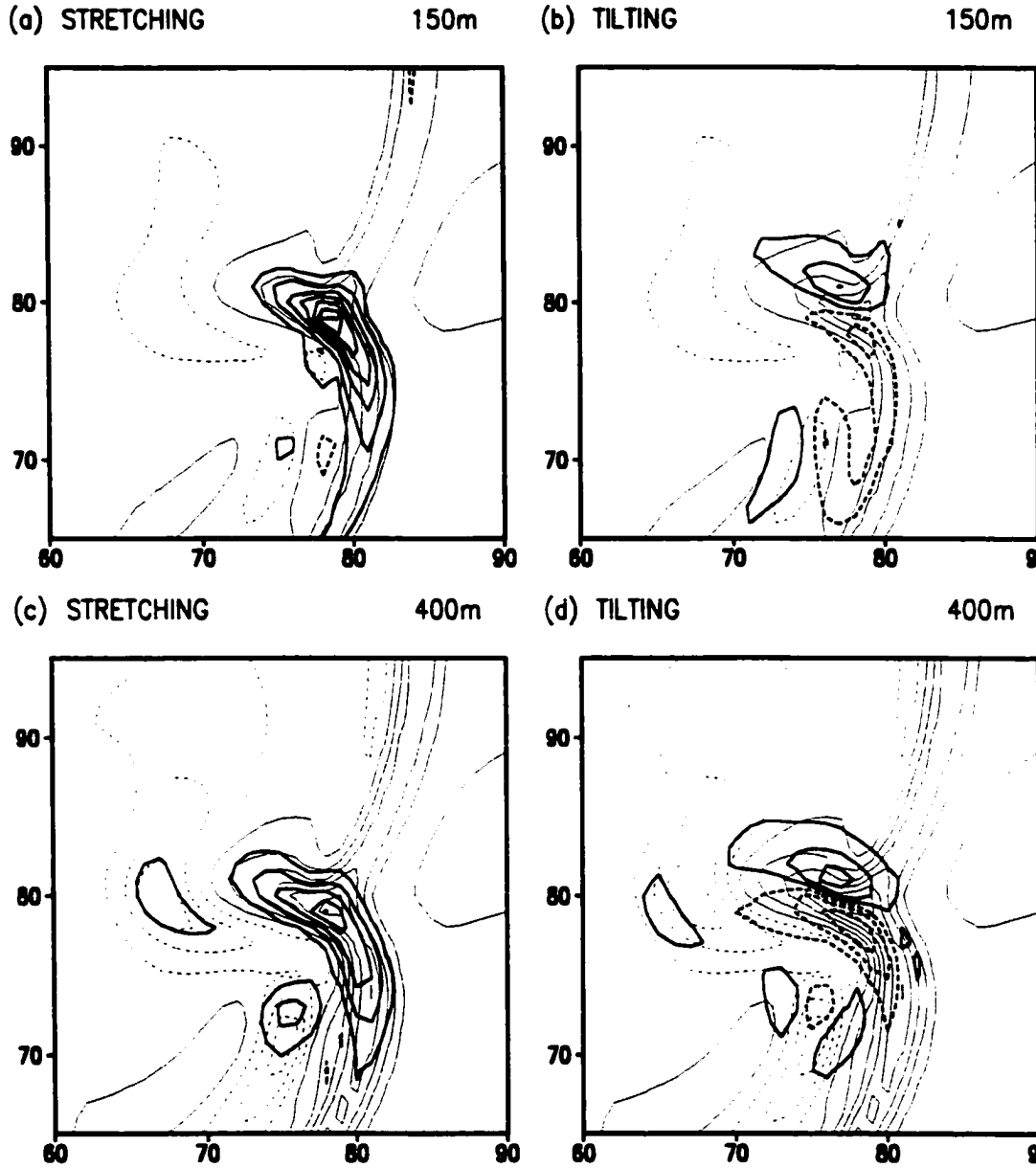


**Figure 4.40: Contribution made by the stretching and tilting terms in the vertical vorticity tendency equation ($D\zeta/Dt$) for the 3mm case at 70 minutes at 150 m (a,b), and 400m AGL (c,d). Contour interval is 1m.s$^{-1}$ for the vertical velocity (thin lines), and 3 s$^{-2}$ for the vorticity terms. All vorticity terms are multiplied by 1e5 and the zero line is not shown for these terms.**

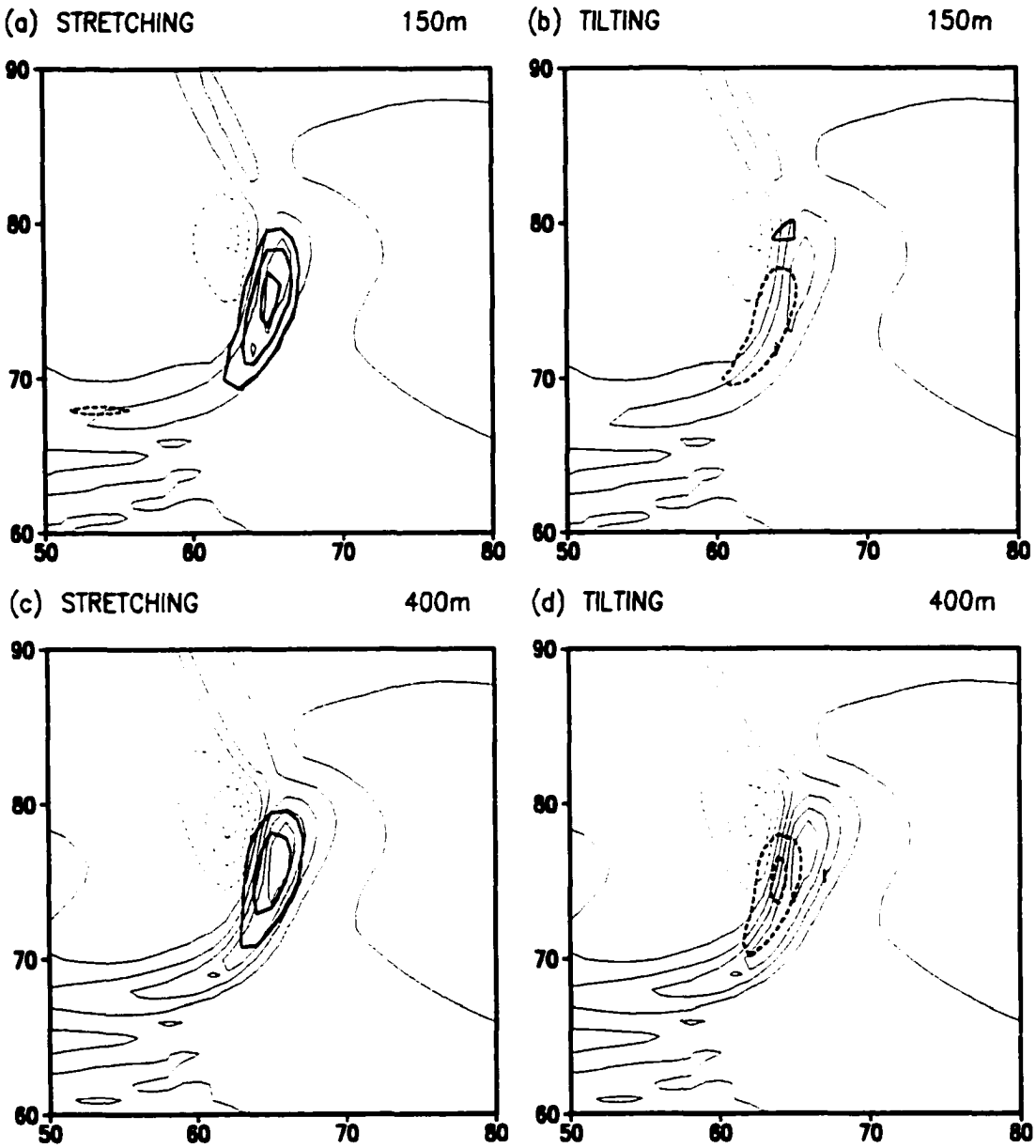


**Figure 4.41: Same as Figure 4.40 except for the 2cm case.**

The question that now needs addressing is why the stretching term in the 3mm case is so much greater than in the 2cm case? We saw earlier that the updraft occludes in the 3mm case but not in the 2cm case, and that this occlusion enhances the convergence of airflow into the lower regions of the updraft in the former simulation. However, what is the role of changing the mean hail diameter in this? As we have already seen, the

greater melting and evaporation rates in the 3mm case generate stronger downdrafts than in the 2cm run. Examining a vertical cross-section through the center of the RM downdraft for both cases at 70 minutes (Figure 4.42) reveals, that the 3mm downdraft maximum is more than twice the strength of the downdraft maximum in the 2cm case. The deceleration rates of the downdraft, as it approaches the surface, are therefore greater in the 3mm case. In order to force the downdrafts toward zero as they approach the surface, a region of high pressure needs to develop near the surface within the region of the downdraft. $\pi$' maxima within the region of the downdraft are evident in both cases (Figure 4.43 and Figure 4.44). The $\pi$' response in the 2cm case is however, much smaller, both in magnitude and in area (Figure 4.44), as the required downdraft deceleration is less. The region of high $\pi$' values in the 3mm case creates relatively strong, horizontal divergence away from the area of the downdraft, thereby enhancing the inflow of air into the updraft (Figure 4.43). In the 2cm case, the eastward outflow from the downdraft region is weaker than the inflow of ambient air, as the $\pi$' high is relatively weak. As a result, little, if any, downdraft air converges in the updraft. The enhanced convergence of low-level air into the updraft in the 3mm case, results in the significantly stronger stretching term in the vertical vorticity tendency equation, compared with that in the 2cm simulation. The rapid divergence of air away from the $\pi$' high in the 3mm case, also appears to enhance the stretching of horizontal vorticity in this region.

These simulations reveal that horizontal vorticity is generated baroclinically in the source regions to the north of the updraft, in both the 3mm and 2cm cases, being stronger in the 3mm case due to greater temperature gradients along the edge of the cold pool. However, it appears that the stretching contributions in the horizontal vorticity equation are greater in magnitude. These findings are in agreement with the recent results of Adlerman et al. (1999), in which stretching of the horizontal vorticity was also found to be predominant. The stretching contributions are also dominant in the vertical vorticity tendency equation, both in the 3mm and 2cm cases. Tilting is, however, still necessary to

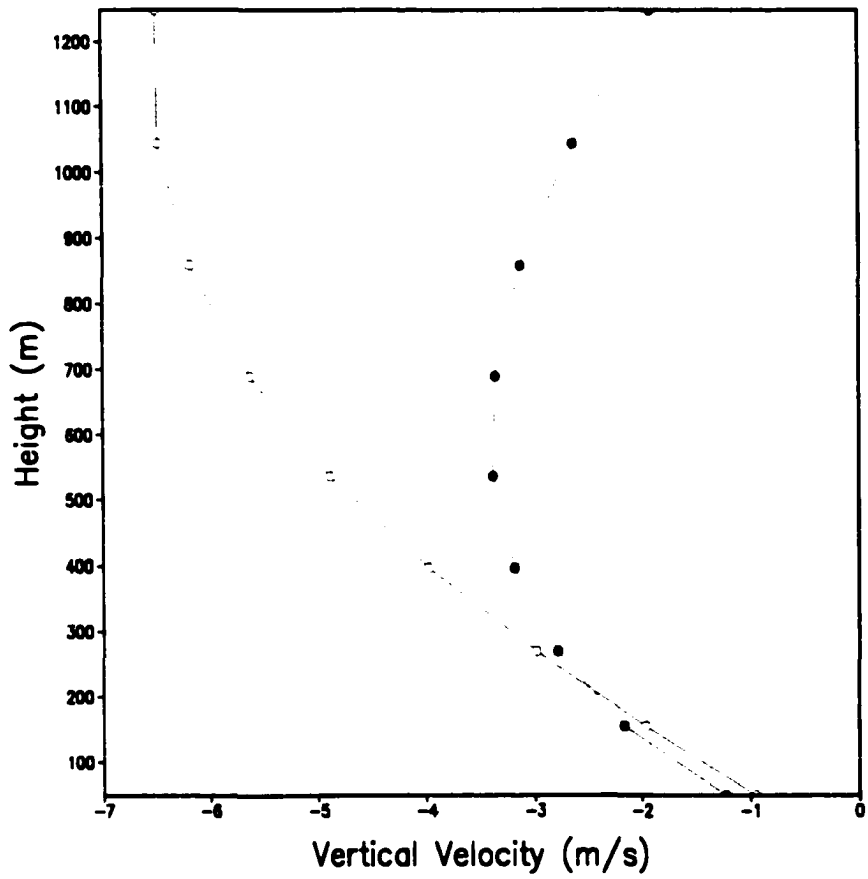


**Figure 4.42: Vertical velocity ($m.s^{-1}$) field within the center of the RM downdraft as a function of height at 70 minutes for the 3mm (open circles) and 2cm (closed circles) simulations.**

provide the initial vertical vorticity to stretch. Whether it is tilting by the updraft alone (Rotunno and Klemp, 1985), or tilting by both the updraft and downdraft (Davies-Jones and Brooks, 1993), that is important in the generation of vertical vorticity at the surface, cannot be determined with the grid resolutions used here.

Finally, the decrease in low-level vertical vorticity with an increase in the mean hail diameter may explain why High Plains thunderstorms often produce large quantities of hail but are not frequent tornado producers. It may also help explain the failure of the Hays storm to produce a tornado in spite of appearing so similar to the Garden City storm that did produce a tornado (Wakimoto and Cai, 2000). The Hays storm produced softball size hail. Also, a tornado formed following the cessation of cloud seeding to reduce the

hail size, recently in Alberta, Canada (T. Krauss, pers. comm.), implying that the reduced hail size could have produced the tornado.

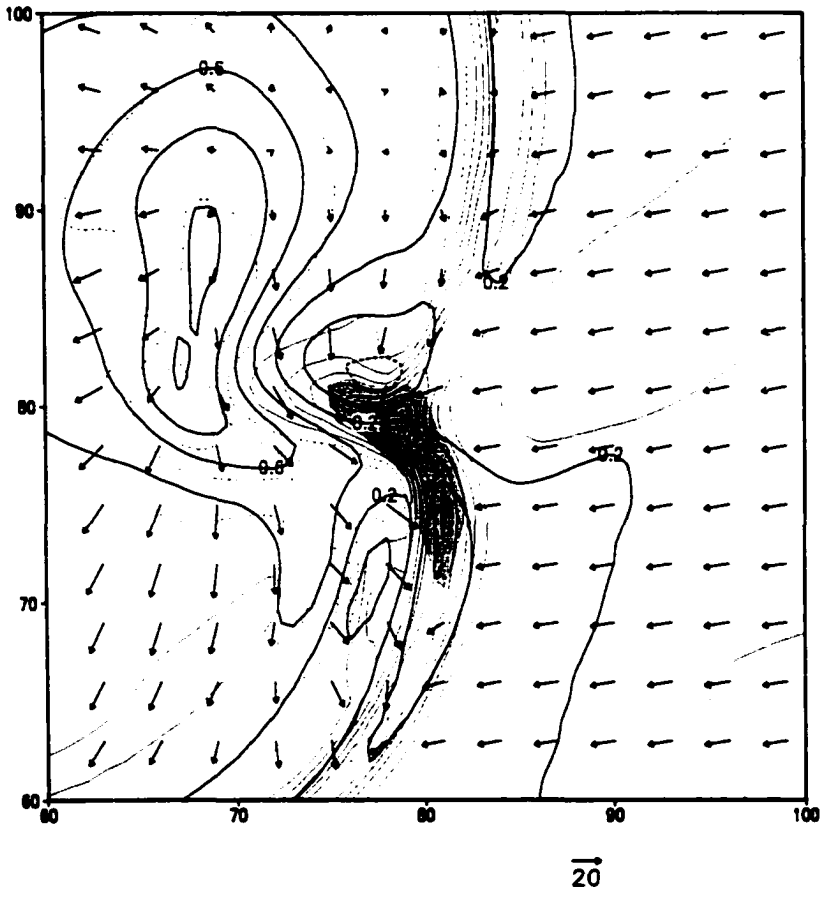


**Figure 4.43: Vertical velocity (thin lines, interval 0.5 m.s$^{-1}$), π' (thick lines, interval 0.2), and storm-relative wind vectors for the 3mm case at 150m AGL at 70 minutes. The shaded region represents the region in which the stretching term*1e5 in the vertical vorticity equation is greater than 3 s$^{-2}$.**

## 4.9 Storm Type

Many of the features of the 3mm RM storm are characteristic of the typical CL-type supercell (Browning, 1964; Lemon and Doswell, 1979). These include moderate amounts of precipitation at the surface, only a little precipitation within the mesocyclone, a hook in the condensate field, what would be a hook echo in the radar output, a BWER,

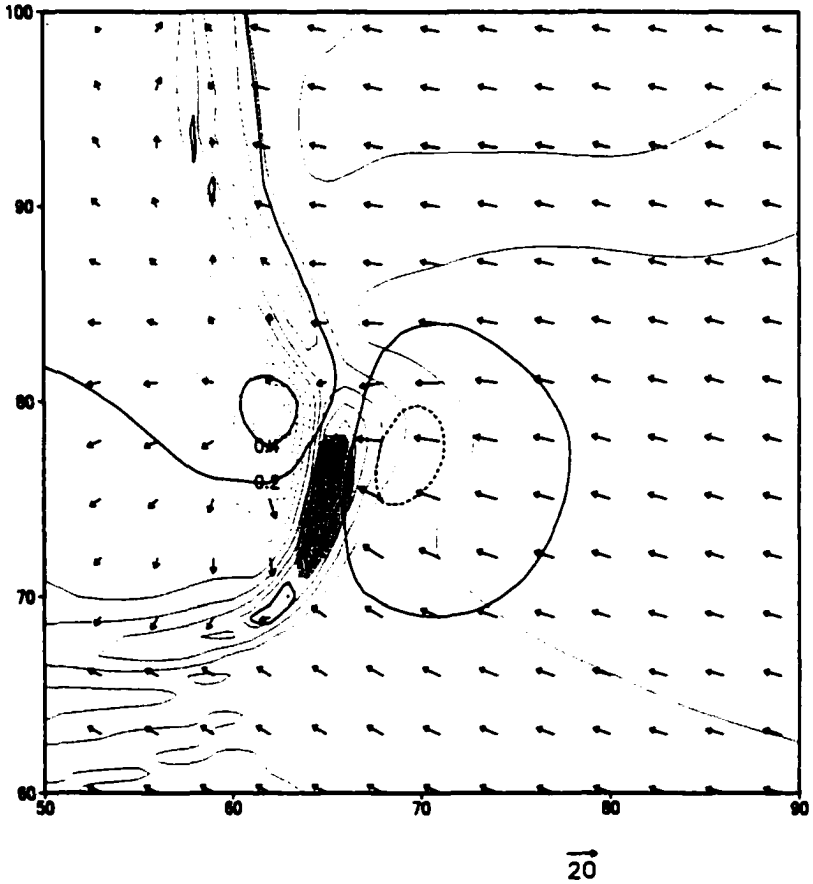


**Figure 4.44: Same as Figure 4.43 except for the 2cm case.**

and the strongest low-level vertical vorticity for the cases presented here, which is in agreement with the high frequency of tornadoes produced by CL supercells (Figure 4.45). The 2cm RM features are more in keeping with the characteristics of an HP type supercell (Doswell et al., 1990; Moller et al., 1994). These include relatively heavy precipitation at the ground, substantial precipitation near and within the mesocyclone, an almost indistinguishable hook echo, and the weakest low-level vertical vorticity of these mean hail diameter sensitivity tests, which supports the observational evidence that tornadoes produced by HP supercells are not as strong, frequent or violent as those in CL supercells (Figure 4.46). It appears that the type of supercell that develops may be influenced by the precipitation characteristics of the storm, in particular the hail size.

(a)

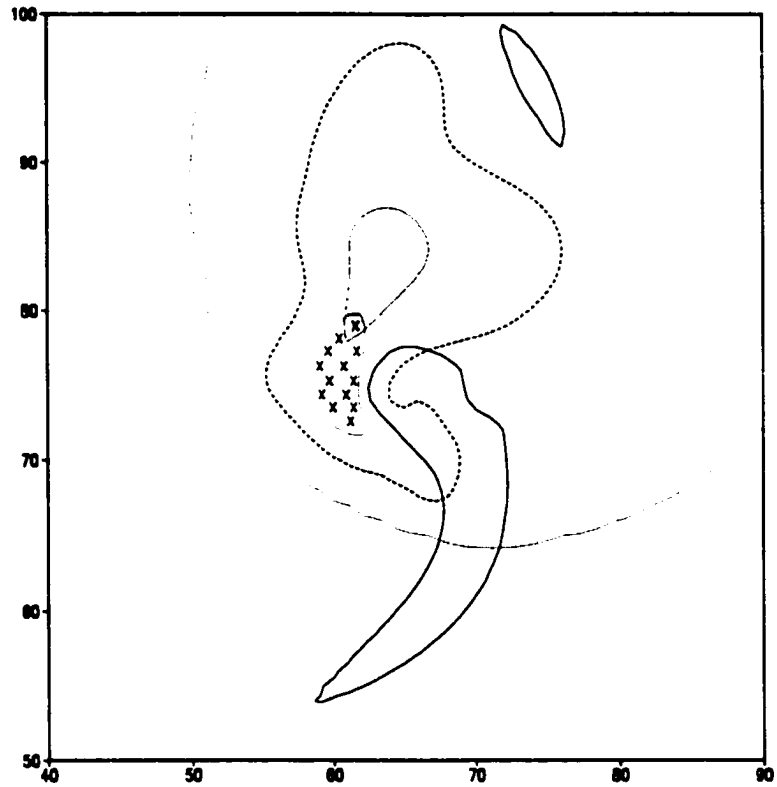


(b)

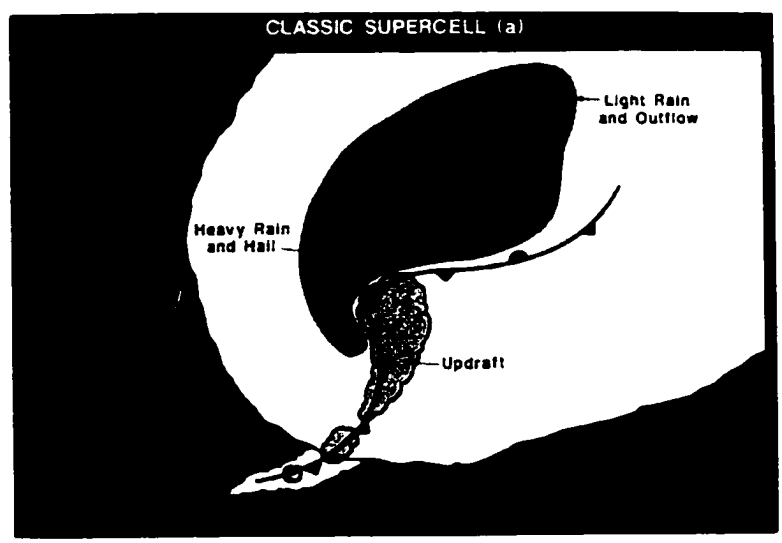


**Figure 4.45: (a) Simulated classic supercell (3mm simulation) showing the updraft (thick line), heavy hail (shaded region), heavy rain ('x' region), area of light rain (within thick dashed line), and anvil (thin line), (b) Observed classic supercell features shown by a plan view of the precipitation (stippling), surface outflow boundaries (frontal symbols), updraft maxima (scalloped line) and cloud boundaries (also scalloped) (after Doswell and Burgess, 1993).**

(a)

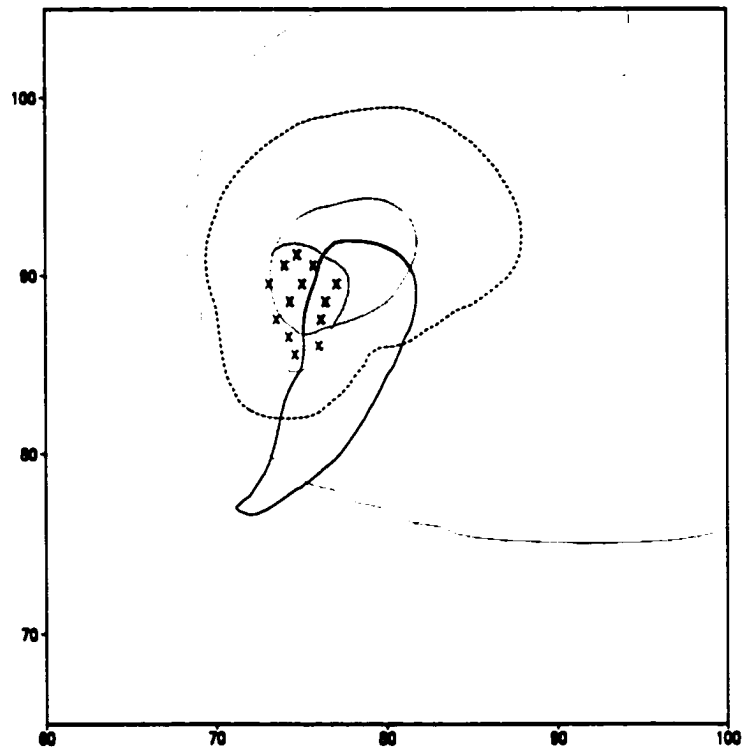


(b)

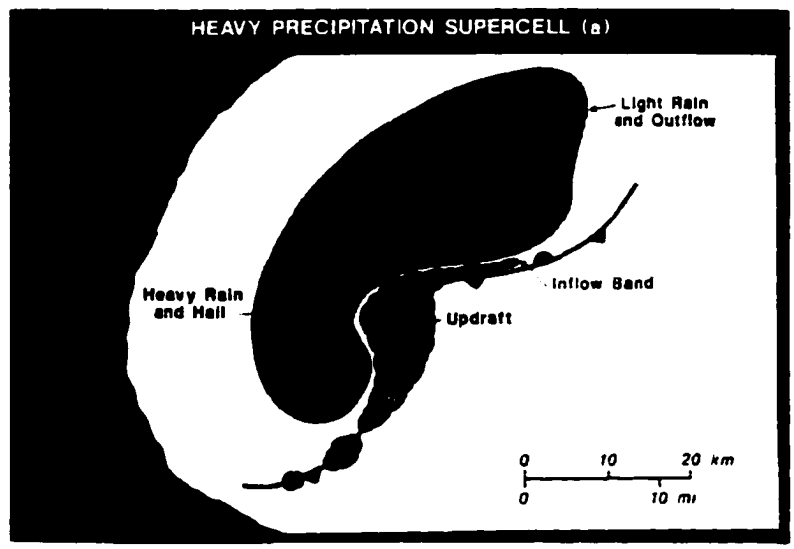


**Figure 4.46: (a) Simulated high-precipitation supercell (2cm simulation) showing the updraft (thick line), heavy hail (shaded region), heavy rain ('x' region), area of light rain (within thick dashed line), and anvil (thin line), (b) Observed high-precipitation supercell features shown by a plan view of the precipitation (stippling), surface outflow boundaries (frontal symbols), updraft maxima (scalloped line) and cloud boundaries (also scalloped) (after Doswell and Burgess, 1993).**

That hail size may be important in determining the type of supercell that is produced is in agreement, to some extent, with the findings of both Brooks et al. (1994b) and Rasmussen and Straka (1998). In both papers, the impact of wind strength and wind shear at different vertical levels on the distribution and amount of precipitation that is produced is highlighted. In the simulations presented here, the transportability and precipitation amounts are dictated by hail size, rather than by the strength of the wind (the hodographs are identical). In the study by Rasmussen and Straka they found, as we saw in Chapter 2, that LP supercells were associated with veering upper level winds, HP supercells were primarily linked with veering upper levels winds, and CL supercells fell in between these two regimes. The upper level winds were found to determine how close the hail falls to the updraft, and hence the probability of the re-ingestion of hydrometeors. In this simulation, the hail certainly falls close to the updraft in the 2cm "HP" supercell, and falls further away from the updraft in the 3mm "CL" supercell.

The 2cm case can in some ways be compared with the weak storm-relative wind case of Brooks et al. (1994b) in terms of precipitation transportability. While the precipitation does fall close to the updraft in 2cm case, and the gust front does propagate with the storm, the mesocyclone forms more slowly than that in the 3mm case, and the generation of low-level horizontal vorticity appears to be dominated by stretching rather than by baroclinic processes as suggested by Brooks et al. These differences may be attributable to the fact that Brooks et al. did not include ice processes, which affect the low-level thermodynamic structure through differences in melting and evaporation rates between liquid water and ice, and which also affects the distribution of precipitation through the greater range of fall velocities associated with ice. Nevertheless, both the simulations conducted by Brooks et al. and those shown here demonstrate the sensitivity of storm dynamics to the distribution of precipitation.

## 4.10 Summary

It is clear, from the results presented above, that varying the mean hail diameter from 3mm to 2cm can have numerous significant influences on the structure, dynamics and precipitation distribution of simulated supercell storms. These impacts are now summarized.

- As the mean hail diameter is increased, the longevity and steady-state nature of the LM and RM storms are increased.

- As the mean hail diameter decreases, the speed at which the RM moves increases, and the storm moves further to the right of the mean shear vector.

- The low-level downdrafts are stronger in the small hail cases as a result of greater melting and evaporation rates due to the larger surface area-to-volume ratios and longer residence times.

- The cold pools are significantly colder, deeper and faster-moving in the small hail cases due to greater melting and evaporation rates.

- The stronger downdrafts in the small hail cases produce stronger low-level divergence, greater convergence of airflow into the lower region of the updraft, and stronger updrafts throughout the storm.

- As a result of the development of a strong RFD, an occlusion of the low-level updraft occurs in the smaller hail cases. This process does not occur in the larger hail cases due to the weaker RFD and reduced low-level vertical vorticity.

- The updraft maxima, potential temperature maxima and the hail maxima curves all mirror one another closely. This demonstrates a positive thermodynamic feedback cycle, in which greater potential temperatures result in stronger updrafts, which then

produce more hail. The production of more hail has two effects. In the first, latent heat is released and this enhances the potential temperature. However, the latent heat release associated with the formation of pristine ice and vapor deposition on cloud water and smaller ice particles has a much greater impact. In the second effect, greater hail production means more melting and evaporative cooling, stronger downdrafts, stronger convergence into the updraft and hence stronger updrafts. The first effect is therefore a direct thermodynamic effect, whereas the second effect is an indirect thermodynamic effect.

- As the mean hail diameter decreases, so the low-level vertical vorticity increases. This is primarily due to the differences in the stretching term contributions between the simulations. The stretching term is greater in the 3mm case, due to the stronger convergence of air into the updraft at lower levels.

- As the mean hail diameter decreases, less hail reaches the ground because of its inability to withstand melting. The magnitude of the precipitation maxima is greatest in the larger hail cases, however, the precipitation is distributed over a much greater area in the smaller hail cases.

- As the mean hail diameter decreases, hail is distributed further away from the updraft, the downdrafts cover a greater area, and the hail maxima occur at higher levels.

- A co-located updraft and mesocyclone, a flow structure similar to that of Browning's (1964), a downshear and upshear anvil, and an overshooting top are evident in all cases. The hook echo, BWER, and RFD are significantly better developed in the smaller hail cases. The 3mm RM resembles a CL-type supercell, whereas the 2cm RM has many HP supercell characteristics.

- The results demonstrate that the precipitation characteristics of the storm may determine the type of supercell that develops. This adds another dimension to the

generally accepted idea that it is the type of supercell that determines the storm's precipitation characteristics.

- There appears to be a critical mean hail diameter that separates two distinct regimes in the simulated storm behavior. It is therefore important to assign an appropriate value to the mean hail diameter, as a "wrong" setting could significantly alter the final model solution. Aspects like the surface area-to-volume ratio, the relative ease of formation of smaller hailstones, and the terminal velocity may determine this critical diameter. Determining suitable values for the mean hail diameter is not, however, an easy task without in situ cloud data.

- These results demonstrate that the dynamics and precipitation characteristics of simulated supercell storms are very sensitive to small changes in the microphysics. Significant differences were produced in these simulations by changing only a single parameter. The processes simulated here suggest that actual storms are also likely to be sensitive to their microphysical properties.

# 5

# The Longevity of the Left-Moving Storms

## 5.1 Introduction

Observations indicate that right-moving storms (RM) occur more frequently and are better developed than left-moving storms (LM), but that LM storms are occasionally long-lived (Wilhelmson and Klemp, 1981; Davies-Jones, 1985). RM (LM) storms tend to be favored when the environmental wind shear vector veers (backs) with height (Browning, 1968; Fankhauser, 1971; Klemp and Wilhelmson, 1978b; Rotunno and Klemp, 1982). Several theories for the RM (LM) dominance under veering (backing) conditions have been proposed. These were discussed in detail in Chapter 2 and are summarized here.

Observations and model output have shown that as the hodograph veers with height, the mid-level inflow into the downdraft of the RM (LM) storm is strengthened (weakened), thereby enhancing (decreasing) the downdraft, the low-level outflow, and the development of the gust front. This in turn increases (decreases) the convergence along the gust front and hence storm longevity (Browning, 1968; Fankhauser, 1971; Klemp and Wilhelmson, 1978b).

Numerical simulations have demonstrated that the mid-level pressure field is important both in the splitting of the initial updraft, and in the subsequent development of the RM and LM storms (Schlesinger, 1980; Rotunno and Klemp, 1982). Using linear theory, Rotunno and Klemp (1982) showed that the perturbation pressure is proportional to $\frac{d\bar{V}_h}{dz} \cdot \nabla_h w'$ where $\frac{d\bar{V}_h}{dz}$ is the vertical shear of the horizontal wind vector, and $\nabla_h w'$ is the horizontal gradient of the vertical velocity. From this relation, it is apparent that a negative pressure gradient develops across the updraft in the direction of the shear vector. As the shear vector veers (backs) with height, vertical pressure gradients develop that favor lifting on the right (left), and that suppress lifting on the left (right) side of the initial updraft. They concluded that the linear contributions to the perturbation pressure field determine the LM/RM bias.

Weisman and Klemp (1984) suggested that dynamically distinct processes control the low-level convergence feeding the updrafts on the flanks of the initial storm. Using a veering hodograph they found that the left flank updrafts were predominantly forced by low-level convergence along the surface gust front, while the right flank updrafts were controlled by the development of a dynamically-induced vertical pressure gradient force. Grasso (2000) recently simulated a long-lived LM storm under veering hodograph conditions by suppressing precipitation processes. He found that when precipitation processes were included, negatively buoyant forcing dominated the total forcing of the LM updraft, resulting in its early dissipation. Grasso's results suggest, like those of Weisman and Klemp, that there may be processes apart from the linear pressure effect that can affect the longevity of the LM storm.

It was shown in Chapter 3 that the hodograph used in the 3mm and 2cm simulations veers with height below 2 km AGL (see Fig. 3.1). Using linear theory, one would expect the RM storm to be favored and the LM updraft to dissipate soon after splitting. As we saw in Chapter 4, the results of the 3mm simulation appear to concur with the predictions of linear theory in that the RM updraft is favored, and the LM storm

dissipates after about 45 minutes. However, in the 2cm run, while the RM is the stronger storm, the LM is a steady storm that exists for the entire simulation. The goal of the research presented in this chapter is to determine the processes governing the longevity of the LM storm as the mean hail diameter is increased. This work expands on that of Grasso (2000), in investigating the impact of precipitation on the longevity of the LM. However, instead of excluding the development of precipitation as Grasso did, the hail characteristics are simply altered in these simulations.

In this chapter, only the 3mm and 2cm cases presented in Chapter 4 will be contrasted in the interests of brevity. The 5mm and 1cm cases are transition cases, and the mechanisms presented are also applicable to these simulations. As discussed in Chapter 2, the thermodynamic sounding and hodograph used in these simulations are similar to those used by Grasso (2000). This facilitates comparisons with his work. Given the hodograph and sounding similarities, we should expect similarities between his "precipitation" simulation and the 3mm simulation presented here. Grasso presented his results at 1 and 2 km AGL. These levels will also be used here. The 2 km level is still within the region of hodograph veering, although the hodograph does start to back above this level; the 1 km level is representative of the forcing at the lower levels.

## 5.2 2 km AGL

### 5.2.1 *3mm Case*

Splitting of the original updraft and the formation of a LM and RM updraft are evident in the vertical velocity fields at 2 km AGL for the 3mm case (Figure 5.1). By 30 minutes, the LM and RM storms are already moving apart, to the left and right of the mean environmental wind respectively (Figure 5.1b). The LM updraft is relatively steady from 25 to 30 minutes (Figure 5.1a-b), after which it continues to weaken (Figure 5.1c-e). By 50 minutes the LM has completely dissipated (Figure 5.1f). The RM is stronger than

the LM for the entire simulation. The dominance of the RM and the weakening and rapid decay of the LM are in keeping with the predictions of linear theory for a veering hodograph.

The first term on the right hand side of the vertical equation of motion, Eq. (4.1), represents forcing due to the vertical gradients in $\pi'$, and shall be referred to as the $\pi'$ forcing term. The second term is the numerical buoyancy, and shall be referred to as the buoyant forcing term. The third term is the turbulent forcing term. Analysis of the three terms on the right hand side of Eq. (4.1) reveals that the vertical gradients in $\pi'$ and the numerical buoyancy are the dominant terms. The sum of these two terms, shall be referred to as the total forcing.

The total forcing within the LM continues to decrease after splitting until the dissipation of the LM (Figure 5.2), and mirrors, not surprisingly, the trends in vertical velocity. From 30 to 45 minutes, the region of total forcing moves from being completely within the LM updraft core at 30 minutes (Figure 5.2b), to being situated east of the updraft by 45 minutes (Figure 5.2e). Thus, even though the magnitude of the total forcing associated with the LM does not decrease between 35 and 40 minutes, the impact that the upward forcing has on the updraft is reduced by virtue of its position with respect to the updraft. The vertical velocity decreases significantly at this time in response to the reduced upward forcing. The total forcing of the LM storm is less than that of the RM throughout the simulation.

Examining the contribution of the vertical gradients in $\pi'$ to the total forcing in the 3mm case reveals that positive $\pi'$ forcing occurs on the right front side of the updraft and negative $\pi'$ forcing occurs on the left rear side of the updraft (with respect to storm motion) (Figure 5.3). This distribution in the vertical gradients of $\pi'$ is the result of the veering hodograph, which causes favorable (unfavorable) stacking of $\pi'$ on the right (left) side of the updraft (Rotunno and Klemp, 1982). The $\pi'$ forcing distribution is

instrumental in the movement of the updrafts. It is also evident that the positive π' forcing within the LM is significantly weaker than that in the RM (Figure 5.3), which is supported by the predictions of linear theory.

From 25 to 30 minutes, the positive π' forcing within the LM updraft remains relatively steady, while the negative forcing increases (Figure 5.3a-b). From 30 to 35 minutes, even though the positive π' forcing increases in magnitude, the impact of this forcing on the updraft actually decreases (Figure 5.3b-c). This, together with an increase in the negative π' forcing, causes a slight weakening of the updraft. From 35 to 40 minutes, the effect both the positive and negative π' forcing have on the updraft remains relatively steady, even though the updraft decreases both in strength and area during this time period. This suggests that other factors, apart from the π' forcing, may have an impact on the updraft at this stage. From 40 to 45 minutes, both the positive and negative π' forcing is reduced (Figure 5.3d-e), and by 50 minutes they have dissipated.

The buoyant contribution to the total forcing in the 3mm case shows positive forcing within the left and right sides of the initial updraft, and a region of negative buoyancy between what are to become the LM and RM storms (Figure 5.4a). The region of negative buoyancy appears to enhance the splitting process. The positive buoyant forcing within the LM remains relatively steady from 25 to 30 minutes (Figure 5.4a-b). From 30 to 35 minutes, the region of positive buoyancy is situated further to the west of the updraft, thereby reducing its impact on the updraft. The region of positive buoyancy is shifted even further to the west with respect to the updraft between 35 and 40 minutes, reducing the positive forcing within the center of the updraft by about 50% (Figure 5.4c-d). During this time period, the strength of the updraft also decreases significantly. Finally, from 40 to 50 minutes, both the positive and negative buoyant forcing continues to weaken, completely disappearing by 50 minutes (Figure 5.4e-f).

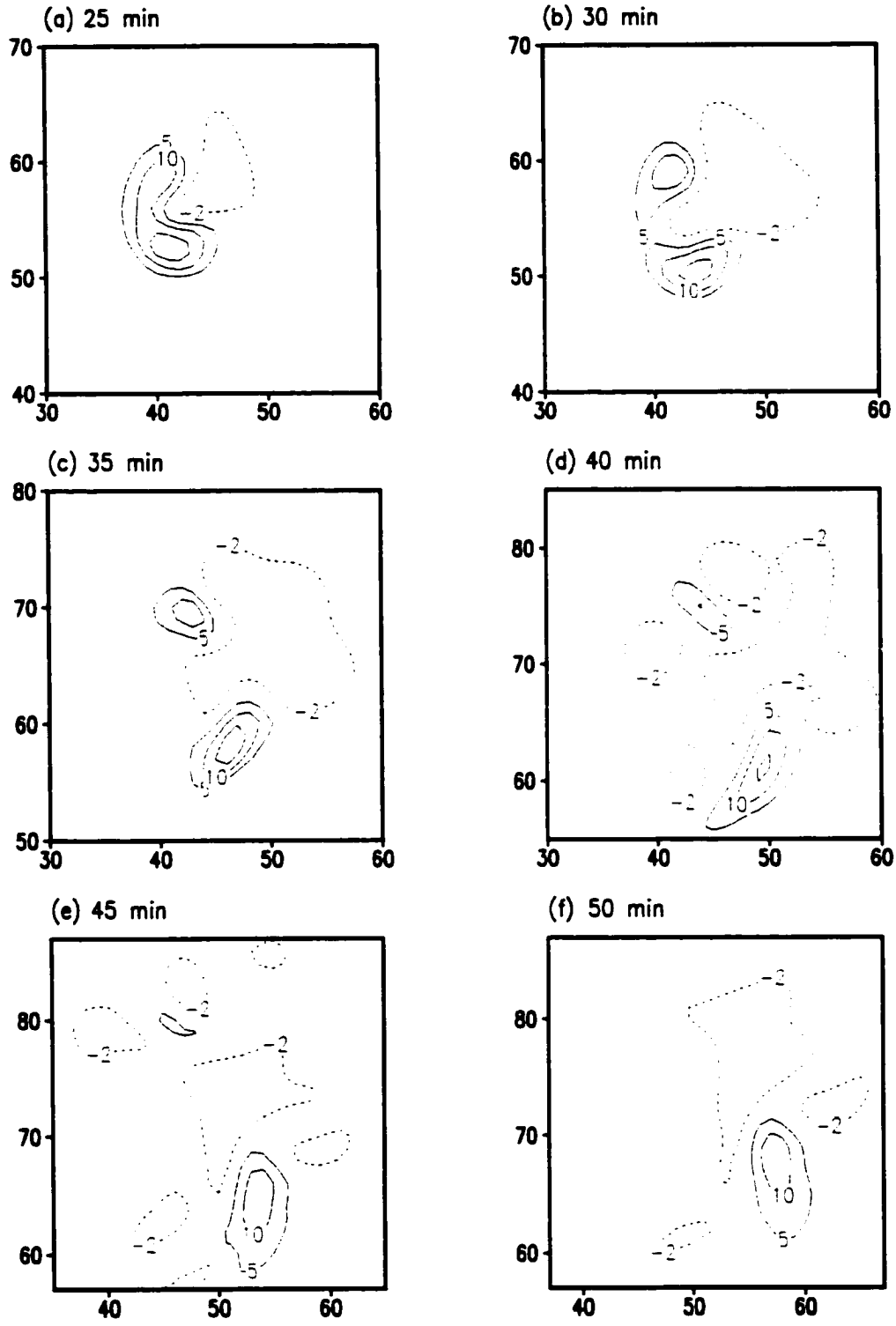


**Figure 5.1: Vertical velocity at ~2 km AGL for the 3mm case at (a) 25, (b) 30, (c) 35, (d) 40, (e) 45 and (f) 50 minutes. Contour interval is 5 m.s$^{-1}$ starting at 5m.s$^{-1}$ for the updraft. The –2 m.s$^{-1}$ isoline is also shown.**

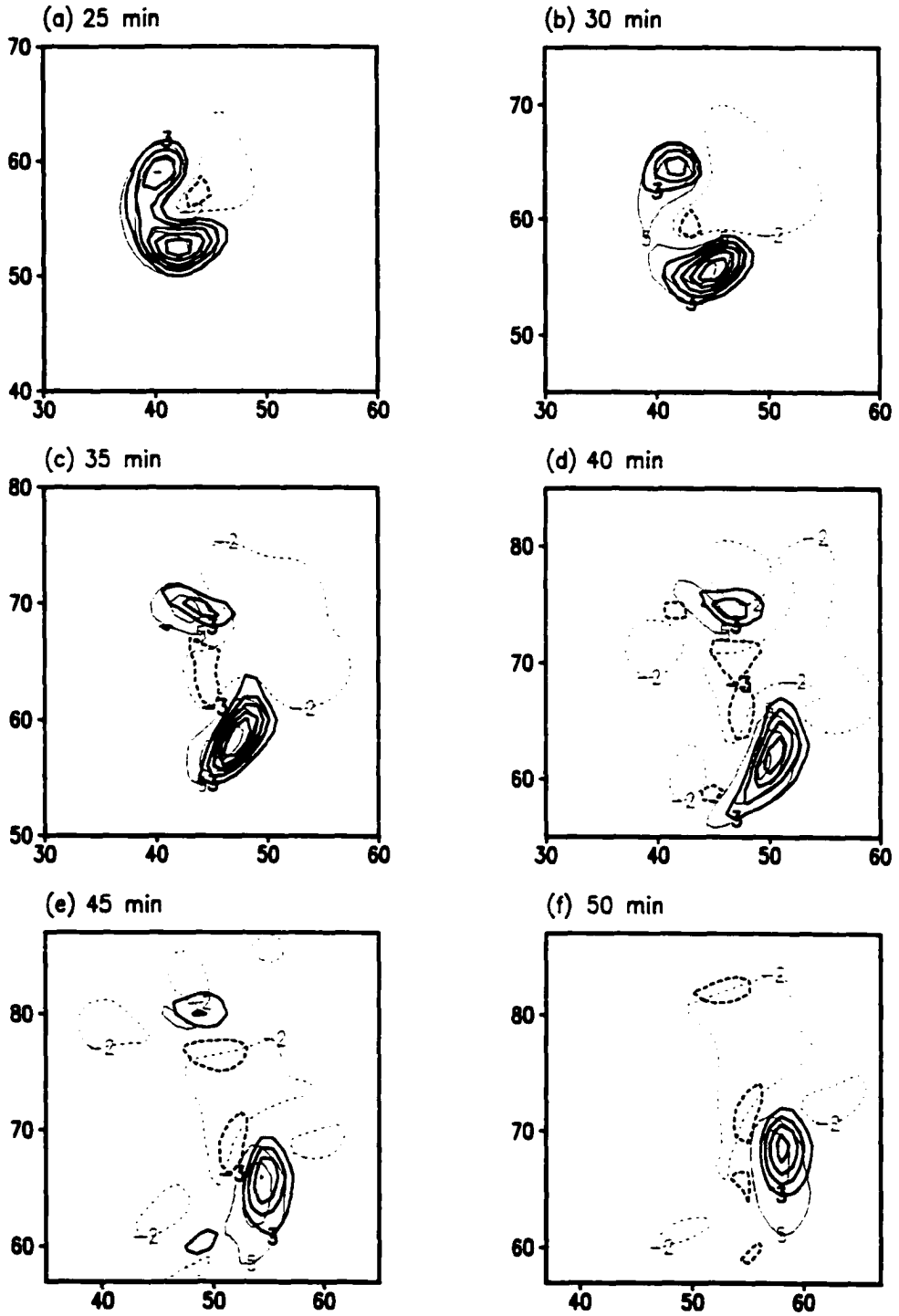


**Figure 5.2: Vertical velocity (thin lines) and the total forcing $-\theta_0 \partial\pi'/\partial z + g(\theta_v'/\theta_0 - r_c)$ (thick lines) at ~2 km AGL for the 3mm simulation at (a) 25, (b) 30, (c) 35, (d) 40, (e) 45 and (f) 50 minutes. Solid lines represent positive magnitudes while dashed lines represent negative values. The contour interval is 3m.s$^{-2}$ for the forcing term and 5m.s$^{-1}$ for the updrafts. The –2m.s$^{-1}$ isoline is also shown. Both zero isolines are omitted. Forcing is multiplied by 100.**

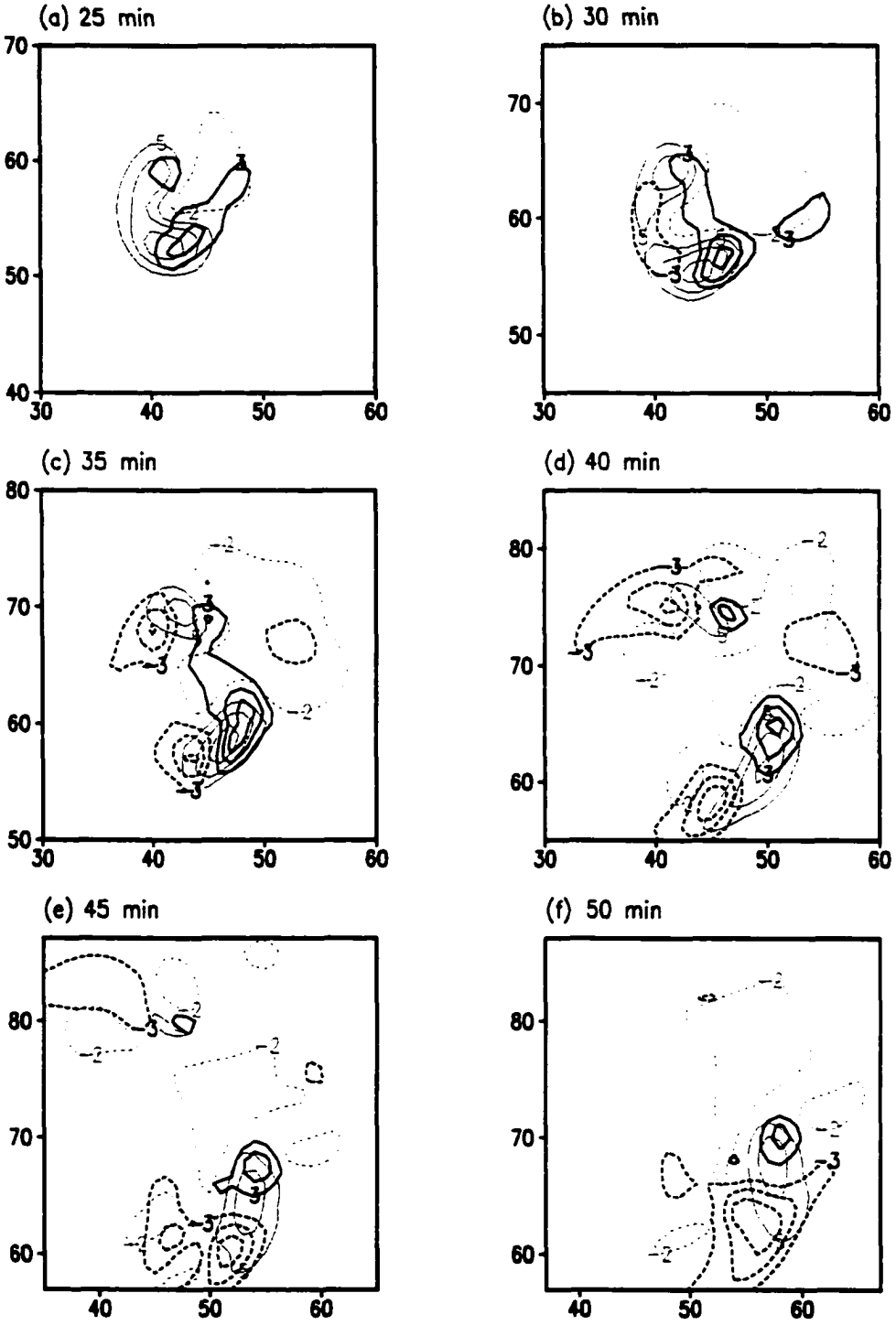


**Figure 5.3: Vertical velocity (thin lines) and $-\theta_0\ \partial\pi'/\partial z$ (thick lines) at ~2 km AGL for the 3mm simulation at (a) 25, (b) 30, (c) 35, (d) 40, (e) 45 and (f) 50 minutes. Solid lines represent positive magnitudes while dashed lines represent negative values. The contour interval is 3m.s$^{-2}$ for the forcing term and 5 m.s$^{-1}$ for the updrafts. The –2m.s$^{-1}$ isoline is also shown. Both zero isolines are omitted. Forcing is multiplied by 100.**

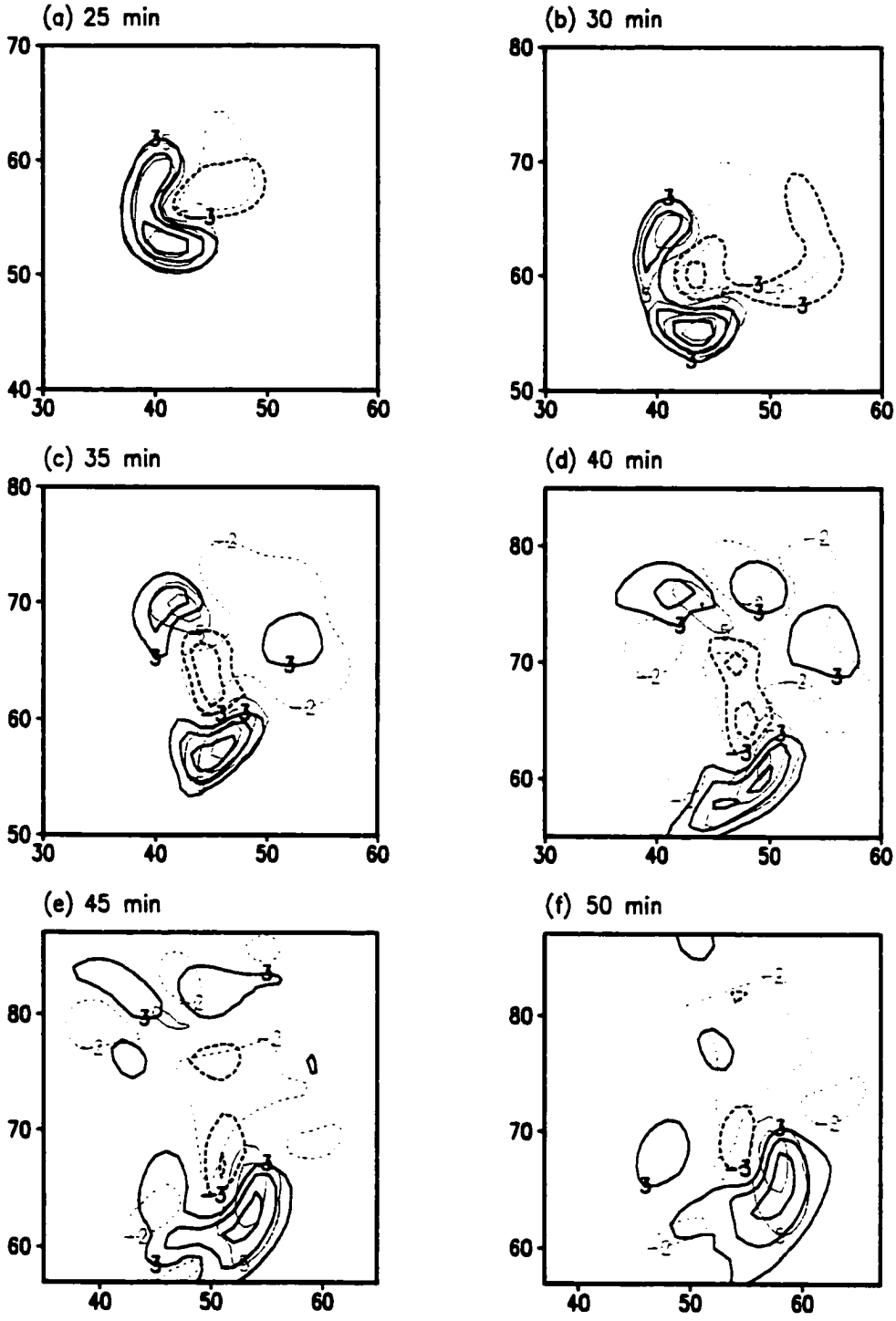


**Figure 5.4: Vertical velocity (thin lines) and $g(\theta_v'/\theta_0 - r_c)$ (thick lines) at ~2 km AGL for the 3mm simulation at (a) 25, (b) 30, (c) 35, (d) 40, (e) 45 and (f) 50 minutes. Solid lines represent positive magnitudes while dashed lines represent negative values. The contour interval is 3m.s$^{-2}$ for the forcing term and 5 m.s$^{-1}$ for the updrafts. The –2m.s$^{-1}$ isoline is also shown. Both zero isolines are omitted. Forcing is multiplied by 100.**

Comparing the contributions made by buoyancy and vertical gradients in π' to the total forcing, it is evident that the positive buoyant forcing associated with the LM is either equal to or greater, both in area and magnitude, than the π' forcing. Between 35 and 40 minutes, when the updraft starts to weaken rapidly, there is little change in the π' forcing of the updraft, whereas the positive buoyant forcing within the region of the LM updraft decreases by ~50%. The positive total forcing at 40 minutes is constituted primarily of forcing due to the vertical gradients in π', which seem insufficient in sustaining the updraft. It therefore appears that the reduction in positive buoyant forcing within the LM updraft contributed primarily to the dissipation of the LM, with the π' forcing playing a lesser role. A similar result was found by Grasso (2000) in his precipitation simulation.

### 5.2.2 *2cm Case*

Splitting of the original updraft in the 2cm case occurs slightly earlier than in the 3mm case (not shown). By 25 minutes, the original updraft splits into LM and RM updrafts that move to the left and right of the mean environmental wind vector, respectively (Figure 5.5a). The LM updraft increases in strength from 25 to 35 minutes (Figure 5.5a-c), decreases from 35 to 40 minutes (Figure 5.5c-d), and then remains relatively steady, decreasing only slightly between 40 to 50 minutes (Figure 5.5d-f). The LM in the 2cm case is therefore relatively steady and long-lived, unlike the LM in the 3mm case that has dissipated by 50 minutes. The RM is stronger than the LM for the entire simulation, both in the 3mm and 2cm cases, which is supported by linear theory. The trends in total forcing (Figure 5.6) coincide closely with the vertical velocity trends. This is no surprise. The total forcing of the RM is greater than that of the LM, as predicted by linear theory, and is similar to the 3mm case. However, the differences in magnitude between the total forcing of the LM and RM in the 2cm case are much less than those in the 3mm case.

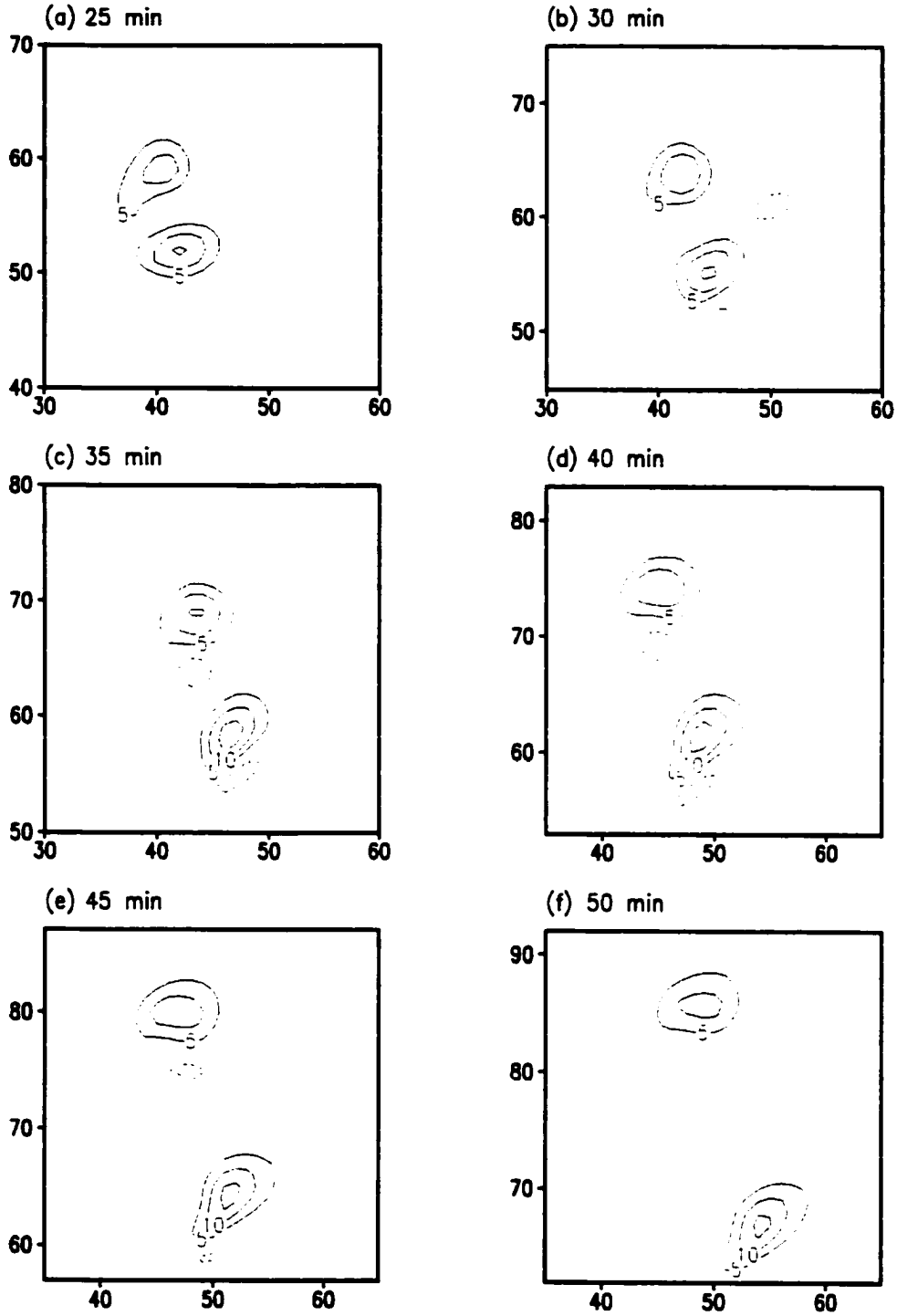


**Figure 5.5: Vertical velocity at ~2 km AGL for the 2cm case at (a) 25, (b) 30, (c) 35, (d) 40, (e) 45 and (f) 50 minutes. Contour interval is 5 m.s$^{-1}$ starting at 5m.s$^{-1}$ for the updraft. The –2 m.s$^{-1}$ isoline is also shown.**

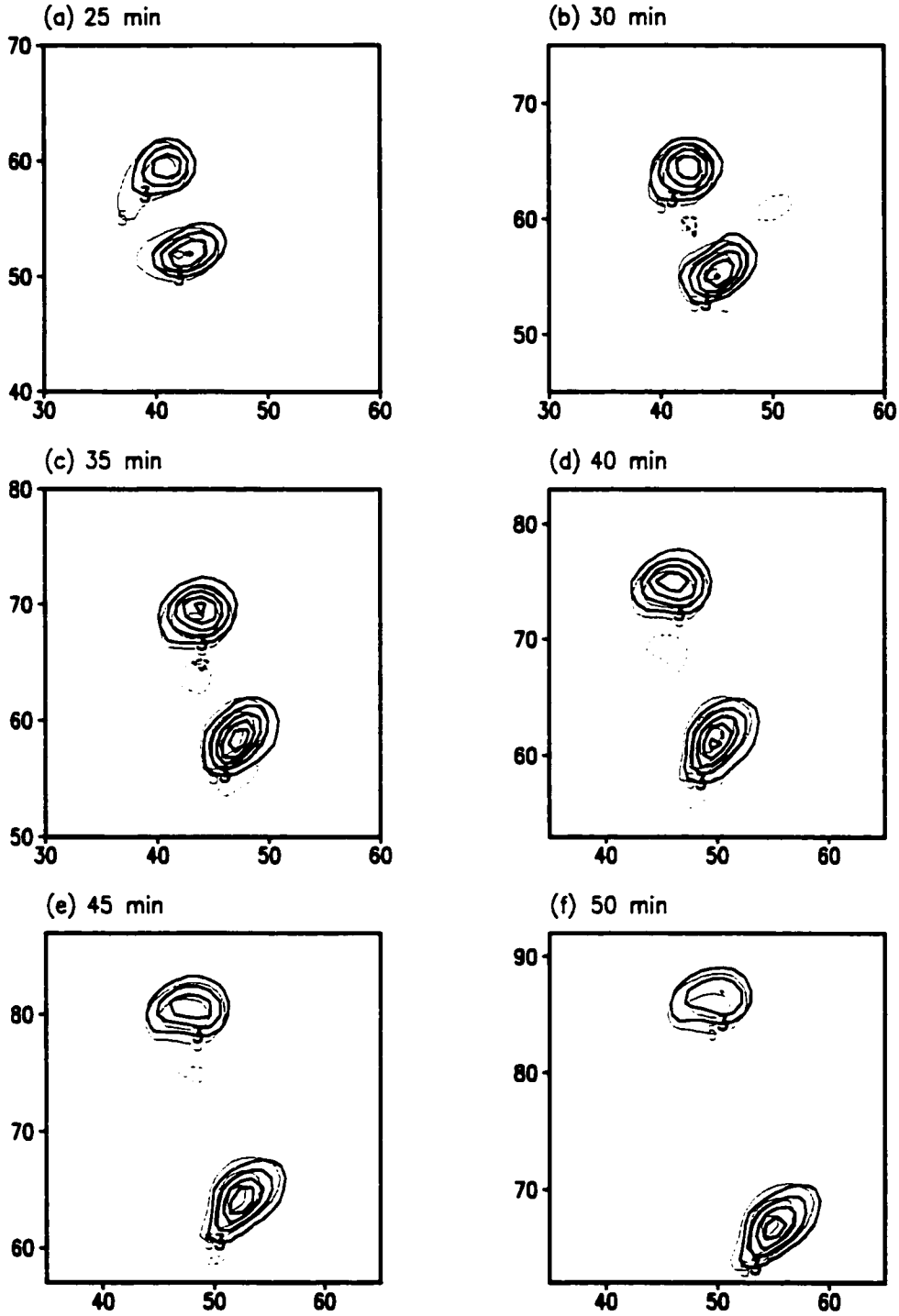


**Figure 5.6: Vertical velocity (thin lines) and the total forcing $-\theta_0 \partial\pi'/\partial z + g(\theta_v'/\theta_0 - r_c)$ (thick lines) at ~2 km AGL for the 2cm simulation at (a) 25, (b) 30, (c) 35, (d) 40, (e) 45 and (f) 50 minutes. Solid lines represent positive magnitudes while dashed lines represent negative values. The contour interval is 3m.s$^{-2}$ for the forcing term and 5m.s$^{-1}$ for the updrafts. The –2m.s$^{-1}$ isoline is also shown. Both zero isolines are omitted. Forcing is multiplied by 100.**

Examining the contribution made by the vertical gradients in $\pi'$ to the total forcing in the 2cm case reveals that the positive $\pi'$ forcing in the region of the LM increases from 25 to 35 minutes (Figure 5.7a-c), and then decreases steadily from 35 to 50 minutes (Figure 5.7c-f). The $\pi'$ forcing of the LM updraft at 50 minutes is about 30% of the $\pi'$ forcing at 35 minutes. Such a marked decrease is not observed in the vertical velocity fields (Figure 5.5c-f). The negative $\pi'$ forcing of the LM shows little change from 25 to 50 minutes, unlike that in the 3mm case. The positive $\pi'$ forcing associated with the 2cm LM storm is initially greater within the LM, however, from 30 minutes onwards, the RM $\pi'$ forcing is similar to or greater than that associated with the LM (Figure 5.7a-f).

Throughout the time period shown here, the positive buoyant forcing (Figure 5.8) of the LM updraft is greater than that due to the $\pi'$ forcing. The buoyant forcing, like the $\pi'$ forcing, decreases between 35 and 45 minutes, although not as rapidly (Figure 5.8c-e). However, from 45 to 50 minutes, while the $\pi'$ forcing decreases by about 50%, the buoyant forcing remains relatively steady (Figure 5.8e-f). As the LM updraft also remains relatively steady during this time, weakening only slightly, this suggests that the positive buoyant forcing is the dominant factor controlling the strength of the LM updraft. The importance of the positive buoyant forcing in the 2cm case is substantiated by the fact that the buoyant forcing is greater than the $\pi'$ forcing within the LM throughout the simulation, and by the similarities between the buoyant and total forcing fields between 45 and 50 minutes. The buoyant forcing, therefore, appears to be the primary factor controlling the longevity of the LM in both the 3mm and 2cm cases. However, in the 3mm case, it is the reduction in positive buoyancy that dissipates the updraft, whereas in the 2cm case, it is the constant positive buoyant forcing that maintains the updraft. The output from these two simulations will now be examined at the 1 km AGL to determine the predominant forcing in the lower levels.

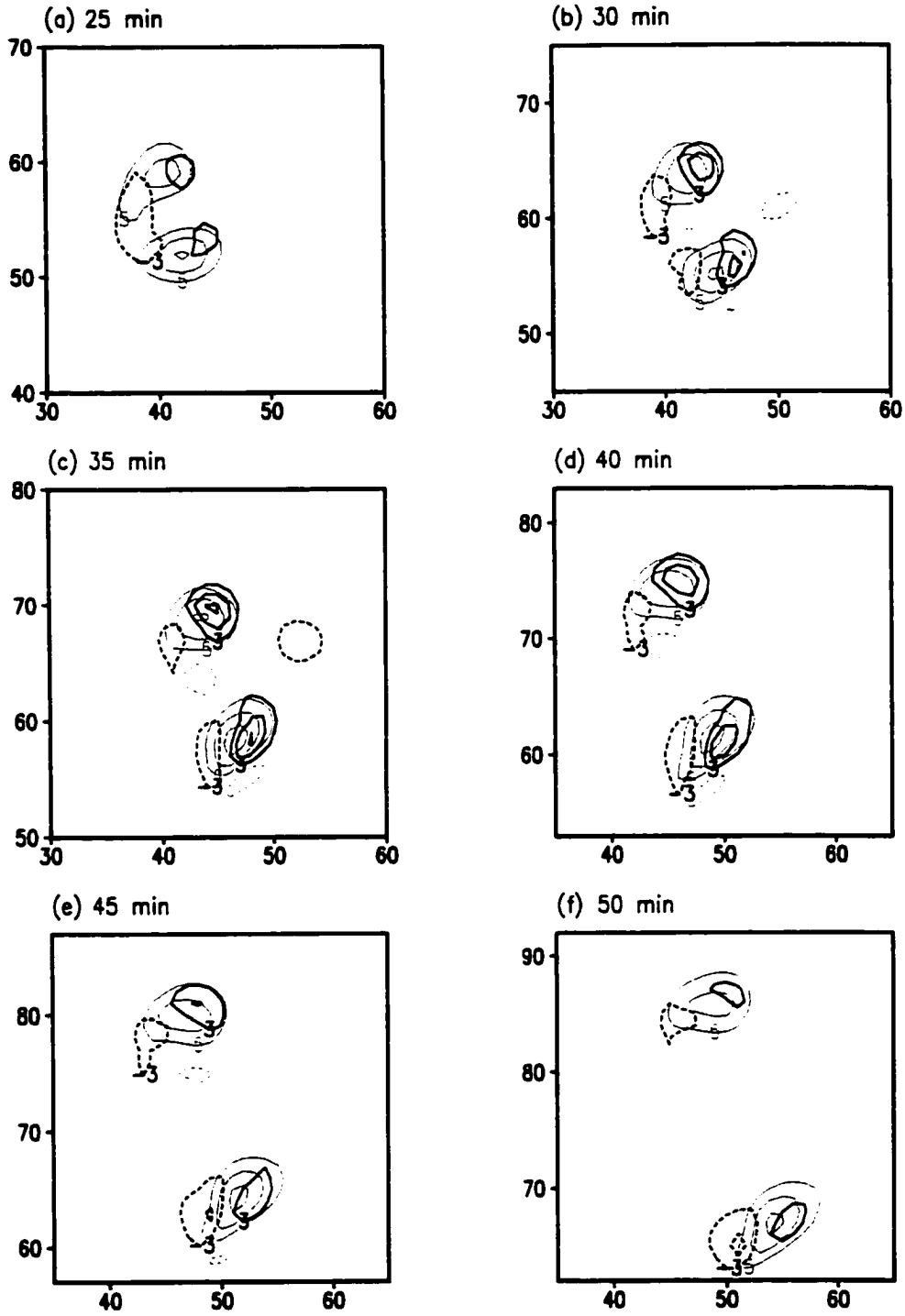


**Figure 5.7: Vertical velocity (thin lines) and $-\theta_0\ \partial\pi'/\partial z$ (thick lines) at ~2 km AGL for the 2cm simulation at (a) 25, (b) 30, (c) 35, (d) 40, (e) 45 and (f) 50 minutes. Solid lines represent positive magnitudes while dashed lines represent negative values. The contour interval is 3m.s$^{-2}$ for the forcing term and 5 m.s$^{-1}$ for the updrafts. The –2m.s$^{-1}$ isoline is also shown. Both zero isolines are omitted. Forcing is multiplied by 100.**

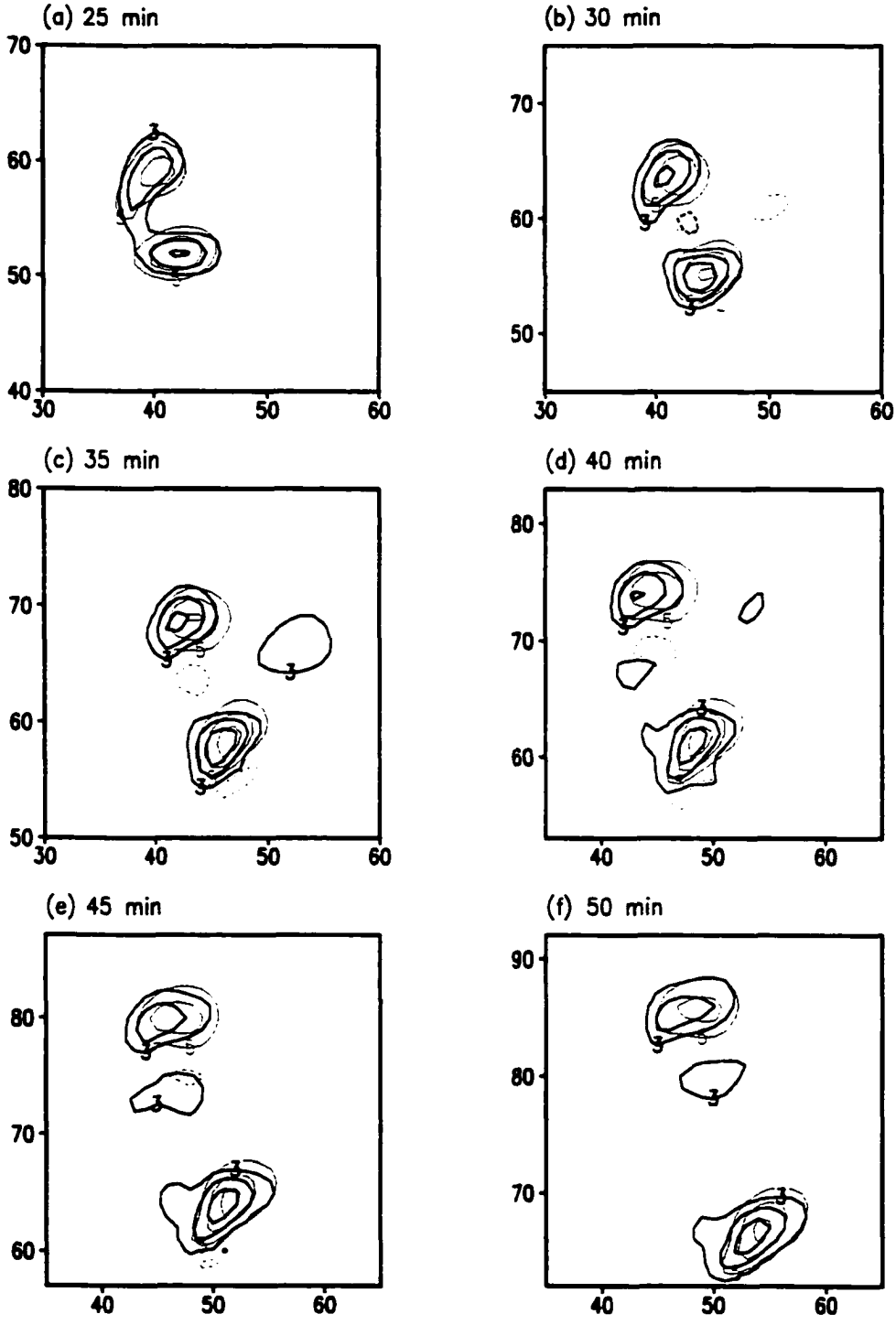


**Figure 5.8: Vertical velocity (thin lines) and $g(\theta_v'/\theta_0 - r_c)$ (thick lines) at ~2 km AGL for the 2cm simulation at (a) 25, (b) 30, (c) 35, (d) 40, (e) 45 and (f) 50 minutes. Solid lines represent positive magnitudes while dashed lines represent negative values. The contour interval is 3m.s$^{-2}$ for the forcing term and 5 m.s$^{-1}$ for the updrafts. The –2m.s$^{-1}$ isoline is also shown. Both zero isolines are omitted. Forcing is multiplied by 100.**

## 5.3 1 km AGL

### 5.3.1 *3mm Case*

Splitting of the updraft and the development of the LM and RM at 1 km AGL in the 3mm case are shown in Figure 5.9. The trends in the vertical velocity are similar to those at 2 km. The LM updraft increases in strength until 30 minutes (Figure 5.9a-b), remains steady from 30 to 35 minutes (Figure 5.9b-c), after which it decreases slightly between 35 and 40 minutes (Figure 5.9c-d), and then more rapidly between 40 to 45 minutes (Figure 5.9d-e). By 50 minutes, the LM is no longer evident (Figure 5.9f). The RM is stronger than the LM throughout the simulation.

The positive total forcing of the LM reaches its maximum at 30 minutes (Figure 5.10c), coinciding, not surprisingly, with the maximum in vertical velocity. The positive total forcing remains steady from 30 to 35 minutes; however, a zone of negative total forcing develops on the southern flank of the updraft at this stage. Between 35 and 40 minutes, the positive total forcing within the updraft decreases, and the region of downward forcing expands toward the center of the updraft (Figure 5.10c-d), causing the updraft to weaken. The positive total forcing decreases again between 40 and 45 minutes, this time by ~50%; the negative total forcing weakens only slightly (Figure 5.10d-e). It is during this time period that the greatest reduction in the vertical velocity of the LM occurs. Finally, all forcing associated with the LM disappears by 50 minutes (Figure 5.10f). The magnitude of the total positive forcing is similar at 1 and 2 km AGL; however, the negative total forcing has a much greater impact on the LM updraft at 1 km.

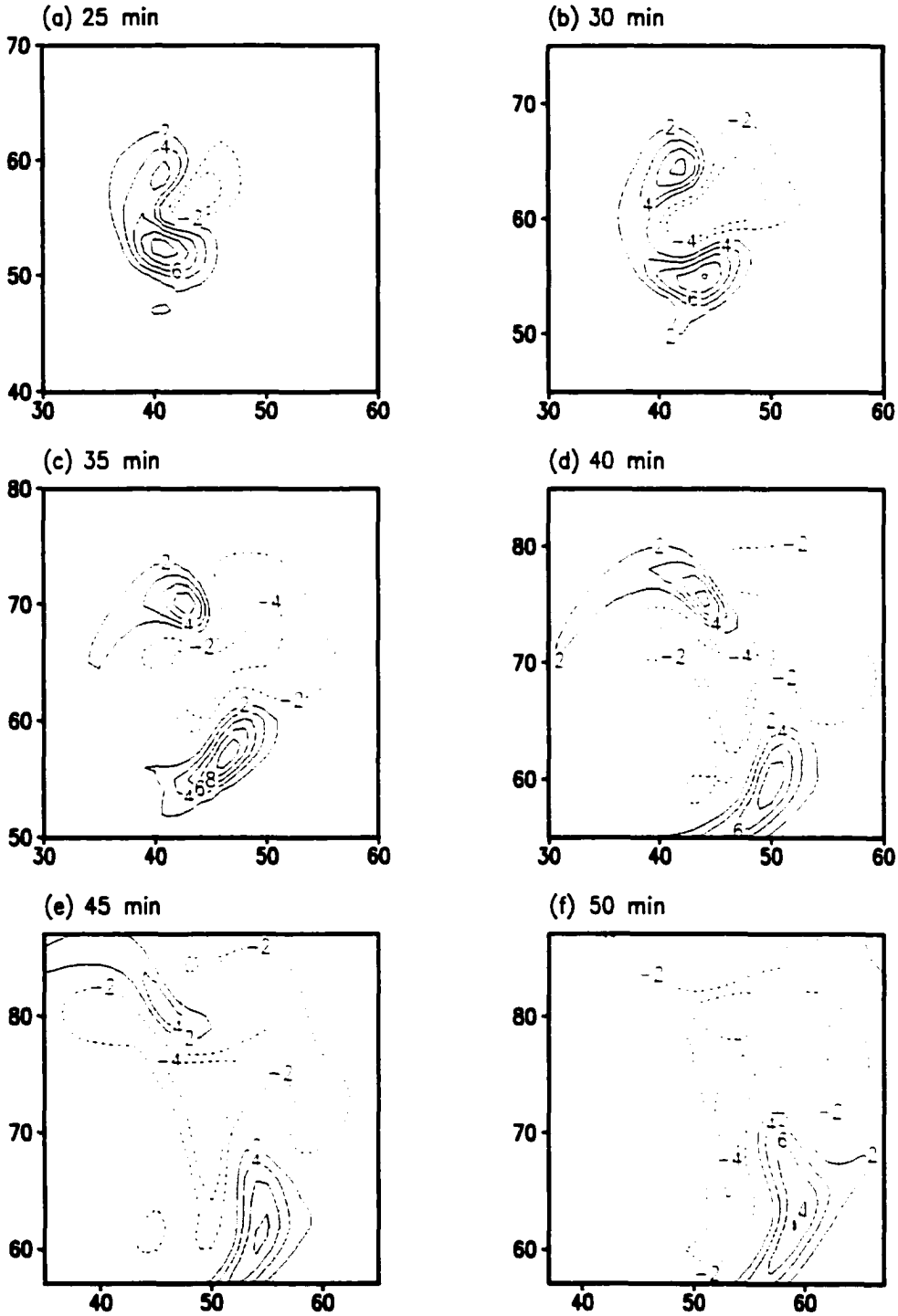


**Figure 5.9: Vertical velocity at ~1 km AGL for the 3mm case at (a) 25, (b) 30, (c) 35, (d) 40, (e) 45 and (f) 50 minutes. Contour interval is 2 m.s$^{-1}$ . The zero line is omitted.**

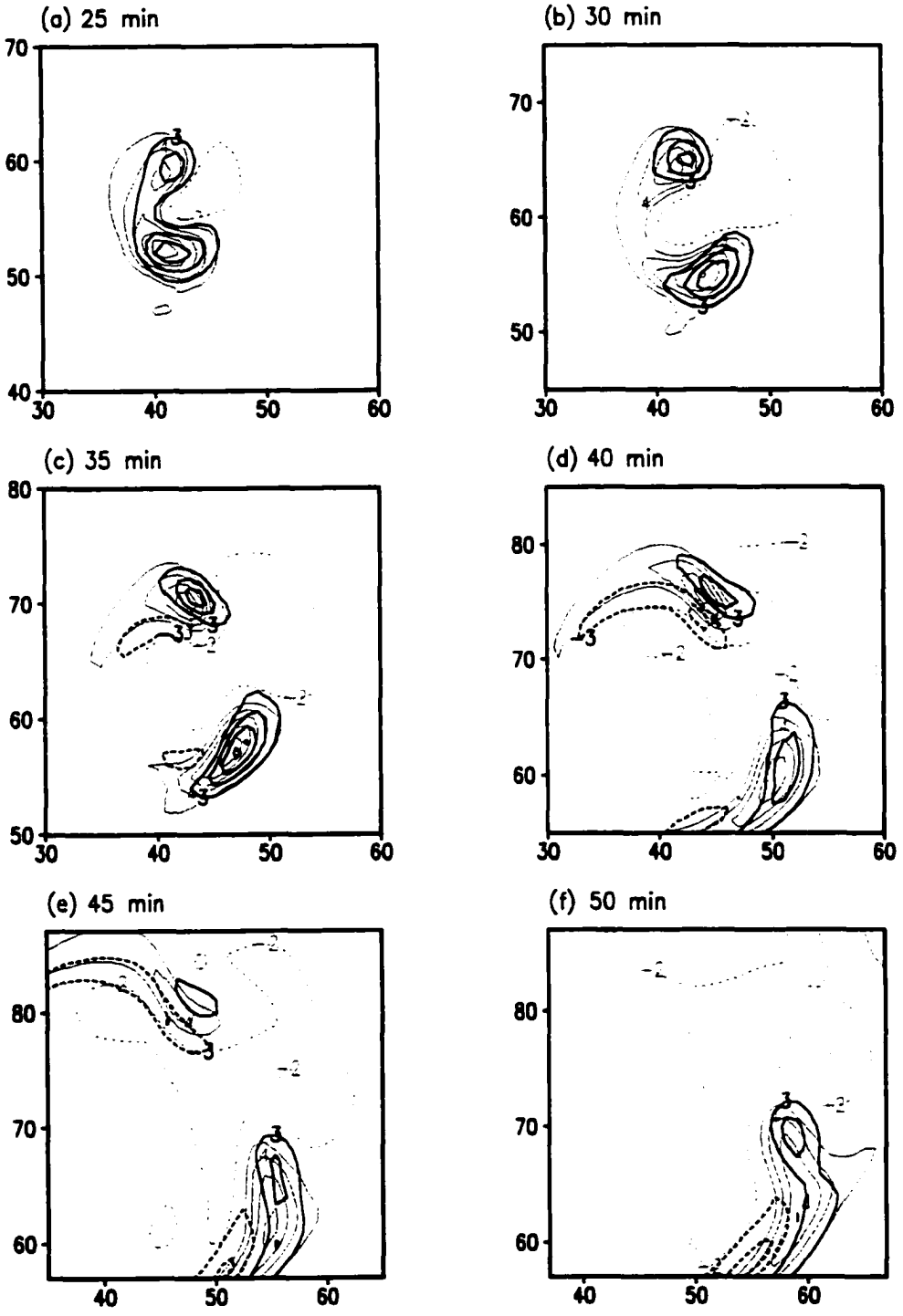


**Figure 5.10: Vertical velocity (thin lines) and the total forcing $-\theta_0 \partial\pi'/\partial z + g(\theta_v'/\theta_0 - r_c)$ (thick lines) at ~1 km AGL for the 3mm simulation at (a) 25, (b) 30, (c) 35, (d) 40, (e) 45 and (f) 50 minutes. Solid lines represent positive magnitudes while dashed lines represent negative values. The contour interval is 3m.s$^{-2}$ for the forcing term and 2m.s$^{-1}$ for the updrafts. The –2m.s$^{-1}$ isoline is also shown. Both zero isolines are omitted. Forcing is multiplied by 100.**

Unlike at 2 km, where the total forcing within the RM is much greater than that within the LM, the total forcing associated with LM at the 1 km level is similar to that associated with the RM between 30 and 40 minutes. This can be attributed to the contribution by the vertical gradients in $\pi$' within the LM (Figure 5.11). From 25 to 35 minutes, the $\pi$' forcing within the LM is significantly greater than in the RM (Figure 5.11a-c), and they are of similar magnitude at 40 minutes (Figure 5.11d). This result is inconsistent with linear theory, which predicts that the lifting in the region of the RM should be greater than within the LM. The reasons for the high magnitudes of $\pi$' forcing within the LM will be examined below.

The buoyant forcing for the 3mm case at 1 km AGL is completely negative for the time periods shown here (Figure 5.12). By 25 minutes, a region of negative buoyant forcing is already extending toward the center of the LM updraft (Figure 5.12a). As the simulation progresses, the buoyant forcing within the LM continues to decrease, and from 35 minutes onward, the LM updraft is comprised predominantly of negatively buoyant air (Figure 5.12c-e). The region of negative total forcing from 35 to 45 minutes (Figure 5.10c-e) is the result of this enhanced negative buoyant forcing. The buoyant forcing within the RM is also negative. However, only about half of the RM updraft consists of negatively buoyant air, which, together with the positive $\pi$' forcing within the RM, allows for the continued existence of the updraft.

Examining the storm-relative wind flow at ~250 m AGL for the LM and RM storms between 35 and 45 minutes, provides some insight into why the entire LM updraft becomes negatively buoyant, whereas only a portion of the RM is affected by the downward buoyant forcing (Figure 5.13). The low-level storm-relative wind flow into the LM updraft during this period comes entirely from the region of the cold pool (Figure 5.13a,c,e). The evaporatively-cooled cold pool air is negatively buoyant. Thus, the low-level inflow into the LM updraft results in increasing and maintaining the negative buoyancy within the LM. The storm-relative flow into the RM comes partially from the

region of the cold pool and partially from the unperturbed environmental air (Figure 5.13b,d,f). Thus, while some of the low-level inflow into the RM transports negatively buoyant air into the RM updraft, the contribution from the environmental air prevents the RM from becoming completely negatively buoyant. Therefore, while the LM becomes embedded within the cold pool and appears to decay due to the ingestion of cold air from the downdraft and cold pool region, the RM avoids becoming completely swamped by negative buoyancy by moving faster than the cold pool, thereby also allowing for the ingestion of the warmer, unstable undisturbed environmental air that offsets the effects of the cold pool air.

The analysis above shows that the $\pi$' forcing within the LM does decrease between 35 and 45 minutes, which will weaken the updraft. However, as the $\pi$' forcing remains positive, even at 50 minutes, the updraft should not completely dissipate as a result of the reduced vertical gradients in $\pi$'. During the same period, negative buoyant forcing increases and is maintained throughout most of the LM updraft. It appears that while the $\pi$' forcing contributes to the weakening of the LM updraft, it is the negative buoyant forcing that actually causes the dissipation of the LM. The $\pi$' forcing also decreases within the RM during this period, and is associated with a slight weakening of the updraft. However, the RM does not dissipate, as the negative buoyant forcing affects on the RM are much less than those on the LM. These findings are similar to those of Grasso (2000), which is expected given the similarities between his precipitation case and the 3mm run presented here.

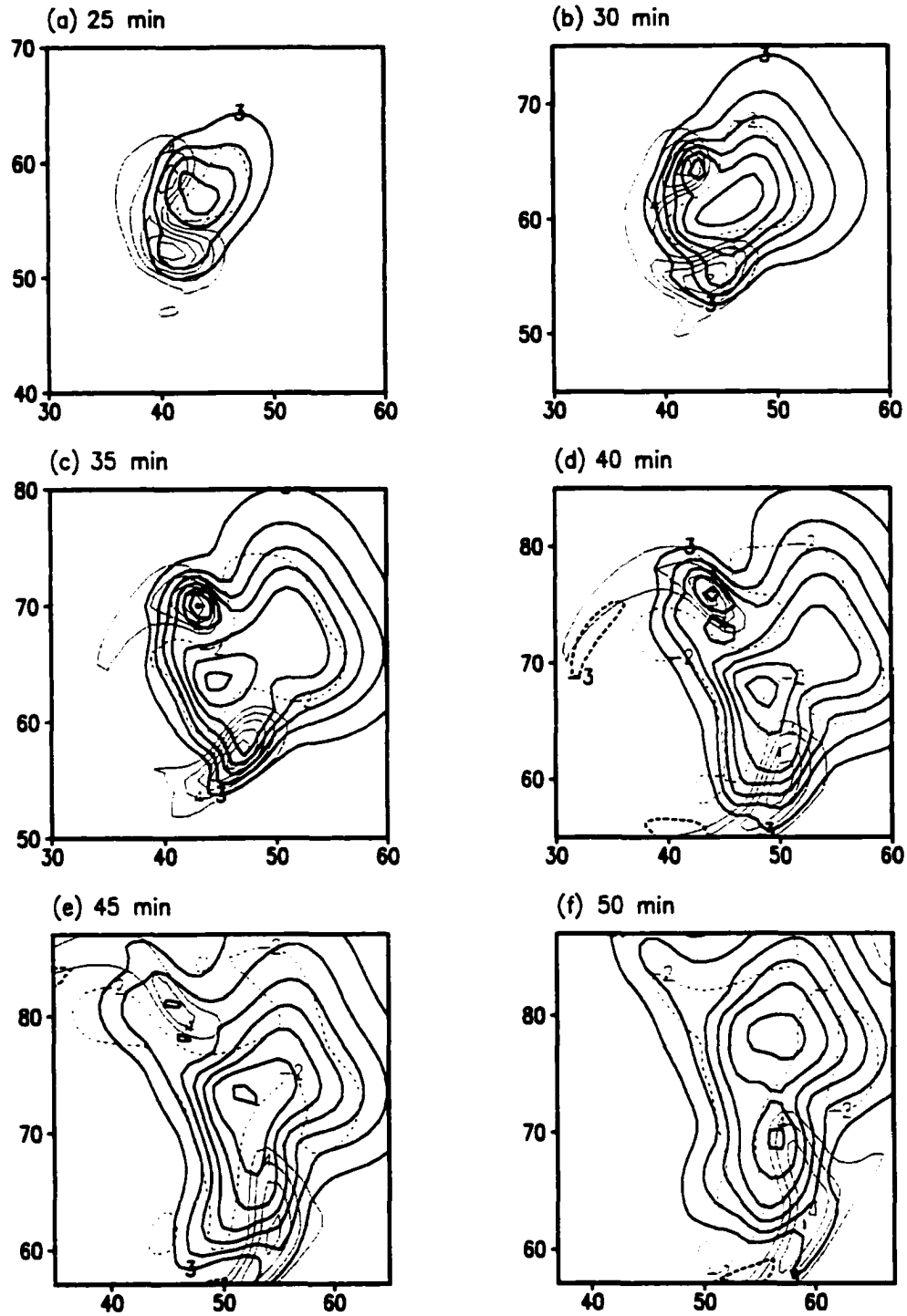


**Figure 5.11: Vertical velocity (thin lines) and $-\theta_0\ \partial\pi'/\partial z$ (thick lines) at ~1 km AGL for the 3mm simulation at (a) 25, (b) 30, (c) 35, (d) 40, (e) 45 and (f) 50 minutes. Solid lines represent positive magnitudes while dashed lines represent negative values. The contour interval is 3m.s$^{-2}$ for the forcing term and 2 m.s$^{-1}$ for the updrafts. The –2m.s$^{-1}$ isoline is also shown. Both zero isolines are omitted. Forcing is multiplied by 100.**

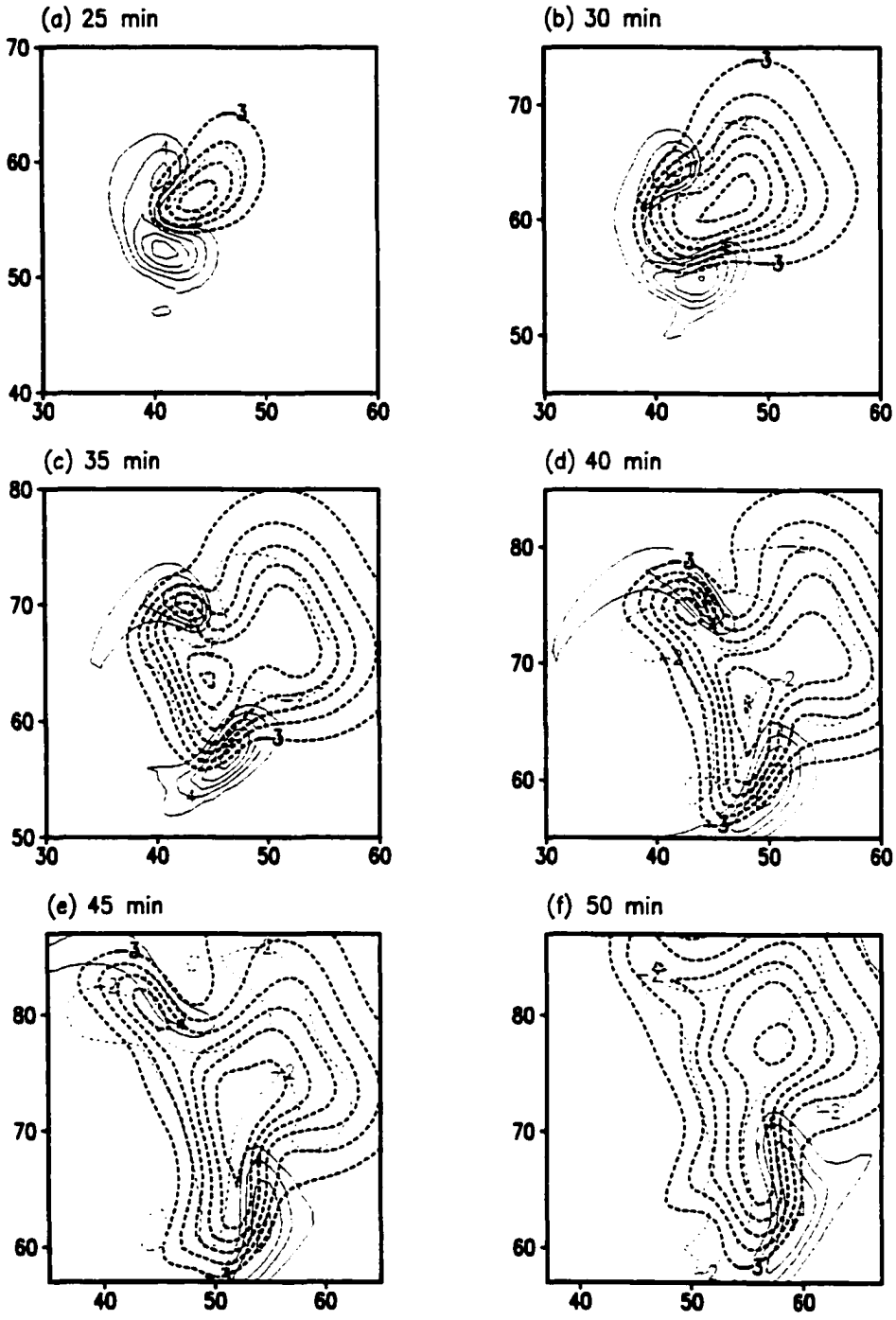


**Figure 5.12: Vertical velocity (thin lines) and $g(\theta_v'/\theta_0 - r_c)$ (thick lines) at ~1 km AGL for the 3mm simulation at (a) 25, (b) 30, (c) 35, (d) 40, (e) 45 and (f) 50 minutes. Solid lines represent positive magnitudes while dashed lines represent negative values. The contour interval is 3m.s$^{-2}$ for the forcing term and 2 m.s$^{-1}$ for the updrafts. The –2m.s$^{-1}$ isoline is also shown. Both zero isolines are omitted. Forcing is multiplied by 100.**

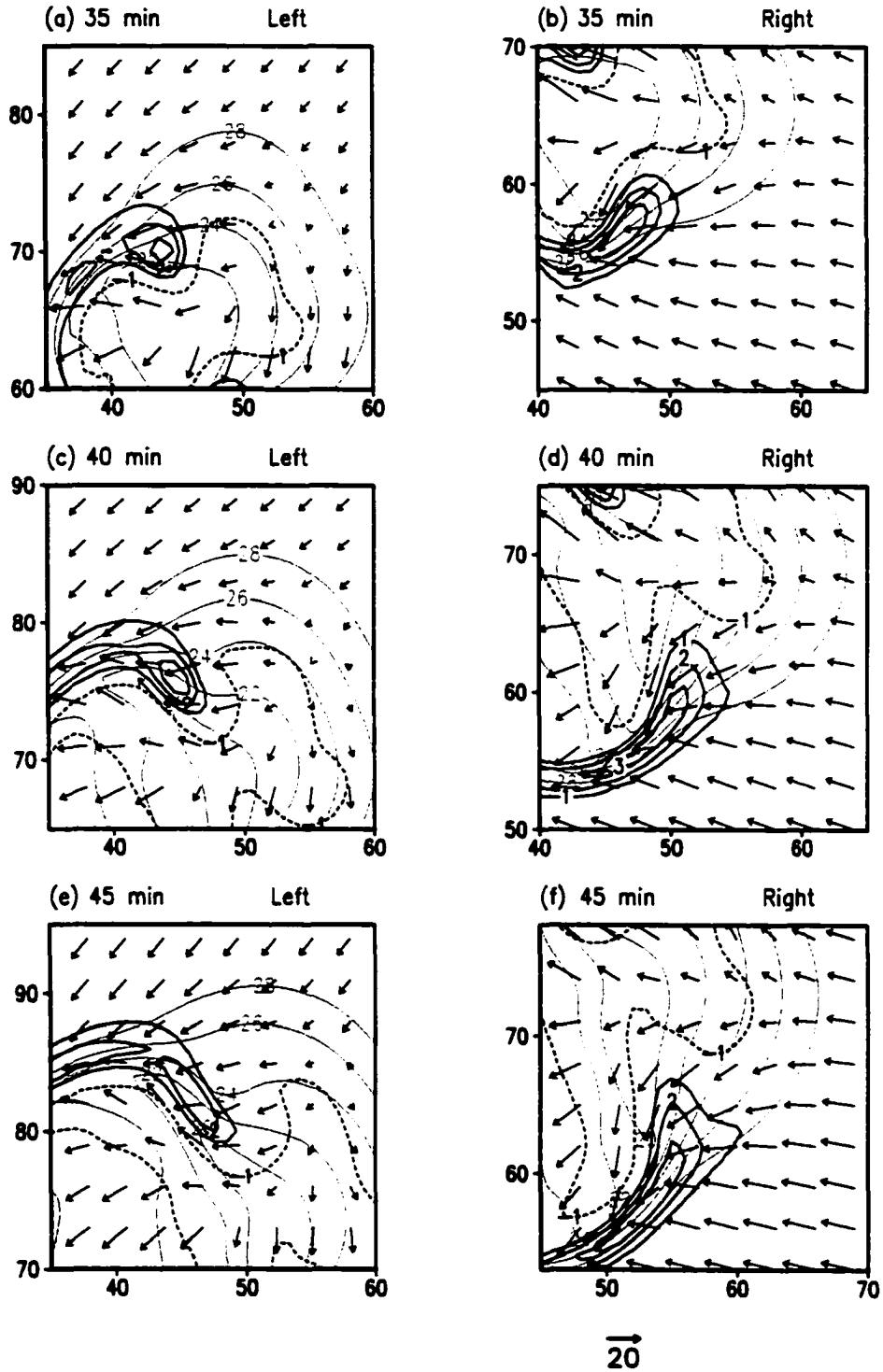


**Figure 5.13: Vertical velocity (thick lines) and temperature (thin lines) for the LM at (a) 35, (c) 40 and (e) 45 minutes, and for the RM at (b) 35, (d) 40 and (f) 45 minutes at ~ 250m AGL for the 3mm case. The vectors are storm-relative wind vectors, relative to the LM in (a), (c), and (e) and to the RM in (b), (d) and (f). The contour interval for the vertical velocity is 1m.s$^{-1}$ and for the temperature is 2°C.**

### 5.3.2 *2cm*

The vertical velocity field at 1 km AGL for the 2cm case reveals an increase in the strength of the LM from 25 to 35 minutes (Figure 5.14a-c), followed by a slight decrease in strength from 35 to 50 minutes (Figure 5.14d-f). Also, the RM storm is stronger than the LM. The total forcing field (Figure 5.15) follows a similar trend. An obvious difference between the total forcing in the 2cm case and that in the 3mm run is that the negative forcing associated with the LM in the 3mm case is much greater.

The $\pi$' forcing within the LM of the 2cm case decreases gradually from 25 to 50 minutes (Figure 5.16a-f). The $\pi$' forcing associated with the RM is greater than with the LM, except initially. The vertical gradients in $\pi$' at this level are much greater in the 3mm run than in the 2cm simulation, and yet it is the 3mm LM that dissipates. This suggests that other factors, apart from the $\pi$' forcing, may be responsible for the longevity of the LM storms. The buoyant forcing in the 2cm case (Figure 5.17) is completely negative, like that in the 3mm case. The negative buoyant forcing associated with the LM and RM are similar in magnitude, being slightly stronger in the region of the LM. In this case, unlike the 3mm case, the cold pool does not surge out to the northeast of the updrafts. A plot of storm-relative flow into the LM and RM updrafts shows that the low-level inflow into both these storms comes primarily from the undisturbed environment (Figure 5.18). To the north of the RM, and to the south of the LM, there is some ingestion of the downdraft air into the updrafts. This causes the small regions of negative buoyancy observed at 1 km AGL. However, the impact of the negative buoyant forcing on the LM in the 2cm case is significantly less than in the 3mm run, both in magnitude and area.

In the 2cm case, the positive total forcing of the LM is determined primarily by the vertical gradients in $\pi$'. As the $\pi$' forcing decreases slowly from 40 to 50 minutes, the vertical velocity also slowly decreases. Soon after 50 minutes, the $\pi$' forcing stabilizes, as does the vertical velocity (not shown). The negative buoyant forcing has an impact on the

southern section of the updraft, reducing the total upward forcing in this region, and causing the more elongated structure of the updraft at this stage. However, the LM updraft does not become increasingly negatively buoyant throughout most of the updraft, as happens in the 3mm case. It therefore appears that the LM updraft in the 2cm case is maintained by the upward forcing due to the vertical gradients in $\pi'$, and that the storm does not dissipate, as it does in the 3mm simulation, due to the impact of negatively buoyant air. This is similar to the results from the 2 km level.

## 5.4 Factors Affecting the Buoyant and $\pi'$ Forcing

The negative buoyant forcing within the LM at the 1 km level is as much as 2.5 times greater in the 3mm case than in the 2cm simulation. This is directly attributable to the strength of the cold pool, which in turn is a direct result of the mean hail diameter. The strength of the cold pool determines the actual magnitude of the negative buoyancy, as well as the speed at which the cold pool propagates. These in turn determine the characteristics of the air being transported into the LM by the low-level inflow. As a result of the enhanced evaporative cooling rates in the 3mm case, the air being ingested into the LM is more negatively buoyant than that in the 2cm case. Also, the rate at which the cold pool moves means that the low-level inflow into the LM comes predominantly from the region of the cold pool. The reduced evaporative cooling rates and weaker cold pool in the 2cm case mean that the air within the cold pool region is less negatively buoyant than that in the 3mm case and, as the cold pool is a lot slower moving, the low-level inflow into the LM in the 2cm case comes primarily from the undisturbed environment. These effects may be seen in Figure 5.19 where Figure 5.13 and Figure 5.18 have been combined for comparative purposes. In this way, a simple change in the mean hail diameter has an effect on the longevity of the LM storm.

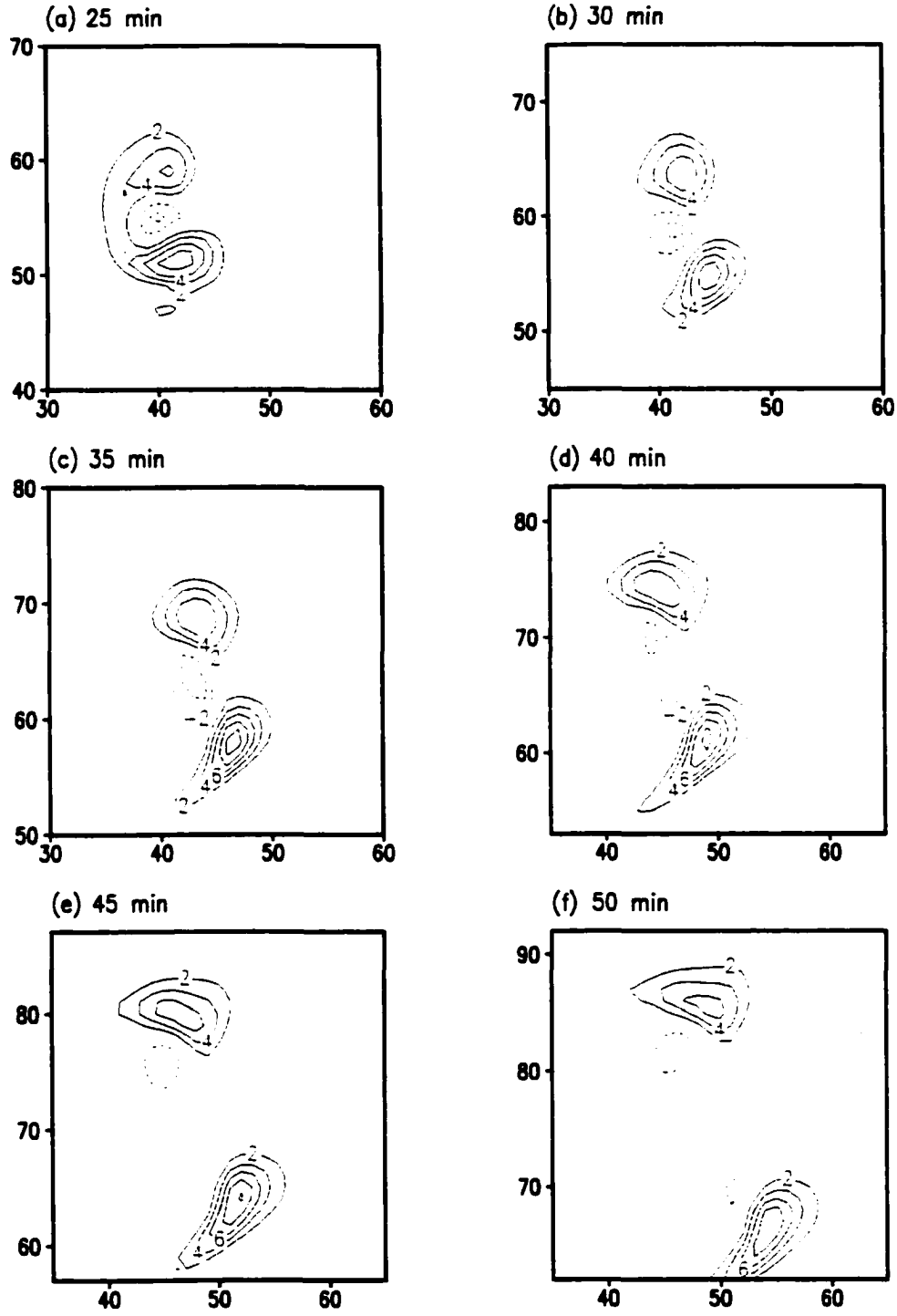


**Figure 5.14: Vertical velocity at ~1 km AGL for the 2cm case at (a) 25, (b) 30, (c) 35, (d) 40, (e) 45 and (f) 50 minutes. Contour interval is 2 m.s$^{-1}$ . The zero line is omitted.**

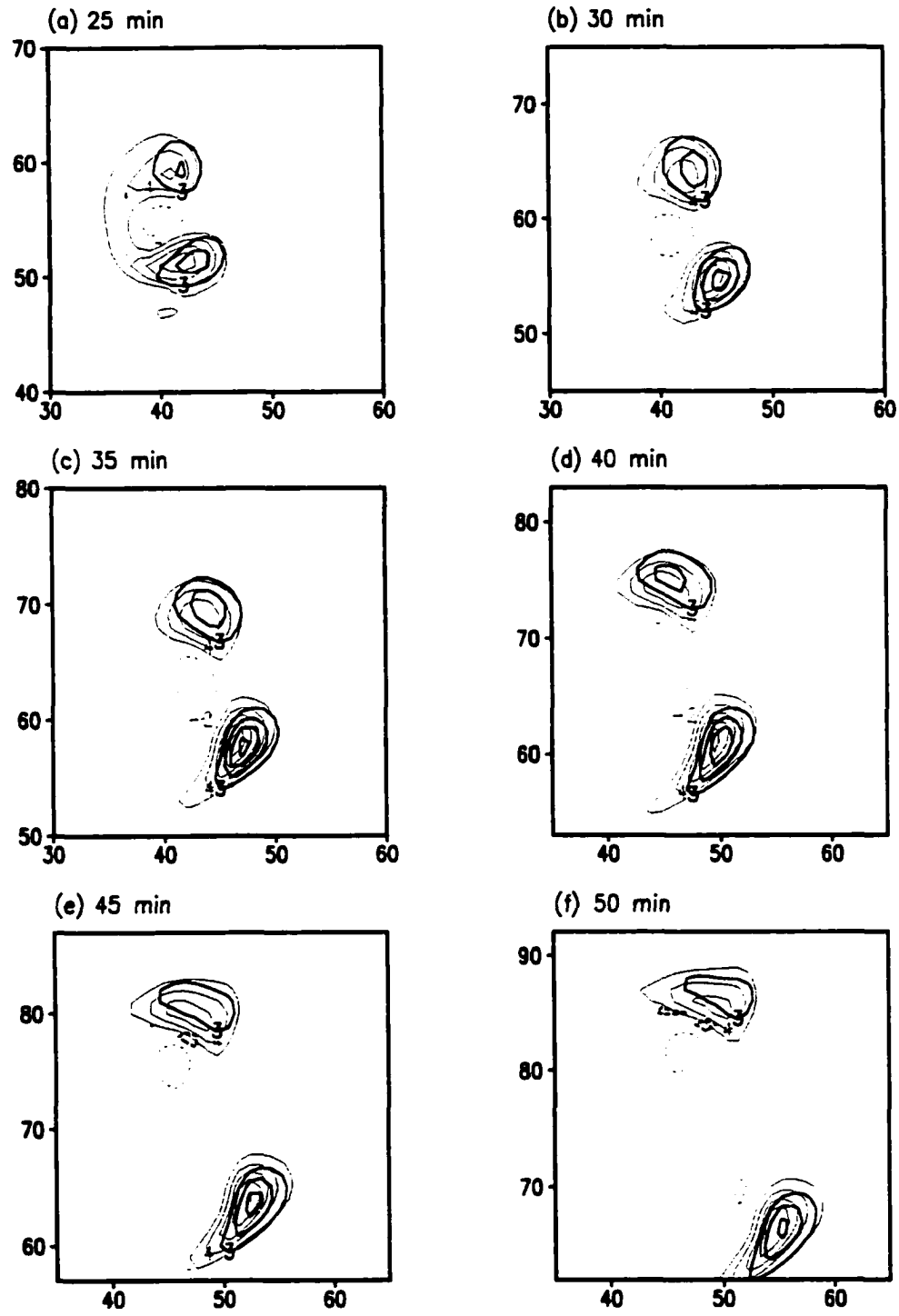


**Figure 5.15: Vertical velocity (thin lines) and the total forcing $-\theta_0 \partial\pi'/\partial z + g(\theta_v'/\theta_0 - r_c)$ (thick lines) at ~1 km AGL for the 2cm simulation at (a) 25, (b) 30, (c) 35, (d) 40, (e) 45 and (f) 50 minutes. Solid lines represent positive magnitudes while dashed lines represent negative values. The contour interval is $3 m.s^{-2}$ for the forcing term and $2 m.s^{-1}$ for the updrafts. The $-2 m.s^{-1}$ isoline is also shown. Both zero isolines are omitted. Forcing is multiplied by 100.**

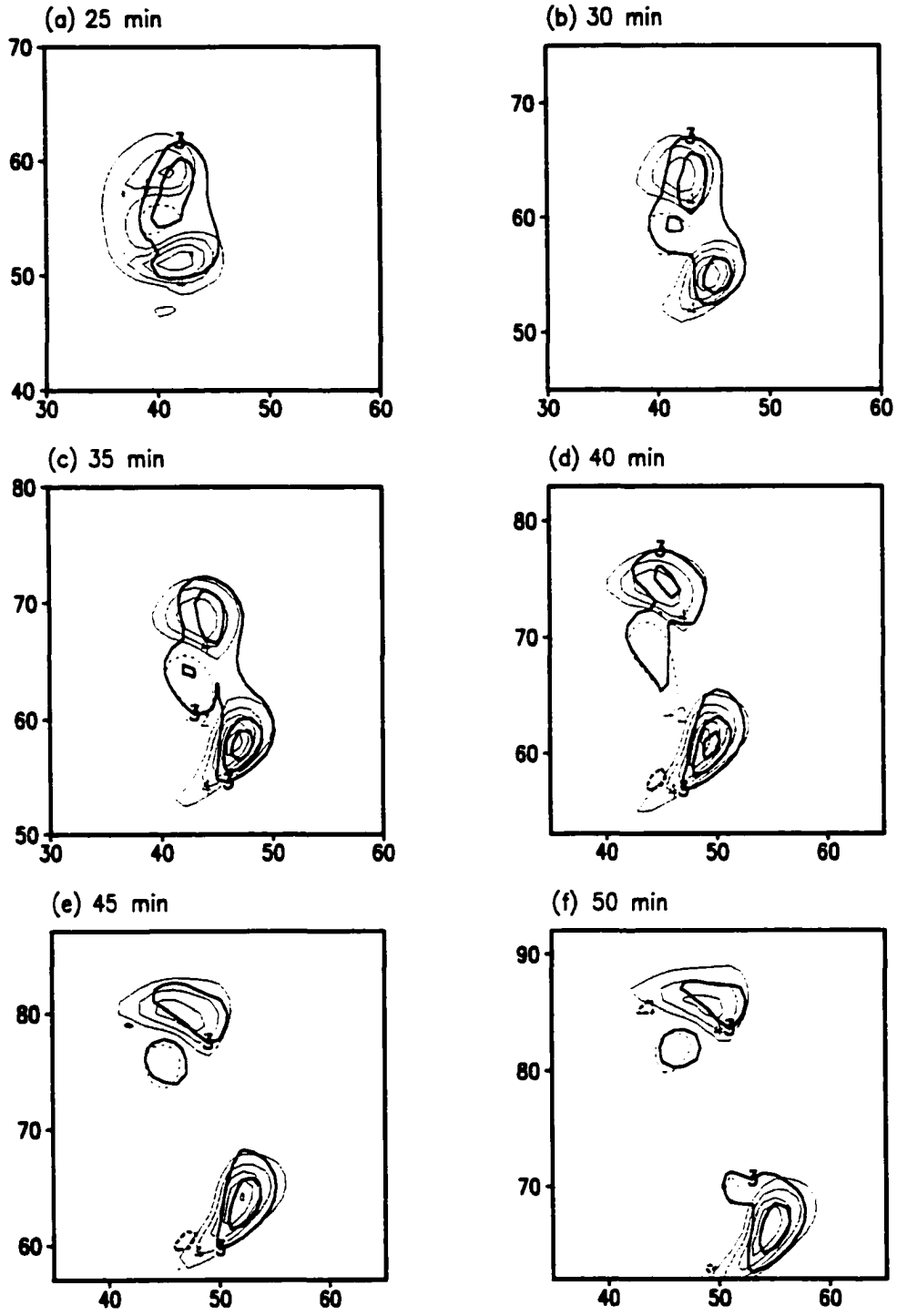


**Figure 5.16: Vertical velocity (thin lines) and $-\theta_0\ \partial\pi'/\partial z$ (thick lines) at ~1 km AGL for the 2cm simulation at (a) 25, (b) 30, (c) 35, (d) 40, (e) 45 and (f) 50 minutes. Solid lines represent positive magnitudes while dashed lines represent negative values. The contour interval is 3m.s$^{-2}$ for the forcing term and 2 m.s$^{-1}$ for the updrafts. The –2m.s$^{-1}$ isoline is also shown. Both zero isolines are omitted. Forcing is multiplied by 100.**

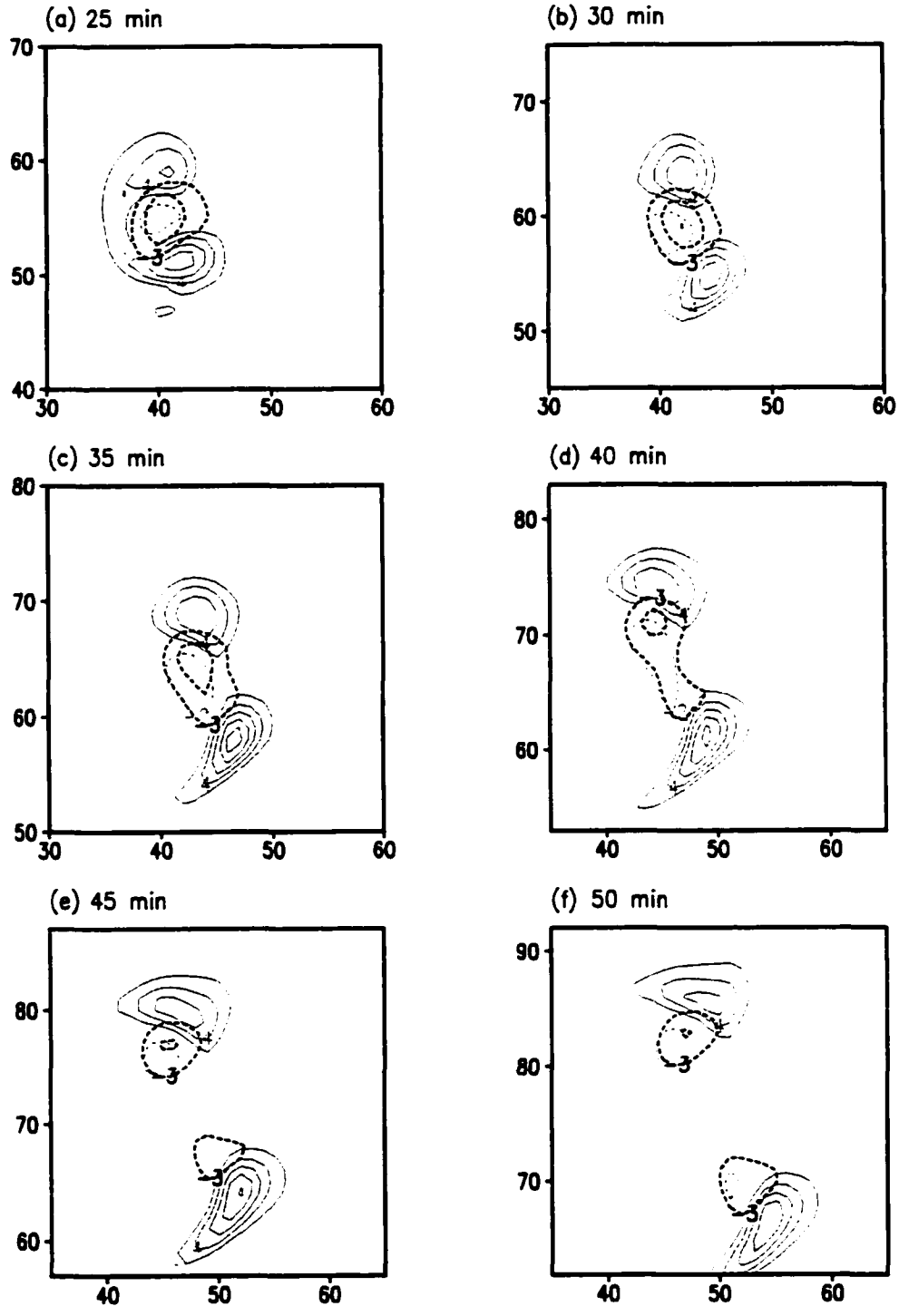


**Figure 5.17: Vertical velocity (thin lines) and $g(\theta_v'/\theta_0 - r_c)$ (thick lines) at ~1 km AGL for the 2cm simulation at (a) 25, (b) 30, (c) 35, (d) 40, (e) 45 and (f) 50 minutes. Solid lines represent positive magnitudes while dashed lines represent negative values. The contour interval is 3m.s$^{-2}$ for the forcing term and 2 m.s$^{-1}$ for the updrafts. The -2m.s$^{-1}$ isoline is also shown. Both zero isolines are omitted. Forcing is multiplied by 100.**

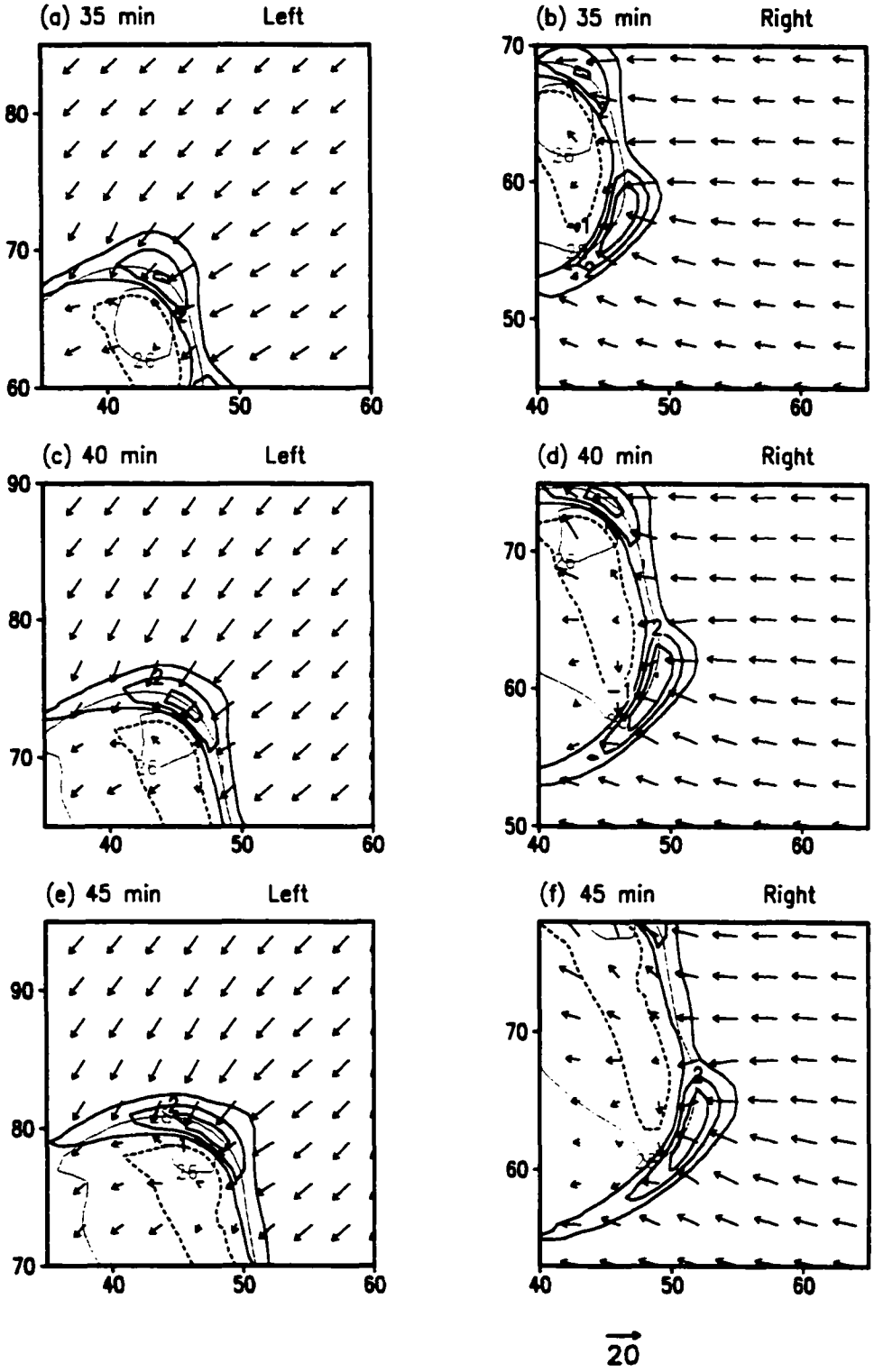


**Figure 5.18: Vertical velocity (thick lines) and temperature (thin lines) for the LM at (a) 35, (c) 40 and (e) minutes, and for the RM at (b) 35, (d) 40 and (f) 45 minutes at ~ 250m AGL for the 2cm case. The vectors are storm-relative wind vectors, relative to the LM in (a), (c), and (e) and to the RM in (b), (d) and (f). The contour interval for the vertical velocity is 1m.s$^{-1}$ and for the temperature is 2°C.**

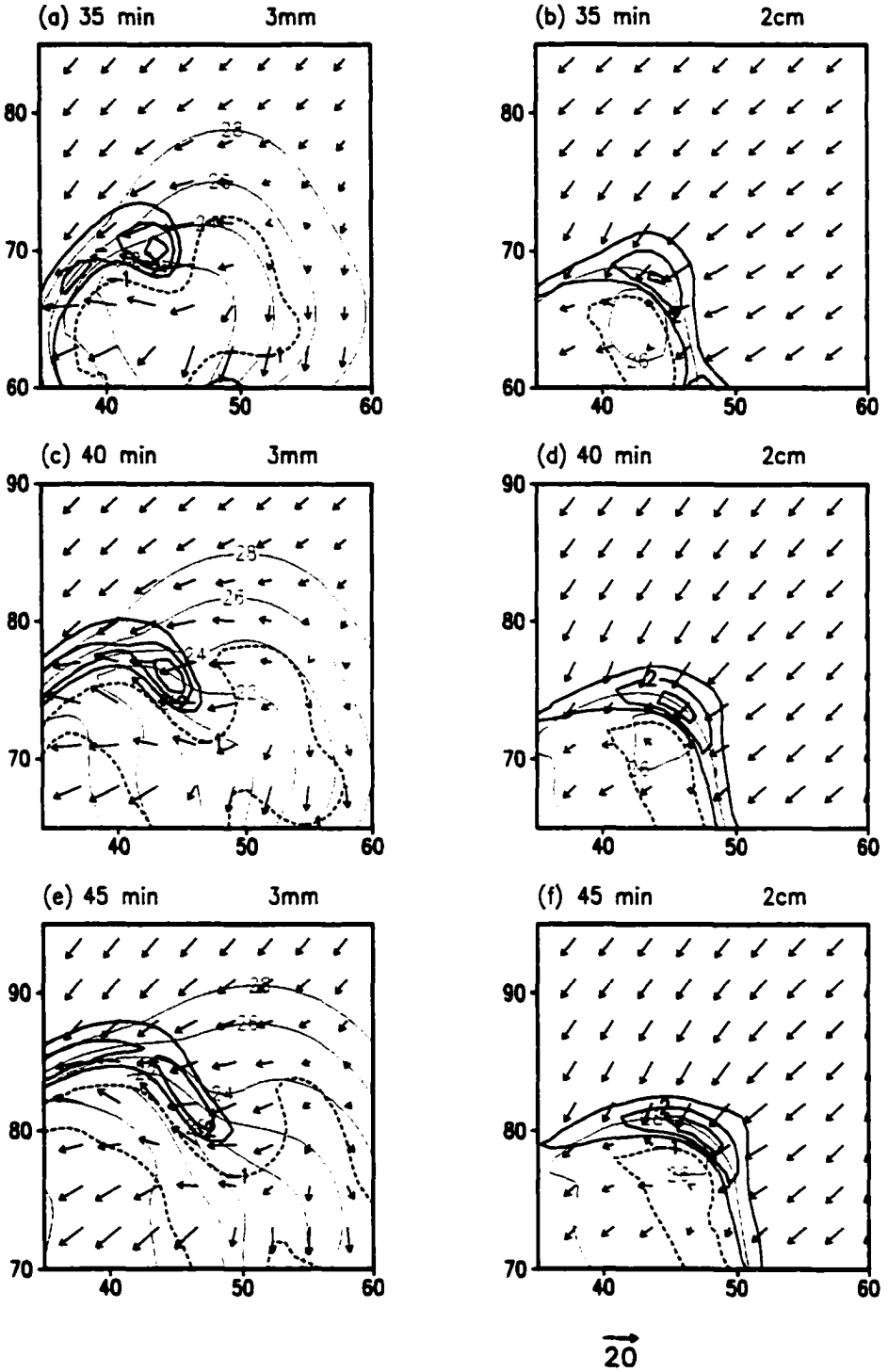


**Figure 5.19: Vertical velocity (thick lines) and temperature (thin lines) for the LM in the 3mm case at (a) 35, (c) 40 and (e) minutes, and for the LM in the 2cm run at (b) 35, (d) 40 and (f) 45 minutes at ~250m AGL for the 2cm case. The vectors are storm-relative wind vectors, relative to the 3mm LM in (a), (c), and (e) and to the 2cm LM in (b), (d) and (f). The contour interval for the vertical velocity is 1m.s$^{-1}$ and for the temperature is 2°C.**

As we saw from Eq. (4.1), the numerical buoyancy is comprised of two terms:

$$B = g\frac{\theta_v'}{\theta_0} - gr_c, \tag{5.1}$$

where the symbols are as described above. The first term on the right hand side of Eq. (5.1), the thermodynamic term, shall be referred to as the "theta" term. The second term, the condensate loading term, shall be called the "loading" term. The contribution made by the "loading" term and the "theta" term, as well as the ratio of the absolute value of the "theta" contribution to that of the "loading" contribution, will be shown in the next four figures (Figure 5.20 - Figure 5.23). The light shading represents regions in which the ratio is less than one, hence regions in which the "loading" term dominates.

In the 3mm case at 2 km, the negative buoyant forcing (Figure 5.4) is due to the "loading" term (Figure 5.20a,b), whereas the positive buoyant forcing is primarily due to the "theta" term (Figure 5.20c,d). This means the negative buoyancy is due to the precipitation loading within the downdraft, whereas the positive buoyancy occurs as a result of latent heat release within the updraft. The "loading" term is, not surprisingly, dominant in the regions of greatest condensate mixing ratios. However, within the updraft, the effects of latent heat release are greater than the drag, due to the presence of condensate in these regions. A similar result is obtained for the 2cm case at 2 km AGL, although the "loading" term affects a smaller region (Figure 5.21a,b). This, as we saw in Chapter 4, is due to the smaller area of condensate in the 2cm case resulting from the greater fall velocities associated with larger hail.

In the 3mm (Figure 5.22) and 2cm cases (Figure 5.23) at 1 km level, the contributions from the "loading" term and the "theta" term both contribute to downward forcing; however, there are significant differences between the two cases. The "loading" term and the contributions made by the "theta" term are of similar magnitude in the 2cm case (Figure 5.23), with the "theta" term being slightly greater at 35 minutes. Condensate loading and evaporative cooling therefore appear to contribute almost equally to the

downward forcing in the 2cm case. In the 3mm case, the "theta" term contribution is significantly larger than the contribution made by the "loading" term, even though the condensate mixing ratios are relatively large (Figure 5.22). The ratio of these terms is greater than one throughout most of the domain, indicating the dominance of the "theta" term, and hence of the evaporative cooling, even in regions of high condensate mixing ratios. These results demonstrate the impact of the hail size on the buoyant forcing. In the smaller hail cases, the greater melting and evaporative rates enhance the "theta" term, and resultant negative buoyant forcing. In the larger hail cases, the reduced melting and evaporation rates, and the greater fall speeds, result in the comparable magnitudes of these terms. Also, it is the loading term that primarily controls the region of negative buoyant forcing with the LM updraft in the 2cm case.

We saw earlier that the forcing due to the vertical gradients in $\pi$' within the 3mm LM at 1 km (Figure 5.11) were significantly greater than the same forcing with the 3mm RM, and within the LM and RM of the 2cm case (Figure 5.16). This is not observed at the 2 km level, where the $\pi$' forcing within the RM is actually greater than within the LM. What is causing this small region of strong $\pi$' forcing within the 3mm LM at 1 km? Rotunno and Klemp (1982) showed, using the linearized divergence equation and the assumption that $\nabla^2\pi' \approx -\pi'$, that for a wind field in pure rotation, $\pi' \approx -\zeta^2$, where $\zeta$ is the vertical vorticity. Based on this relationship, wherever there is rotation, whether in a positive or negative sense, the perturbation Exner function (and the perturbation pressure) is lowered ($\pi = c_p\left(\frac{p}{p_0}\right)^{R/c_p}$ and hence can be written in terms of pressure). The vertical vorticity at 35 minutes, the time period when the $\pi$' forcing is strongest in the 3mm LM, is shown in Figure 5.24, for both the 3mm and 2cm cases. In the 3mm case, the negative vertical vorticity within the updraft increases rapidly in magnitude between 400m and ~1 km AGL. Using the relationship above, this implies that the pressure around 1 km is decreasing more rapidly than at the lower levels, and a strong upward-directed pressure gradient force develops. This is manifested in the strong $\pi$' forcing observed within the

LM updraft at 1 km in the 3mm case (Figure 5.11). Between 1 and 2 km, the negative vorticity changes only slightly and, as a result, the vertical gradients in $\pi$' are not as strong at 2 km (Figure 5.3) as they are at 1 km. The vertical vorticity increases slowly between 400 m and 1 km in the 2cm case, and then far more rapidly between 1 and 2 km (Figure 5.24). This explains the relatively weak $\pi$' forcing at 1 km (Figure 5.16) and the relatively strong $\pi$' forcing at 2 km in the 2cm case (Figure 5.7).

The question that now needs addressing is why the negative vertical vorticity is so much stronger at the lower levels in the 3mm case than in the 2cm case? The horizontal vorticity at 250 m is much greater in the 3mm case than in the 2cm case. This is due to the stronger baroclinic forcing in the 3mm case caused by the greater temperature gradients along the edge of the cold pool (Figure 4.35). Also, to the east of the 3mm LM, the horizontal vorticity vectors point predominantly eastward due to the surge of the cold pool out ahead of the LM. To the east of the 2cm LM, the horizontal vorticity is primarily determined by the environmental conditions, and the vectors point predominantly westward in this region.

Overlaying the storm-relative wind vectors and the horizontal vorticity vectors for the 3mm case (Figure 5.26a,c), it is apparent that, in the region of inflow into the LM, the vorticity and storm-relative wind vectors are almost parallel, although they point in opposite directions. This means the streamwise component of the horizontal vorticity ($\omega_s = \vec{\omega} \cdot \vec{p}$ where $\omega_s$ is the streamwise vorticity and p is the unit vector in the direction of the storm-relative wind), is negative and large compared to the crosswise component. As the low-level inflow air enters the LM updraft, the negative streamwise vorticity is tilted and then stretched by the updraft. In this way, the negative vertical vorticity is enhanced within the lower levels of the LM. From 35 to 40 minutes there is an increase in the horizontal vorticity (Figure 4.35a,c), which subsequently causes an increase in the low-level vertical vorticity (Figure 5.27a,c). The vertical vorticity at the 1 km level remains

relatively constant (Figure 5.28a,c). This results in a decrease in the vertical $\pi'$ gradients within the LM, as is observed (Figure 5.11).

In the 2cm case, the horizontal vorticity vectors to the east of the LM updraft point toward the west and are much smaller than those in the same region of the 3mm case (Figure 5.26b,d). In the inflow region to the east of the LM, the storm-relative vectors and the horizontal vorticity vectors are at ~45° to one another. This, together with the weak horizontal vorticity, result in a much weaker streamwise component of vorticity in the 2cm case, as compared with the 3mm case. The streamwise vorticity in the 2cm case is also positive, and once tilted in the updraft enhances positive, not negative, vertical vorticity within the updraft. In the 2cm case, the horizontal vorticity and storm-relative winds change little between 35 and 40 minutes. As a result, the low-level vertical vorticity changes little, and the vertical gradients in $\pi'$ remain relatively constant (Figure 5.16). While the vorticity couplets at 1 and 2 km are predicted by linear theory (Rotunno and Klemp, 1982), the low-level vertical vorticity changes appear to be controlled by the cold pool strength and movement. In this way, changes in the mean hail diameter feed back to changes in the low-level vertical velocity, and hence have an impact on the $\pi'$ forcing within the LM. This highlights the impact that changing a single microphysical parameter (the mean hail diameter) can have on numerous aspects of the storm dynamics.

## 5.5 Discussion

Linear theory predicts that when the hodograph veers (backs) with height, the RM (LM) dominates the LM (RM). This effect tends to be most pronounced for hodograph curvature in the lower levels (Klemp and Wilhelmson, 1978b; Rotunno and Klemp, 1982). The hodograph used in the simulations shown here veered with height below 2 km AGL (see Fig. 3.1). Under such conditions, linear theory predicts the weakening of the LM and the enhancement of the RM.

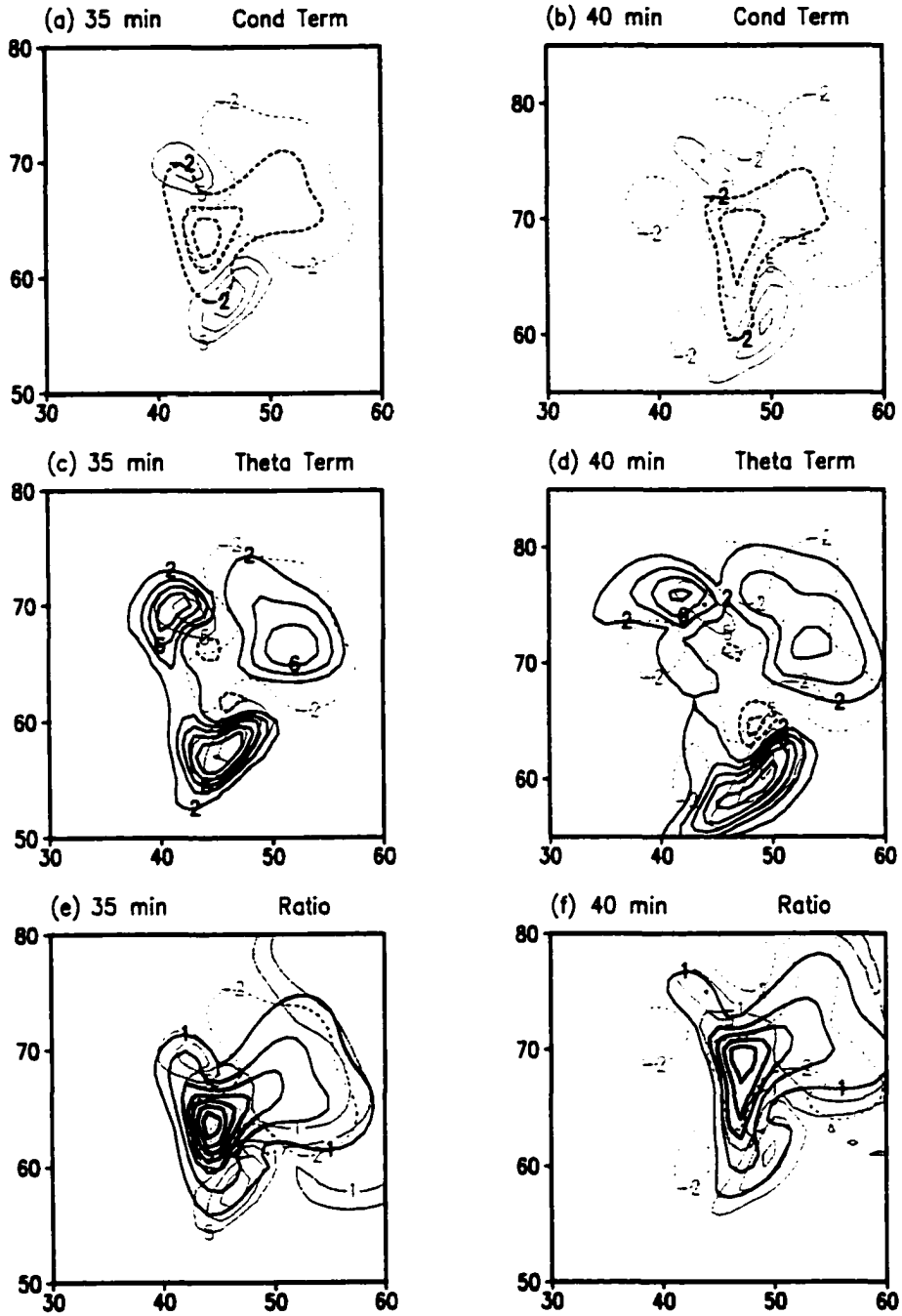


**Figure 5.20: 3mm case at 2 km AGL. In (a) and (b) are the vertical velocity (thin lines) and the -g($r_c$) term (thick) at 35 and 40 minutes respectively; (c) and (d) show the vertical velocity (thin lines) and the g($\theta_v'/\theta_0$) term (thick lines) at 35 and 40 minutes respectively; (e) and (f) depict the vertical velocity (thin lines), the condensate mixing ratio (thick lines) and the ratio $|g(\theta_v'/\theta_0)|/|gr_c|$ (shaded) at 35 and 40 minutes respectively. Solid lines represent positive magnitudes while dashed lines represent negative values. The contour interval is 1 g.kg$^{-1}$ for the condensate mixing ratio, 2m.s$^{-2}$ for the forcing terms (forcing terms are multiplied by 100), and 5 m.s$^{-1}$ for the updrafts. The –2m.s$^{-1}$ isoline is also shown. All zero isolines are omitted. Shaded regions are where the ratio < 1 and unshaded regions are where the ratio > 1.**

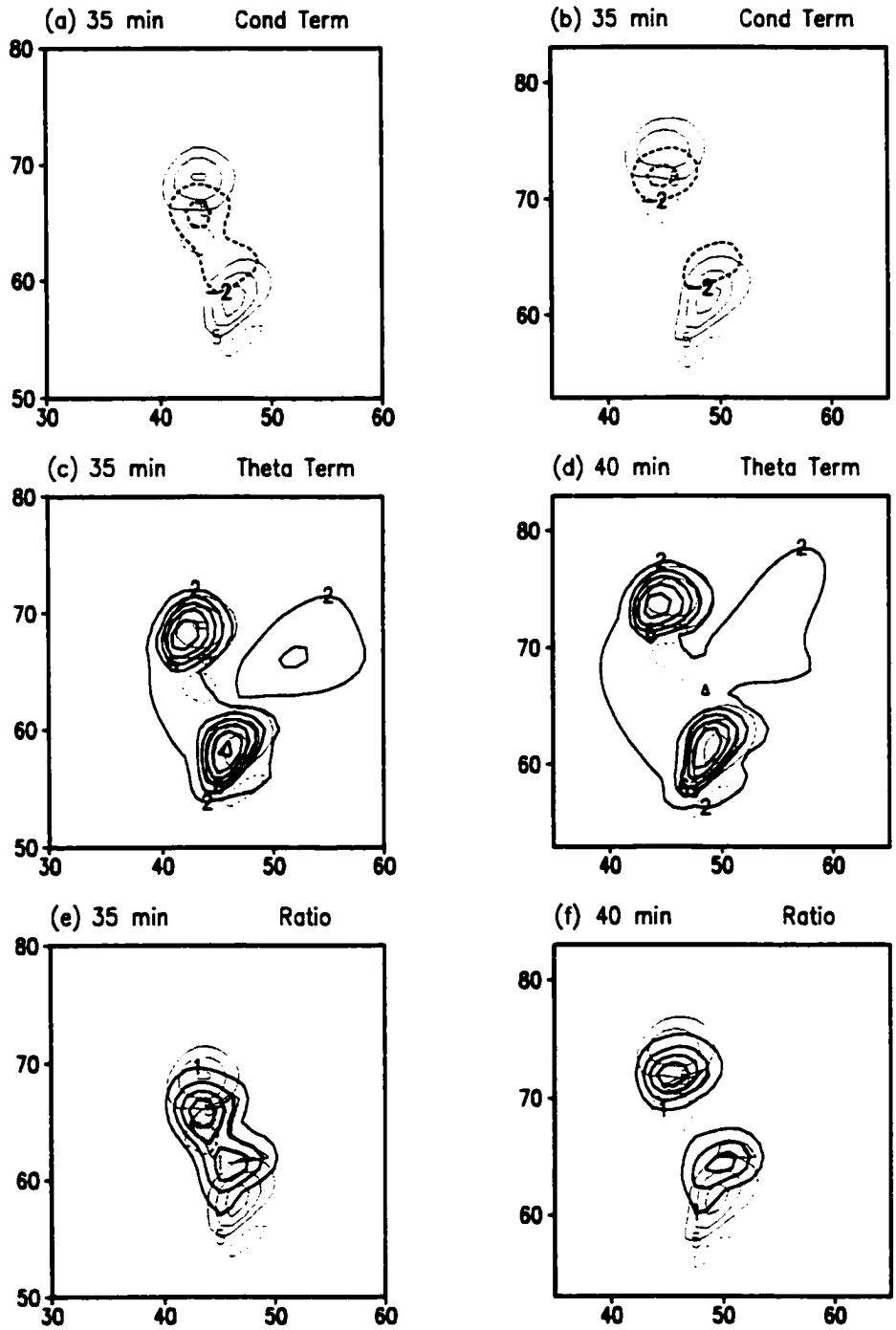


**Figure 5.21: 2cm case at 2 km AGL. In (a) and (b) are the vertical velocity (thin lines) and the -g($r_c$) term (thick) at 35 and 40 minutes respectively; (c) and (d) show the vertical velocity (thin lines) and the g($\theta_v'/\theta_0$) term (thick lines) at 35 and 40 minutes respectively; (e) and (f) depict the vertical velocity (thin lines), the condensate mixing ratio (thick lines) and the ratio $|g(\theta_v'/\theta_0)|/|gr_c|$ (shaded) at 35 and 40 minutes respectively. Solid lines represent positive magnitudes while dashed lines represent negative values. The contour interval is 1 g.kg$^{-1}$ for the condensate mixing ratio, 2m.s$^{-2}$ for the forcing terms (forcing terms are multiplied by 100) and 5 m.s$^{-1}$ for the updrafts. The –2m.s$^{-1}$ isoline is also shown. All zero isolines are omitted. Shaded regions are where the ratio < 1 and unshaded regions are where the ratio > 1.**

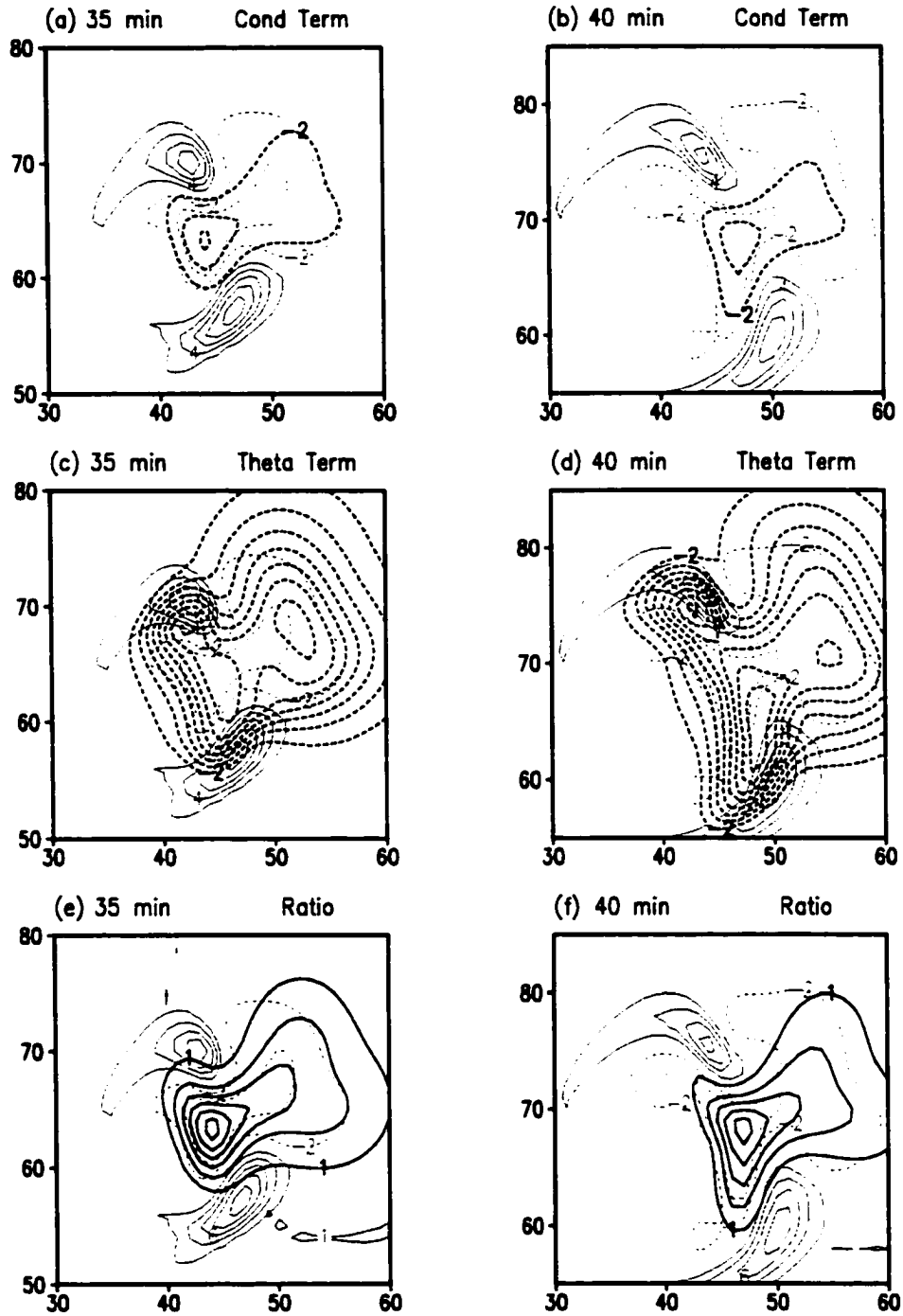


**Figure 5.22: 3mm case at 1 km AGL. In (a) and (b) are the vertical velocity (thin lines) and the $-g(r_c)$ term (thick) at 35 and 40 minutes respectively; (c) and (d) show the vertical velocity (thin lines) and the $g(\theta_v'/\theta_0)$ term (thick lines) at 35 and 40 minutes respectively; (e) and (f) depict the vertical velocity (thin lines), the condensate mixing ratio (thick lines) and the ratio $|g(\theta_v'/\theta_0)|/|gr_c|$ (shaded) at 35 and 40 minutes respectively. Solid lines represent positive magnitudes while dashed lines represent negative values. The contour interval is 1 $g.kg^{-1}$ for the condensate mixing ratio, 2 $m.s^{-2}$ for the forcing terms (forcing terms are multiplied by 100) and 2 $m.s^{-1}$ for the updrafts. The $-2m.s^{-1}$ isoline is also shown. All zero isolines are omitted. Shaded regions are where the ratio < 1 and unshaded regions are where the ratio > 1.**

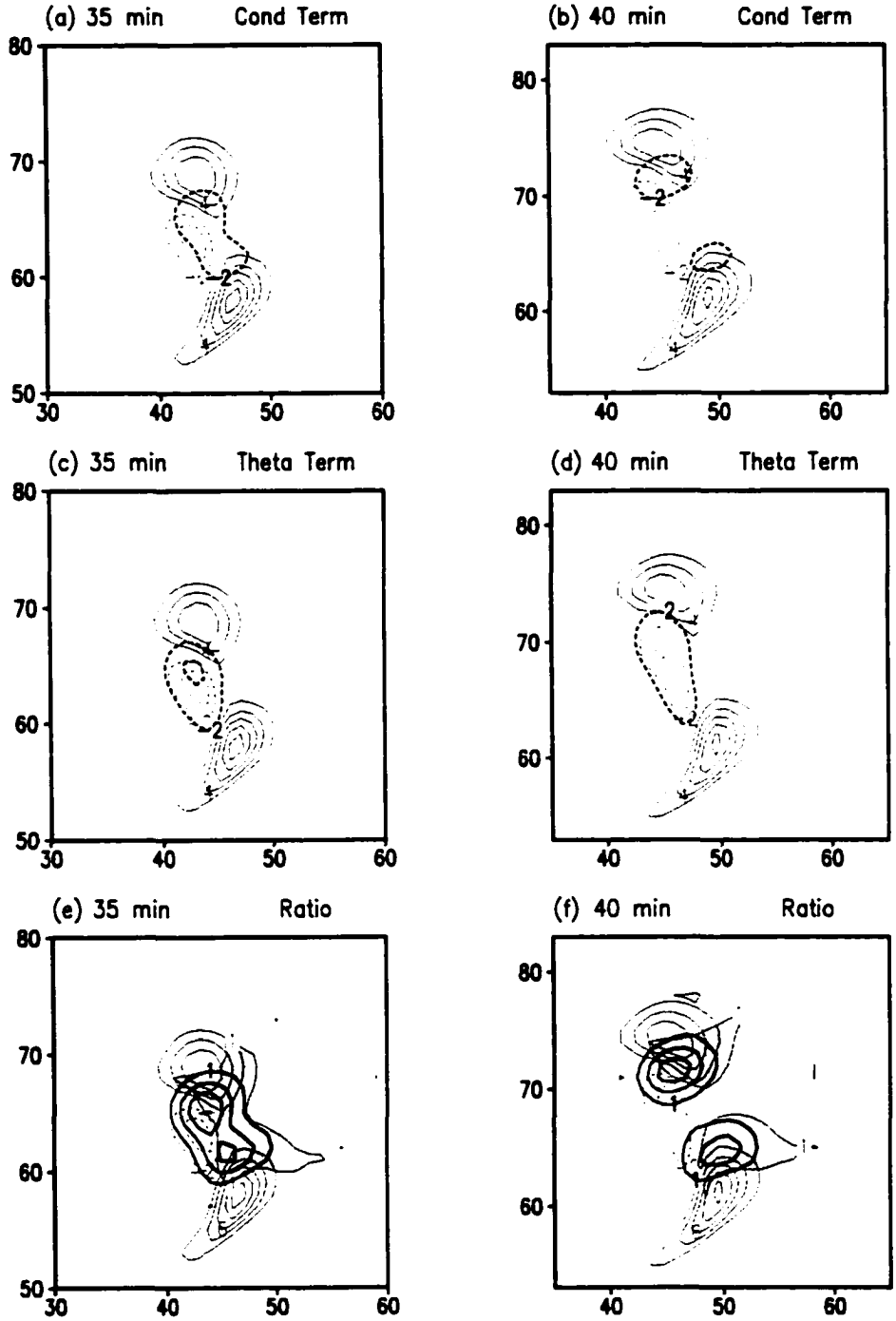


**Figure 5.23: 2cm case at 1 km AGL. In (a) and (b) are the vertical velocity (thin lines) and the $-g(r_c)$ term (thick) at 35 and 40 minutes respectively; (c) and (d) show the vertical velocity (thin lines) and the $g(\theta_v'/\theta_0)$ term (thick lines) at 35 and 40 minutes respectively; (e) and (f) depict the vertical velocity (thin lines), the condensate mixing ratio (thick lines) and the ratio $|g(\theta_v'/\theta_0)|/|gr_c|$ (shaded) at 35 and 40 minutes respectively. Solid lines represent positive magnitudes while dashed lines represent negative values. The contour interval is 1 $g.kg^{-1}$ for the condensate mixing ratio, $2m.s^{-2}$ for the forcing terms (forcing terms are multiplied by 100), and 2 $m.s^{-1}$ for the updrafts. The $-2m.s^{-1}$ isoline is also shown. All zero isolines are omitted. Shaded regions are where the ratio < 1 and unshaded regions are where the ratio > 1.**

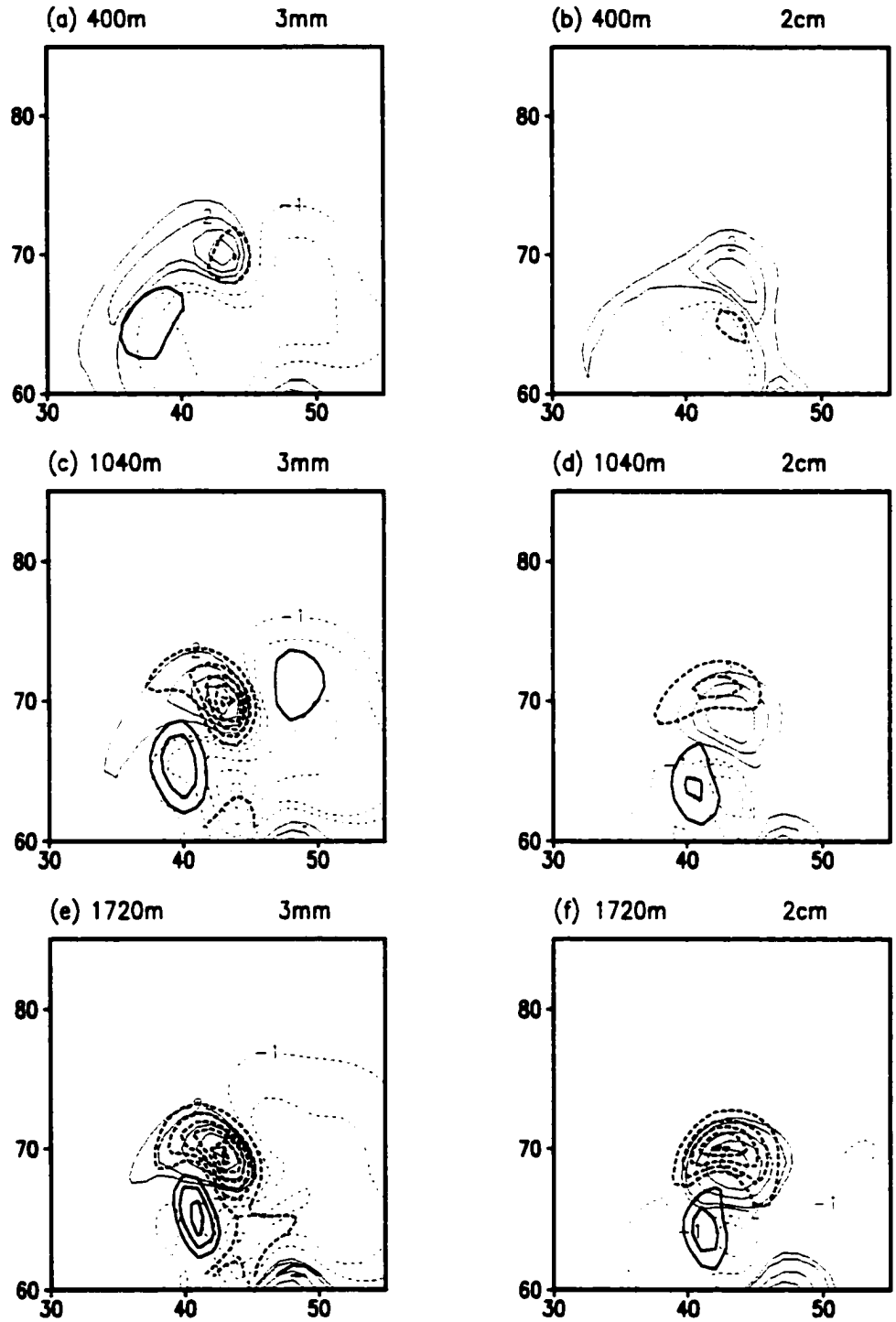


**Figure 5.24: Vertical velocity (thin lines) and vertical vorticity (thick lines) for the 3mm (left column) and 2cm (right column) cases at 400 m (a,b), 1040m (c,d) and 1720m AGL (e,f). Solid lines represent positive magnitudes while dashed lines represent negative values. The contour interval for the vertical velocity is 2m.s$^{-1}$ at the 400 m level, and 5 m.s$^{-1}$ at 1040m and 2000m levels. The contour interval for vertical vorticity is 0.002 s$^{-1}$ for all figures.**

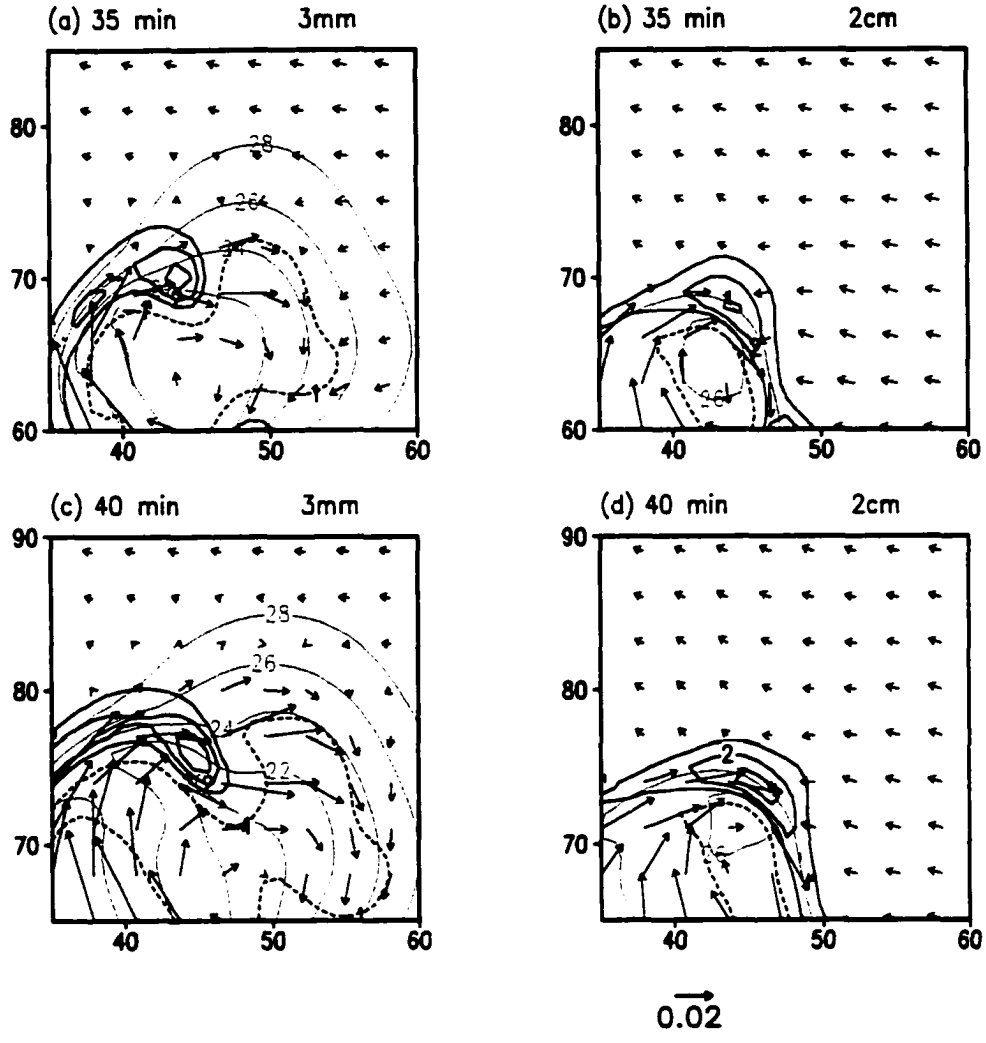


**Figure 5.25: Vertical velocity (thick lines), temperature (thin lines), and horizontal vorticity vectors for the 3mm (left column) and 2cm (right column) cases at 250m AGL at 35 (a,b) and 40 (c,d) minutes. The contour interval for the vertical velocity is 1m.s$^{-1}$ and for the temperature is 2°C. The vector scale (s$^{-1}$) is indicated at the bottom right of the figure.**

In both the 3mm and 2cm simulations, the RM was stronger than the LM, at both the 1 km and 2 km levels, which is consistent with linear theory. In the 3mm case, the LM storm dissipates after ~45 minutes of simulation time, which also appears supported by linear theory. However, in the 2cm case, which is run using the identical hodograph and sounding as in the 3mm case, the LM storm is long-lived. If the veering of the hodograph is the predominant cause of the demise of the LM in the 3mm case, then the LM in the 2cm case should also dissipate as it is subject to the same environmental wind conditions. However, this is not the case. Also, the $\pi'$ forcing within the 3mm LM at the

1km level is significantly greater than that within the RM, which is inconsistent with linear theory. Finally, the $\pi$' forcing at 1km is greater in the 3mm case than the 2cm case, and yet the LM dissipates in the 3mm case. These points suggest that other processes, apart from the linear response of the updraft interacting with the environmental shear, may affect the longevity of the LM storm.

In the 3mm case, the dissipation of the LM was associated with a reduction in positive buoyancy at the 2 km level, and a substantial increase in negative buoyant forcing throughout the entire LM updraft at the 1 km level. The negative buoyant forcing within the LM in the 3mm case was maintained by the low-level storm-relative inflow, which came almost entirely from the region of the cold pool. The negative buoyant forcing had less of an impact on the RM storm, as a significant amount of the low-level inflow air originated from the undisturbed environment. In the 2cm case, downward forcing due to negative buoyancy effects, had very little impact on both the LM and the RM. It would appear, from these results, that the 3mm LM dissipates as a result of the ingestion of highly negatively buoyant air from the downdraft and cold pool; whereas, the 2cm LM does not dissipate as it ingests significantly less negatively buoyant air.

From the discussion and analysis of the results presented above, buoyant effects appear to play an important role in the longevity of the LM. This is supported by the fact that the only difference between the 3mm and 2cm simulations was a change in the mean hail diameter, which influences the buoyant forcing through both latent heat absorption and release. The importance of buoyant forcing is also supported by the increase in the longevity of the LM as the mean hail diameter is increased from 3mm to 5mm, from 5mm to 1cm, and from 1cm to 2cm (see Figure 4.2). In all of these cases, the hodograph was identical. However, the low-level buoyant forcing varied significantly due to differences in the cold pool strength and rate of movement of the cold pool.

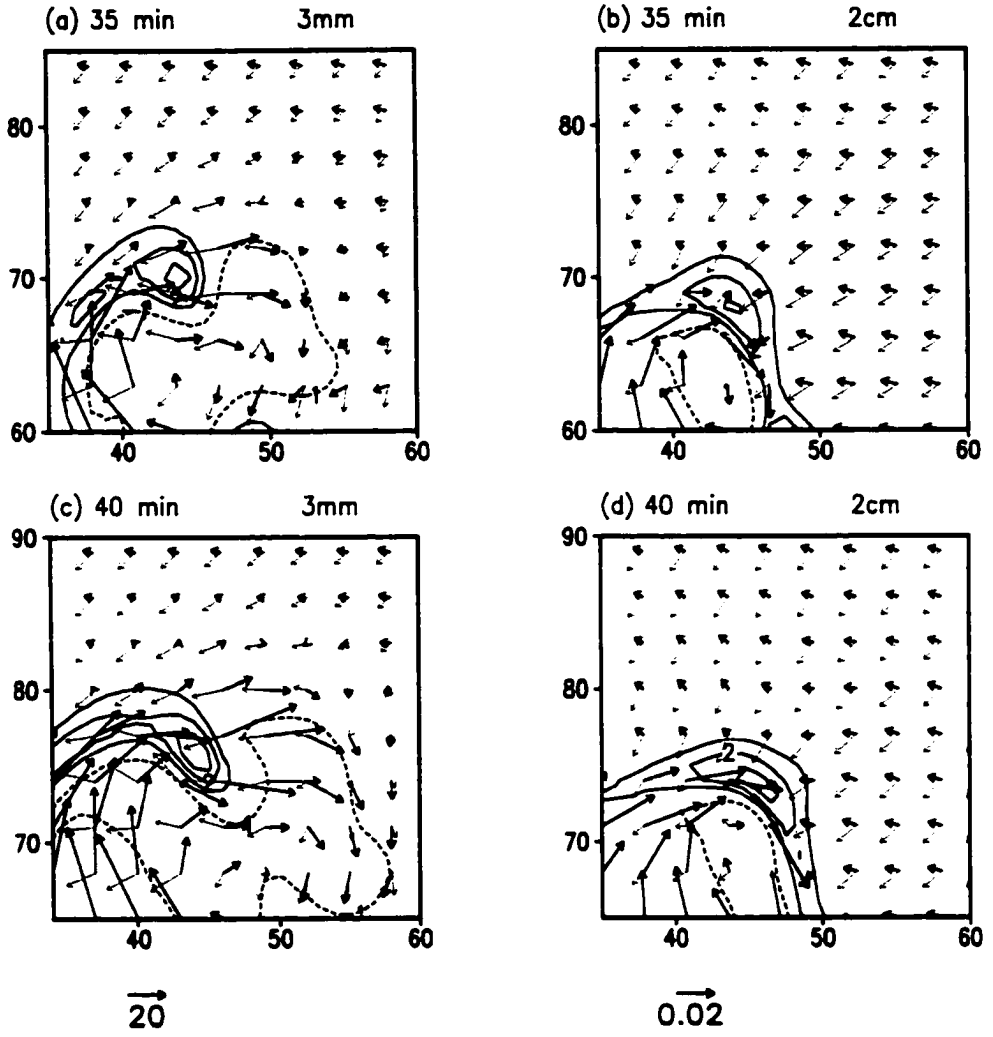


**Figure 5.26: Vertical velocity (thick lines), horizontal vorticity vectors (thick) and storm-relative wind vectors (thin) for the 3mm (left column) and 2cm (right column) cases at 250m AGL at 35 (a,b) and 40 (c,d) minutes. The contour interval for the vertical velocity is 1m.s$^{-1}$. The scale for the storm-relative wind vectors (m.s$^{-1}$) is shown on the bottom left and for the horizontal vorticity vectors (s$^{-1}$) on the bottom right of the figure.**

Even though buoyancy appears to play an important role in the longevity of the LM, this does not imply that the linear effect does not have an influence on the LM. In both the 3mm and 2cm case, the $\pi$' forcing associated with the RM was similar to or greater than that with the LM, which supports the predictions made by linear theory. The exception to this was at the 1km level in the 3mm case, where the baroclinic generation and subsequent tilting of horizontal vorticity in the LM updraft, affected the low-level vertical vorticity and resultant vertical gradients in $\pi$'.

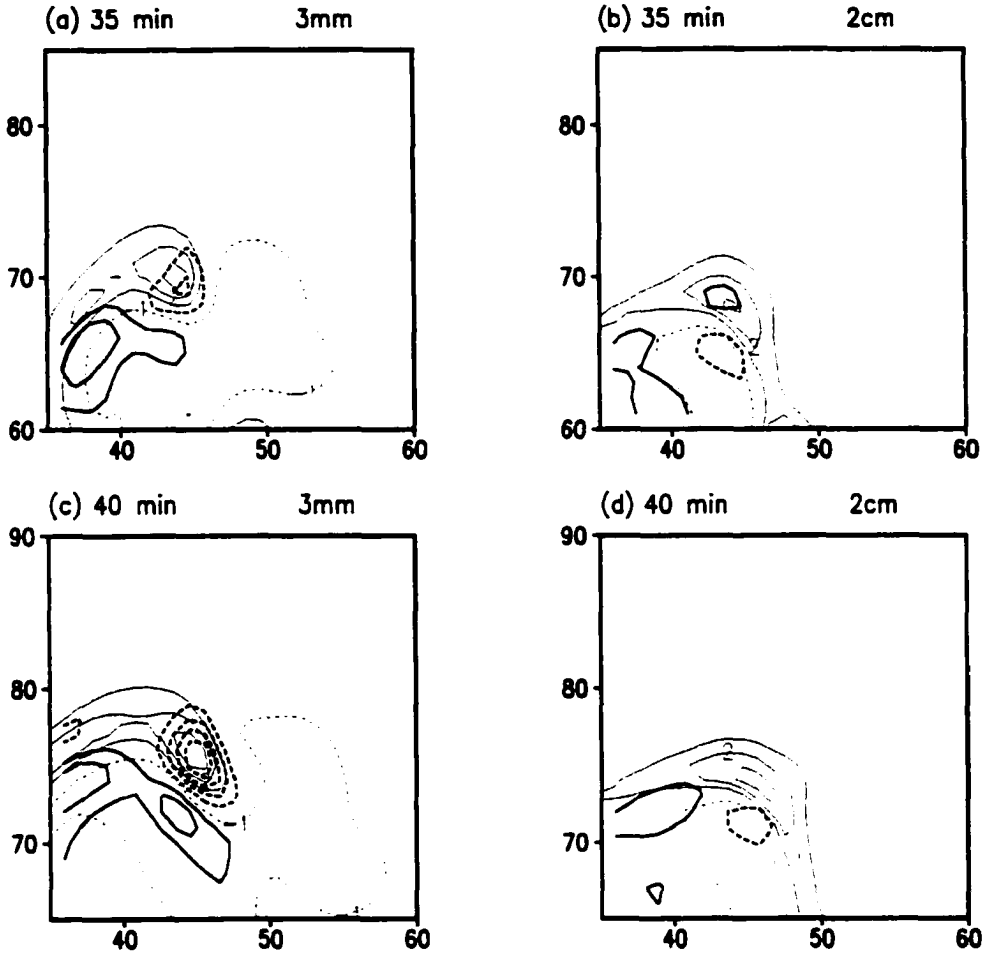


**Figure 5.27: Vertical velocity (thin lines) and vertical vorticity (thick) for the 3mm (left column) and 2cm (right column) cases at 250m AGL at 35 (a,b) and 40 (c,d) minutes. Solid lines represent positive magnitudes while dashed lines represent negative values. The contour interval for the vertical velocity is 1m.s$^{-1}$ and for the vertical vorticity is 0.002 s$^{-1}$.**

Examining the contribution made by the "theta" and "loading" terms to the numerical buoyancy reveals how reducing the mean hail diameter affects the buoyant forcing, and hence the longevity of the LM. In the 2cm simulation, the contributions made by the "loading" and "theta" terms to the negative buoyant forcing were comparable, indicating that evaporative cooling and drag due to condensate loading have similar effects on the downward forcing. However in the 3mm case, the "theta" term is significantly greater than the drag term, demonstrating the importance of evaporative cooling in generating negative buoyant forcing in this case.

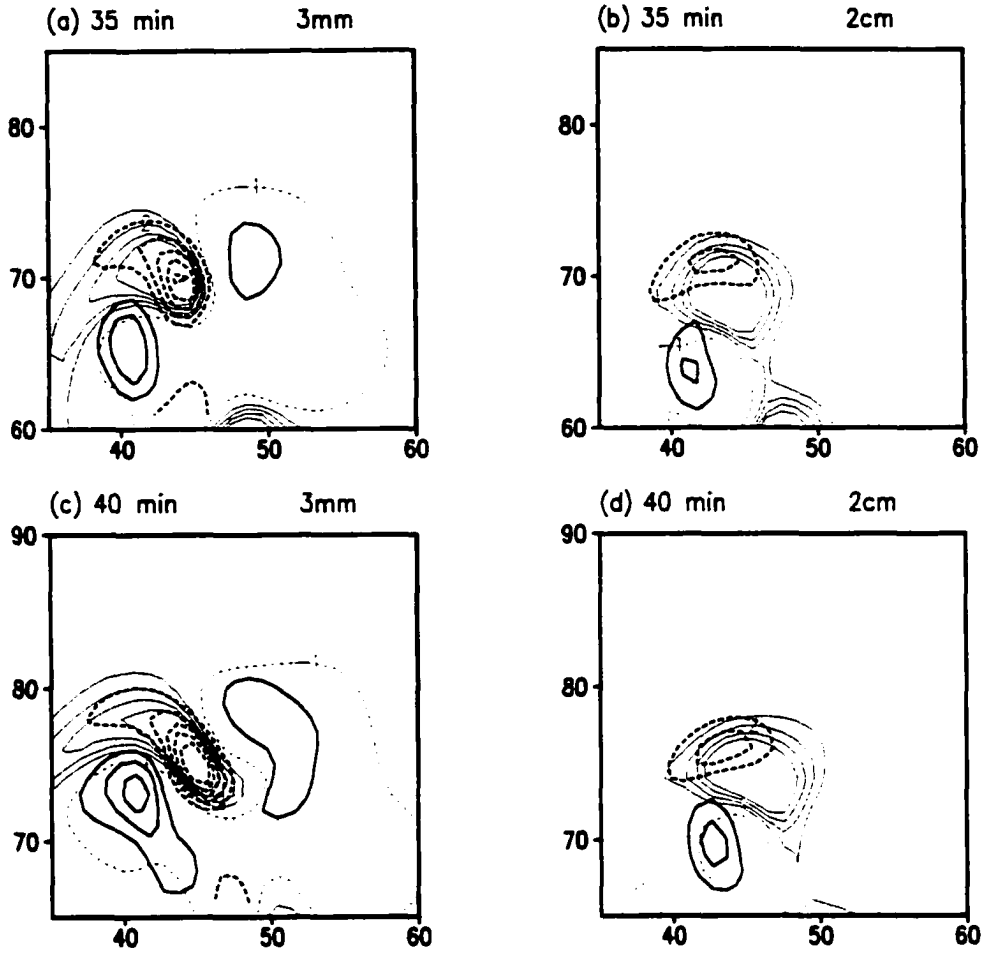


**Figure 5.28: Vertical velocity (thin lines) and vertical vorticity (thick) for the 3mm (left column) and 2cm (right column) cases at 1km AGL at 35 (a,b) and 40 (c,d) minutes. Solid lines represent positive magnitudes while dashed lines represent negative values. The contour interval for the vertical velocity is 1m.s$^{-1}$ and for the vertical vorticity is 0.002 s$^{-1}$.**

As discussed by Weisman and Klemp (1984), and summarized by Grasso (2000), $\pi'$ is governed by both dynamic and buoyant contributions, and the buoyant contribution to the $\pi'$ forcing should be included with the numerical buoyancy term as such:

$$-\theta_0 \frac{\partial \pi'_{dyn}}{\partial z} - \left[ \theta_0 \frac{\partial \pi'_{buo}}{\partial z} - g\left( \frac{\theta'_v}{\theta_0} - r_c \right) \right], \tag{5.2}$$

where the subscripts dyn and buo refer to the dynamic and buoyant contributions to $\pi'$, respectively. This is suggested as future work. This research simply serves as an

introductory study of the importance of microphysical processes to storm dynamics, and it demonstrates the impact that negative buoyant forcing has on the LM updraft.

Finally, the conclusions drawn here support, as well as extend, those of Grasso (2000). He compared his 'precipitation' simulation in which the LM decayed, to a simulation in which he suppressed precipitation completely and the LM was long-lived. In the simulations presented here, precipitation has not been suppressed, and a cold pool does form in both simulations, which is a step closer toward what is observed in actual storms. These results demonstrate that, even in the presence of hail and rain, a long-lived LM storm may develop. Both Grasso's results and those presented here demonstrate that other processes, apart from the linear interactions associated with the environmental shear and the updraft, may be important in determining the longevity of the LM. Buoyancy appears to be such a process in these simulations. This, in turn, points to the impact of the cold pool and microphysical processes on storm longevity.

## 5.6 Summary

The main findings of the research presented in this chapter may be summarized as follows:

- In the 3mm case, the LM storm dissipates after 45 minutes of simulation time. In the 2cm case, the LM exists for the entire simulation. As the hodograph in the simulations were identical, this suggests that processes other than the linear response of the updraft interacting with the environmental shear vector may affect the longevity of the LM.

- The LM in the 3mm case dissipated as the entire updraft become progressively negatively buoyant through the ingestion of cold downdraft and cold pool air. The negative buoyant forcing was enhanced by the strength of the cold pool and by the storm-relative flow, which was almost entirely from the cold pool region. Negative

buoyant forcing had very little impact on the LM in the 2cm case, which allowed for the updraft to exist throughout the simulation, supported by positive $\pi'$ forcing. Negative buoyant forcing, or the lack thereof, therefore appears to exert an important influence on the longevity of the LM.

- The RM in the 3mm case did not dissipate. The storm-relative low-level flow into the RM was partially from the region of the cold pool; however, the rest of the inflow air came from the undisturbed environment, which prevented the RM updraft from becoming completely negatively buoyant.

- The RM was stronger than the LM in both the 3mm and 2cm cases, and the $\pi'$ forcing associated with the RM was greater than within the LM in both cases. This shows, that even though the buoyant forcing appears to be the primary factor controlling the longevity of the LM in these simulations, the vertical gradients in $\pi'$ still influence the RM/LM bias.

- The $\pi'$ forcing at the 1 km level is an exception to the previous point, as the forcing within the LM is greater than within the RM. This appears to be caused by the tilting of the negative streamwise horizontal vorticity, that is baroclinically generated, into the LM updraft, thereby strengthening the low-level negative vertical vorticity, which drops the low-level $\pi'$. As the $\pi'$ remains relatively steady at the 1 km level, the vertical gradients in $\pi'$ are reduced.

- The impact of increasing the mean hail diameter on the longevity of the LM is realized through the control that the buoyant forcing has on the LM updraft. As the mean hail diameter is decreased, the evaporative cooling rates increase and a stronger, faster-moving, cold pool develops. This has two effects on the negative buoyancy: (1) the faster moving cold pool surges out ahead of the LM, forcing more of the low-level storm-relative inflow air to originate within the cold pool itself; and (2) the colder cold pool means the air being ingested by the LM in the smaller hail cases is more

negatively buoyant. Therefore, as the mean hail diameter is decreased, the longevity of the LM decreases as the impact of negative buoyant forcing on the LM updraft increases.

# 6

# Sensitivity to the Shape Parameter, Exclusion of Ice Species, and the Scheme Complexity

## 6.1 Introduction

In Chapters 4 and 5, the impact of changing the mean hail diameter on supercell storm characteristics was examined. The mean hail diameter is, however, only one of the microphysical parameters that may need to be determined, when utilizing microphysical parameterization schemes in mesoscale and cloud models. In this chapter, the sensitivity of simulated severe storms to several other microphysical factors is investigated. In particular, the sensitivity to changes in the shape parameter of the hail size distribution will be examined in the first section, the sensitivity to the species included will be determined in the second section, and the sensitivity to the microphysical scheme complexity will be assessed in the third section.

## 6.2 Sensitivity to Changes in the Gamma Distribution Shape Parameter

### 6.2.1 *Introduction*

It is generally thought that an exponential distribution (v=1) of a hydrometeor species is not an accurate representation of the actual hydrometeor distribution observed within

clouds. Nevertheless, exponential distributions are regularly used. The variation in the hail size distribution due to changes in $\nu$ was shown in Figure 3.2. It is apparent from this figure that increasing $\nu$ narrows the spectral width of the distribution. There are a greater number of small and large hail particles, and fewer medium-sized particles for the smaller values of the shape parameter. For the 3mm mean hail diameter case, the model diameter (see Eq. 3.3) is 0 mm when $\nu$=1, 2 mm when $\nu$=3, and 2.4 mm when $\nu$=5. As $\nu$ increases, the modal diameter approaches the mean diameter, and the distribution curve gets narrower. The shape parameter therefore controls the relative amount of smaller versus larger hydrometeors in the distribution.

The question that now needs addressing is whether smaller or large values of $\nu$ will favor more rapid melting and evaporation rates? In the $\nu$=1 case, the larger number of small hail particles will enhance melting and evaporation rates. However, in this case there are also more large hailstones that can withstand melting more effectively. Also, if the predicted hail mixing ratios are the same in the simulations, the number concentration in the $\nu$=5 case is ~3.5 times greater than in the $\nu$=1 case. This reduces the difference between the number of small particles in the $\nu$=1 and $\nu$=5 cases. It is not therefore immediately apparent from the size distribution which shape parameter will result in the greatest melting and evaporation rates.

Sensitivity tests have been conducted using values of 3 and 5 for $\nu$ in all four of the mean hail diameter cases referred to in Chapter 4. The value of $\nu$ in these cases was originally 1 (exponential distribution). The details of the simulations were shown in Table 3.2. It was found that varying the shape parameter led to similar results and trends in all four diameter cases. Thus, only those results obtained using a mean hail diameter of 3mm will be presented. The sensitivity test results presented here, therefore, all have a mean hail diameter of 3mm, and $\nu$ values of 1, 3 or 5. The model setups are otherwise identical. The tests will be referred to as the NU1 ($\nu$=1), NU3 ($\nu$=3) and NU5 ($\nu$=5) cases. It should be noted that $\nu$ has been varied only for the hail species. The shape parameter of all the

other species has been kept at 1. The NU1 case referred to here is identical to the 3mm case in chapters 4 and 5. The 3mm notation will also be used again in the sensitivity tests that follow this one.

### 6.2.2 *Results*

The impact of changing ν on the supercell characteristics is evident in the storm tracks (Figure 6.1). In all three ν cases, the LM dissipates early in the simulation, although the longevity of the LM does increase as the value of ν increases. The RM storm is also longer-lived and steadier as ν increases. The low-level occlusion-type processes, discussed in detail in Chapter 4, occur later in the NU3 and NU5 cases, and have less of an impact on the strength and re-development of the RM storm. Varying the shape parameter therefore has an impact on the development rate and storm strength; however, the impact is not as great as when the mean hail diameter is varied from 3mm to 2cm (see Figure 4.2).

After the initial response to the thermal perturbation, the updrafts in the NU3 and NU5 cases lag the NU1 updraft slightly in their development, but they recover more rapidly and do not collapse to the extent of the NU1 updraft (Figure 6.2). There appears to be a critical value of the shape parameter, below which the updraft continues to collapse and takes longer to recover. The vertical velocity is controlled primarily, although not exclusively, by the low-level convergence (Figure 6.3). This is evident in the close correspondence of the trends in vertical velocity and low-level convergence. Similar results were observed in the diameter sensitivity tests in Chapter 4.

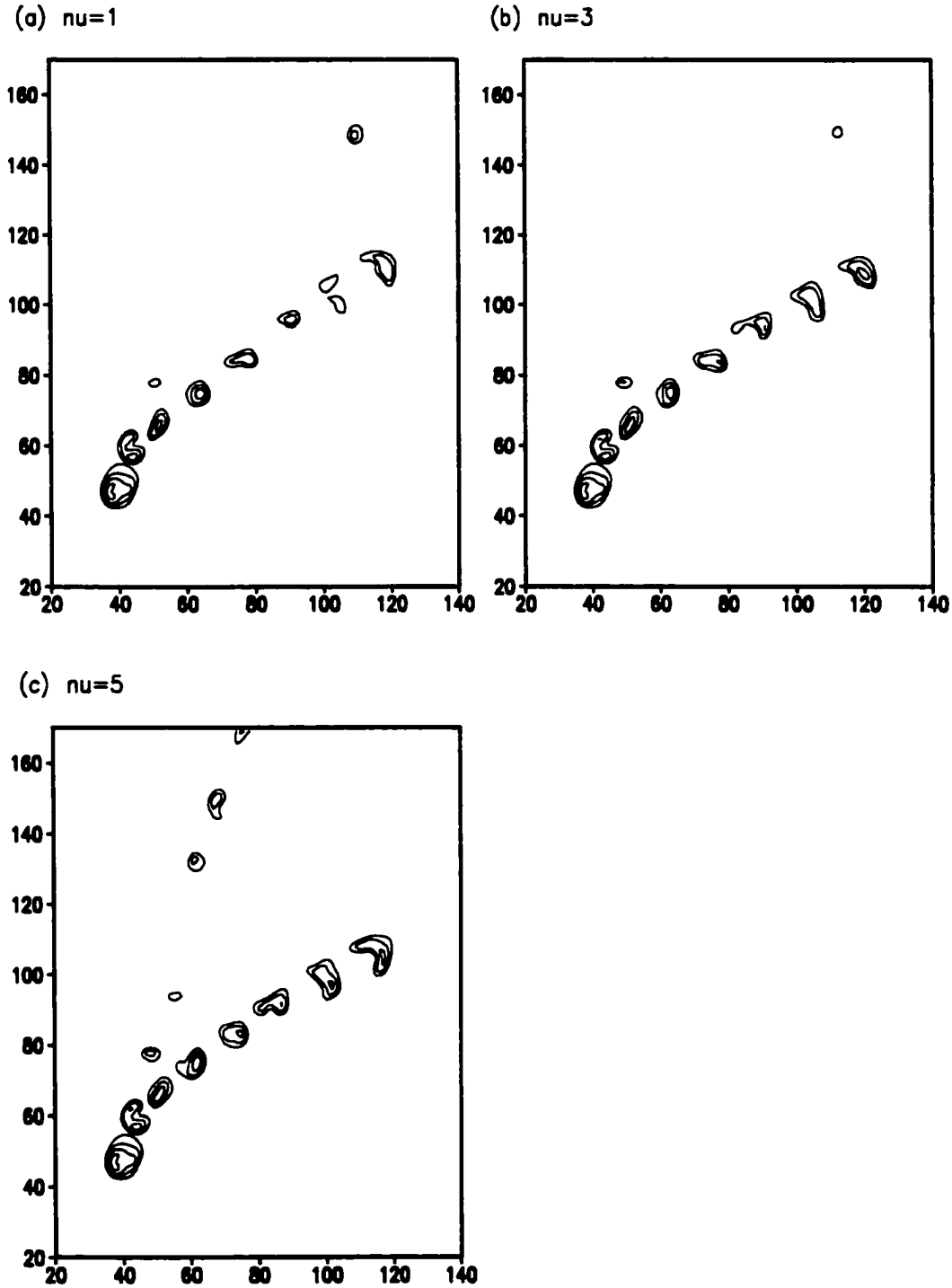


**Figure 6.1: Storm tracks for the (a) NU1, (b) NU3, and (c) NU5 cases. Field shown is vertical velocity ($m.s^{-1}$) at 4830m AGL. Contour interval is $10m.s^{-1}$ starting 10 $m.s^{-1}$. Storm positions are shown at 15 minute intervals starting from the southwest grid corner.**

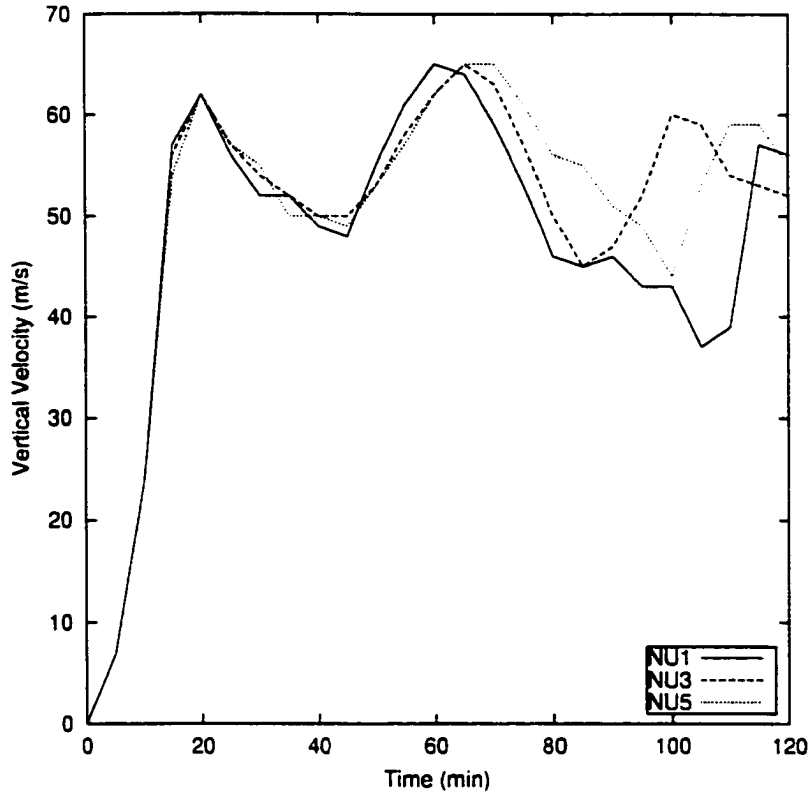


**Figure 6.2: Maximum updraft velocity as a function of time for the NU1 (solid line), NU3(dashed line), and NU5 (dotted line) simulations.**

The low-level convergence fields also help explain why the NU1 updraft collapses to a greater extent than in the other cases. Convergence along the NU1 gust front to the southeast of the updraft is greater than within the main updraft from 70 until 110 minutes (Figure 6.3a). This does not occur in the NU5 case until the end of the simulation (Figure 6.3b). The strong eastward surge of the gust front in the NU1 case intersects the low-level southeasterly flow into the updraft, thereby almost completely reducing the supply of moisture and heat to the updraft, while at the same time increasing the convergence of the inflow air into the extended region of the gust front (Figure 6.4). Deprived of its thermal energy, the updraft collapses. In the NU3 and NU5 cases, even though the gust front extends eastward, it does not extend as far as in the NU1 case. The

(a)

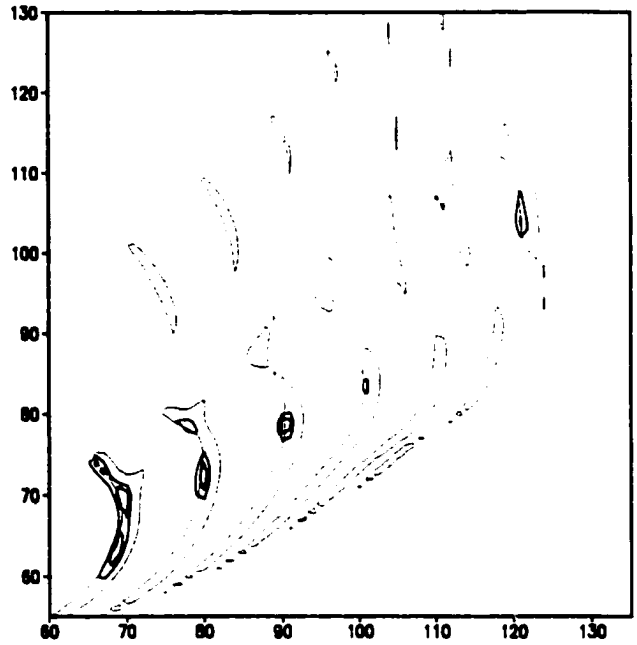


(b)

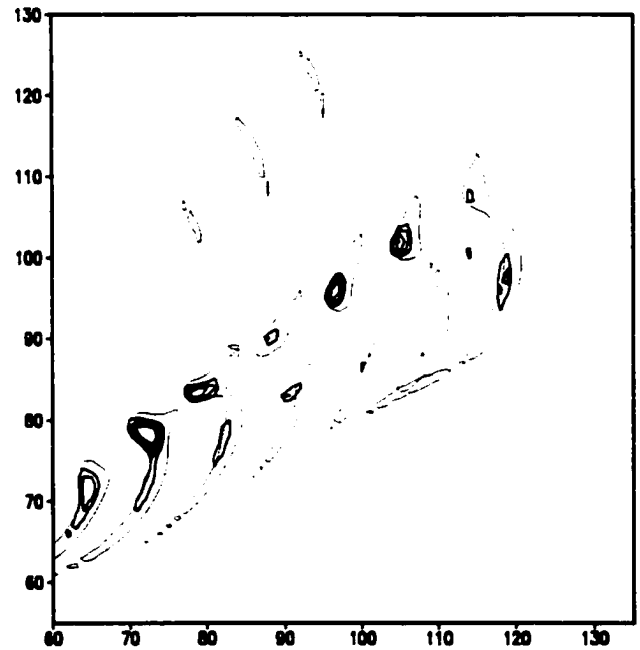


**Figure 6.3: Convergence (thick lines, contours 0.007, 0.008, 0.009, 0.01 $s^{-1}$) and vertical velocity (thin lines, contour shown is 2 $m.s^{-1}$) at 400m AGL for the (a) NU1 and (b) NU5 cases. The fields are at 10 minute intervals from 60 to 120 minutes from left to right in each figure.**

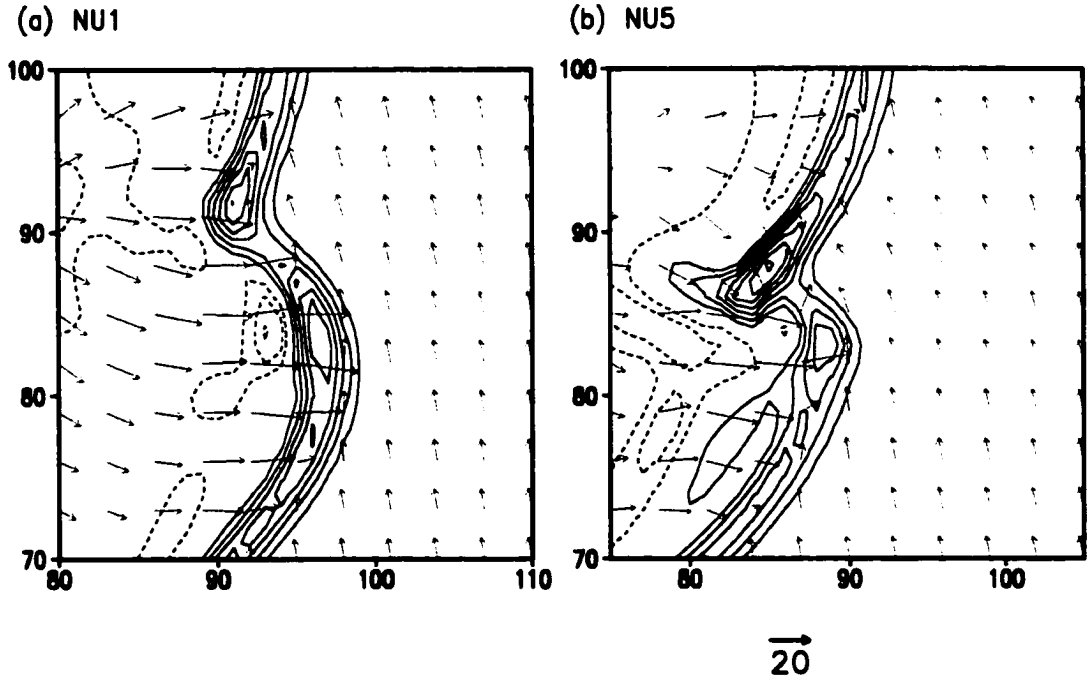


**Figure 6.4: Vertical velocity (thick lines, interval 0.5 m.s$^{-1}$) and ground-relative wind vectors at 150m AGL at 80 minutes for (a) NU1 and (b) NU5 cases.**

low-level inflow air can still reach the main updraft, and does not primarily converge within the gust front extension. The transport of the low-level air into the updraft in the NU3 and NU5 cases is also aided by the low-level vertical vorticity. As the updrafts are still being fed with heat and moisture, they do not collapse to the extent of the updraft in the NU1 case.

The low-level downdrafts show an overall increase in strength with a decrease in the shape parameter (Figure 6.5). Examination of the contribution of the three terms in the vertical velocity tendency equation (see Eq. 4.1) revealed that the buoyant forcing is the dominant factor controlling the development of the low-level downdrafts in all three cases. The turbulent forcing is relatively small compared to the other terms, and the pressure gradient forcing is actually positive in the region of the downdraft in every case (not shown). As we saw from Eq. (4.1), the buoyant forcing is comprised of a

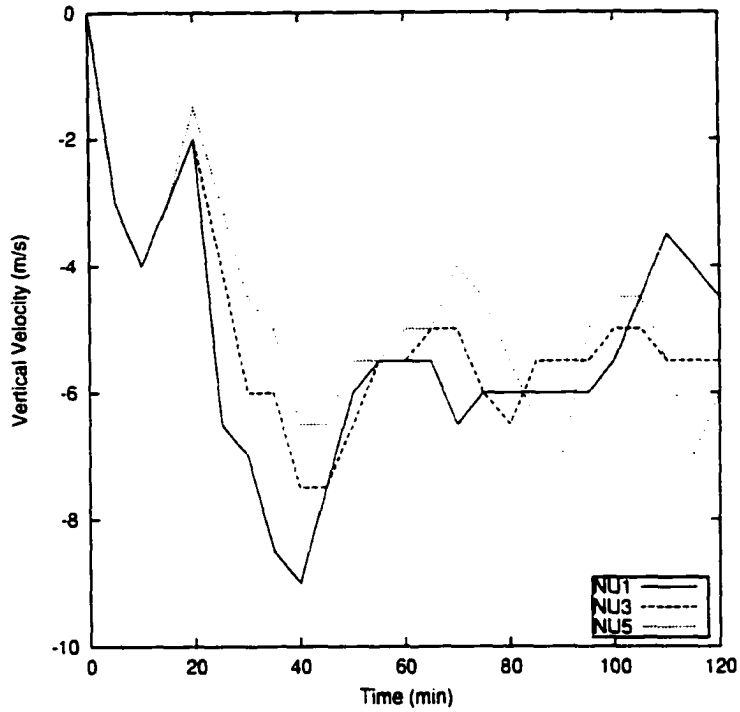


**Figure 6.5: Maximum downdraft strengths below 1km AGL as a function of time for the NU1 (solid line), NU3 (dashed line), and NU5 (dotted line) simulations.**

thermodynamic term ($g\theta_v'/\theta_0$) and a condensate loading term ($-gr_c$). It is apparent from Figure 6.6 that the thermodynamic forcing of the downdraft is significantly greater than the forcing due to condensate loading in both the NU1 and NU5 cases. Also, the thermodynamic forcing and the condensate loading are both greater in the NU1 case than their respective counterparts in the NU3 (not shown) and NU5 cases. These results indicate that the melting and evaporation rates increase as the shape parameter decreases. The larger condensate loading term in the NU1 case is due to the greater hail mixing ratios.

The development of the cold pool in the three cases supports the observation that melting and evaporation rates are greater when the shape parameter is smaller (Figure 6.7). At 60 minutes, cold pool temperature perturbations differ by 4K between the NU1 and NU5 cases. However, by 90 minutes the perturbation potential temperature differences are less (Figure 6.8a,b), and by 120 minutes, the NU3 and NU5 cold pools are

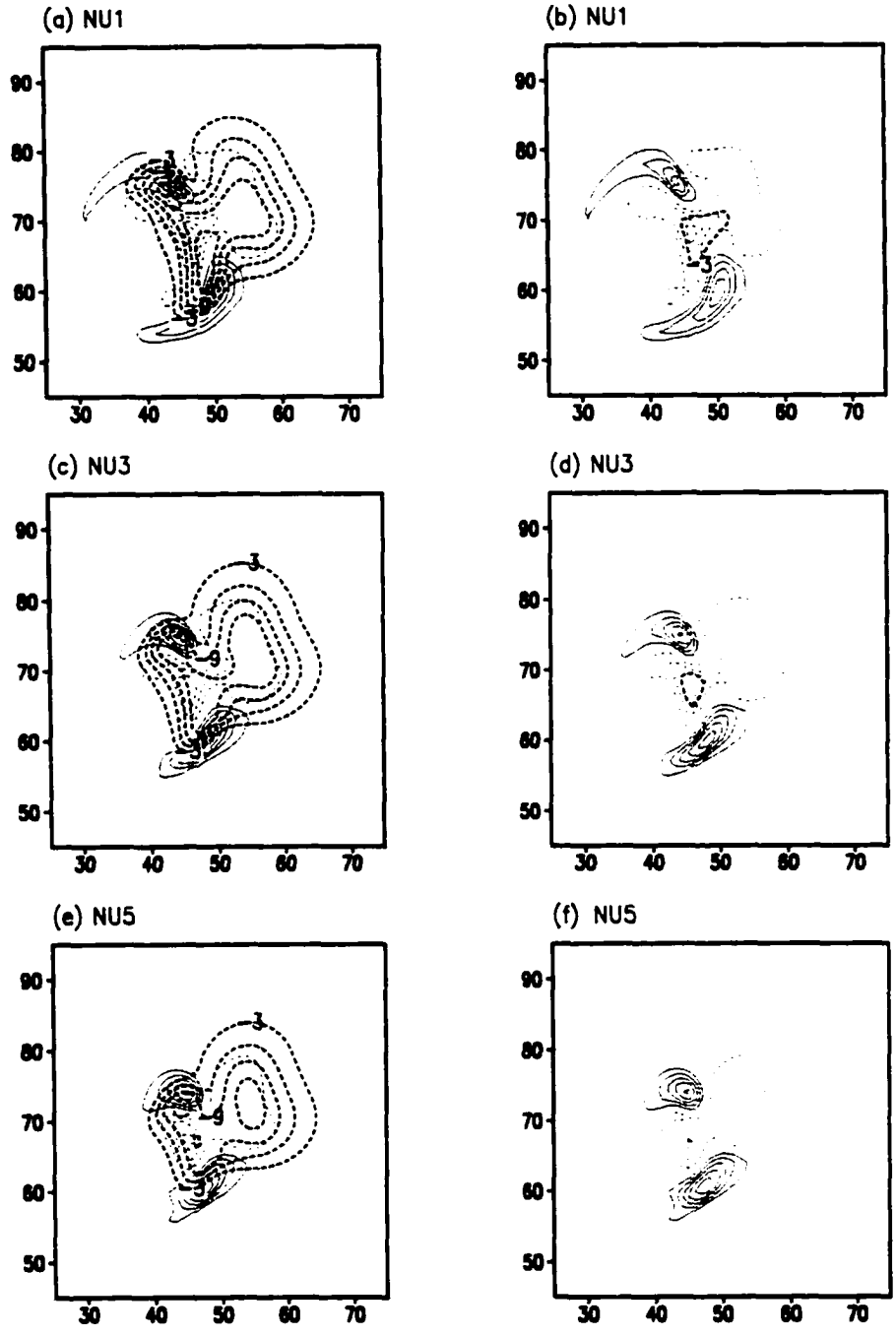


**Figure 6.6: The contributions made by the thermodynamic term ($g\theta_v'/\theta_0$) for the (a) NU1, (c) NU3, and (e) NU5 cases, and by the condensate loading term ($-gr_c$) for the (b) NU1, (d) NU3 and (f) NU5 cases at 40 minutes at 1 km AGL. The contour interval for the vertical velocity (thin lines) is 2 $m.s^{-1}$, and for the forcing terms (thick lines) is 3 $m.s^{-2}$. Forcing terms are multiplied by 100. Solid lines indicate positive values and dashed lines represent negative values.**

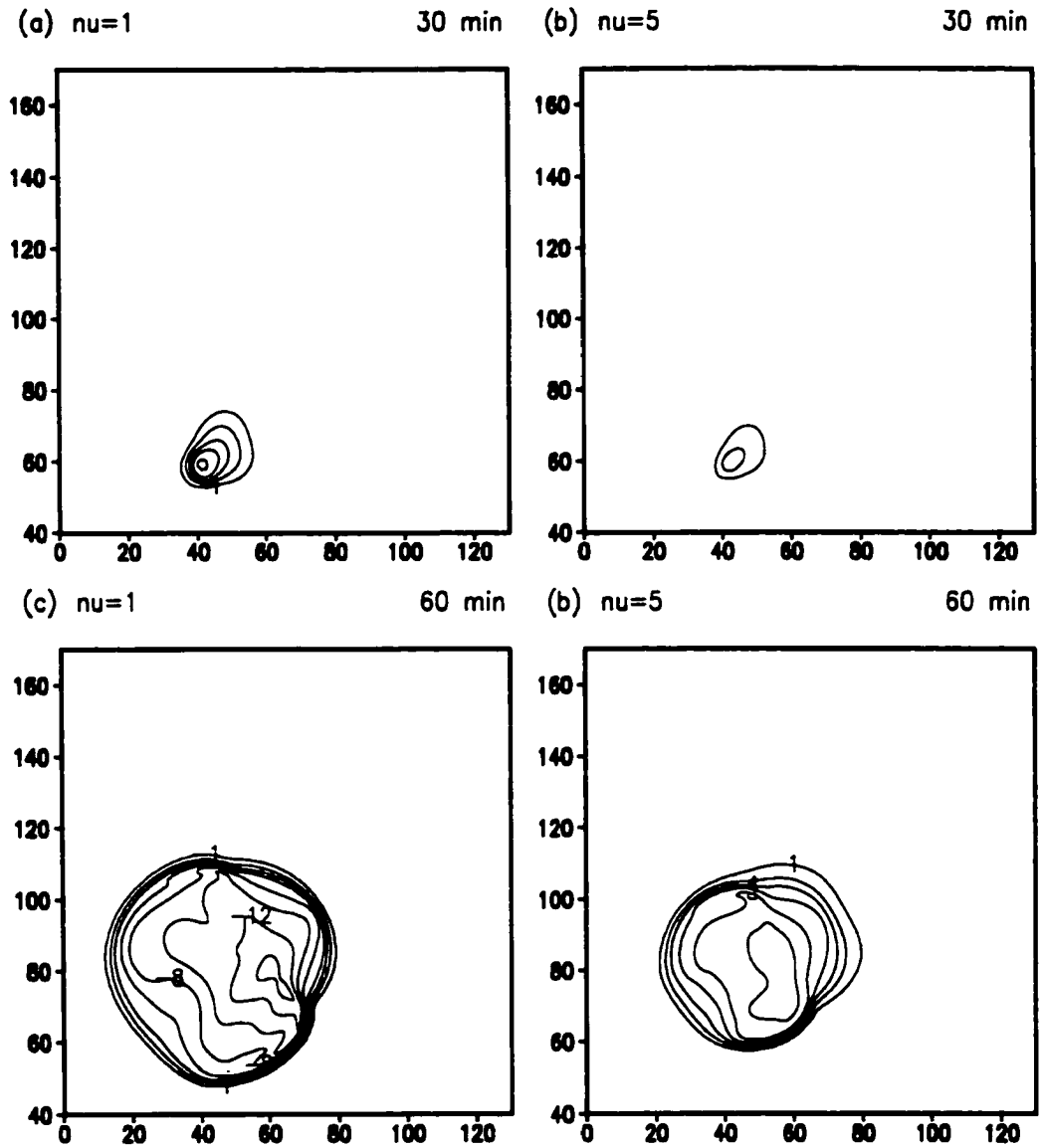


**Figure 6.7: Perturbation potential temperature (K) at the lowest model level (48m AGL) at 30 minutes for the (a) NU1 and (b) NU5 simulations, and at 60 minutes for the (c) NU1 and (d) NU5 simulations. Contour interval is –2K. The –1K isotherm is also shown.**

colder than those in the NU1 case (Figure 6.8c,d). The weakening of the NU1 cold pool toward the end of the simulation is directly related to the collapse of the updraft and the reduction in the amount of hail being produced. The maximum potential temperature differences in these sensitivity tests (~4K) is less than observed in the mean hail diameter tests (~ 10K). This is due to the greater disparity between the number of small and large

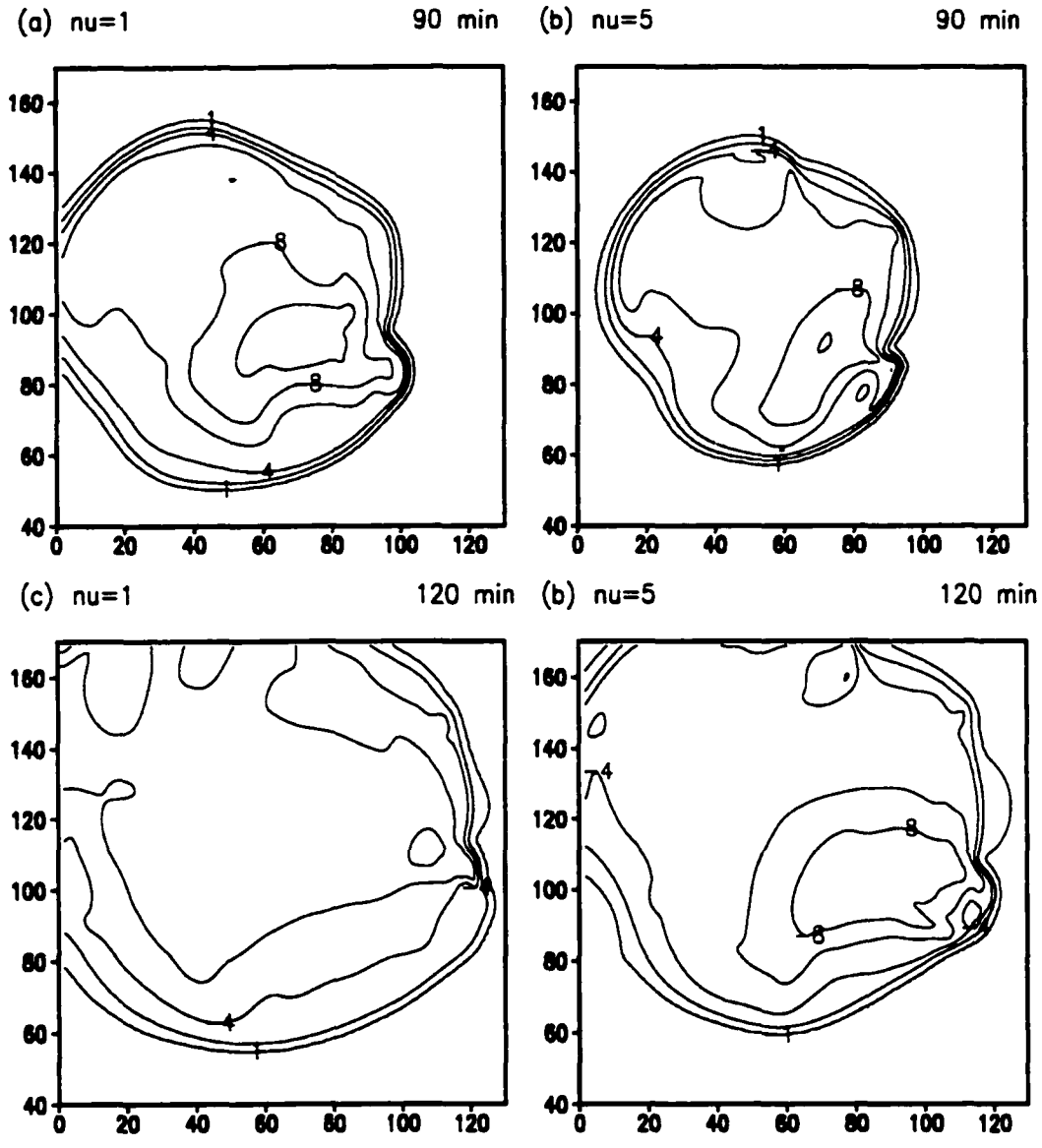


**Figure 6.8: Perturbation potential temperature (K) at the lowest model level (48m AGL) at 90 minutes for the (a) NU1 and (b) NU5 simulations, and at 120 minutes for the (c) NU1 and (d) NU5 simulations. Contour interval is –2K. The –1K isotherm is also shown.**

hailstones in the latter tests. The cold pools in the ν tests are more sensitive to the reduction in hail production as a result of the reduced disparity between the hailstone sizes. Soon after the collapse of the NU1 updraft and the reduction in hail production, the cold pool in the NU5 case is stronger than that in the NU1 run (Figure 6.8c,d).

The maximum hail mixing ratios decrease with an increase in the shape parameter (Figure 6.9). The trends in the hail mixing ratios closely follow those of the maximum updraft velocities, highlighting the dependence of hail formation on updraft strength. The difference in the hail mixing ratio magnitudes between the three cases is due to increasing the hail distribution spectral width as the shape parameter is decreased. Increasing the spectral width makes the fall velocities less uniform, and increases the collection and coalescence processes associated with hail. At 20 minutes, the cloud water is less in the NU1 case than in the NU5 run (Figure 6.10). This indicates that the cloud water is being collected more rapidly in the NU1 case, thereby generating the larger hail mixing ratios. Cloud water forms a source of rain, and as this source is reduced through interactions with hail, the rain mixing ratios in the NU1 case are less than those in the NU5 case (not shown). The greater spectral width in the NU1 case also results in the reduced mixing ratios of the other ice species through the increased coalescence and collisions of these species with hail. The pristine ice mixing ratios in the NU1 case are about half of those in the NU5 (Figure 6.10). The NU3 results are similar (not shown).

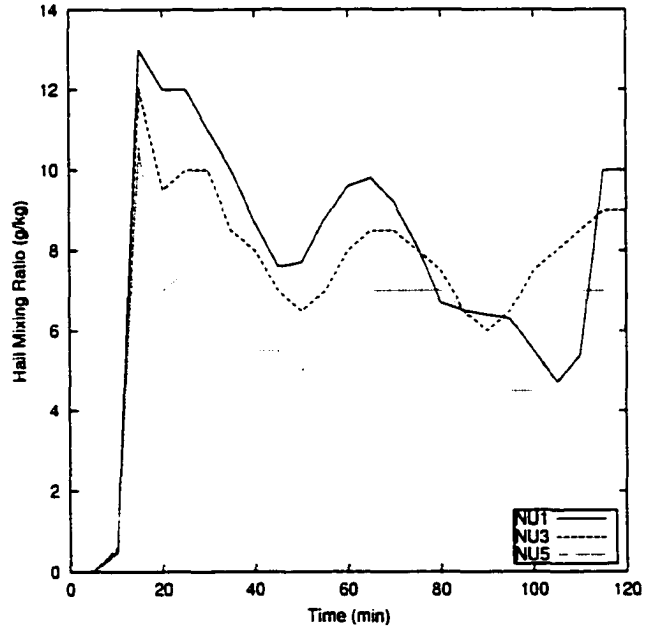


**Figure 6.9: Maximum hail mixing ratio ($g.kg^{-1}$) throughout the model domain as a function of time for the NU1 (solid line), NU3 (dashed line), and NU5 (dotted line) simulations.**

(a)

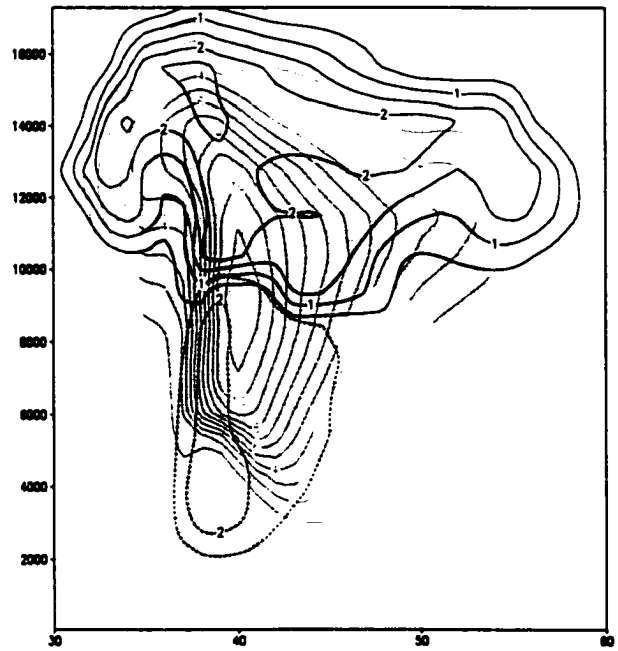

(b)

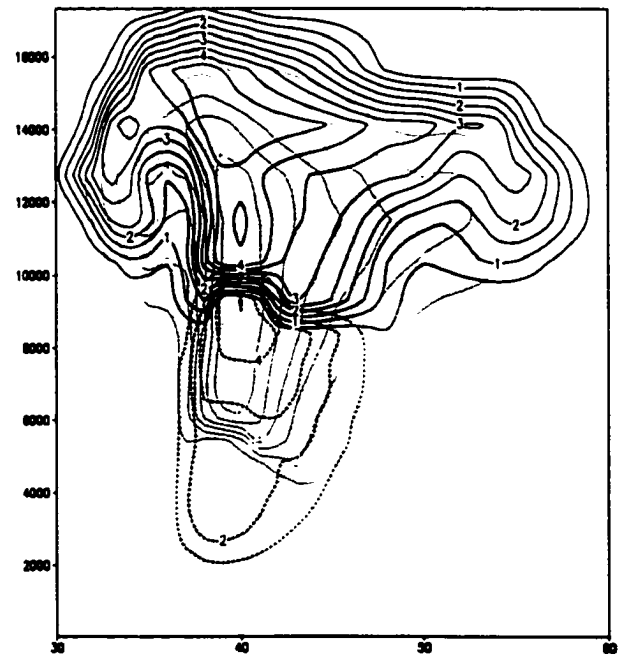

**Figure 6.10: Vertical cross-section through the cloud water mixing ratio (dashed line, interval 1 g.kg$^{-1}$), hail mixing ratio (thin solid line, interval 1g.kg$^{-1}$) and pristine ice mixing ratio (thick solid line, interval 0.5 g.kg$^{-1}$) at 20 minutes for the (a) NU1 and (b) NU5 cases. The shaded region is the updraft, where the vertical velocity is greater than 10m.s$^{-1}$.**

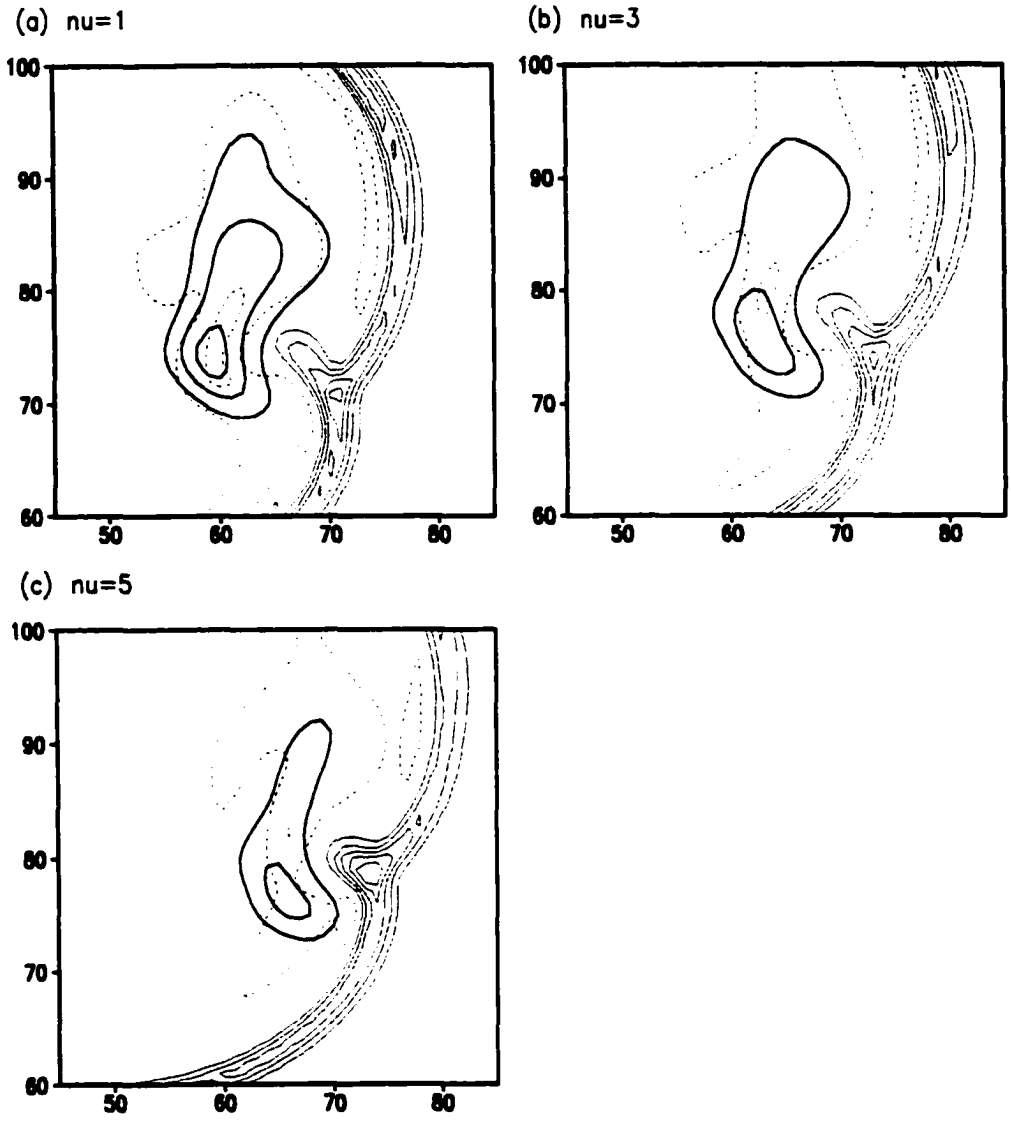


**Figure 6.11: Vertical velocity (thin lines, interval 0.3 $m.s^{-1}$, no zero line) and rain mixing ratio (thick lines, interval 0.5 $g.kg^{-1}$, no zero line) at 48 m AGL for the (a) NU1 case at 60 minutes, (b) NU3 case at 65 minutes, and (c) NU5 case at 70 minutes.**

Hook echoes are evident in all three simulations at the lower levels (not shown). Only trace amounts of hail occur at the surface in all three cases. The rain mixing ratios at the surface decrease as the shape parameter increases (Figure 6.11). This is due to the larger hail mixing ratios and the greater melting rates in the smaller ν cases. Also, the rain is distributed over a greater area in the smaller ν cases due to the smaller terminal fall velocities of hail in this case.

The maximum low-level vertical vorticity increases from 0.017 to 0.024 $s^{-1}$ as ν increases from 1 to 5 (Figure 6.12). Examining the contributions made by all the terms in the vertical and horizontal vorticity tendency equation for all three cases reveals, as in the diameter sensitivity tests, that the stretching term is the primary contributor in both the horizontal and vertical vorticity equations (not shown). Also, as ν increases, the stretching term increases (Figure 6.13a,b). Comparing the trends in the low-level vertical vorticity maxima between 60 and 100 minutes for the NU1 and NU5 cases (Figure 6.12), with the corresponding surface convergence fields (Figure 6.14), shows a strong positive correlation between the two fields. Similar results are obtained for the NU3 case (not shown). The stronger low-level vertical vorticity in the larger ν cases is therefore caused primarily by the greater low-level convergence in the regions of the updraft in these cases.

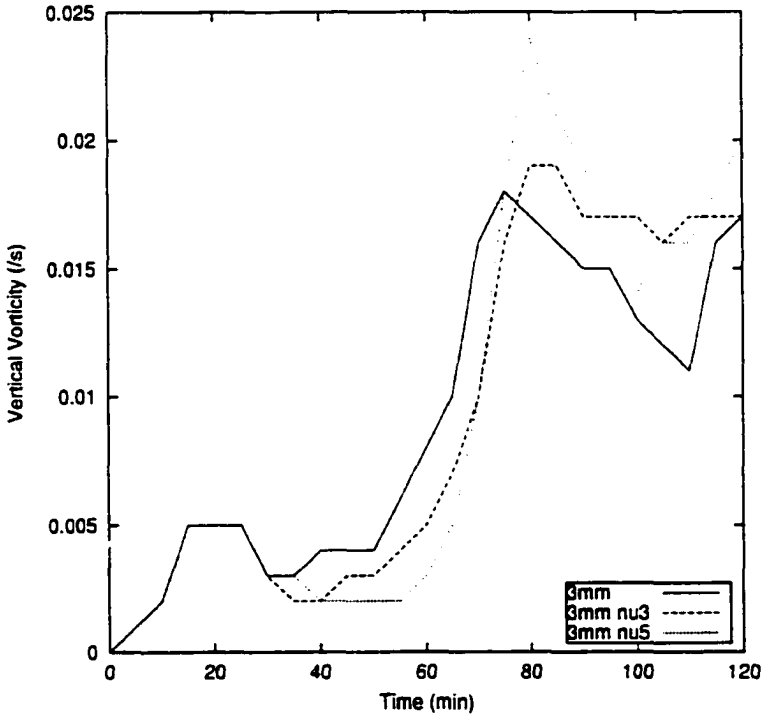


**Figure 6.12: Vertical component of vorticity ($s^{-1}$) at 150m AGL as a function of time for the NU1 (solid line), NU3 (dashed line), and NU5 (dotted line) simulations.**

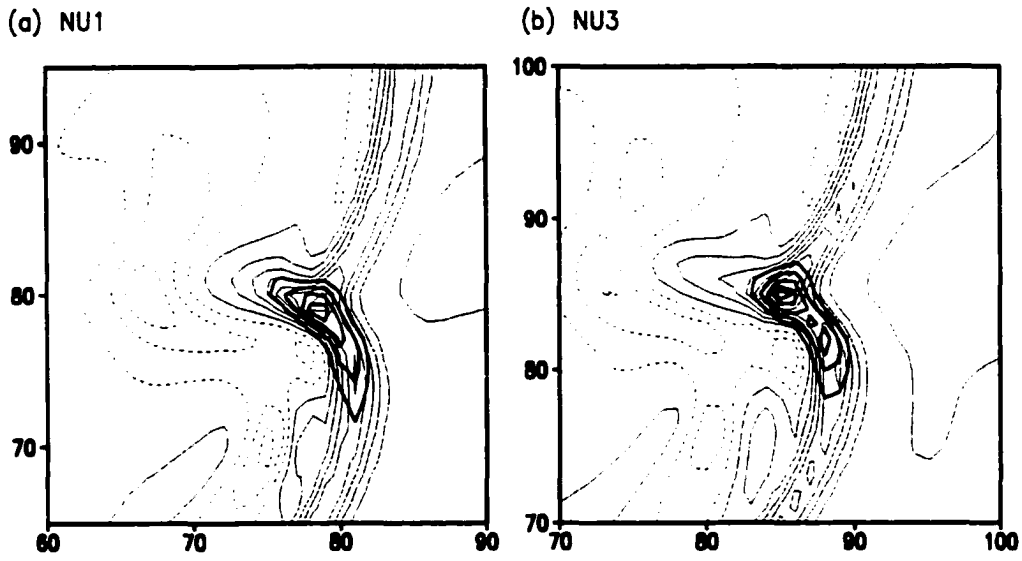


**Figure 6.13: The vertical velocity (thin lines, interval 1 m.s$^{-1}$) and contribution made by the stretching term in the low-level vertical vorticity equation (thick lines, interval 4 s$^{-2}$, contours multiplied by 1e5) for (a) NU1 case at 75 minutes, and (b) NU3 case at 80 minutes. Both plots are at 150m AGL. Solid lines indicate positive values and dashed lines negative values, and all zero isolines are excluded.**

That the low-level vertical vorticity increases as ν increases presents a different scenario to than in the mean hail diameter cases. The stronger low-level downdrafts in the NU1 (3mm) case provided greater convergence in the region of the updraft compared to the convergence produced by the weaker downdrafts in the 2cm case. In the ν sensitivity tests, stronger convergence in the regions of the low-level updraft occurs in the larger ν cases, in spite of the weaker downdrafts. Why do these differences occur? At 70 minutes, the convergence in the NU1 and NU5 cases is similar (Figure 6.14), even though the downdraft is stronger in the former case (Figure 6.15a,b). The weaker downdrafts in the NU5 case do not force the gust front to surge eastward as rapidly as in the NU1 case and, as a result, the downdraft is positioned closer to the updraft in the NU5 case. The closer proximity of the downdraft to the updraft, and the slower storm propagation speed in the

(a)

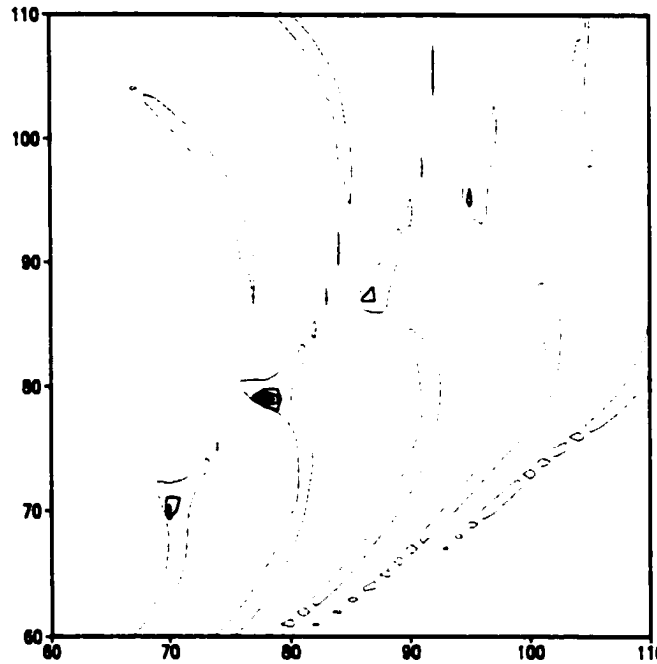


(b)

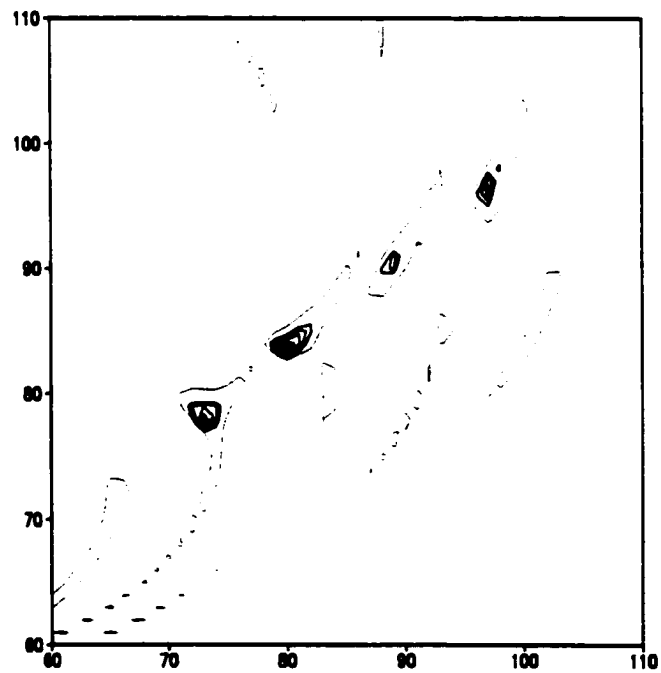


**Figure 6.14: Convergence (thick lines, contours 0.014, 0.015, 0.016, 0.017 $s^{-1}$) and vertical velocity (thin lines, contour shown at 2 $m.s^{-1}$) at 50m AGL for the (a) NU1 and (b) NU5 cases. The fields at 10 minute intervals from 60 to 100 minutes are shown from left to right in each figure.**

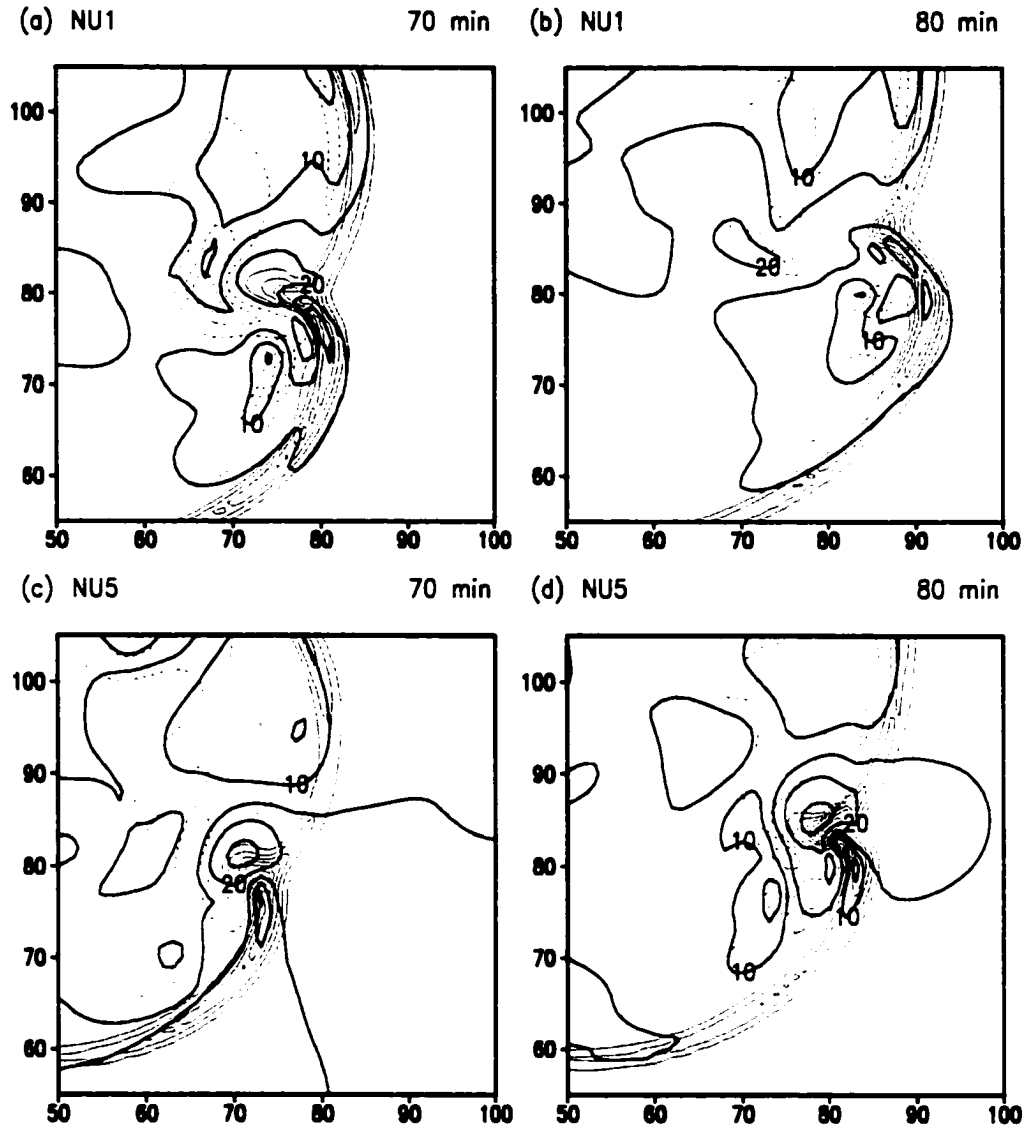


**Figure 6.15: Vertical velocity (thin lines, interval 0.5 m.s$^{-1}$) and magnitude of the storm-relative winds (thick lines, interval 5 m.s$^{-1}$) at 50m AGL for the NU1 case at (a) 70 minutes and (b) 80 minutes, and for the NU5 case at (c) 70 minutes and (d) 80 minutes.**

NU5 case, enhance the storm-relative inflow winds (entering the updraft from the northeast), and associated convergence in the region of the updraft. The differences are even more apparent 10 minutes later when the updraft in the NU5 case is located close to the RFD, whereas the gust front and updraft in the NU1 case have rapidly moved away from the downdraft (Figure 6.15b,d). Thus, even though the strong downdrafts in the

NU1 case do enhance convergence into the updraft region, the strength of the downdraft is not as important as the proximity of the downdraft to the updraft in these cases.

The sensitivity tests presented in this section reveal that changes in the shape parameter of the hail size distribution do have an impact on the storm dynamics and precipitation characteristics. Increasing $\nu$ increases the longevity of the LM and RM storms, decreases the strength of the low-level downdrafts and cold pool, decreases the rate at which the occlusion takes place, and increases the low-level mesocyclone.

## 6.3 Sensitivity to Species Included

### 6.3.1 *Introduction*

In this section, the sensitivity of supercell storm characteristics to the exclusion of various species is investigated. This work builds on work by Jewett et al. (1990) and Johnson et al. (1993), in which the role of ice in severe storms was investigated. Three tests were conducted, the details of which were shown in Table 3.2. In the first sensitivity test, referred to as the NOPREC test, condensation was allowed to occur, but precipitation was prevented from forming. In the second test, which we call the NOICE test, all ice species were excluded. The only forms of water present are therefore water vapor, cloud water and rain. In the third test, all hydrometeor species were allowed to occur except hail. This test is called the NOHAIL sensitivity test. The results of these three sensitivity tests are compared with the 3mm run.

### 6.3.2 *Results*

#### *NOPREC Case*

The storm tracks reveal the impact the presence of different hydrometeors has on storm structure and dynamics (Figure 6.16). When precipitation is prevented from falling,

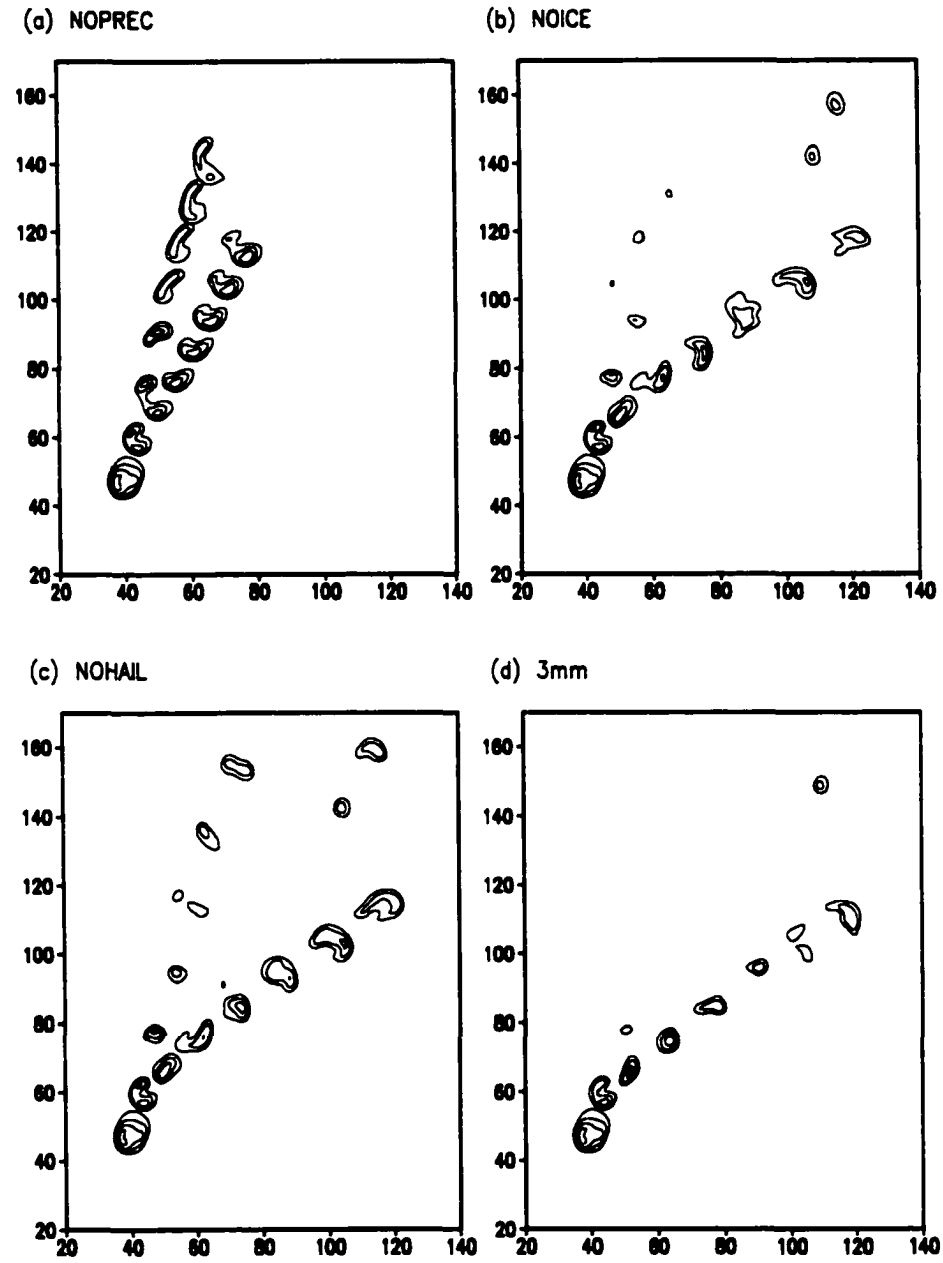


**Figure 6.16: Storm tracks for the (a) NOPREC, (b) NOICE, (c) NOHAIL, and (d) 3mm cases. Field shown is vertical velocity ($m.s^{-1}$) at 4830m AGL. Contour interval is $10m.s^{-1}$ starting $10\ m.s^{-1}$. Storm positions are shown at 15 minute intervals starting from the southwest grid corner.**

as in the NOPREC case, evaporatively-cooled low-level downdrafts and the development of a cold pool are inhibited. The LM is long-lived in spite of the hodograph veering below 2 km (Figure 6.16a). It is also the strongest and longest-lived LM storm to develop

in all the sensitivity tests that were conducted. This supports our findings in Chapter 5 regarding the dominant role of negative buoyancy in the demise of the LM, as such forcing does not exist in this case.

The RM is stronger than the LM, which is in keeping with the hodograph veering. The RM is stronger and steadier in this run than in all the other cases, and does not undergo the structural changes due to the low-level occlusion processes occurring in the other three cases. This highlights the importance of the evaporatively-cooled downdrafts in changing the storm structure. Both the LM and RM storms are starting to split again toward the end of the simulation. Storm splitting in this case occurs regardless of the absence of precipitation, and points to the importance of pressure gradient forcing in storm splitting, as has been previously observed (e.g. Schlesinger, 1980; Rotunno and Klemp, 1982; Weisman and Klemp, 1984). Finally, the NOPREC RM storm does not veer to the right of the mean wind shear vector to the extent of the RM updrafts in the other cases. This has an effect on the low-level convergence. The impact of the evaporatively-cooled low-level downdrafts and the cold pool on the development of supercell storms is therefore clearly demonstrated by the absence of these features in the NOPREC case.

### *NOHAIL Case*

It is evident from the storm tracks that the RM is steadier and longer-lived in the NOHAIL case than in the 3mm case (Figure 6.16c,d). The LM storm is also longer-lived in the NOHAIL case. The LM updraft does progressively weaken until 75 minutes, after which it develops again. The small updraft to the west of the LM at 75 minutes actually develops later in the simulation as a result of convergence along the gust front. The steadier nature of the RM in the NOHAIL case is also evident in the maximum vertical velocity fields (Figure 6.17).

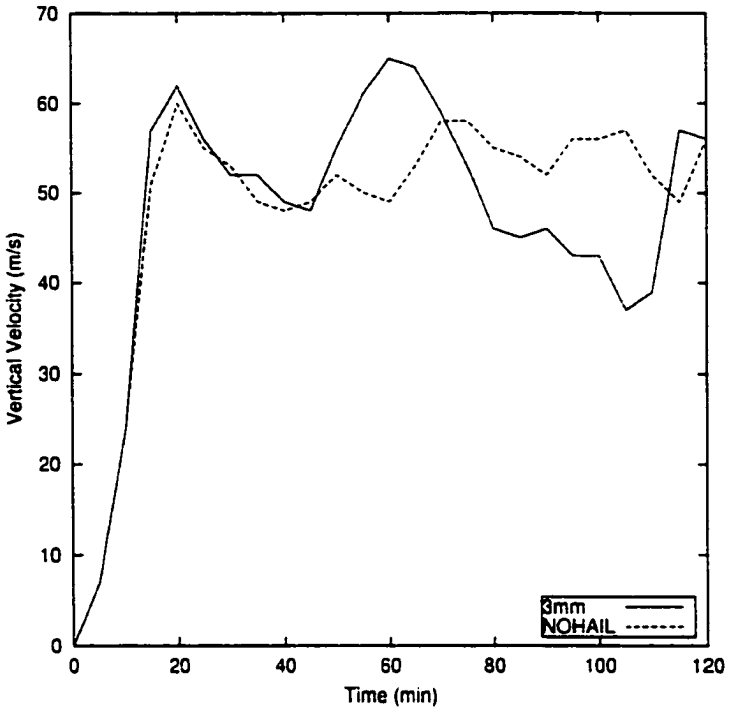


**Figure 6.17: Maximum updraft velocity as a function of time for the 3mm (solid line) and NOHAIL (dashed line) simulations.**

In order to examine the rest of the storm structure and dynamics, we need to understand how the 3mm and NOHAIL simulations differ in a microphysical sense. The maximum rain mixing ratios in the NOHAIL simulation are 1.5 to 2 times greater than the rain generated in the 3mm case (Figure 6.18). In the 3mm case hail, which forms primarily from the freezing of raindrops, is a significant sink for rainfall. As this sink is absent in the NOHAIL case, the maximum rain mixing ratios are much larger. While some rain is collected by the other ice species (graupel, snow, aggregates), the amounts are insignificant in comparison to the collection by hail.

Even though the rain mixing ratios are greater in the NOHAIL case, most of the rain remains suspended at much higher levels in the cloud than in the 3mm case (Figure 6.19). As we just saw, hail is a raindrop sink. The rain mixing ratios in the 3mm case are therefore substantially less than those in the NOHAIL case above the freezing level

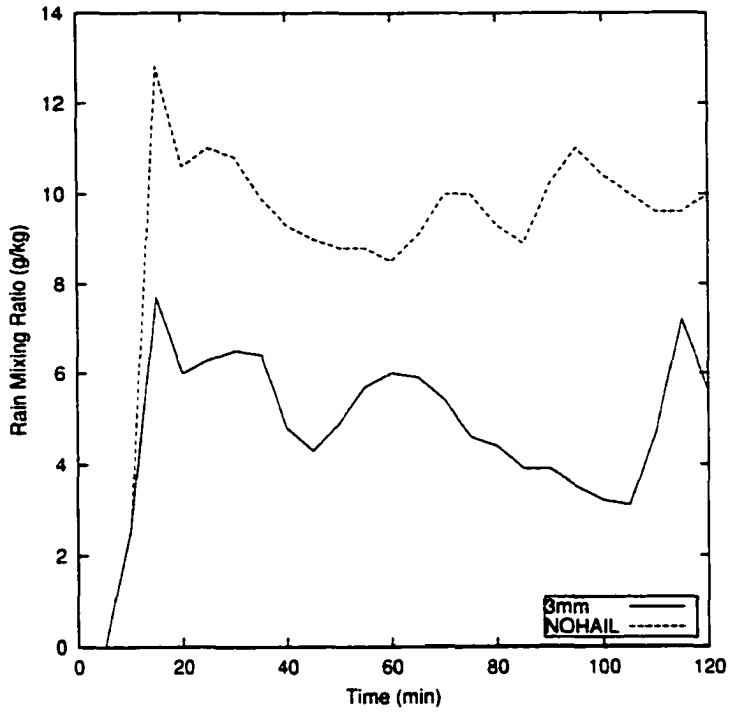


**Figure 6.18: Maximum rain mixing ratio ($g.kg^{-1}$) throughout the model domain as a function of time for the 3mm (solid line) and NOHAIL (dashed line) simulations.**

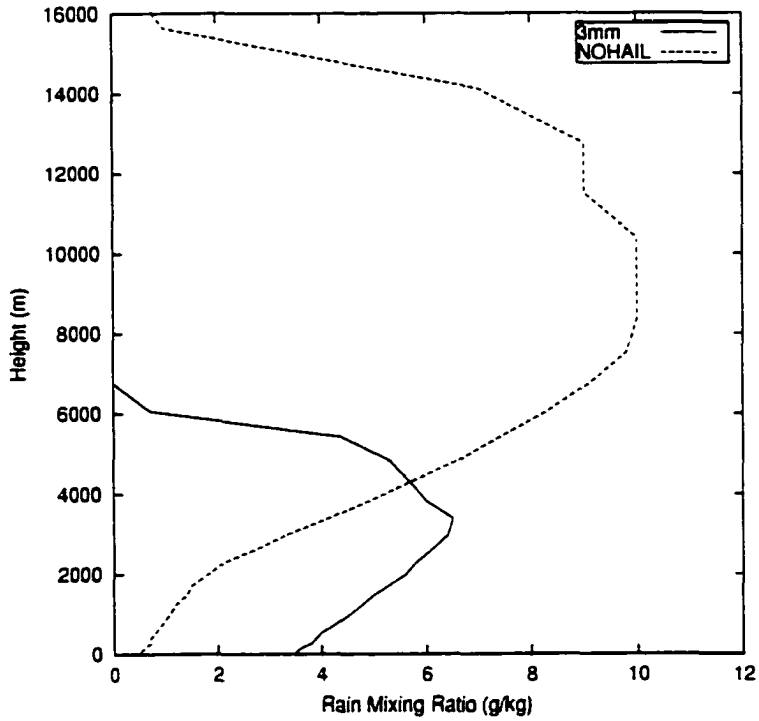


**Figure 6.19: Maximum rain mixing ratio (g/kg) as a function of height at 30 minutes for the 3mm (solid line) and NOHAIL (dashed line) simulations.**

(~4km). At the lower levels, the 3mm rain mixing ratios are enhanced by melting and shedding processes, which cannot occur in the NOHAIL case. If the rain mixing ratios are so large in the upper regions of the NOHAIL case, why are they not greater lower down? For the simulations presented here, the ratio of the mean terminal fall speeds of hail to rain is 1.87. As hail falls faster than rain, it reaches the lower levels more rapidly, where melting, shedding and the formation of rain make then take place. The presence of hail, therefore, changes the distribution of rain within the cloud by acting as a sink in the upper levels and a source lower down. Also, as the fall speeds of rain are less than hail, there will be a critical updraft velocity above which the rain will remain suspended within the updraft, but hail will still be able to fall. Hail may be viewed as a means of transporting rain more rapidly from the upper levels to the lower levels. The greater rain mixing ratios at the surface in the 3mm case are evidence of the arguments just made (Figure 6.20). The surface rainfall is relatively constant in the NOHAIL case, but closely follows the hail production in the 3mm case.

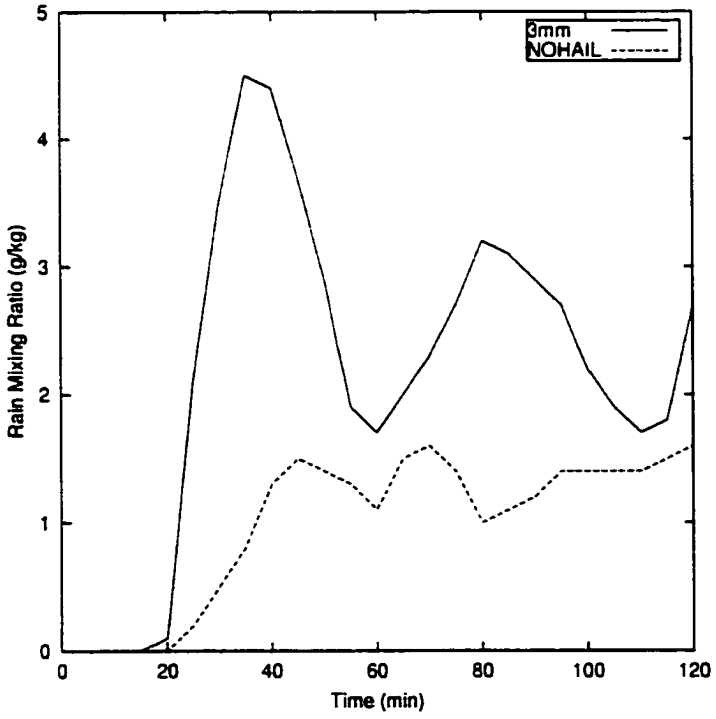


**Figure 6.20: Maximum rain mixing ratio ($g.kg^{-1}$) at the lowest model level (48m AGL) as a function of time for the 3mm (solid line) and NOHAIL (dashed line) simulations.**

The low-level downdrafts in the 3mm case are stronger than those in the NOHAIL case until after the low-level occlusion (Figure 6.21). Examining the forcing controlling the low-level downdrafts revealed that the buoyant forcing term dominates the pressure gradient forcing (not shown). Of the two factors constituting the buoyant forcing, the thermodynamic forcing is dominant in both cases (Figure 6.22). Both the thermodynamic forcing and the condensate loading are greater in the 3mm case. This is due to the presence of hail and the greater rain mixing ratios, which enhance both the loading and thermodynamic terms, and the contribution of both evaporation and melting processes, instead of just evaporation, which increases the thermodynamic term.

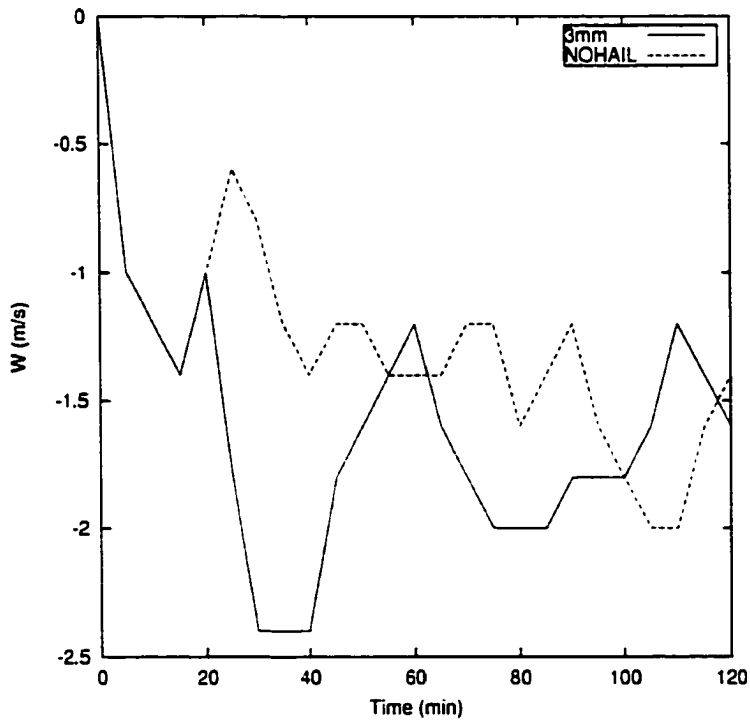


**Figure 6.21: Maximum downdraft strengths at 48 m AGL as a function of time for the 3mm (solid line) and NOHAIL (dashed line) simulations.**

In the NOHAIL case, the downdraft maximum is displaced to the east of the updrafts, whereas the downdraft maximum occurs between the two updrafts in the 3mm case (Figure 6.22). The downdraft displacement to the east of the updrafts is due primarily to the thermodynamic term. In the NOHAIL case rain, which is the primary

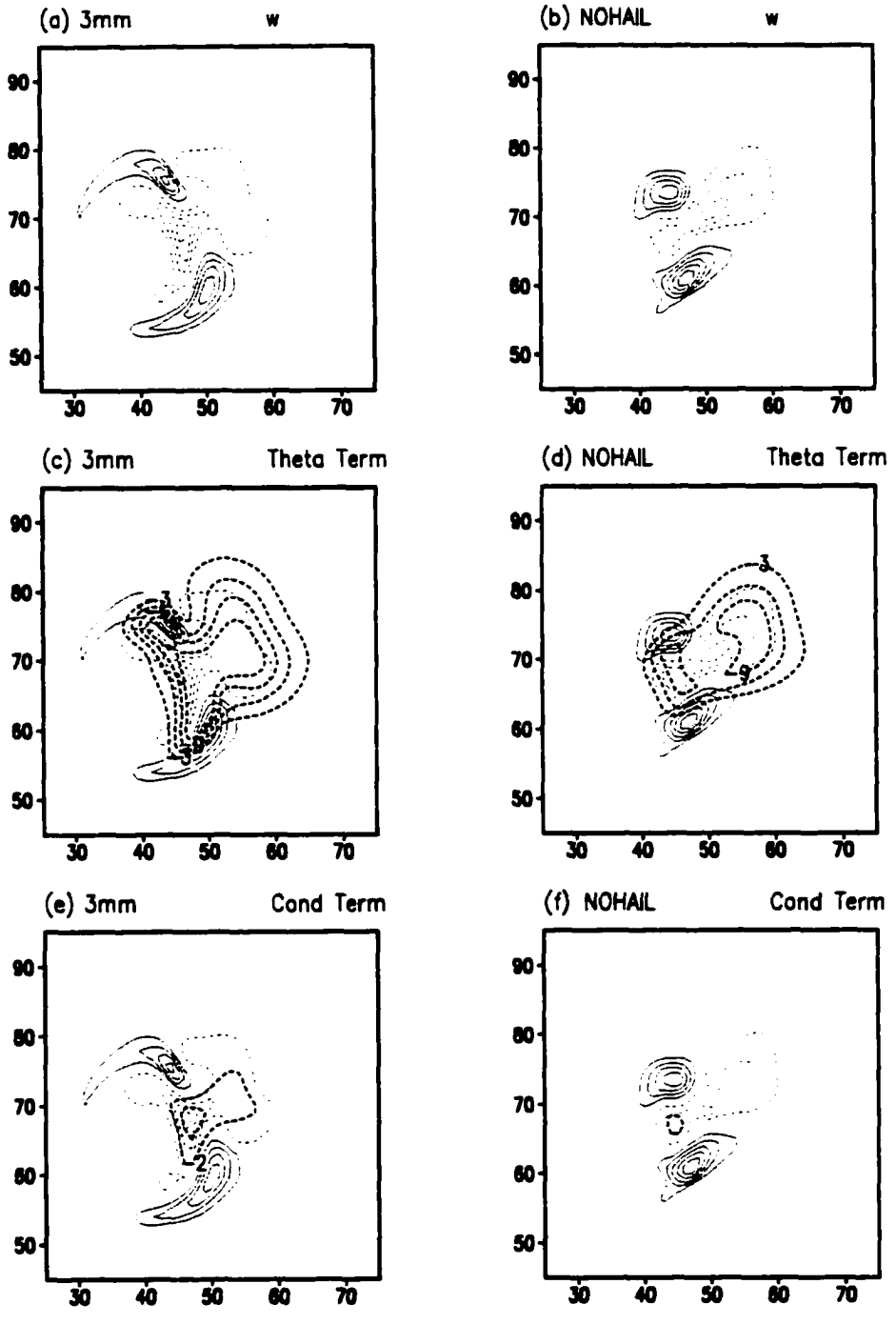


**Figure 6.22: Vertical velocity (thin lines, interval 2 m.s$^{-1}$) for the (a) 3mm and (b) NOHAIL cases, and the contributions to the buoyant forcing made by the thermodynamic ($g\theta_v'/\theta_0$) forcing (thick lines, interval 2 m.s$^{-2}$) in the (c) 3mm and (d) NOHAIL cases, and by the condensate loading ($-gr_c$) term (thick lines, interval 2m.s$^{-2}$) for the (e) 3mm and (f) NOHAIL cases, at 40 minutes at 1 km AGL. Forcing terms are multiplied by 100. Solid lines indicate positive values and dashed lines represent negative values.**

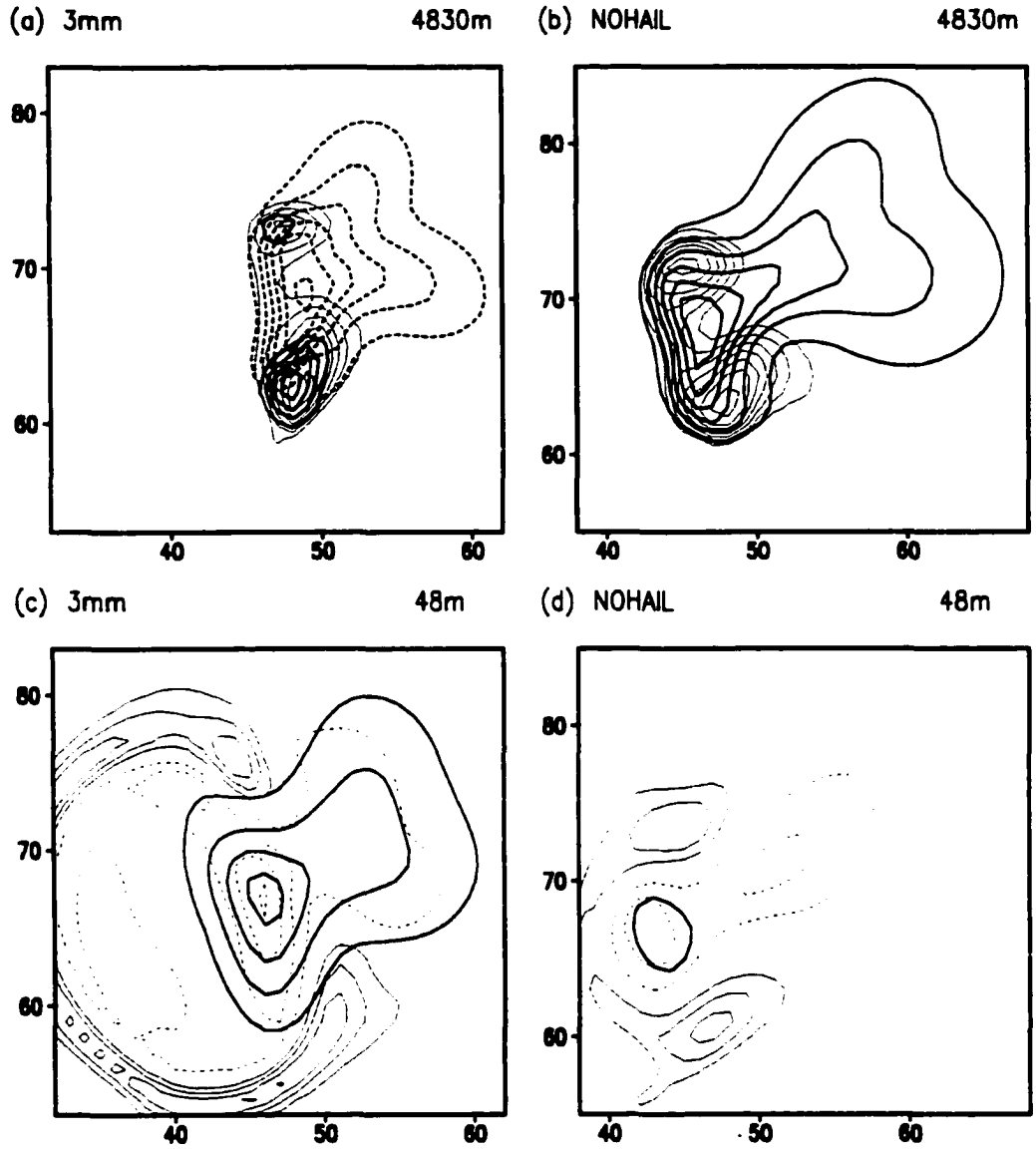


**Figure 6.23: (a) Vertical velocity (thin lines, interval 5m.s$^{-1}$), rain mixing ratio (thick solid lines, interval 1 g.kg$^{-1}$) and hail mixing ratio (thick dashed lines, interval 1 g.kg$^{-1}$) for the 3mm case at 40 minutes at 4830m AGL, (b) vertical velocity (thin lines, interval 5m.s$^{-1}$) and rain mixing ratio (thick solid lines, interval 1 g.kg$^{-1}$) for the NOHAIL case at 40 minutes at 4830m AGL, (c) vertical velocity (thin lines, interval 0.3m.s$^{-1}$) and precipitation mixing ratio (thick solid lines, interval 1 g.kg$^{-1}$) for the 3mm case at 40 minutes at 48m AGL, and (d) vertical velocity (thin lines, interval 0.3m.s$^{-1}$) and precipitation mixing ratio (thick solid lines, interval 1 g.kg$^{-1}$) for the NOHAIL case at 40 minutes at 48m AGL.**

contributor to the total condensate, is transported further away from updraft than the hail is in the 3mm case, due to the differences in the rain and hail fall speeds (Figure 6.23). The evaporation and melting of both species lead to the observed locations of the downdrafts.

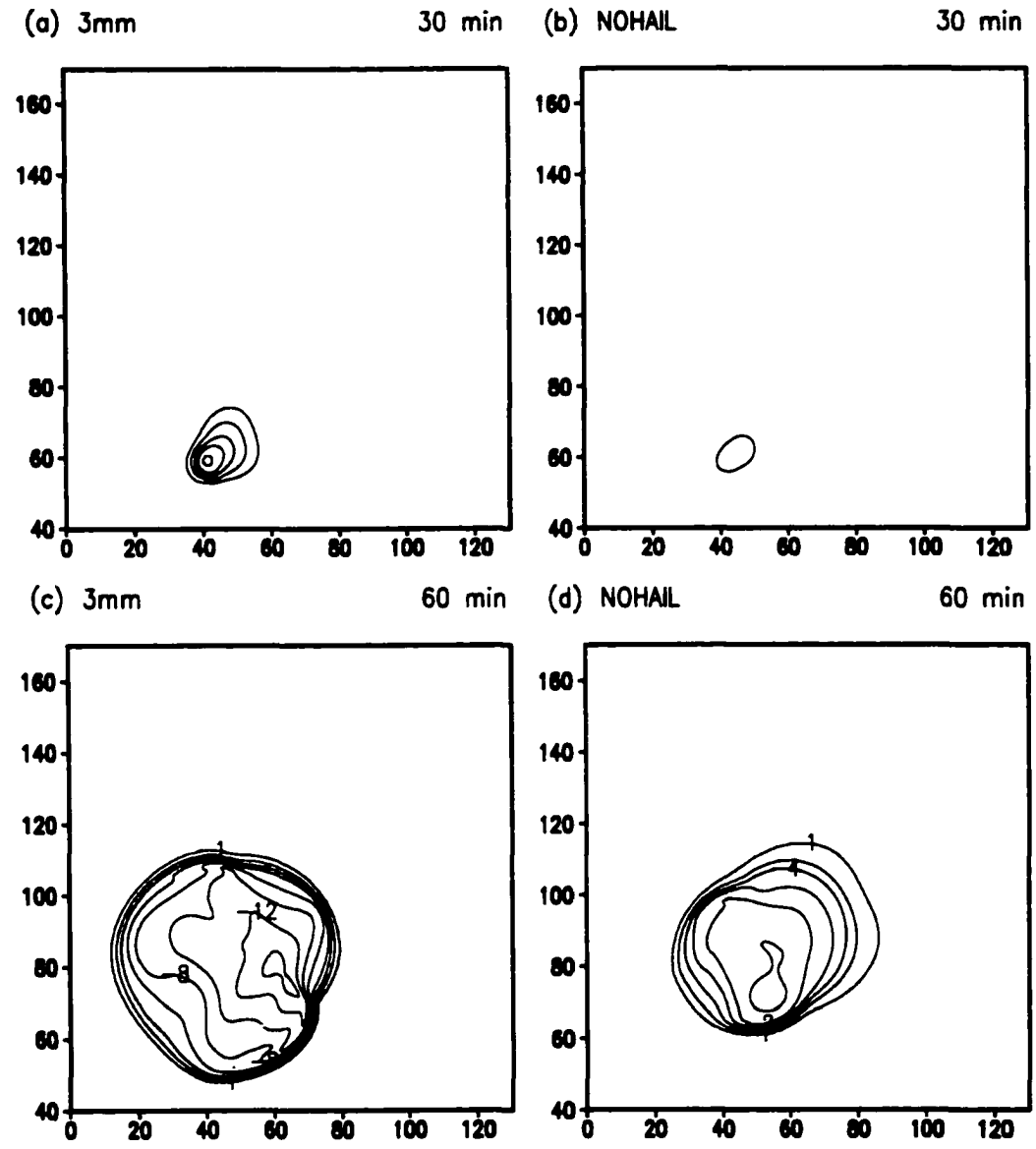


**Figure 6.24: Perturbation potential temperature (K) at the lowest model level (48m AGL) at 30 minutes for the (a) 3mm and (b) NOHAIL simulations, and at 60 minutes for the (c) 3mm and (d) NOHAIL simulations. Contour interval is –2K. The –1K isotherm is also shown.**

The cold pools that develop in the 3mm and NOHAIL cases are indicative of the greater cooling rates and stronger downdrafts in the former case (Figure 6.24, Figure 6.25), although the temperatures are comparable toward the end of the simulation, following the collapse of the 3mm updraft. The shape of the cold pool in the NOHAIL

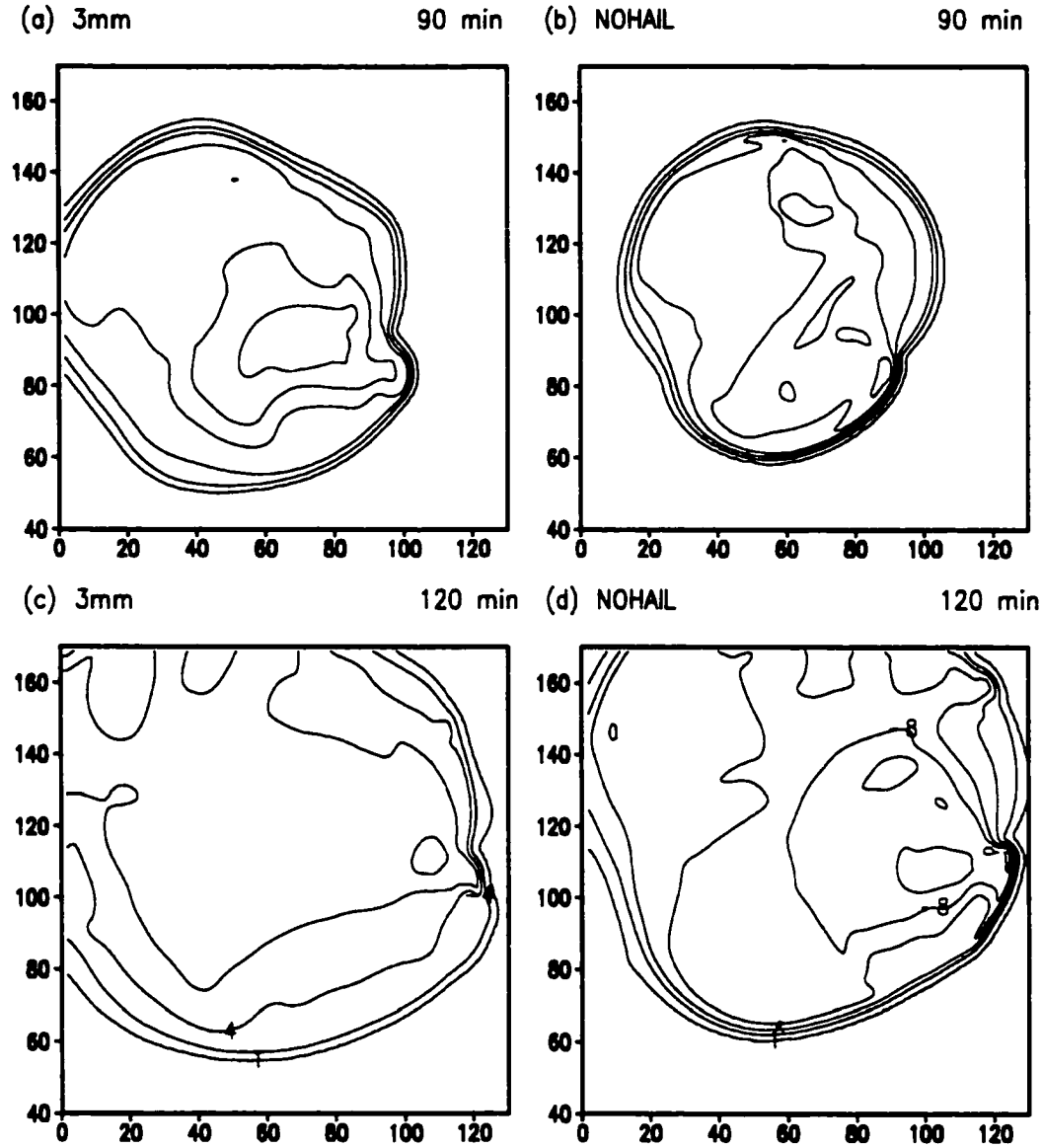


**Figure 6.25: Perturbation potential temperature (K) at the lowest model level (48m AGL) at 90 minutes for the (a) 3mm and (b) NOHAIL simulations, and at 120 minutes for the (c) 3mm and (d) NOHAIL simulations. Contour interval is –2K. The –1K isotherm is also shown.**

case is initially more oval in nature than the near circular shape of the 3mm case. This is due to the position of the downdraft with respect to the updraft, as well as to the strength of the low-level downdrafts. The shape of the cold pool is important since it affects the

angle of the gust front with respect to inflow air, and hence the magnitude of convergence along the gust front. Johnson et al. (1993) also observed differences in the gust front structure between their ice and no-ice cases. The downdraft position and the downdraft strength in the NOHAIL case do not result in the rapid eastward surge of the gust front as in the 3mm case. The upper-level regions of the updraft therefore remain in close proximity to the gust front, instead of being outrun by the gust front as in the 3mm case (Figure 6.26). This allows the development of the relatively steady RM observed in the NOHAIL case.

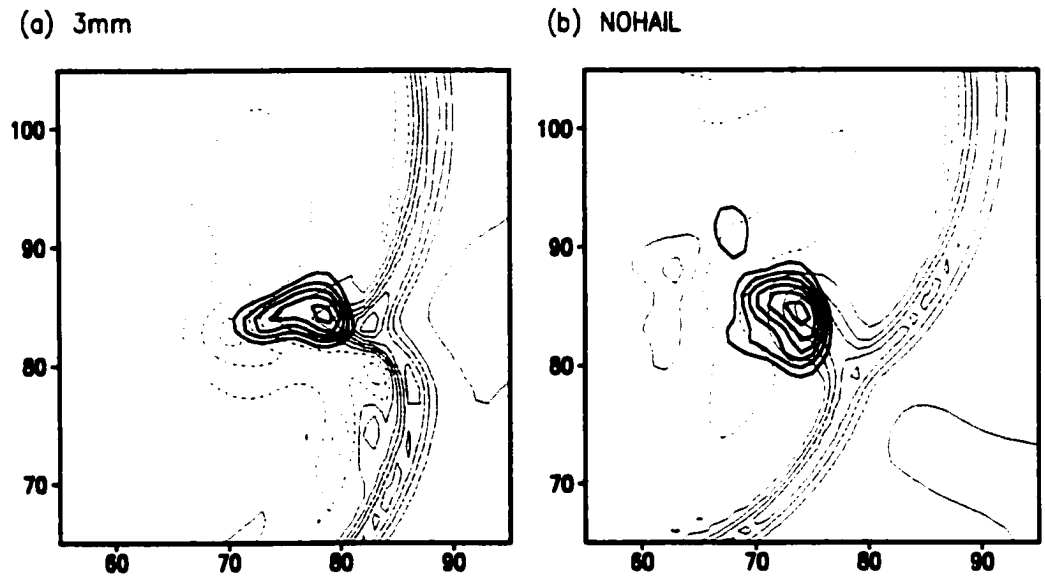


**Figure 6.26: Vertical velocity at 75 minutes at 48m AGL (thin lines; interval 0.3m.s$^{-1}$) and 4830m AGL (thick lines; interval 5m.s$^{-1}$) for the (a) 3mm and (b) NOICE cases.**

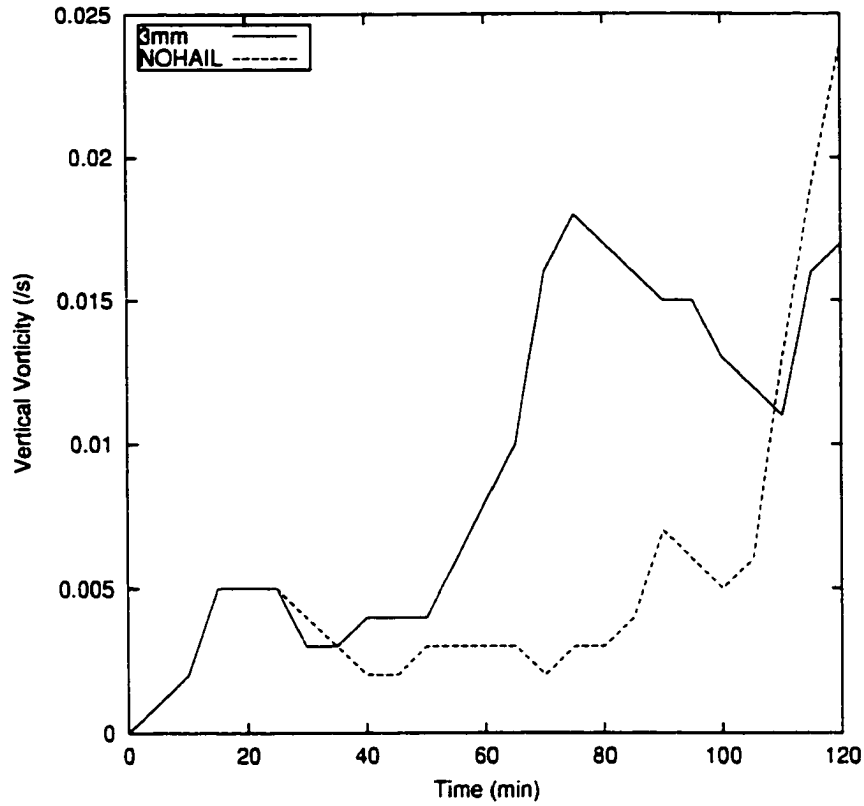


**Figure 6.27: Vertical component of vorticity ($s^{-1}$) at 150m AGL as a function of time for the 3mm (solid line) and NOHAIL (dashed line) simulations.**

One of the greatest impacts of excluding hail is the delay in the development of low-level vertical vorticity compared with the smaller hail cases (Figure 6.27). The development of vertical vorticity also begins later in both the 1cm and 2cm simulations, although not as late as in the NOHAIL case (see Figure 4.36). Even though the development of the vorticity is delayed in the NOHAIL case, once it starts to develop it develops more rapidly, and to a greater extent than the low-level vertical vorticity in any of the other hail cases. This is directly related to the strength of the low-level downdrafts, and their position with respect to the updraft, as determined by the precipitation distribution. The rapid development of the low-level vertical vorticity in the NOHAIL case begins around 105 minutes, coinciding with the development of the strongest

downdrafts at the surface (Figure 6.21). Like in the mean hail diameter cases, the stretching term is the largest contributor in both the vertical and horizontal vorticity equations of the NOHAIL simulation (not shown). The stretching term is stronger in the NOHAIL case than in the 3mm case, at the time of their respective maxima. This is caused by the differences in the low-level convergence, which in turn is controlled by the shape of the cold pool, the slower moving gust front and storm, and the stronger storm-relative inflow from the northwest.

### *NOICE Case*

The results of the NOICE case are similar to those of the NOHAIL case, as can be seen from the storm tracks (Figure 6.16b,c), and differ mainly in magnitude, rather than in trend. This occurs because hail is by far the most predominant ice species, except in the upper levels of the cloud where pristine ice occurs. Excluding all the ice species is therefore similar to excluding hail. The results of the NOICE case will not be shown here. However, the output from the NOHAIL case may be used as evidence for the following discussion.

The NOICE case was conducted and compared with all of the ice cases (3mm to 2cm cases) in order to determine whether the results were consistent with the findings of Jewett et al. (1990) and Johnson et al. (1993) (referred to as JJ9093). The similarities between the tests conducted here and those reported in these two papers include a greater updraft maximum in all the ice cases (3mm to 2cm), more diffusive precipitation characteristics in the NOICE case due to the smaller fall speeds of rain, and greater precipitation at the ground in all of the ice cases compared with the NOICE case. The anvils are better developed in the ICE cases, both in the simulations of JJ9093 and those shown here.

Differences do occur between our results and those of JJ9093. However, these differences arise depending on which of the ice cases (3mm, 5mm, 1cm or 2cm) the NOICE output is compared with. JJ9093 found that the LM dissipated earlier in their no-ice case than in their ice case. The LM in the NOICE case here lives 15 minutes longer than in the 3mm case (Figure 6.16, the convection to the west of the LM develops later as a result of convergence along the gust front), but dissipates an hour earlier than the LM in the 2cm case (see Figure 4.2). JJ9093 found that the RM in their ice case was steadier and longer-lived. The updraft in their no-ice run occluded earlier, and the updraft dissipated due to the stronger low-level potential temperature perturbations within the cold pool that forced the gust front to outrun the updraft. In the 1cm and 2cm simulations conducted here, the cold pools are warmer, the gust front moves slower and the updrafts are steadier and longer-lived than those in the NOICE case; however, the opposite is true in the 3mm and 5mm cases.

The supercell features (BWER, hook echo, overshooting tops, anvil development etc) were better developed in the ICE cases of JJ9093. In the tests conducted here, the classic-type supercell characteristics are better developed in the smaller hail cases than with the NOICE characteristics; however, the supercell characteristics in the large hail cases are more like an HP-type supercell. Finally, JJ9093 found that the low-level vertical vorticity was greater in their no-ice simulations until the collapse of the updraft. The maximum vorticity values below 1 km were 0.006 $s^{-1}$ (see Figure 2.18), and they attributed the differences in the low-level vorticity fields to the baroclinic effect, but did not perform an analysis of the terms contributing to the low-level vertical vorticity. In all of the ice simulations conducted here, the low-level vertical vorticity values are greater than those in the NOICE case until the end of the simulation, and the differences in the vorticity magnitudes between the cases is primarily due to the stretching term. In spite of the differences between the simulations of JJ9093 and those conducted here, all the

simulations reveal the significant impact ice has on the structure and dynamics of severe storms, and that the size of the hail may amplify these differences.

### 6.3.3 *Sensitivity to the Scheme Complexity*

#### *Introduction*

In this section, the sensitivity of the model solution to the use of the two-moment bulk microphysics scheme will be assessed. All the sensitivity tests until now have been conducted using the single-moment bulk microphysics scheme, in which only the mixing ratio is predicted, and the mean hail diameter has to be specified at the beginning of the simulation. When using the two-moment scheme, the mixing ratio and the number concentration are both predicted. Using the predictions of these two quantities, the mean hail diameter is then diagnosed, and therefore need not remain fixed for the entire simulation. This has an impact on the distribution of the hydrometeors, as well as on their fall speeds. However, the shape parameter still needs to be set in the two-moment scheme.

The two-moment scheme only became available in a later version of RAMS (version 4.2.9). When the 3mm simulations were rerun using this version of the model, the results compared favorably with those using version 3B. However, the output from the 3mm case using version 4.2.9 will be shown here, to ensure that the differences between the two cases are due solely to the differences between the single-moment and two-moment schemes. The 3mm single-moment run and the two-moment run differ only by the number of moments they predict. In both cases, the shape parameter is set to 1. The two-moment test is referred to as the 2MOM simulation. The details of the simulations were described in Table 3.2. The simulations are examined at 20 minutes in order to compare the microphysical characteristics before differences in the kinematics have an effect.

***Results***

At 20 minutes, the updraft structure differs little between the 3mm (Figure 6.28) and 2MOM simulations (Figure 6.29). The pristine ice mixing ratios are greater in the 3mm case than in the 2MOM case; however, this is at the expense of the snow and graupel mixing ratios within the regions of the updraft, which are much less in the 3mm case. The mean diameter settings for snow (1 mm) and graupel (1 mm) are larger than those diagnosed in the two-moment scheme (~0.1 and ~0.2 mm respectively) throughout most of the cloud. The greater mean diameters increase the collection rates of these species by hail, and reduce their residence time in the regions of liquid water, leading to the observed reduction in their mixing ratios in the 3mm case. The mean aggregates diameter (1 mm) set in the 3mm case is similar to those diagnosed in the 2MOM case and, as a result, the aggregate mixing ratios do not differ greatly between the simulations.

Examining the diagnosed mean hail diameter at 20 minutes (Figure 6.30) and 60 minutes (Figure 6.31) in the 2MOM case shows that the mean hail diameter reaches 6 mm in the lower regions of the cloud, but is less than 2mm throughout most of the cloud. This variation of the mean hail diameter throughout the cloud is a more realistic representation of an actual cloud, than when the mean hail diameter is fixed throughout the cloud, as larger hailstones will be found in the lower regions due to their larger fall speeds. As the mean hail diameter is less than 2mm above the melting level, the fall speeds will be smaller in the 2MOM run than in the 3mm case, above this level. This affects the precipitation type, amount and distribution and, as we have already seen, can have a significant impact on the downdraft strength and position.

As a result of the increased mean hail diameter, as well as the increased sizes of the low density ice species, the collection of snow, aggregates and graupel by hail is more rapid in the 3mm cases. The hail mixing ratios are therefore greater in this case. The hail maximum is, however, positioned higher in the cloud in the 2MOM case, which is a function of the reduced fall speeds. The 9 $g.kg^{-1}$ isoline, for example, occurs at ~12 km in

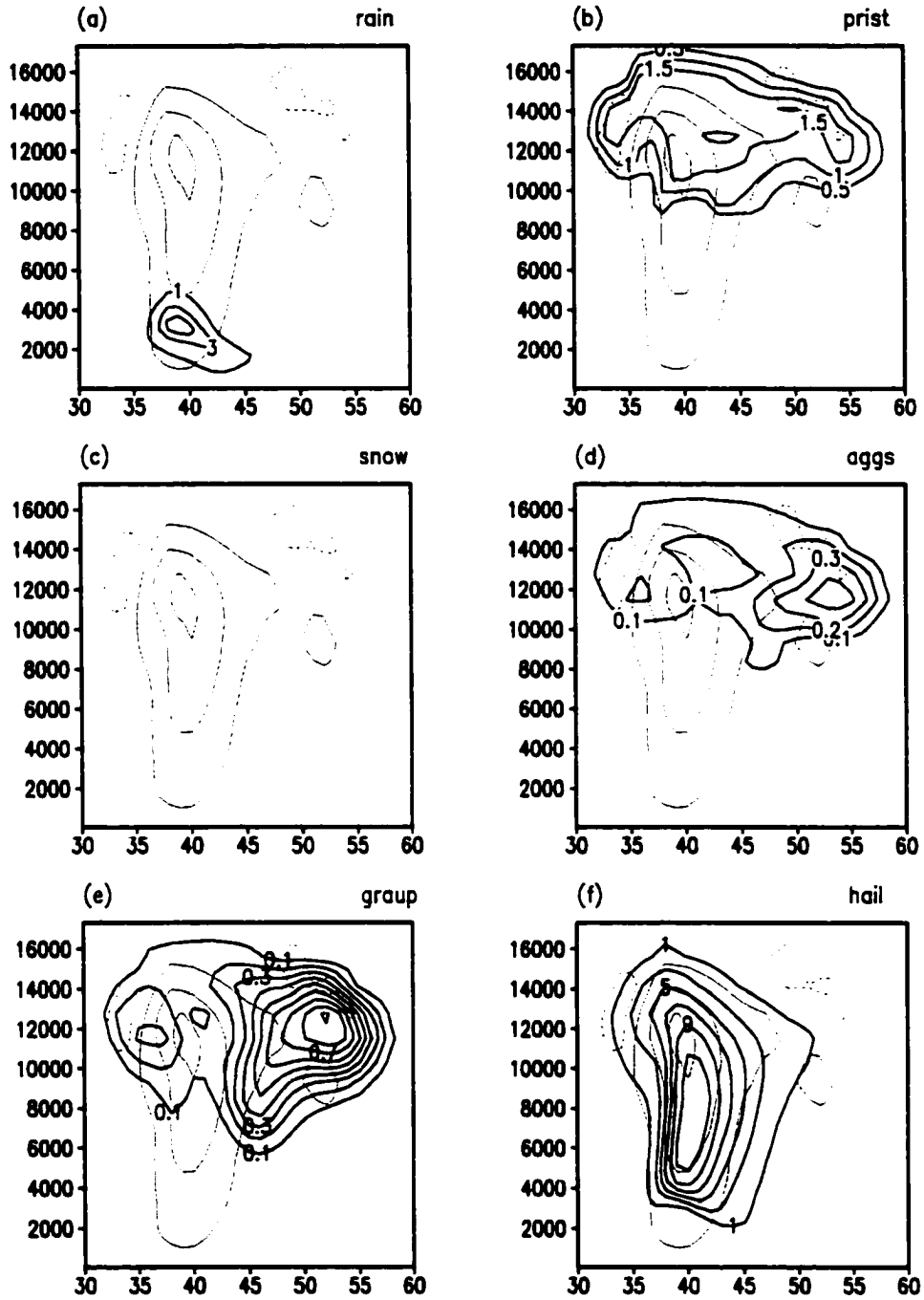


**Figure 6.28: Vertical cross section through the vertical velocity (thin lines, interval 20m.s$^{-1}$ starting at –10 m.s$^{-1}$) and (a) rain mixing ratio (thick lines, interval 2 g.kg$^{-1}$ starting at 1), (b) pristine ice mixing ratio (thick lines, interval 0.5 g.kg$^{-1}$), (c) snow mixing ratio (thick lines, interval 0.1 g.kg$^{-1}$), (d) aggregates mixing ratio (thick lines, interval 0.1 g.kg$^{-1}$), graupel mixing ratio (thick lines, interval 0.1 g.kg$^{-1}$) and (f) hail mixing ratio (thick lines, interval 2 g.kg$^{-1}$ starting at 1) for the 3mm case at 20 minutes.**

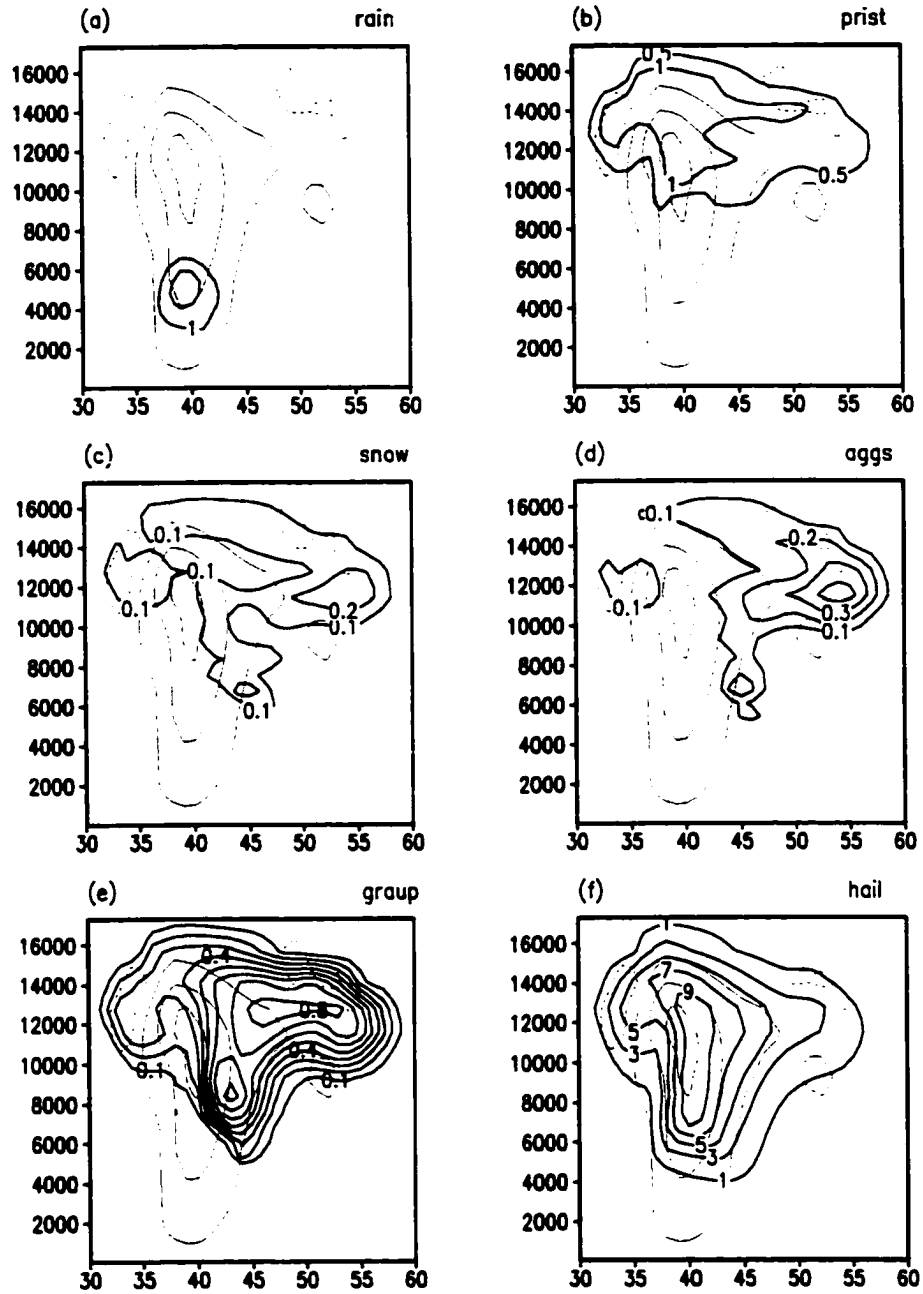


**Figure 6.29: Vertical cross section through the vertical velocity (thin lines, interval 20m.s$^{-1}$ starting at −10 m.s$^{-1}$) and (a) rain mixing ratio (thick lines, interval 2 g.kg$^{-1}$ starting at 1), (b) pristine ice mixing ratio (thick lines, interval 0.5 g.kg$^{-1}$), (c) snow mixing ratio (thick lines, interval 0.1 g.kg$^{-1}$), (d) aggregates mixing ratio (thick lines, interval 0.1 g.kg$^{-1}$), graupel mixing ratio (thick lines, interval 0.1 g.kg$^{-1}$) and (f) hail mixing ratio (thick lines, interval 2 g.kg$^{-1}$ starting at 1) for the 2mom case at 20 minutes.**

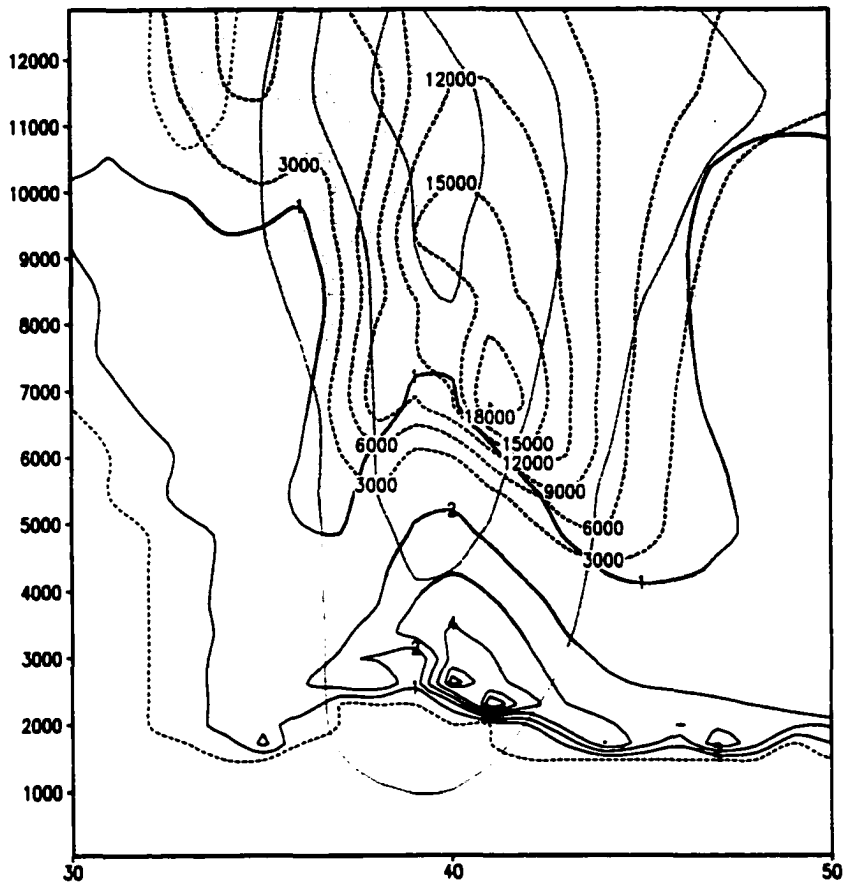


**Figure 6.30: Vertical cross-section through the vertical velocity (thin lines, interval 20m.s$^{-1}$ starting at −10m.s$^{-1}$), mean hail diameter (thick lines, interval 1mm), hail number concentration (thick dashed lines, interval 3000 #m$^{-3}$) for the 2MOM case at 20 minutes. The shaded area is the region where the hail mixing ratios are greater than 0.5 g.kg$^{-1}$.**

the 3mm case, but above 13 km in the 2MOM case. The 2MOM hail is distributed further away from the updraft core at higher levels, which again represents the impact of the fall velocity. As this is an idealized study, it is difficult to argue the merits of the two-moment simulation over the single-moment simulation, since there are no observations to compare the output to. However, the two-moment scheme does allow: a more realistic distribution of hail (and other species for that matter) throughout the cloud, a variation in the mean diameters of all the species which is also more realistic, and for the existence of the smaller ice species, which only occur in trace amounts in all of the single-moment simulations conducted here, due to the excessively rapid collection processes.

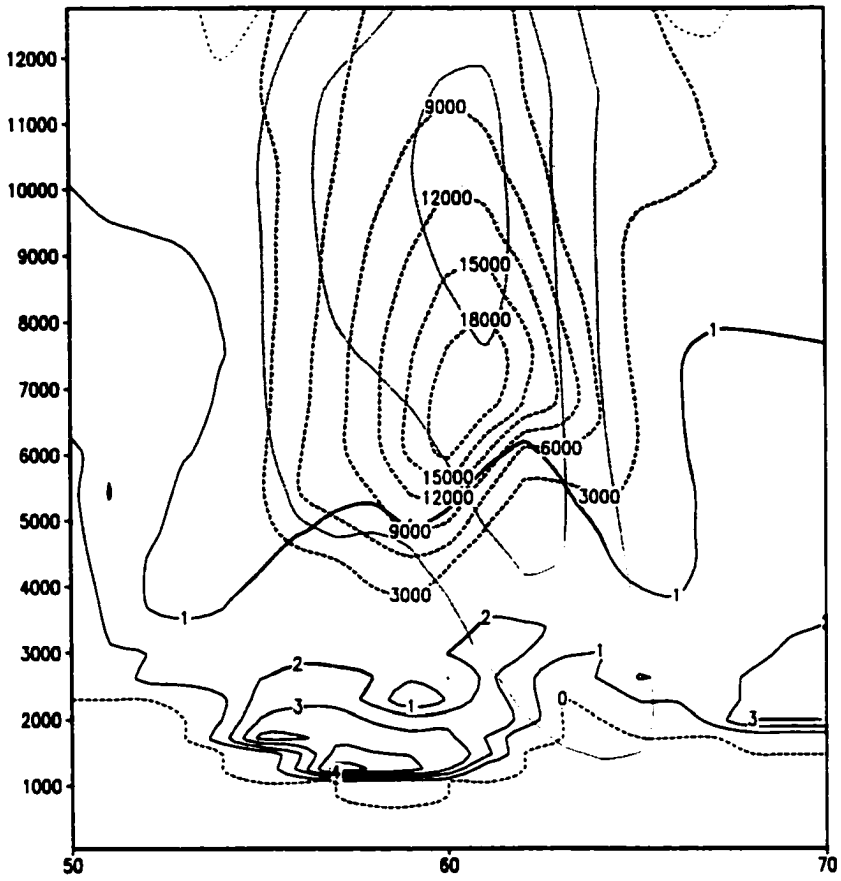


**Figure 6.31: Vertical cross-section through the vertical velocity (thin lines, interval 20m.s$^{-1}$ starting at −10m.s$^{-1}$), mean hail diameter (thick lines, interval 1mm), hail number concentration (thick dashed lines, interval 3000 #m$^{-3}$) for the 2MOM case at 60 minutes. The shaded area is the region where the hail mixing ratios are greater than 0.5 g.kg$^{-1}$.**

In both the 3mm and 2MOM cases, rain develops within the updraft as air is forced to rise, but is soon depleted by collision and coalescence processes with the ice species, as well as by freezing to form hail. A further source of rain is melting and shedding. In the 3mm case, 35% more rain is produced, and the maximum mixing ratios closely coincide with the minimum hail mixing ratios, indicating the production of rain through the loss of hail (Figure 6.32a). This is enhanced by the greater fall velocities in the 3mm case, which permits hail to fall further below the melting level (~4km AGL). Little rain occurs above the melting level, indicating the loss of rain through freezing to form hail, as well as the greater collection due to the larger mean rain diameters in the

(a)

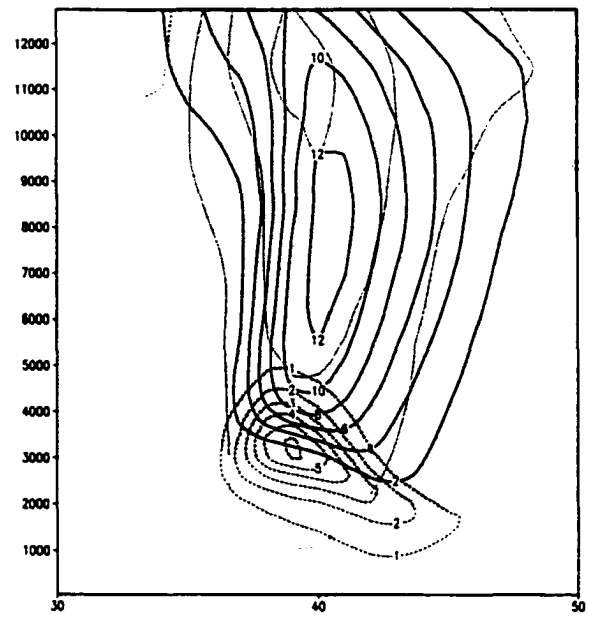


(b)

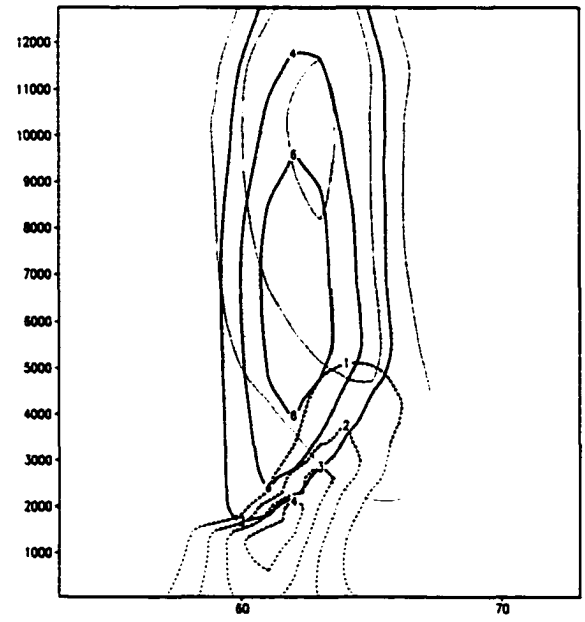


**Figure 6.32: Vertical cross section through the vertical velocity (thin lines, interval 20 $m.s^{-1}$ starting at –10 $m.s^{-1}$), hail mixing ratio (thick lines, interval 2 $g.kg^{-1}$) and rain mixing ratio (thick dashed lines, interval 1 $g.kg^{-1}$) for the 3mm case at (a) 20 minutes and (b) 60 minutes. The shaded area represents that region where the hail mixing ratios are greater than 0.5 $g.kg^{-1}$.**

3mm case. In the 2MOM case, the reduced fall velocities mean that less hail extends below the melting level at this stage (Figure 6.33a). The production of rain is also impeded at the lower levels by the larger mean hail sizes in this region, which reduce melting rates. This is demonstrated more clearly at 60 minutes (Figure 6.32b, Figure 6.33b). At this stage, rain is produced in the updraft in the 3mm case, however, the maximum rain mixing ratios uniformly coincide, as at 20 minutes, with the hail minima. In the 2MOM case, the impact of the varying hail sizes is apparent on the rain mixing ratios. Greater rain mixing ratios occur in the regions of the smaller hail diameters and visa-versa, as the melting rates vary with the change in hail size. This affects the amount of rain, as well as the distribution of rain at the surface. In the 3mm case, 3.5 $g.kg^{-1}$ of rain reach the surface at 60 minutes, whereas only 1.5 $g.kg^{-1}$ occurs at the surface in the 2MOM case, even though the maximum hail mixing ratios are identical at this time (7 $g.kg^{-1}$). The smaller rain mixing ratios at the surface in the 2MOM case are also affected by the smaller fall speeds of rain in the 2MOM case.

Several supercell characteristics are better developed in the 2MOM case. These include the BWER region, the presence of only a few, small hail particles within the echo region itself, the occurrence of larger hail in the hook, and a better-developed anvil. The low-level mesocyclone is also stronger. These may be attributed to the variations in fall speeds associated with the variations in the mean hail diameter.

Finally, the dynamics of the storms that develop in the 2MOM case fall between those of the 3mm and 2cm cases. The RM updraft is steadier, the occlusion and associated vorticity maxima occur later, the vertical vorticity is greater, the cold pool is warmer, and the LM is longer-lived in the 2MOM case than in the 3mm run. This occurs even though the mean hail diameter above the melting level is less than 2 mm, therefore highlighting the influence of a variable mean hail (and other hydrometeor) diameter. The

(a)

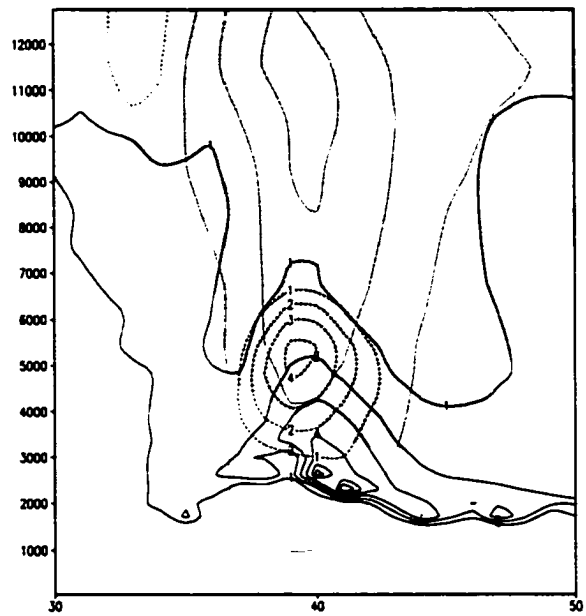


(b)

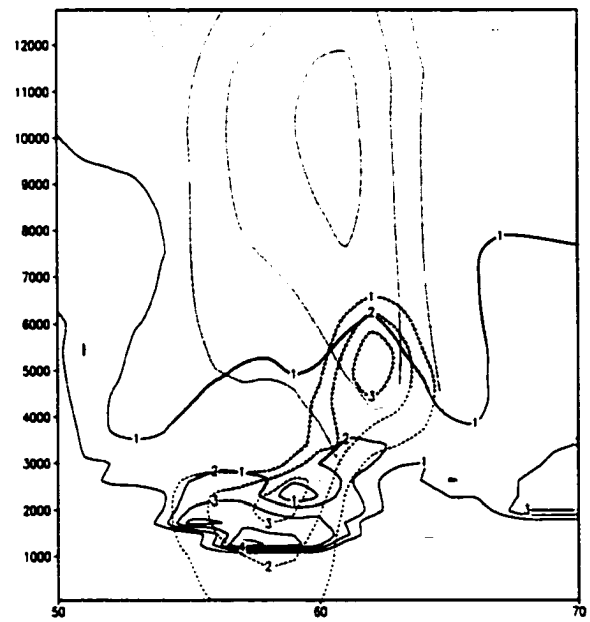


**Figure 6.33: Vertical cross section through the vertical velocity (thin lines, interval 20 $m.s^{-1}$ starting at $-10m.s^{-1}$), mean hail diameter (thick lines, interval 1mm) and rain mixing ratio (thick dashed lines, interval 1 $g.kg^{-1}$) for the 3mm case at (a) 20 minutes and (b) 60 minutes. The shaded area represents that region where the hail mixing ratios are greater than 0.5 $g.kg^{-1}$.**

smaller hail in the upper levels of the 2MOM case permits a more widespread distribution, both vertically and horizontally. Also, the hail mixing ratios are greater higher up in the cloud due to the reduced fall speeds. The larger hail diameters just below cloud base reduce the melting rates and the rain production, produce a warmer cold pool, and reduce the strengths of the low-level downdrafts, while maintaining the proximity of the downdraft to the updraft. This results in the development of stronger low-level vertical vorticity in the 2MOM case.

### 6.3.4 *Balance Theory*

In the $\nu$ sensitivity tests there exists a critical value of $\nu$ (between 1 and 3) below which, the RM updraft and mesocyclone develops more rapidly but weakens to a greater extent, and above which, the RM updraft and mesocyclone take longer to develop, but the storm is steadier and longer-lived. These results demonstrate that a balance is needed between the hail distribution characteristics and the strength of the low-level inflow air, if a long-lived, relative steady updraft and mesocyclone are to develop. When there are a greater number of smaller hailstones, evaporative and melting processes occur more rapidly, and a stronger, evaporatively-generated downdraft develops. If the downdraft and associated cold pool are too strong, the gust front and updraft become displaced too far from the downdraft too rapidly for the downdraft to maintain the low-level convergence within the updraft. This reduces both the updraft strength and the low-level vertical vorticity, which is dominated by the stretching term in all the tests conducted here. Thus, while the updraft and vertical vorticity may initially increase rapidly due to the stronger downdrafts, they are not sustained. The weaker fall velocities of the smaller hail also result in its distribution, and hence the position of the evaporatively-cooled downdraft, further away from the low-level updraft. This scenario occurs in the 3mm ($\nu$=1) case. An increase in the number of larger hailstones relative to the number of smaller hailstones

results in a weaker low-level downdraft situated closer to the updraft. The weaker outflow associated with the weaker downdraft keeps the gust front and low-level updraft in close proximity to the downdraft. This, together with the initially close location of the downdraft to the updraft by virtue of the larger terminal fall speeds, enhances the storm-relative inflow and convergence within the updraft, and results in a stronger, steadier storm, and a stronger mesocyclone. This scenario occurs in the NU5 case, and to a lesser extent in the NU3 case.

A critical mean hail diameter (between 5mm and 1cm) separating two modes of storm development is also found in the diameter sensitivity tests. As in the $\nu$ sensitivity tests, for cases in which the mean hail diameter is above the critical diameter, the RM updrafts take longer to achieve their maxima, but the storms are steadier than those below the critical diameter, which develop rapidly, but also dissipate more rapidly and take longer to recover. The low-level vertical vorticity trends in the diameter tests differ from those in the shape parameter tests. In the diameter tests, the vorticity is greater in the 3mm and 5mm tests, in which the diameter is below the apparent critical diameter. In the 1cm case, the strength of the low-level mesocyclone remains relatively steady, and in the 2cm case, the mesocyclone is only starting to reach its maximum toward the end of the simulation. While greater vertical vorticity values are achieved in the 3mm and 5mm cases, they are more variable, becoming less than those of the 1cm and 2cm cases at times (see Figure 4.36). In summary, the updrafts and low-level mesocyclone develop more rapidly and achieve greater maxima in the smaller diameter cases, however, the updrafts and low-level-mesocyclone while stronger, are not as steady and long-lived.

The theory just described above is somewhat similar to that presented by Brooks et al. (1994b), as outlined in detail in Chapter 2. However, two significant differences exist. Brooks et al. emphasized the proximity of the downdraft to the updraft in order to facilitate the baroclinic generation of vertical vorticity. While the baroclinic generation of low-level vertical vorticity is seen to occur along regions of the RFD, and is recognized

as being important because it generates horizontal vorticity instead of simply modifying it, the contributions of the stretching term are seen to be much greater here, and the proximity of the downdraft to the updraft is therefore necessary to enhance the low-level convergence.

The second difference between the theory proposed here and that of Brooks et al., involves the importance of the mid-level storm-relative shear. Brooks et al. claimed that the relative strength of the mid-level shear and mesocyclone are important in determining the longevity of the low-level mesocyclone and the type of supercell that develops. In their observational study of the winds associated with supercells, Rasmussen and Straka (1998) found little difference in the mid-level wind structure across a wind range of supercell storm types and environments. In the simulations conducted here, the mid-level storm-relative wind shear is relatively similar in each case, since the hodographs are identical, and the storm speeds are comparable. It is the variations in hail size that permit differences in the distribution of both rain and hail with respect to the updraft, and hence the strength and the location of the evaporatively-driven downdraft with respect to the updraft. In the simulations conducted by Brooks et al., ice processes were not included, and the fall speeds of rain differ less than that of ice, given the many different densities and forms of ice that are present in a cloud. It would therefore seem that the hail size distribution may be more important than the mid-level wind structure in determining the strength and longevity of the RM storm and its associated mesocyclone. As the hail size distribution appears to be important in determining the supercell storm characteristics, aspects affecting the distribution, like the shape parameter and the mean hail diameter, should therefore be chosen carefully.

### 6.3.5 *Conclusions*

Numerous conclusions may be drawn from the sensitivity tests discussed in this chapter. The main findings may be summarized as follows:

- The results from the ν sensitivity tests show that evaporation and melting rates decrease as the shape parameter is increased from 1 to 5. Even though the low-levels downdrafts are thus weaker in the larger ν cases, they are positioned closer to the updraft. The close proximity of the downdraft to the updraft permits greater low-level convergence in the region of the updraft in the higher ν cases. The low-level environmental winds are insufficient to prevent the gust front and updraft from becoming separated from the strong low-level downdraft in the NU1 case. The low-level convergence and associated mesocyclone development is therefore weaker in this case. The longevity and steadiness of the storm appear to depend on a balance between the characteristics of the hail size distribution and the low-level inflow. This is also applicable in the mean hail diameter sensitivity tests.

- The results from the NOHAIL simulation indicate the importance of hail in the distribution of rain throughout the storm. Significantly less rain occurs above the melting level in the 3mm case as hail acts as a raindrop sink. However, more rain occurs in the 3mm case at the lower levels through melting processes. In the NOHAIL simulation, even though the rain mixing ratios are greater due to the absence of hail, the rain remains largely suspended in the higher regions of the cloud as a result of its lower fall speeds. Another impact of excluding hail was the delayed onset of the development of the low-level vertical vorticity. This is due to the slower development of the low-level downdrafts, which is a function of the smaller fall speeds of rain.

- The 2MOM tests reveal that the variation in the mean hail diameter results in: the wider distribution of hail, both vertically and horizontally within the storm due to the smaller hail sizes aloft, a reduction in the rain produced near the surface due to the larger hail sizes in the lower regions of the storm which slow melting, weaker low-level downdrafts that are located closer to the updraft, and stronger low-level vertical vorticity. Many of the typical supercell characteristics are better represented in the 2MOM simulation.

# 7

# Summary and Future Research

## 7.1 Summary

The results of the sensitivity tests presented in the previous chapters, demonstrate that the presence of hail, and the way that it is parameterized, affects numerous characteristics of the supercell storms that develop. When hail and its associated processes are not included in the simulation, the maximum rain mixing ratios are greater in the NOHAIL case. However, more rain is received at the surface in the hail cases. The rain in the NOHAIL case remains suspended in the upper levels, as hail, which acts as a sink of rain in the upper regions and a source of rain in the lower regions, is absent. Also, the development of the low-level downdrafts, and associated low-level vertical vorticity, is delayed due to the smaller fall speeds of rain. Excluding hail in supercell simulations may, therefore, result in an inaccurate representation of the rain distribution, as well as the rate at which the storm and mesocyclone develop.

The results presented here show when hail is included, the storms that develop are sensitive to the hail size distribution. The aspects of the simulated supercells that are affected by changes in the size distribution include the longevity of the LM and RM storms, the strength of the low-level downdrafts and associated cold pools, the strength of the low-level mesocyclone, and the magnitude and distribution of precipitation within the

storm, as well as at the surface. These effects are due to the differences in the melting and evaporation rates, as well as differences in the fall speeds, that occur as the size distribution of hail is varied.

It appears from these results that the precipitation characteristics of a supercell may determine the type of supercell storm that develops. This emphasizes the fact that, not only do the dynamics of supercells have an impact on the storm's precipitation characteristics, but that the precipitation characteristics have an influence on the storm dynamics as well.

The hail size distribution sensitivity tests suggest that, if a long-lived, steady mesocyclone is to develop, a balance is needed between the hail distribution characteristics and the strength of the low-level inflow air. The hail distribution characteristics determine both the strength of the low-level downdrafts, as well as the location of the downdraft with respect to the updraft. The low-level inflow air controls the position of the gust front with respect to the updraft. The strength of the downdrafts, and the proximity of the downdraft to the updraft, are both important in enhancing the convergence of air in the lower regions of the updraft. Stronger updrafts and low-level vertical vorticity result from the enhanced convergence within the updraft. In the simulations conducted here, stronger low-level vertical vorticity occurs in the smaller hail diameter cases. Should this hypothesis be found to be robust, it has implications for surface hail fall reduction by cloud seeding, in which the goal is to reduce the hail size of the storm.

In the larger hail cases, the LM storm is long-lived, in spite of the veering of the hodograph in the lower levels. Veering of the hodograph is traditionally associated with the development of an unfavorable (favorable) vertical pressure gradient in the lower levels of the LM (RM), due to the linear response of the storm to the environmental winds. The RM storm is indeed stronger than the LM storm in all of the simulations,

which indicates that this effect does influence the storm development. However, the buoyant forcing appears to play a greater role in the dissipation of the LM storm. This supports the recent findings of Grasso (2000). Further examination of the buoyant forcing reveals, that the thermodynamic contribution to the buoyant forcing is greater in the smaller hail cases, whereas the condensate loading and thermodynamic forcing are of similar magnitude in the larger hail cases. This highlights the dominance of the melting and evaporative processes in the smaller hail cases, the importance of the greater fall speeds in the larger hail cases, and the impact of the hail size distribution.

In the two-moment scheme, the mixing ratio and number concentration are both predicted, and the mean hail diameter is diagnosed. As such, the mean hail diameter can vary throughout the simulation. This has an impact on the size distribution characteristics and the fall speeds. Sensitivity tests conducted using the two-moment scheme reveal, that several supercell characteristics are better developed, than when using the single-moment scheme. The RM storm that develops when using the two-moment scheme possesses characteristics of both the RM storms in the single-moment small hail cases, and of the RM storms in the single-moment large hail cases. This is due to the variation in the mean hail diameter with space and time in the two-moment simulations. In the absence of in situ cloud data, the two-moment scheme could be used as guidance in determining the values for the hail parameters in the single-moment scheme.

Finally, these results indicate the sensitivity of simulated supercell storms to the characteristics of the hail size distribution. This points to the need to ensure that the parameters determining the size distribution are accurately set or predicted. It also highlights the need to understand the factors that influence the hail size distribution of observed storms. Such factors may include cloud condensation nuclei (CCN), giant cloud condensation nuclei (GCCN), ice nuclei (IN) and the vertical velocity.

## 7.2 Future Work

- The sensitivity tests conducted here suggest that hail has a significant impact on the development of the updraft and the low-level mesocyclone. It would be useful to determine if hail has a similar effect on the storm dynamics when the environmental conditions are different. The simulations performed here could be rerun using different vertical wind shear conditions and different low-level relative humidity profiles. The wind shear will affect the distribution of the precipitation with respect to the updraft, and the low-level relative humidity influences the evaporation rates, and the relative importance of melting to evaporation.

- The tests conducted here involved changing only several of the parameters pertaining to hail. The same simulations could be run for rain, and for the other ice species such as snow, aggregates, and graupel in order to determine the impact of these species on the storm dynamics. Also, once an understanding has been obtained regarding the influence of changing in a single hydrometeor species, the parameters of several hydrometeor types could be varied simultaneously, in order to determine whether the impact of the individual species on the storm dynamics is enhanced or inhibited by changes in another species.

- In the simulations conducted above, the occlusion process was retarded by what appears to be insufficient grid resolution. Performing the simulations above with a finer grid resolution may provide us with further insight regarding the role of hail in the occlusion and cyclic mesocyclogenesis process. Also, the ideas of Rasmussen and Straka (1998) regarding the re-ingestion of hail particles falling from the anvil could be further investigated using a finer vertical grid resolution.

- We saw from the results reported here that several supercell characteristics were better developed when the two-moment scheme, in which the mean hail diameter could vary, was used. It would be most interesting to repeat the simulations described here using

bin model microphysics, which allows for even greater degrees of freedom. The hydrometeor size distribution is represented by a series of discrete bins, and the distribution is allowed to evolve throughout the simulation. The use of such a scheme would provide us with the opportunity to gain further insight into the impact that hail has on the dynamics and precipitation characteristics of supercell storms. It would also allow for an investigation into the factors that determine the size-spectra of hydrometeors. Possible factors include the CCN, GCCN, IN, and the vertical velocity.

- Finally, given the sensitivity of the simulated storms to the hail size distribution characteristics, more observational studies of the microphysical aspects of supercell storms would be most beneficial.

# 8

# References


Adlerman, E.J., K.K. Droegemeier and R. Davies-Jones, 1999: A numerical simulation of cyclic mesocyclogenesis. *J. Atmos. Sci.*, **56**, 2045-2069.

Admirat, P., 1985: Comparative study of hailstorms in Switzerland, Canada and South Africa. *J. Climatology*, **5**, 35-51.

Barnes, S.L., 1970: Some aspects of a severe, right-moving thunderstorm deduced from mesonetwork rawinsonde observations. *J. Atmos. Sci.*, 27, 634-648.

Batten, L.J., 1959: *Radar Meteorology*. Chicago, University of Chicago Press, 161pp.

Bluestein, H.B., 1984: Further examples of low-precipitation severe thunderstorms. *Mon. Wea. Rev.*, **112**, 1885-1888.

Bluestein, H.B., and D.R. MacGorman, 1998: Evolution of cloud-to-ground lightning characteristics and storm structure in the Spearman, Texas, tornadic supercells of 31 May 1990. *Mon. Wea. Rev.*, **126**, 1451-1467.

Bluestein, H.B., and C.R. Parks, 1983: A synoptic and photographic climatology of low-precipitation severe thunderstorms in the Southern Plains. *Mon. Wea. Rev.*, **111**, 2034-2046.

Bluestein, H.B., and C.J. Sohl, 1979: Some observations of a splitting severe thunderstorm. *Mon. Wea. Rev.*, **107**, 861-873.

Bluestein, H.B., and G.R. Woodall, 1990: Doppler-radar analysis of a low-precipitation severe storm. *Mon. Wea. Rev.*, **118**, 1640-1664.

Brandes, E.A., 1978: Mesocyclone evolution and tornadogenesis: Some observations. *Mon. Wea. Rev.*, **106**, 995-1101.

Brandes, E.A., 1981: Fine structure of the Del City-Edmond tornadic mesocirculation. *Mon. Wea. Rev.*, **109**, 635-647.

Brandes, E.A., 1984: Vertical vorticity generation and mesocyclone sustenance in tornadic thunderstorms: The observational evidence. *Mon. Wea. Rev.*, **112**, 2253-2269.

Brooks, H.E., C.A. Doswell III, and J. Cooper, 1994a: On the environments of tornadic and nontornadic mesocyclones. *Wea. Forecasting*, **9**, 606-618.

Brooks, H.E., C.A. Doswell, and R. Davies-Jones, 1993: Environmental helicity and the maintenance and evolution of low-level mesocyclones. *The Tornado: Its Structure, Dynamics, Prediction, and Hazards. Geophys. Monogr. No. 79*, C.R. Church, D. Burgess, C. Doswell, and R. Davies-Jones, Eds. Amer. Geophys. Union Press, **79**, 97-104.

Brooks, H.E., C.A. Doswell III, and R.B. Wilhelmson, 1994b: The role of midtropospheric winds in the evolution and maintenance of low-level mesocyclones. *Mon. Wea. Rev.*, **122**, 126-136.

Brooks, H.E., and R.B. Wilhelmson, 1992: Numerical simulation of a low-precipitation supercell thunderstorm. *Meteor. Atmos. Phys.*, **49**, 3-17.

Browning, K.A., 1963: The growth of large hail within a steady updraught. *Quart. J.Roy. Meteor. Soc.*, **89,** 490-506.

Browning, K.A., 1964: Airflow and precipitation trajectories within severe local storms which travel to the right of the winds. *J. Atmos. Sci.*, **21**, 634-639.

Browning, K.A., 1968: The organization of severe local storms. *Weather*, **23**, 429-434.

Browning, K.A., 1977: The structure and mechanism of hailstorms. *Hail: A Review of Hail Science and Hail Suppression, Meteor. Monogr.*, No. 38, Amer. Meteor. Soc., 1-43.

Browning, K.A., and R.J. Donaldson, 1963: Airflow and structure of a tornadic storm. *J. Atmos.Sci.*, **20**, 533-545.

Browning, K.A., and G.B. Foote, 1976: Airflow and hail growth in supercell storms and some implications for hail suppression. *Quart. J.Roy. Meteor. Soc.*, **102**, 499-533.

Browning, K.A., and C.R. Landry, 1963: Airflow within a tornadic storm. Preprints, *10th Weather Radar Conference*, Boston, MA, Amer. Meteor. Soc., 116-122.

Browning, K.A., and F.H. Ludlam, 1962: Airflow in convective storms. *Quart. J. R. meteor. Soc.*, **88**, 117-135.

Burgess, D.W., and E.B. Curran, 1985: The relationship of storm type to environment in Oklahoma on 26 April 1984. Preprints, *14th Conf. on Severe Local Storms*, Indianapolis, IN, Amer. Meteor. Soc., 208-211.

Burgess, D.W., and R.P. Davies-Jones, 1979: Unusual tornadic storms in eastern Oklahoma on 5 December 1975. *Mon. Wea. Rev.*, **107**, 451-457.

Burgess, D.W., and L.R. Lemon, 1991: Characteristics of mesocyclones detected during a NEXRAD test. Preprints, *25th Int. Conf. On Radar Meteorology*, Paris, France, Amer. Meteor. Soc., 39-42.

Burgess, D.W., V.T. Wood, and R.A. Brown, 1982: Mesocyclone Evolution Statistics. Preprints, *12th Conf. on Severe Local Storms*, San Antonio, TX, Amer. Meteor. Soc., 422-424.

Charba, J., and Y. Sasaki, 1971: Structure and movement of the severe thunderstorms of 3 April 1964 as revealed from radar and surface mesonetwork analysis. *J. Meteorol. Soc. Jpn.*, **49**, 191-213.

Chisolm, A.J., 1973: Alberta Hailstorms: Part I. Radar studies and airflow models. *Alberta Hailstorms. Meteor. Monogr.*, No. 36, Amer. Meteor. Soc., 1-36.

Chisolm, A.J., and J.H. Renick, 1972: The kinematics of multicell and supercell Alberta hailstorms. Alberta Hail Studies, 1972, Research Council of Alberta Hail Studies Report No. 72-2, 24-31.

Clark, T.L., 1977: A small-scale dynamic model using a terrain-following coordinate transformation. *J. Comput. Phys.*, **24**, 186-215.

Clark, T.L., 1979: Numerical simulations with a three-dimensional cloud model: Lateral boundary condition experiments and multicellular storm simulations. *J. Atmos. Sci.*, **36**, 2191-2215.

Cotton, W.R., and R.A. Anthes, 1989: *Storm and Cloud Dynamics*. Academic Press, Inc., San Diego, 883pp.

Cotton, W.R., R.A. Pielke, R.L. Walko, G.E. Liston, C.J.Tremback, H. Jiang, R.L. McAnnelly, J.Y. Harrington, and M.E. Nicholls, 2001: RAMS 2001: Current status and future directions. Accepted to *Meteor. Atmos. Phys.*

Cotton, W.R., M.A. Stephens, T. Nehrkorn, and G.J. Tripoli, 1982: The Colorado State University three-dimensional cloud model – 1982. Part II: An ice phase parameterization. *J. Rech. Atmos.*, **16**, 295-320.

Cotton, W.R., G.J. Tripoli, R.M. Rauber, and E.A. Mulvihill, 1986: Numerical simulation of the effects of varying ice crystal nucleation rates and aggregation processes on orographic snowfall. *J. Clim. Appl. Meteor.*, **25**, 1658-1680.

Curran, E.B., and W.D. Rust, 1992: Positive ground flashes produced by low-precipitation thunderstorms in Oklahoma on 26 April 1984. *Mon. Wea. Rev.*, **120**, 544-553.

Danielson, E.F., 1977: Inherent difficulties in hail probability prediction. *Meteorol. Monogr.*, **38**, 135-143.

Darkow, G.L., and D.W. McCann, 1977: Relative environmental winds for 121 tornado bearing storms. Preprints, *10th Conf. Severe Local Storms*, Omaha, NB, Amer. Meteor. Soc., 413-417.

Darkow, G.L., and J.C. Roos, 1970: Multiple tornado producing thunderstorms and their apparent cyclic variations in intensity. Preprints, *14th Conf. on Radar Meteorology*, Tucson, AZ, Amer. Meteor. Soc., 305-308.

Davies, J.M., 1993: Hourly helicity, instability, and EHI in forecasting supercell tornadoes. Preprints, *17th Conf. on Severe Local Storms*, St. Louis, MO, Amer. Meteor. Soc., 107-111.

Davies, J.M., and R.H. Johns, 1993: Some wind and instability parameters associated with strong and violent tornadoes. 1. Wind shear and helicity. *The Tornado: Its Structure, Dynamics, Prediction, and Hazards. Geophys. Monogr. No. 79*, C.R.

Church, D. Burgess, C. Doswell, and R. Davies-Jones, Eds. Amer. Geophys. Union Press, **79**, 573-582.

Davies-Jones, R.P., 1982: Tornado dynamics. *Thunderstorms: A Social, Scientific and Technological Documentary, Vol. 2*, E. Kessler, Ed., U.S. Govt. Printing Office, Washington DC, 297-361.

Davies-Jones, R., 1984: Streamwise vorticity: The origin of updraft rotation in supercell storms. *J. Atmos. Sci.*, **41**, 2991-3006.

Davies-Jones, R.P., 1992a: Thunderstorm. *Encyclopedia of Science and Technology*, 7th ed., McGraw-Hill, New York.

Davies-Jones, R.P., 1992b: Tornado. *Encyclopedia of Science and Technology*, 7th ed., McGraw-Hill, New York.

Davies-Jones, R.P., and H.E. Brooks, 1993: Mesocyclogenesis from a theoretical perspective. *The Tornado: Its Structure, Dynamics, Prediction, and Hazards. Geophys. Monogr. No. 79*, C.R. Church, D. Burgess, C. Doswell, and R. Davies-Jones, Eds. Amer. Geophys. Union Press, **79**, 105-114.

Davies-Jones, R.P., D.W. Burgess, and M. Foster, 1990: Test of helicity as a tornado forecast parameter. Preprints, *16th Conf. on Severe Local Storms*, Kananaskis Park, Alberta, Canada, Amer. Meteor. Soc., 588-592.

Davies-Jones, R.P., D.W. Burgess, and L.R. Lemon, 1976: An atypical tornado-producing cumulonimbus. *Weather*, **31**, 336-347.

Danielson, E.F., 1975: A conceptual theory of tornadogenesis based on marco-, meso- and microscale processes. Preprints, *9th Conf. on Severe Local Storms*, Norman, OK, Amer. Meteor. Soc., 376-383.

Dessens, J., and J.T. Snow, 1989: Tornadoes in France. *Wea. Forecasting*, 4, 110-132.

Donaldson, R., A. Spatola, and K. Browning, 1965: Visual observations of severe weather phenomena. A family outbreak of severe local storms – A comprehensive study of the storms in Oklahoma on 26 May 1963. Part I. Air Force Cambridge Lab., Spec. Rep. No. 32, 73-97. [Available from AFGL, Hanscomb AFB, MA 01731.]

Doswell, C.A., 1996: What is a supercell? Preprints, *18th Conf. On Severe Local Storms*, San Francisco, CA, Amer. Meteor. Soc., 641.

Dowell, D.C., H.B. Bluestein, and D.P. Jorgensen, 1997: Airborne Doppler radar analysis of supercells during COPS-91. *Mon. Wea. Rev.*, 125, 365-383.

Doswell, C.A., and D.W. Burgess, 1993: Tornadoes and tornadic storms: A review of conceptual models. *The Tornado: Its Structure, Dynamics, Prediction, and Hazards. Geophys. Monogr. No. 79*, C.R. Church, D. Burgess, C. Doswell, and R. Davies-Jones, Eds. Amer. Geophys. Union Press, **79**, 161-172.

Doswell, C.A., A.R. Moller, and R. Przybylinski, 1990: A unified set of conceptual models for variations on the supercell there. Preprints, *16th Conf. on Severe Local Storms*, Kananaskis Park, Alberta, Canada, Amer. Meteor. Soc., 40-45.

Droegemeier, K.K., S.M. Lazarus, and R.P. Davies-Jones, 1993: The influence of helicity on numerically simulated convective storms. *Mon. Wea. Rev.*, **121**, 2005-2029.

English, M., 1973: Alberta hailstorms, Part II: Growth of large hail in the storm. *Meteorol. Monogr.*, **14**, 37-98.

Fankhauser, J.C., 1971: Thunderstorm-environment interactions determined from aircraft and radar observations. *Mon. Wea. Rev.*, **99**, 171-172.

Fankhauser, J.C., and C.G. Mohr, 1977: Some correlations between various sounding parameters and hailstorm characteristics in northeast Colorado. Preprints, *10th Conf. on Severe Local Storms*, Omaha, NE, Amer. Meteor. Soc., 218-225.

Farley, R.D., 1987a: Numerical modeling of hailstorms and hailstone growth. Part II: The role of low density riming growth in hail production. *J. Clim. Appl. Meteor.*, **26**, 234-254.

Farley, R.D., 1987b: Numerical modeling of hailstorms and hailstone growth. Part III: Simulation of an Alberta hailstorm – Natural and seeded cases. *J. Clim. Appl.* Meteor., **26**, 789-812.

Farley, R.D., and H.D. Orville, 1986: Numerical modeling of hailstorms and hailstone growth. Part I: Preliminary model verification and sensitivity tests. *J. Clim. Appl. Meteor.*, **25**, 2014-2036.

Fawbush, E.J., and R.C. Miller, 1954: The types of air masses in which North American tornadoes form. *Bull. Amer. Meteor. Soc.*, **35**, 154-165.

Ferrier, B.S., 1993: A double-moment multiple phase four-class bulk ice scheme. Part I: Description. *J. Atmos. Sci.*, **51**, 249-280.

Finley, C.A., 1997: Numerical simulation of intense multi-scale vortices generated by supercell thunderstorms. Ph.D. Dissertation, Dep. Atmos. Sci., Colorado State Univ.

Flateau, P.J., G.J. Tripoli, J. Verlinde, and W.R. Cotton, 1989: The CSU-RAMS Cloud Microphysical Module: General Theory and Code Documentation. Colorado State Univ., Dep. Atmos. Sci., Fort Collins, Colorado 80523. Atmos. Sci. Pap., 451, 88pp.

Foote, G.B., 1984: A study of hail growth utilizing observed storm condition. *J. Clim. Appl. Meteorol.*, **23**, 84-101.

Foote, G.B., and H.W. Frank, 1983: Case study of a hailstorm in Colorado. Part III. Airflow from triple-Doppler measurements. *J.Atmos. Sci.*, **40**, 686-707.

Fujita, T., 1958: Mesoanalysis of the Illinois tornadoes of 9 April 1953. *J. Meteor.*, **15**, 288-296.

Fujita, T., and H. Grandoso, 1968: Split of a thunderstorm into anticyclonic and cyclonic storms and their motion determined from numerical model experiments. *J. Atmos. Sci.*, **25**, 416-439.

Gal-Chen, T., and R.C.J. Somerville, 1975: On the use of a coordinate transformation for the solution of the Navier-Stokes equations. *J. Comput. Phys.*, **17**, 209-228.

Gilmore, M.S., and L.J. Wicker, 1998: The influence of midtropospheric dryness on supercell morphology and evolution. *Mon. Wea. Rev.*, **126**, 943-958.

Goral, G.G., and L.M. Fedchenko, 1992: Connection of the hail climatology with the surface relief in the USSR regions with danger of hail. *Problemy klimata*. 24-49.

Grasso, L.D., 2000: The dissipation of a left-moving cell in a severe storm environment. *Mon. Wea. Rev.*, **128**, 2797-2815.

Grasso, L.D., and W.R. Cotton, 1995: Numerical simulation of a tornado vortex. *J. Atmos. Sci.*, **52**, 1192-1203.

Hart, J.A., and W. Korotky, 1991: The SHARP workstation v1.50 users guide. National Weather Service, NOAA, US. Dept. of Commerce, 30pp.

Hill, G.E., 1974: Factors controlling the size and spacing of cumulus clouds as revealed by numerical experiments. *J. Atmos. Sci.*, **31**, 646-673.

Hjelmfelt, M.R., H.D. Orville, R.D. Roberts, J.P. Chen, and F.J. Kopp, 1989: Observational and numerical study of a microburst line producing storm. *J. Atmos. Sci.*, **46**, 2731-2743.

Hoecker, W.H., 1959: History and measurement of two major Scottsbluff tornadoes of 27 June 1955. *Bull. Amer. Meteor. Soc.*, **40**, 117-133.

Hong, Y., and F. Pen, 1999: Numerical simulation study of hail cloud – Part I: The numerical model. *Acta. Meteor. Sinica*, **13**, 188-199.

Hubbert, J., V.N. Bringi, L.D. Carey, and S. Bolen, 1998: CSU-CHILL polarimetric radar measurements from a severe hail storm in eastern Colorado. *J. Appl. Meteor.*, **37**, 749-775.

Jewett, B.F., R.B. Wilhelmson, J.M. Straka, and L.J. Wicker, 1990: Impact of ice parameterization on the low-level structure of modeled supercell thunderstorms. Preprints, *16th Conf. on Severe Local Storms*, Kananaskis Park, Alberta, Amer. Meteor. Soc., 275-280.

Johns, R.H., J.M. Davies, and P.W. Leftwich, 1993: Some wind and instability parameters associated with strong and violent tornadoes. Part II: Variations in the combinations of wind and instability parameters. *The Tornado: Its Structure, Dynamics, Prediction, and Hazards. Geophys. Monogr. No. 79*, C.R. Church, D. Burgess, C. Doswell, and R. Davies-Jones, Eds. Amer. Geophys. Union Press, **79**, 583-590.

Johns, R.H., and C.A. Doswell, 1992: Severe local storms forecasting. *Wea. Forecasting*, **7**, 588-612.

Johnson, D.E., P.K. Wang, and J.M. Straka, 1993: Numerical simulations of the 2 August 1981 CCOPE supercell storm with and without ice microphysics. *J. Appl. Meteor.*, **32**, 745-759.

Kessler, E., 1969: On the distribution and continuity of water substance in atmospheric circulation. *Meteor. Monogr.*, No. 32, Amer. Meteor. Soc., 84pp.

Klemp, J.B., 1987: Dynamics of tornadic thunderstorms. *Annu. Rev. Fluid Mech.*, **19**, 369-402.

Klemp, J.B., and R. Rotunno, 1983: A study of the tornadic region within a supercell thunderstorm. *J. Atmos. Sci.*, **40**, 359-377.

Klemp, J.B., and R.B. Wilhelmson, 1978a: The simulation of three-dimensional convective storm dynamics. *J. Atmos. Sci.*, **35**,1070-1096.

Klemp, J.B., and R.B. Wilhelmson. 1978b: Simulations of right- and left-moving storms produced through storm splitting. *J. Atmos. Sci.*, **35**, 1097-1110.

Klemp, J.B., R.B. Wilhelmson, and P.S. Ray, 1981: Observed and numerically simulated structure of a mature supercell thunderstorm. *J. Atmos. Sci.*, **38**, 1558-1580.

Klimowski, B.A., M.R. Hjelmfelt, M.J. Bunkers, D. Sedlacek, and L.R. Johnson, 1998: Hailstorm damage observed from the GOES-8 satellite: the 5-6 July 1996 Butte-Meade storm. *Mon. Wea. Rev.*, **126**, 831-834.

Knight, C.A., 1982: The Cooperative Convective Precipitation Experiment (CCOPE), 18 May-7 August 1981. *Bull. Amer. Meteor. Soc.*, **63**, 386-398.

Knight, C.A., N.C. Knight, J.E. Dye, and V. Toutenhoofd, 1974: The mechanism of precipitation formation in northeastern Colorado cumulus. I. Observations of the precipitation itself. *J. Atmos. Sci.*, **31**, 2142-2147.

Knight, C.A., and K.R. Knupp, 1986: Precipitation growth trajectories in a CCOPE storm. *J. Atmos.Sci.*, **43**, 1057-1073.

Knupp, K.R., 1985: Precipitation convective downdraft structure: A synthesis of observations and modeling. Ph.D. Dissertation, Dep. Atmos. Sci., Colorado State Univ.

Knupp, K.R., 1989: Numerical simulation of low-level downdraft initiation within precipitating cumulonimbi: Some preliminary results. *Mon. Wea. Rev.*, **117**, 1517-1529.

Knupp, K.R., and W.R. Cotton, 1982: An intense, quasi-steady thunderstorm over mountainous terrain. Part II: Doppler radar observations of the storm morphological structure. *J. Atmos. Sci.*, **39**, 343-358.

Krauss, T.W., and J.D. Marwitz, 1984: Precipitation processes within an Alberta supercell hailstorm. *J. Atmos. Sci.*, 41, 1025-1034.

Krueger, S.K., R.M. Wakimoto, and S.J. Lord, 1986: Role of ice-phase microphysics in dry microburst simulations. Preprints, *23rd Radar Meteorology Conf.*, Snowmass, Amer. Meteor. Soc., R73-R76.

Kulie, M.S., and Y.-L Lin, 1998: The structure and evolution of a numerically simulated high-precipitation supercell thunderstorm. *Mon. Wea. Rev.*, **126**, 2090-2116.

Lazarus, S.M., and K.K. Droegemeier, 1990: The influence of helicity on the stability and morphology of numerically simulated storms. Preprints, *16th Conf. Severe Local Storms*, Kananaskis Park, Alberta, Canada, Amer. Meteor. Soc., 269-274.

Lemon, L.R., 1980: Severe thunderstorm radar identification techniques and warning criteria. NOAA Tech. Memo. NWS NSSFC-3, 60pp. National Severe Storms Forecast Center, 60 pp. [NTIS PB81-234809].

Lemon, L.R., and C.A. Doswell III, 1979: Severe thunderstorm evolution and mesocyclone structure as related to tornadogenesis. *Mon. Wea. Rev.*, **107**, 1184-1197.

Lilly, D.K., 1962: On the numerical simulation of buoyant convection. *Tellus*, **14**, 148-172.

Lilly, D.K., 1986: The structure, energetics and propagation of rotating convective storms, II, Helicity and storm stabilization. *J. Atmos. Sci.*, **43**, 126-140.

Lin, Y.L., R.D. Farley, and H.D. Orville, 1983: Bulk parameterization of the snow field in a cloud model. *J. Clim. Appl. Meteor.*, **22**, 1065-1092.

List, R., 1982: Properties and growth of hailstones. *Thunderstorms: A Social, Scientific, and technological Documentary, Vol. 2, Thunderstorm Morphology and Dynamics*. E. Kessler, Ed., U.S. Govt. Printing Office, Washington, D.C., 409-445.

List, R., R.B. Charlton and P.I. Buttuls, 1968: A numerical experiment on the growth and feedback mechanisms of hailstones in a one-dimensional steady-state model cloud. *J. Atmos. Sci.*, **25**, 1061-1074.

Ludlam, F.H., 1963: Severe local storms: A review. *Severe Local Storms, Meteorol. Monogr.* No. 27, 1-30.

Maddox, R.A., 1976: An evaluation of tornado proximity wind and stability data. *Mon. Wea. Rev.*, **104**, 133-142.

Markowski, P.M., and J.M. Straka, 2000: Some observations of rotating updrafts in a low-buoyancy, highly sheared environment. *Mon. Wea. Rev.*, **128**, 449-461.

Marwitz, J.D., 1972: The structure and motion of severe hailstorms. Part III: Severely sheared storms. *J. Appl. Meteor.*, **11**, 189-201.

McPherson, R.A., and K.K. Droegemeier, 1991: Numerical predictability experiments of the 20 May 1977 Del City, OK supercell storm. Preprints, *9th Conf. on Numerical Weather Prediction*, Denver, CO, Amer. Meteor. Soc., 734-738.

Mesinger, F., and A. Arakawa, 1976: Numerical methods used in atmospheric models. GARP Publication Series, No. 14, WMO/ICSU Joint Organizing Committee, 64pp.

Meyers, M.P., R.L. Walko, J.Y. Harrington, and W.R. Cotton., 1997: New RAMS cloud microphysics parameterization. Part II: The two-moment scheme. *Atmos. Res.*, **45**, 3-39.

Miller, L.J., and J.C. Fankhauser, 1983: Radar echo structure, air motion and hail formation in a large stationary multicellular thunderstorm. *J. Atmos. Sci.*, 40, 2399-2418.

Miller, L.J., J.D. Tuttle, and G.B. Foote, 1990: Precipitation production in a large Montana hailstorm: Airflow and particle growth trajectories. *J. Atmos.Sci.*, **47**, 1619-1646.

Miller, L.J., J.D. Tuttle, and C.A. Knight, 1988: Airflow and hail growth in a severe northern High Plains supercell. *J. Atmos. Sci.*, **45**, 736-762.

Moller, A.R., and C.A. Doswell, 1988: A proposed advanced storm spotter's training program. Preprints, *15th Conf. on Severe Local Storms*, Baltimore, MD, Amer. Meteor. Soc., 173-177.

Moller, A.R., C.A. Doswell III, M.P.Foster, and G.R. Woodall, 1994: The operational recognition of supercell thunderstorm environments and storm structures. *Wea. Forecasting*, **9**, 327-347.

Moller, A.R., C.A. Doswell, and R. Przybylinski, 1990: High-precipitation supercells: A conceptual model and documentation. Preprints, *16th Conf. on Severe Local Storms*, Kananaskis Park, Alberta, Canada, Amer. Meteor. Soc. 52-57.

Musil, D.J., A.J. Heymsfield, and P.L. Smith, 1986: Microphysical characteristics of a well-developed weak echo region in a high plains supercell thunderstorm. *J. Clim. Appl. Meteor.*, **25**, 1037-1051.

Nelson, S.P., 1983: The influence of storm flow structure on hail growth. *J. Atmos. Sci.*, **40**, 1965-1983.

Nelson, S.P., 1987: The hybrid multicellular-supercellular storm – an efficient hail producer. Part. II: General characteristics and implications for hail growth. *J. Atmos. Sci.*, **44**, 2060-2073.

Nelson, S.P., and S.K. Young, 1979: Characteristics of Oklahoma hailfalls and hailstorms. *J. Appl. Meteor.*, **18**, 339-347.

Niino, H., O. Suzuki, H. Nirasawa, T. Fujitani, H. Ohno, I. Takayabu, N. Kinoshita and Y. Ogura, 1993: Tornadoes in Chiba Prefecture on 11 December 1990. *Mon. Wea. Rev.*, **121**, 3001-3018.

Nunez, J.M., 1980: Hail suppression projects in Argentina. *Meteorologica*, 11, 31-51.

Orville, H.D., R.D. Farley, Y-C. Chi, and F.J. Kopp, 1989: The primary cloud physics mechanisms of microburst formation. *Atmos. Res.*, **24**, 343-357.

Orville, H.D., and F.J. Kopp, 1977: Numerical simulation of the life history of a hailstorm. *J. Atmos. Sci.*, **34**, 1596-1618.

Pielke, R.A., W.R. Cotton, R.L. Walko, C.J. Tremback, W.A. Lyons, L.D. Grasso, M.E. Nicholls, M.D. Moran, D.A. Wesley, T.J. Lee, and J.H. Copeland, 1992: A comprehensive meteorological modeling system – RAMS. *Meteor. and Atmos. Phys.*, **49**, 69-91.

Proctor, F.H., 1983: Numerical simulation of a bell-shaped cumulonimbus. Preprints, *13th Conf. on Severe Local Storms*. Tulsa, OK, Amer. Meteor. Soc., 235-240.

Proctor, F.H., 1988: Numerical simulations of an isolated microburst. Part I: Dynamics and structure. *J. Atmos. Sci.*, **45**, 3137-3160.

Proctor, F.H., 1989: Numerical simulations of an isolated microburst. Part II: Sensitivity experiments. J. Atmos. Sci., **46**, 2143-2165.

Rasmussen, E.N., R.E. Peterson, J.E. Minor, and B.D. Campbell, 1982: Evolutionary characteristics and photogrammetric determination of wind speeds within the Tulia outbreak tornadoes 28 May 1980. Preprints, *12th Conf. on Severe Local Storms*, San Antonio, TX, Amer. Meteor. Soc., 301-304.

Rasmussen, E.N., and J.M. Straka, 1998: Variations in supercell morphology. Part I: Observations of the role of upper-level storm-relative flow. *Mon. Wea. Rev.*, **126**, 2406-2421.

Rasmussen, E.N., and R.B. Wilhelmson, 1983: Relationships between storm characteristics and 1200 GMT hodographs, low-level shear, and stability. Preprints, *13th Conf. on Severe Local Storms*, Amer. Meteor. Soc., J5-J8.

Ray, P.S., 1976: Vorticity and divergence within tornadic storms from dual Doppler radar. *J. Appl. Meteor.*, **15**, 879-809.

Ray, P.S., R.J. Doviak, G.B. Walker, D. Sirmans, J. Carter, and B. Baumgarner, 1975: Dual-Doppler observations of a Tornadic storm. *J. Appl. Meteor.*, **14**, 1521-1530.

Ray, P.S., B.C. Johnson, K.W. Johnson, J.S. Bradberry, J.J. Stephens, K.K. Wagner, R.B. Wilhelmson, and J.B. Klemp, 1981: The morphology of several tornadic storms on 20 May 1977. *J. Atmos. Sci.*, **38**, 1643-1663.

Ray, P.S., C.L. Ziegler, W. Bumgarner, and R.J. Serafin, 1980: Single- and multiple-Doppler radar observations of tornadic storms. *Mon. Wea. Rev.*, **108**, 1607-1625.

Reisin, T., Z. Levin, and S. Tzivion, 1996: Rain production in convective clouds as simulated in an axisymmetric model with detailed microphysics. Part II: Effects of varying drops and ice initiation. *J. Atmos. Sci.*, **53**, 1815-1837.

Renick, J.H., 1971: Radar reflectivity profiles of individual cells in a persistent multicellular Alberta hailstorm. Preprints, *7th Conf. on Severe Local Storms*, Kansas City, MO, Amer. Meteor. Soc., 63-70.

Rotunno, R., 1981: On the evolution of thunderstorm rotation. *Mon. Wea. Rev.*, **109**, 577-586.

Rotunno, R., and J.B. Klemp, 1982: The influence of the shear-induced pressure gradient on thunderstorm motion. *Mon. Wea. Rev.*, **110**, 136-151.

Rotunno, R., and J.B. Klemp, 1985: On the rotation and propagation of simulated supercell thunderstorms. *J. Atmos. Sci.*, **42**, 271-292.

Schlesinger, R.E., 1973: A numerical model of deep moist convection: Part I. Comparative experiments for variable ambient moisture and wind shear. *J. Atmos. Sci.*, **30**, 835-856.

Schlesinger, R.E., 1975: A three-dimensional numerical model of an isolated deep convective cloud: Preliminary results. *J. Atmos. Sci.*, **32**, 934-957.

Schlesinger, R.E., 1980: A three-dimensional numerical model of an isolated thunderstorm. Part II: Dynamics of updraft splitting and mesovortex couplet evolution. *J. Atmos. Sci.*, **37**, 395-420.

Schlesinger, R.E., 1999: Heat, moisture, and momentum budgets of isolated deep midlatitude and tropical convective clouds as diagnosed from three-dimensional model output. Part II: Sensitivity to ice phase and small change in ambient shear strength and low-level moisture supply. *J. Atmos. Sci.*, **56**, 3520-3543.

Schmid, W., H.H. Schiesser, and B. Bauer-Messmer, 1997: Supercell storms in Switzerland: case studies and implications for nowcasting severe winds with Doppler radar. *Meteor. Appl.*, 4, 49-67.

Smagorinsky, J., 1963: General circulation experiments with the primitive equations. I. The basic experiment. *Mon. Wea. Rev.*, **91**, 99-164.

Srivastava, R.C., 1987: A model of intense downdrafts driven by the melting and evaporation of precipitation. *J. Atmos. Sci.*, **44**, 1752-1773.

Steiner, J.T., 1973: A three-dimensional model of cumulus cloud development. *J. Atmos. Sci.*, **30**, 414-435.

Stout, G.E., 1957: Mesometeorological systems from dense network stations. Paper presented at IUGG meeting, IUGG, Toronto, Ont. Canada.

Takahashi, T., 1976: Hail in an axisymmmetric cloud model. *J. Atmos. Sci.*, **33**, 1579-1601.

Tartaglione, N., A. Buzzi, and M. Fantini, 1996: Supercell simulations with simple ice parameterization. *Meteor. Atmos. Phys.*, **58**, 139-149.

Thompson, R.L., 1998: Eta model storm-relative winds associated with tornadic and nontornadic supercells. *Wea. Forecasting*, **13**, 125-137.

Thorpe, A.J., and M.J. Miller, 1978: Numerical simulations showing the role of the downdraught in cumulonimbus motion and splitting. *Quart. J. Roy. Meteorol. Soc.*, **104**, 873-893.

Tripoli, G.J., and W.R. Cotton, 1982: The Colorado State University three-dimensional cloud/mesoscale model – 1982. Part I: General theoretical framework and sensitivity experiments. *J. de. Rech. Atmos.*, **16**, 185-200.

Tripoli, G.J., and W.R. Cotton, 1986: An intense, quasi-steady thunderstorm over mountainous terrain. Part IV: Three-dimensional numerical simulation. *J. Atmos. Sci.*, **43**, 894-912.

Vasiloff, S.V., E.A. Brandes, R.P. Davies-Jones, and P.S. Ray, 1986: An investigation of the transition from multicell to supercell storms. *J. Climate Appl. Meteor.*, **25**, 1022-1036.

Verlinde, J., P.J. Flateau, and W.R. Cotton, 1990: Analytical solutions to the collection growth equation. Comparison with approximate methods and application to cloud microphysics parameterization schemes. *J. Atmos. Sci.*, **47**, 2871-2880.

Vertez, M., 1992: *The Contribution of the Field Analysis of Barometric Trends to the Forecasting of Thunderstorms*. Institut Royal Meteorologique de Belgique, Publications Serie A, No. 129, 61pp.

Walko, R.L., W.R. Cotton, M.P. Meyers, and J.Y. Harrington, 1995: New RAMS cloud microphysics parameterization. Part I: the single-moment scheme. *Atmos. Res.*, **38**, 29-62.

Weaver, J.F., and S.P. Nelson, 1982: Multiscale aspects of thunderstorm gust fronts and their effects on subsequent storm development. *Mon. Wea. Rev.*, **110**, 707-718.

Weisman, M.L., and H.B. Bluestein, 1985: Dynamics of numerically simulated LP storms. Preprints, *14th Conf. on Severe Local Storms*, Indianapolis, IN, Amer. Meteor. Soc., 167-170.

Weisman, M.L., and J.B. Klemp, 1982: The dependence of numerically simulated convective storms on vertical wind shear and buoyancy. *Mon. Wea. Rev.*, **110**, 504-520.

Weisman, M.L., and J.B. Klemp, 1984: The structure and classification of numerically simulated convective storms in directionally varying wind shears. *Mon. Wea. Rev.*, **112**, 2479-2498.

Weisman, M.L., J.B. Klemp, and L.J. Miller, 1983: Modeling and Doppler analysis of the CCOPE August 2 supercell storm. Preprints, *13th Conf. on Severe Local Storms*, Tulsa, OK, Amer. Meteor. Soc., 223-226.

Weisman, M.L., and R. Rotunno, 2000: The use of vertical wind shear versus helicity in interpreting supercell dynamics. J. Atmos. Sci., 57, 1452-1472.

Wicker, L.J., and R.B. Wilhelmson, 1995: Simulation and analysis of tornado development and decay within a three-dimensional supercell thunderstorm, *J. Atmos. Sci.*, **52**, 2675-2703.

Wilhelmson, R.B., and J.B. Klemp, 1978: A numerical study of storm splitting that leads to long-lived storms. *J. Atmos. Sci*, **35**, 1974-1986.

Wilhelmson, R.B., and J.B. Klemp, 1981: A three-dimensional numerical simulation of splitting severe storms on 3 April 1964. *J. Atmos. Sci.*, **38**, 1581-1600.